FINITE ELEMENT ANALYSIS OF MOMENT CONNECTIONS WITH STEEL SHEAR DAMPERS OF DIFFERENT GEOMETRY

MOHAMMAD IRFAN HOSSAIN

MASTER OF SCIENCE IN CIVIL ENGINEERING (STRUCTURAL)

DEPARTMENT OF CIVIL ENGINEERING

BANGLADESH UNIVERSITY OF ENGINEERING AND TECHNOLOGY, DHAKA

AUGUST, 2020

FINITE ELEMENT ANALYSIS OF MOMENT CONNECTIONS WITH STEEL SHEAR DAMPERS OF DIFFERENT GEOMETRY

By

MOHAMMAD IRFAN HOSSAIN

Student ID No.: 1017042343 P

A thesis submitted to Department of Civil Engineering,
Bangladesh University of Engineering and Technology, Dhaka
in partial fulfillment of the requirements for the degree of

MASTER OF SCIENCE IN CIVIL ENGINEERING
(STRUCTURAL)

DEPARTMENT OF CIVIL ENGINEERING
BANGLADESH UNIVERSITY OF ENGINEERING AND TECHNOLOGY, DHAKA

AUGUST, 2020

The thesis titled "Finite Element Analysis of Moment Connections with Steel Shear Dampers of Different Geometry" submitted by Mohammad Irfan Hossain, Roll No.: 1017042343 P, Session: October, 2017 has been accepted as satisfactory in partial fulfillment of the requirement for the degree of Master of Science in Civil Engineering (Structural) on August 31, 2020.

BOARD OF EXAMINERS

Dr. Khan Mahmud Amanat
Professor,
Department of Civil Engineering,
BUET, Dhaka-1000.

Chairman
(Supervisor)

Dr. Md. Habibur Rahman
Professor and Head,
Department of Civil Engineering,
BUET, Dhaka-1000.

Member
(Ex-Officio)

Dr. Raquib Ahsan
Professor,
Department of Civil Engineering,
BUET, Dhaka-1000.

Member

Dr. Nazrul Islam
Assistant Professor,
Department of Civil Engineering,
BUET, Dhaka-1000.

Member

Lt Col Khondaker Sakil Ahmed, PhD
Associate Professor,
Department of Civil Engineering,
MIST, Mirpur Cantonment, Dhaka-1216.

Member
(External)

DECLARATION

It is hereby declared that, except where specific references to other works are made, the research work presented in this thesis has been performed by the author under the supervision of Dr. Khan Mahmud Amanat, Professor, Department of Civil Engineering, BUET and this thesis or any part of it has not been submitted elsewhere for any other purposes except for research publication.

Mohammad Irfan Hossain

Student ID: 1017042343 P

Date: 31.08.2020

ACKNOWLEDGEMENT

I express my gratitude to ALMIGHTY ALLAH for His blessing and mercy, which has enabled me to accomplish my thesis as a requirement for the degree of Master of Science in Civil Engineering (Structural). Without His grace, this work could not become a reality.

Next to Him are my parents, whom I am greatly indebted for bringing me up with love and encouragement to this stage. I would also like to thank my sister for her continuous support.

I am feeling oblige in taking the opportunity to sincerely thanks to my supervisor Dr. Khan Mahmud Amanat, Professor, Department of Civil Engineering, Bangladesh University of Engineering and Technology (BUET), Dhaka, who has the attitude and the substance of a genius; he continually and convincingly conveyed a spirit of adventure in regard to research and scholarship; and an excitement in regard to teaching. Without his guidance and persistent help this dissertation would not have been possible. One simply could not wish for a better or friendlier supervisor. I will remain ever grateful to him for his supervision and inspiration to work hard in writing this thesis.

Besides, my sincere gratefulness to all the teachers of Department of Civil Engineering, BUET for their entire effort to teach the subjects of Civil Engineering.

At last but not the least I am thankful to all my friends and well-wishers who have been always helping and encouraging me throughout the year.

ABSTRACT

Since late 90s, extensive researches have been conducted on the use of various materials and systems that will absorb seismic energy within the structure itself in order to improve the behavior of the steel structures under seismic effects. In order to address the issue, an innovative structural system with steel shear damper was developed, which could not only provide good seismic performance but also could easily be repaired after a major earthquake. Numerous studies are being carried out with different types of shear dampers around the world. However, interchangeability in the use of such various forms of dampers is yet to be established. Besides, steel shear dampers are not still widely used and its provisions are not included in the codes. Further regularization of existing dampers are also needed. Hence more researches are required regarding steel shear dampers.

In the present study, three-dimensional finite element models are developed considering both material and geometric nonlinearity for investigating the behavior of seismic moment connection system with steel shear dampers of different geometry. The developed finite element models have been used to simulate experimental studies done by past researchers for static cyclic loading and it has been found that good agreements exist between present analysis and past experimental results, which established the acceptability and validity of the present finite element models to carry out further investigation.

Study is then carried on shear dampers made of mild steel and having different geometry such as elliptical steel slit damper, butterfly-shaped steel strut damper and pintle damper to find out equivalency of these with oblong steel slit damper having similar plastic strength. Study shows that the existing formulas for predicting plastic strength of these dampers may not be accurate and further refinement is warranted. Some parametric studies have been performed to observe the effects of different parameters such as strut width, strut height, thickness etc. Based on the pattern of parametric study results, closed-form semi-empirical algebraic expression of damper plastic strength is developed for these shear dampers which shows realistic compliance with analysis results. The results of the parametric studies have been compared with energy quantities and presented graphically to better understand the effects of different parameters on the system. It has been shown that the plastic strength predicted by these closed-form semi-empirical analytical expressions are reasonably accurate as found from numerical finite element simulation of experimental results. The proposed expressions of plastic strength of various types of dampers shall enable us to use any one type alternately in a building for earthquake protection of structures.

TABLE OF CONTENTS

LIST OF ABBREVIATIONS

ADAS	Added Damping and Stiffness
AISC	American Institute of Steel Construction
ANSYS	Analysis System
BFP	Bolted Flange Plate
BRB	Buckling Restrained Brace
BSSD	Butterfly-shaped Steel Strut Damper
CBF	Concentrically Braced Frame
CJP	Complete Joint Penetration
DFMD	Dual Function Metallic Damper
DPD	Dual-Pipe Damper
EBF	Eccentrically Braced Frame
ESSD	Elliptical Steel Slit Damper
FEA	Finite Element Analysis
FEM	Finite Element Method
FEMA	Federal Emergency Management Agency
HSD	Hysteretic Steel Damper
IPD	Infilled-Pipe Damper
KBB	Kaiser Bolted Bracket
MRF	Moment Resisting Frame
OSSD	Oblong Steel Slit Damper
PD	Pintle Damper
RBS	Reduced Beam Section
RC	Reinforced Concrete
SHS	Square Hollow Section
SSD	Steel Slit Damper
SW	Slotted Web

TADAS	Triangular-plate Added Damping and Stiffness
WHP	Web-Hourglass Pin
WUF-W	Welded Unreinforced Flange-Welded Web
YBS	Yielding Bracing System
YSPD	Yielding Shear Panel Device

LIST OF SYMBOLS

A	width of the strut at middle
B	width of the strut at end
B_{eff}	effective width of the strut
b_x	half width of the strut
C_i	hardening modulus for i^{th} kinematic model of Chaboche model
D	diameter of the damper
D_{max}	maximum value of the displacement
E	Young's modulus
E_D	dissipated energy of the last loading cycle
E_{S0}	equivalent static energy
F_{max}	maximum value of the force
H	height of the strut
H'	net height of the strut
H_T	total height of the strut
K_{damper}	lateral stiffness of the damper
L	length of the damper
M	maximum moment of the damper
M_p	plastic moment of the damper
n	number of the struts
P_p	plastic strength of the damper
Pu	ultimate strength of the damper
P_y	yield strength of the damper
R	yield stress
r	fillet radius of the slit
s	deviatoric stress
t	thickness of the damper

Z_x	plastic section modulus
σ_{max}	maximum stress of the damper with variable cross section
σ_y	yield stress of the steel
σ_u	ultimate stress of the steel
α	back stress
δ_y	yield displacement of the damper
ε_{eq}	equivalent damping ratio
ε^{pl}	accumulated plastic strain
ε_y	yield strain of the steel material
θ	temperature
υ	Poisson's ratio
γ_i	decreasing rate of hardening modulus for i^{th} kinematic model of Chaboche model

CHAPTER 1
INTRODUCTION

1.1 GENERAL

The research and development of structural control against wind and earthquake excitation have achieved significant progress over the last few decades (Soong and Spencer 2002). Structural control can broadly be classified into three categories: (i) Passive control systems are those structures equipped with designated devices or dampers which do not require an external source of power, (ii) Active control systems are those structures equipped with real-time processing sensors and force delivery devices which require an external source of power to generate structural control forces, and (iii) Semi-active control systems which use little power to change certain structural parameters. Passive control systems, also known as passive energy dissipation systems, have been considered an effective and inexpensive way to mitigate earthquake risks to structures. With designated energy dissipative devices installed in a structure, a large portion of the input energy supplied by wind and/or earthquake can be dissipated; hence the damage to the parent structure is minimized. Passive devices do not require an external source of power, hence the reliability associated with power supply and computer control during an earthquake event is eliminated. By arranging the devices in a way that facilitates replacement, damaged devices can be replaced with minimum time and cost, hence interruption to human occupancy is minimized which is a crucial benefit to the building owners and occupants (Chan and Albermani 2008).

Structures built throughout history were damaged by the earthquakes that caused devastating property damage and loss of lives. Therefore, different solutions to minimize the destructive effects of earthquakes were proposed with the adoption of technological advances of the last century. Energy dissipation can be achieved by a number of mechanisms: friction sliding, yielding of metals, phase transformation of metals, fluid orificing and deformation of viscoelastic solid or fluid. Structural control mechanisms based on the principle of damping the seismic energy through non-structural members were developed. Among these members, metallic dampers are economical, easy-to-produce, and can effectively dissipate seismic energy through hysteretic behavior. In particular, one of the most popular mechanisms for dissipation of energy input to a structure is through the

yielding of metallic materials. The research in metallic passive energy dissipative devices has been conducted over the last few decades. The use of metallic dampers attracted the attention of researchers, especially after the unexpected damages to the joints of the steel framed structures in the Northridge (1994) and Kobe (1995) earthquakes (Chan and Albermani 2008).

1.2 BACKGROUND AND RESEARCH SIGNIFICANCE

For many years, the basic intent of the building code seismic provisions has been to provide buildings with an ability to withstand intense ground shaking without collapse, but potentially with some significant structural damage. In order to accomplish this, one of the basic principles inherent in modern code provisions is to encourage the use of building configurations, structural systems, materials and details that are capable of ductile behavior. A structure behaves in a ductile manner if it is capable of withstanding large inelastic deformations without significant degradation in strength, and without the development of instability and collapse. Generally, structural systems with more ductility are designed for lower forces than less ductile systems, as ductile systems are deemed capable of resisting demands that are significantly greater than their elastic strength limit (FEMA-351 2000).

Starting in the 1960s, engineers began to regard welded steel moment-frame buildings as being among the most ductile systems contained in the building code. Many engineers believed that welded steel moment-frame buildings were essentially invulnerable to earthquake-induced structural damage and thought that should such damage occur, it would be limited to ductile yielding of members and connections. Earthquake-induced collapse was believed to be avoidable. Partly as a result of this belief, many industrial, commercial and institutional structures employing welded steel moment-frame systems were constructed, particularly in the western United States (FEMA-351 2000).

The Northridge earthquake of January 17, 1994 challenged this paradigm. Following that earthquake, a number of welded steel moment-frame buildings were found to have experienced brittle fractures of beam-to-column connections. The damaged buildings had heights ranging from one story to 26 stories, and a range of ages spanning from buildings as old as 30 years to structures being erected at the time of the earthquake. The damaged buildings were spread over a large geographical area, including sites that experienced only

moderate levels of ground shaking. Although relatively few buildings were located on sites that experienced the strongest ground shaking, damage to buildings on these sites was extensive. Discovery of these unanticipated brittle fractures of framing connections, often with little associated architectural damage to the buildings, was alarming to engineers and the building industry. The discovery also caused some concern that similar, but undiscovered, damage may have occurred in other buildings affected by past devastating earthquakes. The Kobe earthquake, occurred on January 17, 1995 in the southern part of Hyogo Prefecture, Japan, including the region known as Hanshin. Up to 6,434 people lost their lives; about 4,600 of them were from Kobe. Damage was extremely widespread and severe. Structures irreparably damaged by the quake included nearly 400,000 buildings, numerous elevated road and rail bridges, and 120 of the 150 quays in the port of Kobe (FEMA-351 2000).

After the Northridge (1994) and Kobe (1995) earthquakes important experimental programs on beam-to-column connections were developed because of brittle fractures at welded beam-to-column connections. A number of studies are being carried out on a variety of materials and systems that dissipate the seismic loading effects in order to improve the seismic performance of steel frames. Many investigations have been performed in order to solve the problem of low rotational capacity of steel moment connections (Saffari et. al 2013). Yielding of metallic materials is one of the most popular passive control mechanisms for dissipating seismic energy (Zhang et al. 2015). To improve seismic performance of the connections, numerous metallic devices have been proposed such as the ADAS (Bergman and Goel 1987, Bayat and Bayat 2014), honeycomb damper (Kobori et al. 1992), TADAS (Tsai et al. 1993), steel shear panel (Nakashima et al. 1994, Zahrai 2015), steel slit damper (SSD) (Wada et al. 1997), pipe damper (Maleki and Bagheri 2010a, b), U-shaped damper (Tagawa and Gao 2012) and dual pipe damper (Maleki and Mahjoubi 2013). Excellent hysteretic behavior, easy accessibility, simple replacement after earthquake and low fabrication costs are some of advantages of steel slit dampers (Chan and Albermani 2008). Slit devices can be used at different configurations such as bracing joints (Lee et al. 2002, Chan and Albermani 2008), beam-to-column connections (Oh et al. 2009) and steel slit walls as fuses (Ke and Yam 2016, Ke and Chen 2014).

Thus, after a damage-inflicting earthquake, damper elements will not only prevent serious damage to the structure and loss of lives and property, but also it will ensure that the

structure can be repaired and made serviceable as soon as possible with minimal cost by replacing the dampers. However, the stress distribution and energy dissipation during fracture caused by earthquake vary for different types of shear dampers. So, there is further scope of research for identifying the most effective steel shear dampers of different geometry and types of steel to serve the purpose suitably and economically. Nowadays steel structures are accepted as more ductile systems over reinforced concrete structures in our country. Besides, steel shear damper is not widely used and its provision is not included in code and so more researches are needed regarding it. Hence it is essential to find out the dissimilation of shear dampers of different geometry and types of steel with respect to their strength, rigidity and ductility for providing the best seismic performance by numerical analysis and parametric studies as performing experiments on steel structure are very expensive.

1.3 OBJECTIVES OF THE PRESENT STUDY

The specific objectives of the research are as follows:

(i) To investigate the hysteretic behavior of steel shear dampers of different geometry at seismic moment connections of steel frame structures.
(ii) To find out the equivalency of steel shear dampers of different geometry and develop more refined procedure for calculating the plastic strength of the dampers.
(iii) To increase the applicability of steel shear dampers and observe the seismic performance at beam-column connections.

The proposed research work will enable to identify the equivalency of steel shear dampers of different geometry so that they can be alternatively replaced with others, determine the plastic strength of the shear dampers more precisely and recognize new uses of steel shear dampers paving the path for mitigating the damage due to earthquakes in Bangladesh.

1.4 SCOPES OF THE STUDY

The primary objective of the study is to find the equivalency of steel shear dampers of different geometry so that they can be used alternatively with each other. The aimed study will have the following limitations:

a) The buckling phenomenon of the steel shear dampers will not be considered in the developed plastic strength equation.

b) The maximum displacement of the shear dampers up to fracture will not be regarded.
c) The finite element models will not include the time rate dependency in the material modeling.
d) The damage or failure modeling will not be incorporated in the numerical models. Only elasto-plastic material behavior shall be considered.
e) The steel shear dampers will be investigated only for in-plane flexural behavior.
f) The slip-critical connection of bolts will be simulated by coupling of nodes instead of solid bolt.

1.5 METHODOLOGY OF THE STUDY

Three-dimensional finite element models for seismic moment connection of Moment Resisting Frame (MRF) with steel shear dampers of different geometry will be developed using solid brick finite elements considering both material and geometric non-linearity. The finite element models will be validated against past researches to establish the reliability of finite element analysis scheme. Various steel shear dampers of different geometry will be analyzed numerically to investigate their responses due to static cyclic loading. Energy dissipation, rigidity and other characteristics of shear dampers of different geometry will also be studied as a part of finite element simulation. The different types of shear dampers will be compared according to their hysteretic behavior to find the equivalency among them based on the plastic strength of the dampers. New application of steel shear damper will also be introduced for the beam-column connection which can be a substitute of existing dampers to mitigate the earthquake damage. Finally attempts will be made to develop more reformed semi-empirical formula for calculating the plastic strength of the shear dampers with reasonable accuracy.

1.6 ORGANIZATION OF THE THESIS

The research works performed in this study are divided into different topics and presented in seven Chapters so as to best discuss the problem and the resulting findings of the investigation.

Chapter 1 introduces a brief introduction to the background, statement of the present study, the objective and scope of the thesis along with brief description of the research plan.

Chapter 2 reviews the available literature that is required to understand the background theories of moment connections and steel shear dampers of different geometry.

Chapter 3 presents the finite element methodology used in the present study. The chapter describes the modeling, meshing, boundary conditions, coupling and load applications used in the finite element analysis.

Chapter 4 is concerned with the verification of the model developed in Chapter 3 with reference to experimental studies and finite element analysis results carried out by past researches.

Chapter 5 is based on the numerical study of moment connection for steel shear dampers of different geometry to find out equivalency of these with the aid of figures and tables followed by some discussions on the obtained results. It also presents the parametric study to develop the closed-form semi-empirical algebraic expression of plastic strength for the dampers.

Chapter 6 verifies the performance of the proposed equations for the plastic strength of dampers by comparing the finite element analysis results with existing researches and also presents the comparative study of different shear dampers with the developed semi-empirical analytical formulation.

Chapter 7, the concluding chapter, summarizes the entire research work and makes some recommendations for future research.

CHAPTER 2
LITERATURE REVIEW

2.1 INTRODUCTION

Since the introduction of structural steel to building construction, in the late 19th and early 20th centuries, engineers have recognized that steel buildings and structures have performed well in seismic events compared with structures of other types of construction. The observation of the good performance of steel frame structures in the 1906 San Francisco earthquake led to the requirement in present-day building codes that tall structures must have complete vertical load carrying frames. By the early 1990s, many engineers in the western United States believed that steel structures were inherently ductile and, as a result, essentially less vulnerable to earthquake damage. This was reflected in the requirements of building codes of the era. Steel frame structures were permitted to be designed for smaller earthquake forces than buildings of other construction types. Also, relatively few limitations were prescribed on the types of configurations and detailing that could be employed in such structures, relative to the requirements for other types of construction.

The magnitude 6.7 Northridge earthquake that struck the San Fernando Valley, just to the north of Los Angeles, on January 17, 1994, changed this perception. Following the Northridge earthquake, engineers began to discover that a number of steel frame buildings, including both moment frames and braced frames, had experienced significant structural damage, including buckling and fracture of braces in braced frames, and fractures of beam-to-column connections in welded steel moment frames. The damage sustained by moment frame structures was particularly alarming as it became evident that rather than behaving in a ductile manner, these fractures had occurred in a brittle manner. Although no steel frame buildings collapsed in the Northridge earthquake, just one year later, more than 50 steel buildings collapsed in the magnitude 6.8 Kobe, Japan, earthquake of January 17, 1995. These two events led to massive programs of research into the seismic behavior of steel frame structures, both in Japan and the United States. This research quickly fed into the building codes, and by 1997, the American Institute of Steel Construction (AISC) published a new edition of its Seismic Provisions for Structural Steel Buildings that contained many new requirements affecting materials, the design and construction of steel structures

intended to resist strong earthquakes. In order to design and construct steel structures to resist strong earthquakes, it is necessary to have an understanding of structural dynamics and the nonlinear behavior of structures. Structural steel continues to offer several economical and effective means for the design and construction of earthquake-resistant structures (AISC 2009).

Since it is important to restore buildings and the functions of the affected urban area as quickly as possible after an earthquake, a damage-controlled structure was proposed that uses passive energy dissipation devices (Wada et al. 1992). Passive energy dissipation systems have been considered as an effective and inexpensive way to mitigate earthquake risks to structures. Since the Northridge earthquake (1994), passive damping technologies have been increasingly taken into consideration in the USA, and since the Kobe earthquake (1995) in Japan, more buildings have been designed to include dampers. The main reason for using passive energy dissipation devices in a structure is to limit the number of damaging deformations in structural components. Among the available varieties of passive energy dissipation devices, the metallic-hysteretic damper is one of the most effective and economical mechanisms for the dissipation of seismic energy input, which is obtained through the inelastic deformation of metallic material (Oh et al. 2009).

2.2 SEISMIC DESIGN CONCEPT FOR STEEL STRUCTURES

The primary objective of conventional building code philosophy for earthquake-resistant design is to save human life by preventing collapse in the extreme earthquake likely to occur at a building site. The objectives are not to limit damage, maintain function and provide for easy repair. In order to survive strong earthquake without collapse it is mandatory to design for ductile behavior of structures. Ductility describes the extent to which a material (or structure) can undergo large deformations without failing. The term is used in earthquake engineering to designate how well a building will endure large lateral displacements imposed by ground shaking (Engelhardt 2007).

2.2.1 Seismic Load Resisting Systems for Steel Buildings

2.2.1.1 Moment Resisting Frame (MRF)

A moment resisting frame is a special type of frame with no diagonal bracing that uses rigid connections between each of its constituent members. Beams and columns with moment

resisting connections; resist lateral forces by flexure and shear in beams and columns i.e. by frame action. Moment resisting frame develops ductility primarily by flexural yielding of the beams (Engelhardt 2007).

It is preferred for its architectural versatility and high ductility. The main disadvantage of moment resisting frame is low elastic stiffness of the members Fig. 2.1 illustrates a moment resisting frame.

Fig. 2.1: Moment Resisting Frame (MRF) (Engelhardt 2007)

2.2.1.2 Concentrically Braced Frame (CBF)

A concentrically braced frame is a type of frame where beams, columns and braces are arranged to form a vertical truss. This frame resists lateral earthquake forces by truss action. It develops ductility through inelastic action in braces by yielding in tension buckling in compression (Engelhardt 2007).

It is favored for its high elastic stiffness. The demerits of this type of frame are it is less ductile than other systems and it reduces architectural versatility. A concentrically braced frame is depicted in Fig. 2.2.

Fig. 2.2: Concentrically Braced Frame (CBF) (Engelhardt 2007)

2.2.1.3 Eccentrically Braced Frame (EBF)

Eccentrically braced frame is a framing system with beam, columns and braces which is shown in Fig. 2.3. At least one end of every brace is connected to isolate a segment of the beam called a link. This frame resists lateral load through a combination of frame action and truss action. EBFs can be viewed as a hybrid system between moment frames and concentrically braced frames. It develops ductility through inelastic action in the links.

EBFs can supply high levels of ductility (similar to MRFs) but can also provide high levels of elastic stiffness (similar to CBFs) (Engelhardt 2007).

Fig. 2.3: Eccentrically Braced Frame (EBF) (Engelhardt 2007)

2.2.2 Protected Zone

The region at structural members subject to inelastic straining is designated as a protected zone. Earthquake energy will be dissipated in this zone by means of cyclic behavior. The portions of the seismic load resisting system designated as a protected zone, shall comply with the following: (Engelhardt 2007)

i. No welded shear studs are permitted.
ii. No decking attachments that penetrate the beam flange are permitted (no powder actuated fasteners); but decking arc spot welds are permitted.
iii. No welded, bolted, screwed, or shot-in attachments for edge angles, exterior facades, partitions, duct work, piping, etc. are permitted.
iv. Discontinuities from fabrication or erection operations (such as tack welds, erection aids, etc.) shall be repaired.

The examples of protected zones for MRF, CBF and EBF are illustrated in Figs. 2.4-2.6 respectively.

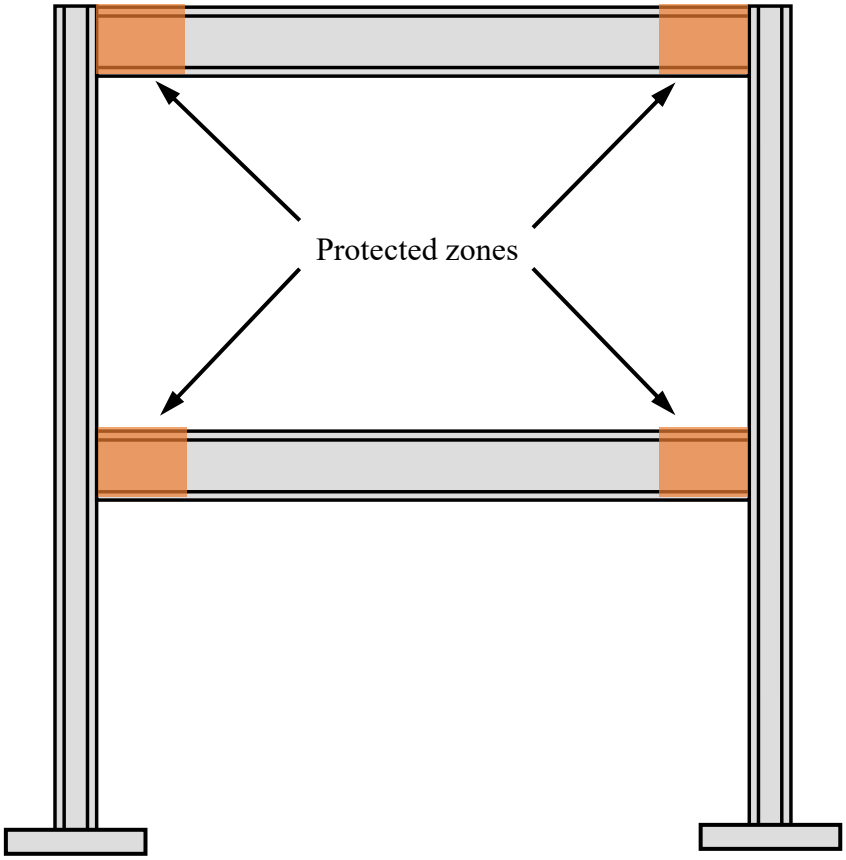

Fig. 2.4: Protected zone of moment resisting frame (Engelhardt 2007)

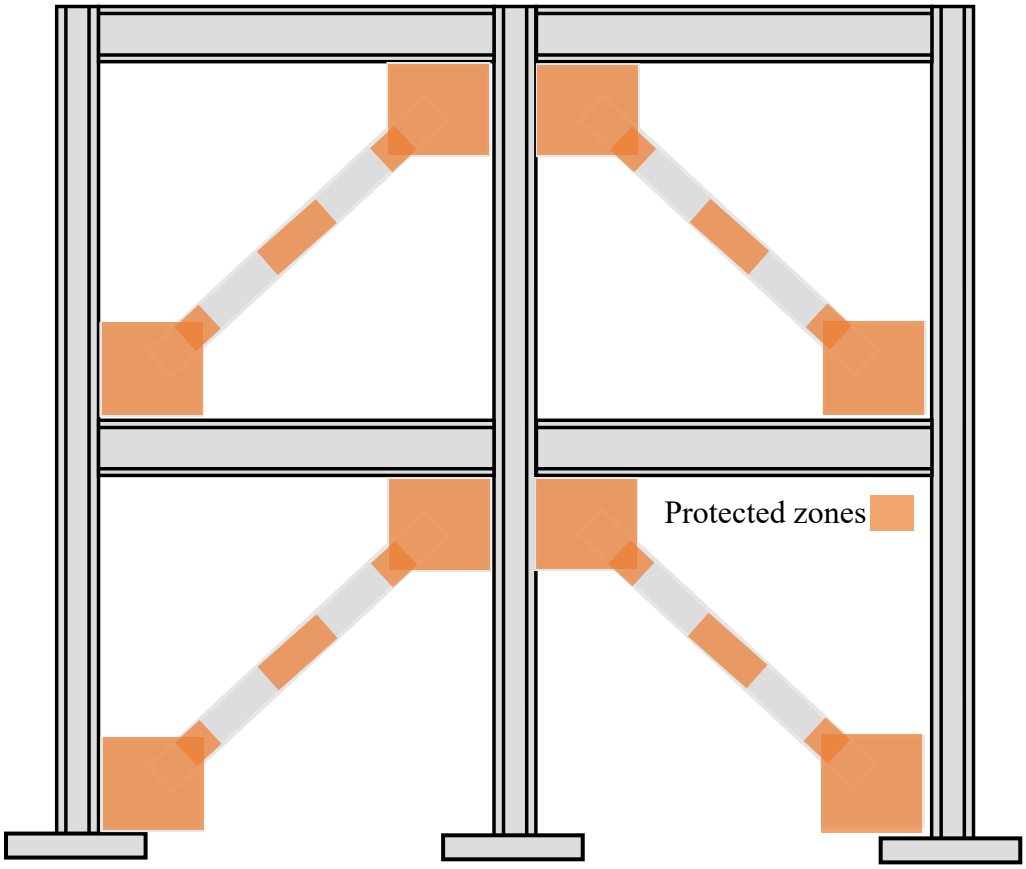

Fig. 2.5: Protected zone of concentrically braced frame (Engelhardt 2007)

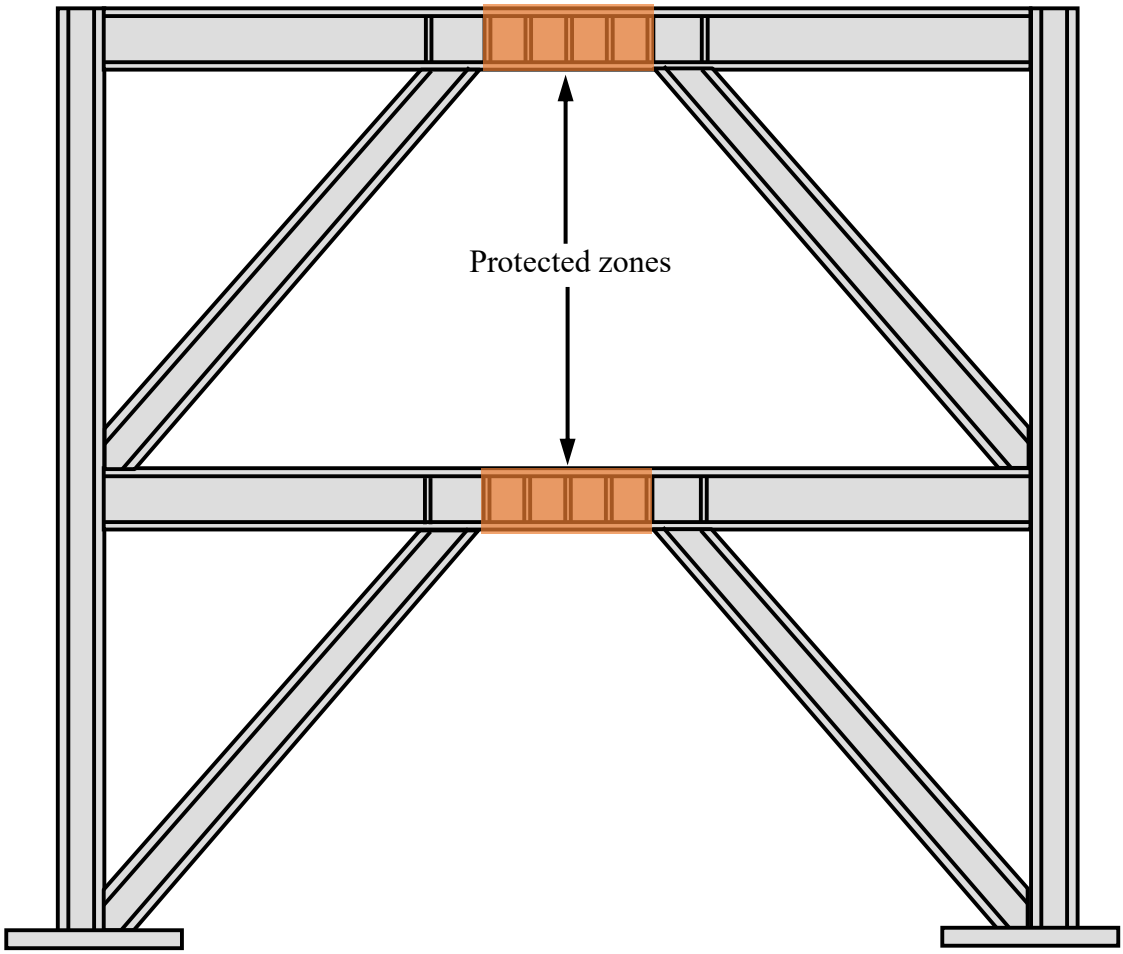

Fig. 2.6: Protected zone of eccentrically braced frame (Engelhardt 2007)

2.2.3 Prequalified Connections for Steel Moment Frames

A moment connection in structural engineering is a joint that allows the transfer of bending moment forces between a column and beam (or any other two members). If a child member (a beam) has some internal moment, the connection should be able to transmit the load due to that moment. The objective of moment connections is to simulate as close as possible a fixed joint, denoted by the fixity code – meaning the connection is rigid in all translation and rotational directions. Some prequalified connections for steel moment frames according to AISC (2016) seismic provisions are narrated below:

2.2.3.1 Reduced Beam Section (RBS) Moment Connection

In a reduced beam section (RBS) moment connection (Fig. 2.7), portions of the beam flanges are selectively trimmed in the region adjacent to the beam-to-column connection. Yielding and hinge formation are intended to occur primarily within the reduced section of the beam (AISC 2016).

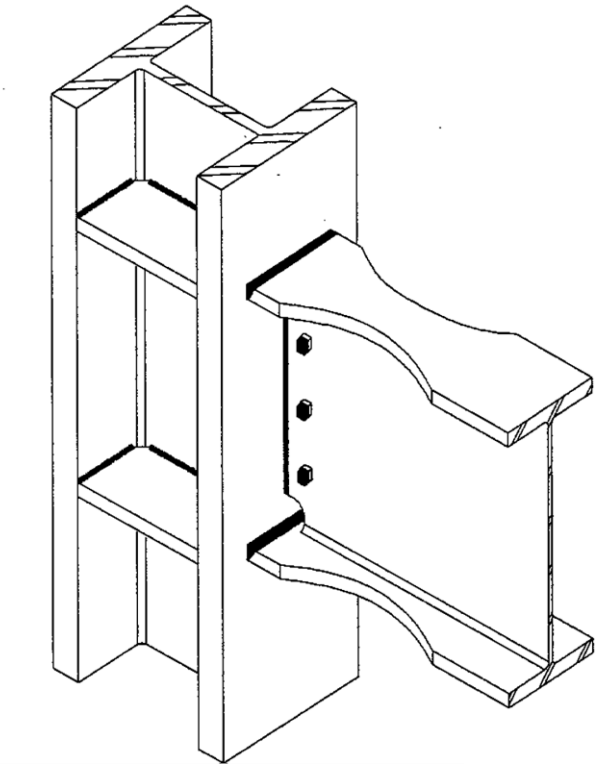

Fig. 2.7: Reduced beam section connection (AISC 2016)

2.2.3.2 Extended End-Plate Moment Connection

Bolted end-plate connections are made by welding the beam to an end-plate and bolting the end-plate to a column flange. The three end-plate configurations shown in Fig. 2.8.

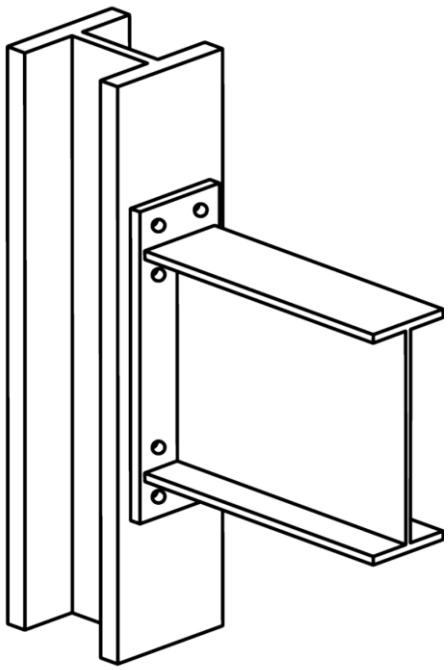

Fig. 2.8: Extended end-plate configuration (AISC 2016)

The behavior of this type of connection can be controlled by a number of different limit states including flexural yielding of the beam section, flexural yielding of the end-plates, yielding of the column panel zone, tension rupture of the end-plate bolts, shear rupture of the end-plate bolts, or rupture of various welded joints (AISC 2016).

2.2.3.3 Bolted Flange Plate (BFP) Moment Connection

Bolted flange plate (BFP) moment connections utilize plates welded to column flanges and bolted to beam flanges. The top and bottom plates must be identical. Flange plates are welded to the column flange using CJP groove welds and beam flange connections are made with high-strength bolts. The beam web is connected to the column flange using a bolted shear tab with bolts in short-slotted holes. Details for this connection type are shown in Fig. 2.9. Initial yielding and plastic hinge formation are intended to occur in the beam in the region near the end of the flange plates (AISC 2016).

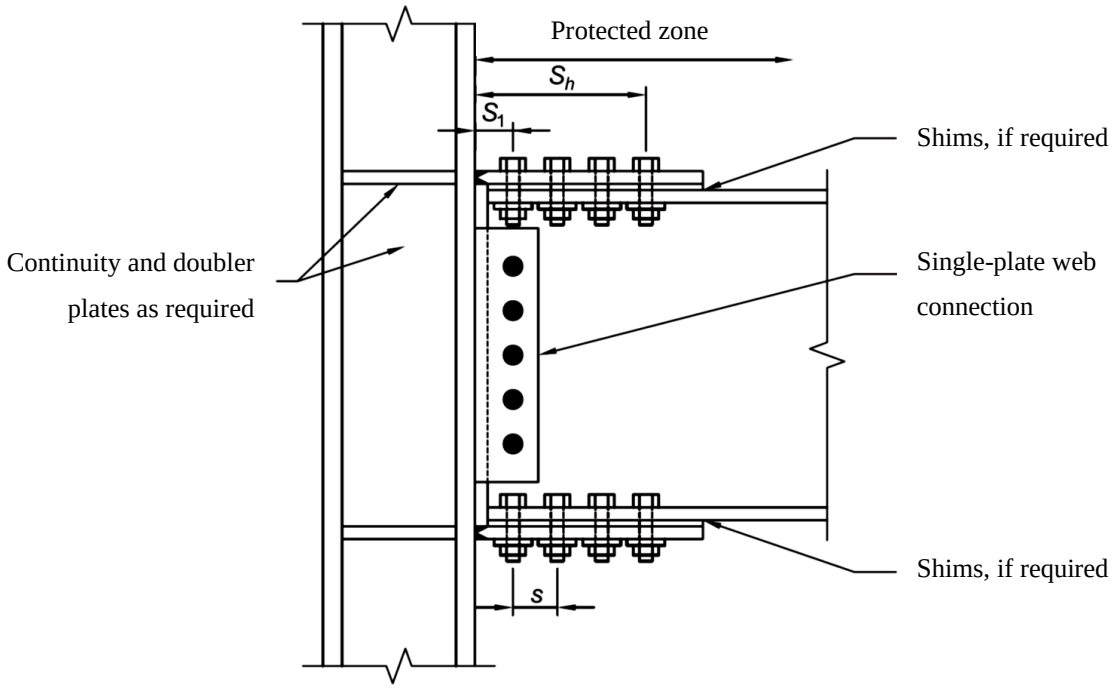

Fig. 2.9: Bolted flange plate moment connection (AISC 2016)

2.2.3.4 Welded Unreinforced Flange-Welded Web (WUF-W) Moment Connection

In the welded unreinforced flange-welded web (WUF-W) moment connection, inelastic rotation is developed primarily by yielding of the beam in the region adjacent to the face of the column. An overall view of this connection is shown in Fig. 2.10 (AISC 2016).

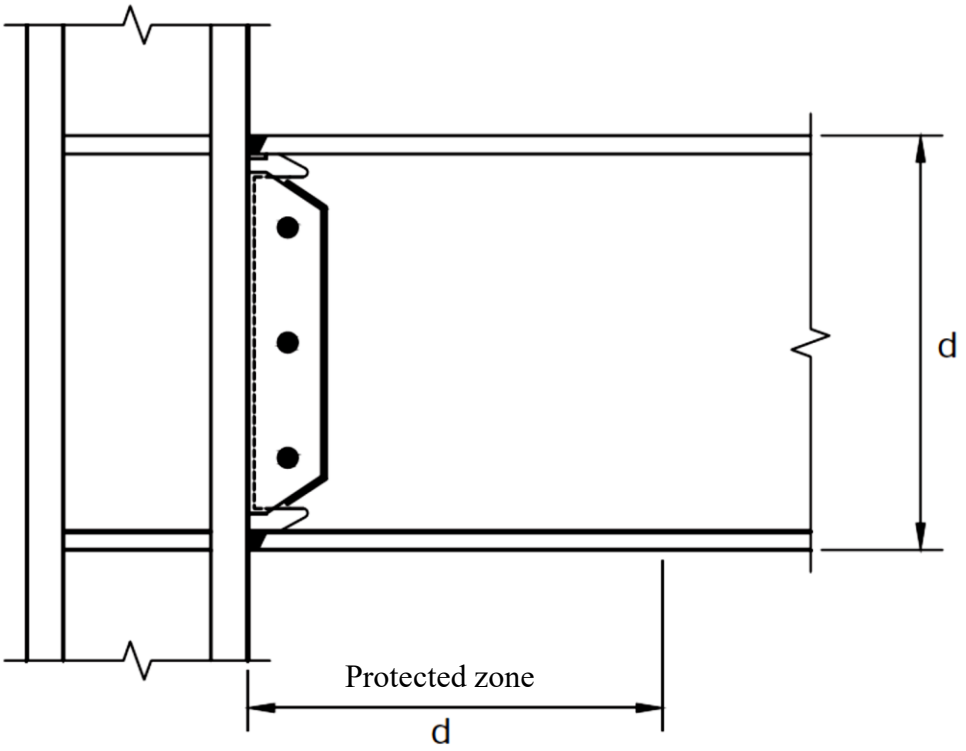

Fig. 2.10: WUF-W moment connection (AISC 2016)

2.2.3.5 Kaiser Bolted Bracket (KBB) Moment Connection

In a Kaiser bolted bracket (KBB) moment connection, a cast high-strength steel bracket is fastened to each beam flange and bolted to the column flange as shown in Fig. 2.11.

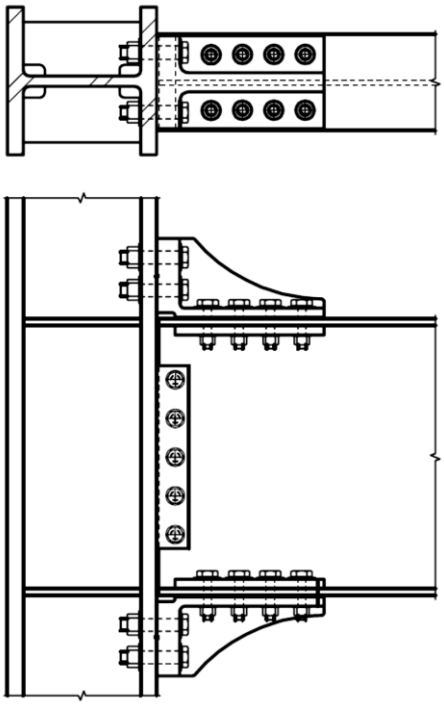

Fig. 2.11: Kaiser bolted bracket connection (AISC 2016)

The bracket configuration is proportioned to develop the probable maximum moment strength of the connected beam. Yielding and plastic hinge formation are intended to occur primarily in the beam at the end of the bracket away from the column face. (AISC 2016)

2.2.3.6 ConXtech ConXL Moment Connection

The ConXtech ConXL moment connection shown in Fig. 2.12 permits full-strength, fully restrained connection of wide-flange beams to concrete-filled 16-in. (400-mm) square HSS or built-up box columns using a high-strength, field-bolted collar assembly. ConXL connections may be used to provide moment connections to columns in orthogonal frames. The behavior of this connection is controlled by flexural hinging of the beams adjacent to the collar assembly (AISC 2016).

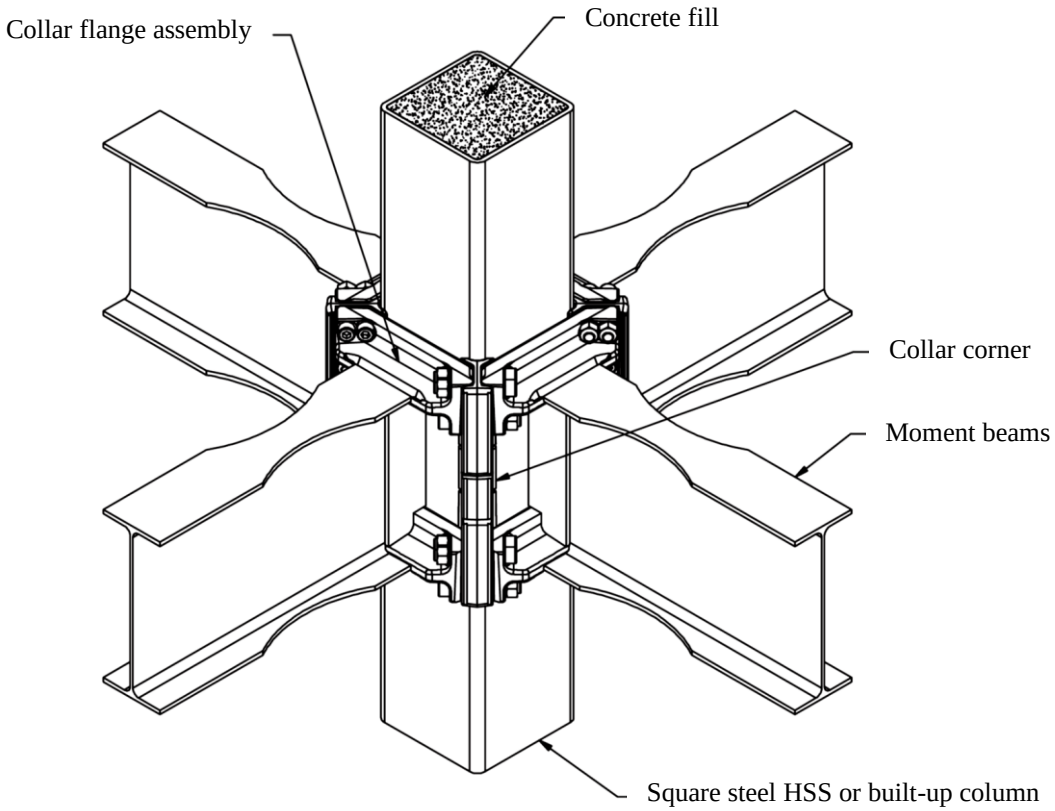

Fig. 2.12: Assembled ConXL moment connection (AISC 2016)

2.2.3.7 Sideplate Moment Connection

The sideplate moment connection depicted in Fig. 2.13 utilizes interconnecting plates to connect beams to columns. The connection features a physical separation, or gap, between the face of the column flange and the end of the beam. Both field-welded and field-bolted

options are available. This moment connection is proportioned to develop the probable maximum moment capacity of the connected beam. Plastic hinge formation is intended to occur primarily in the beam beyond the end of the side plates away from the column face, with limited yielding occurring in some of the connection elements (AISC 2016).

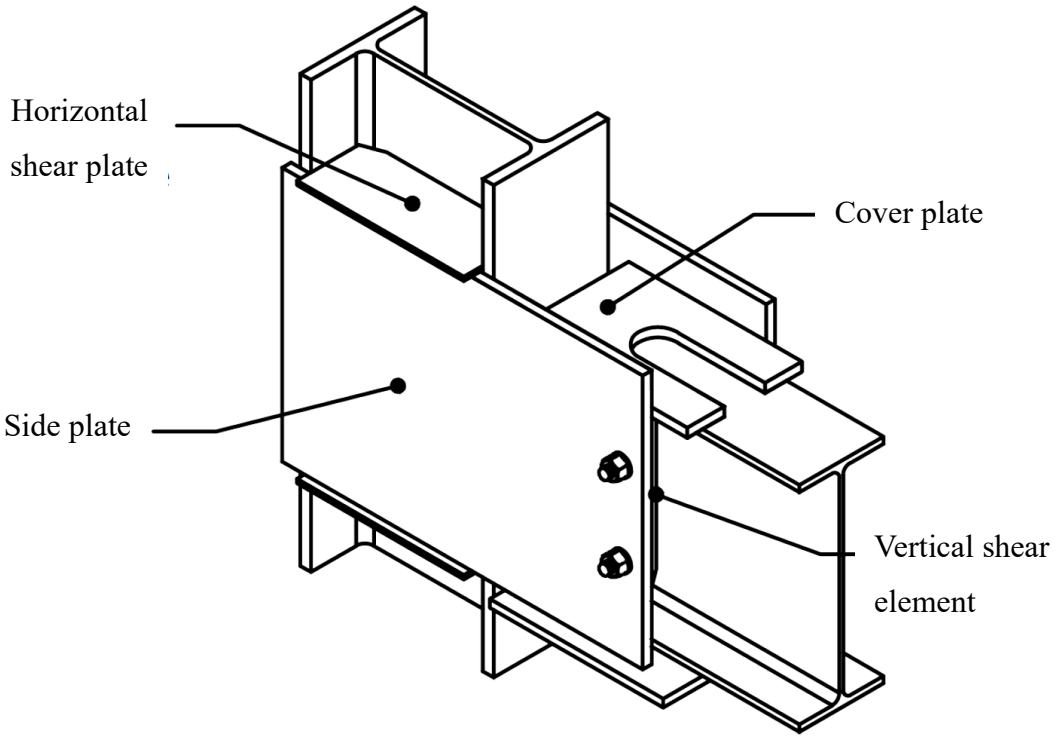

Fig. 2.13: Assembled sideplate configuration (AISC 2016)

2.2.3.8 Simpson Strong-Tie Strong Frame Moment Connection

The Simpson Strong-Tie Strong Frame moment connection is a partially restrained (Type PR) connection that uses a modified shear plate connection (single-plate shear connection) for shear transfer and a modified T-stub connection (the Yield-Link structural fuse) for moment transfer, as shown in Fig. 2.14. The shear plate utilizes a three-bolt connection wherein the upper and lower bolt holes in the shear plate are horizontal slots and the center bolt hole is a standard hole. Matching holes in the beam web are all standard holes. This prevents moment transfer through the shear plate connection. While all shear plate bolts participate in shear resistance, the center bolt is designed to also resist the axial force in the beam at the connection. The connection is based on a capacity-based design approach, wherein connection response remains elastic under factored load combinations, and seismic inelastic rotation demand is confined predominantly within the connection with little, if any, inelastic behavior expected from the members (AISC 2016).

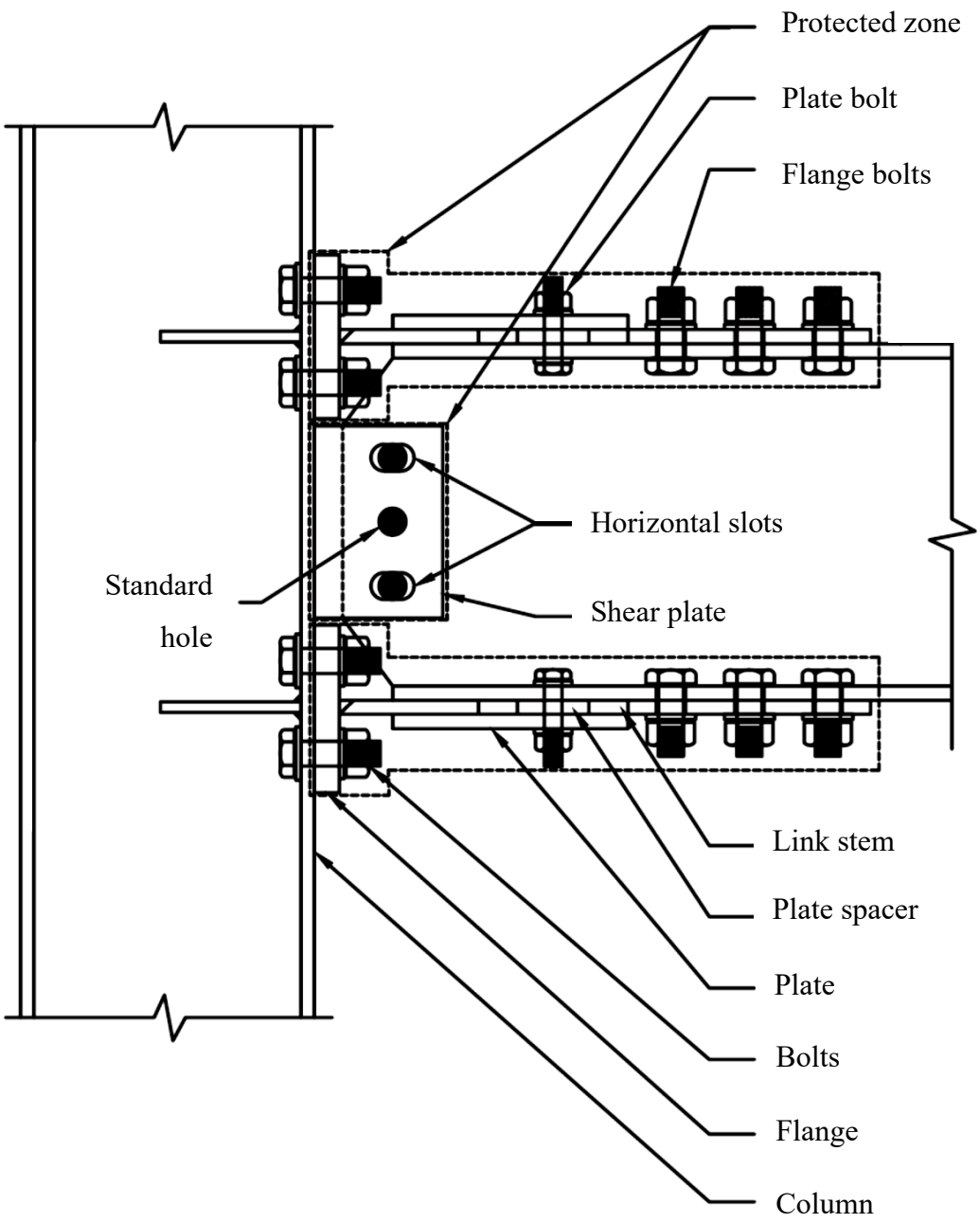

Fig. 2.14: Simpson Strong-Tie Strong Frame moment connection (AISC 2016)

2.2.3.9 Doble-Tee Moment Connection

Double-tee connections utilize T-stub components that are bolted to both the column flange and the beam flanges using high-strength bolts. The beam web is connected to the column with a bolted single-plate shear connection. A detail for this connection is shown in Fig. 2.15. Yielding and hinge formation are intended to occur in the beam (AISC 2016).

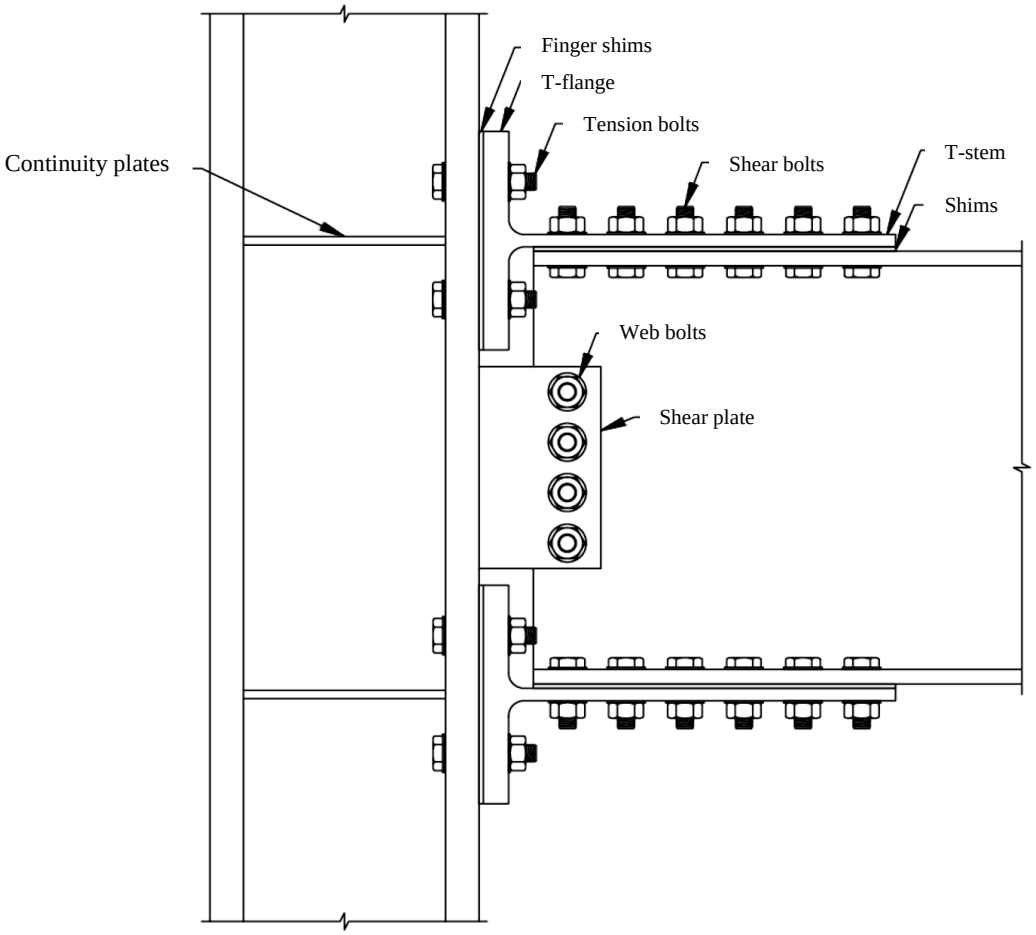

Fig. 2.15: Typical double-tee connection (AISC 2016)

2.2.3.10 SlottedWeb (SW) Moment Connection

The SlottedWeb moment connection features slots in the web of the beam that are parallel and adjacent to each flange, as shown in Fig. 2.16.

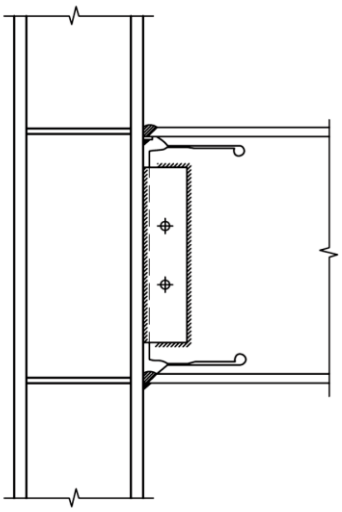

Fig. 2.16: SW beam-to-column moment connection (AISC 2016)

Inelastic behavior is expected to occur through yielding and buckling of the beam flanges in the region of the slot accompanied by yielding of the web in the region near the end of the shear plate (AISC 2016).

2.2.4 Limitations

The seismic provisions provided in AISC (2016) prevent collapse after earthquake by dissipating energy in protected zones. But the structures become unusable and need to be replaced which incur excessive costs. Therefore, it is ineffective to repair these connections after an earthquake. Hence, in order to reuse the structures without rebuilding it, replaceable energy dissipating elements need to be used as an alternative for protected zone so that it can be easily replaced after an earthquake.

2.3 ENERGY DISSIPATION DEVICE OR DAMPER

The seismic resistance of structures can be enhanced by using energy dissipation devices in order to dissipate earthquake energy. Generally structural control can be classified into three main categories: active control, passive control and semi-active control. Active and semi-active controls have a control system to modify the motions of structure. These systems need an external energy supply. Passive control systems effectively reduce the input energy of earthquake to the system and increase the damping of the system as well. These occur by using either isolation system devices or dissipating devices.

The main objective of passive control is to absorb as much of the input energy as possible, to protect the main members from structural damages. Simplicity, ease of installation and replacement, low initial cost and maintenance, free of external power source are the advantages of passive control over the other control systems (Aghlara et al. 2015).

Passive devices utilize different mechanisms to dissipate seismic energy such as, yielding of metals, deformation of viscoelastic materials and fluid orificing. The most effective and economical mechanism is the yielding of metal in dissipative devices. This mechanism was suggested for the first time in the early 1970s (Kelly et al. 1972). A variety of variables are considered in study of the metallic yielding dampers including strength and stiffness of damper, cumulative displacement, total absorbed energy, the weight of damper, equivalent viscous damping ratio, fatigue strength, deformation capacity ratio, dissipated energy to

weight ratio, large force to weight ratio and construction cost. Several studies have been already carried out with different types of dampers. The concept of metallic yielding dampers are described in the following section (Aghlara et al. 2015).

2.4 MODERN SEISMIC DESIGN CONCEPT FOR STEEL STRUCTURES

To determine the optimum damage control design of the frame, it is desirable to construct structures that can be easily repairable, and to facilitate replacement after the earthquake by limiting the damage to the energy absorption devices. Accordingly, if the dampers on which the damage is concentrated are connected to a main frame by exchangeable high-strength bolts, the beams and columns are easier to repair than with welded connections. By designing dampers that are weaker than the beam and column, it is possible to limit damage to the dampers (Oh et al. 2009).

The split-T connection is a typical example of the use of high-strength bolts on existing beam-to-column connections. While the advantages of this connection are the simple construction and superior stiffness of the connection, the compression force can cause local buckling on the beam flange. During an earthquake, it is preferable that the damage be limited to those energy absorption elements that have good hysteretic characteristics and not be transmitted to the main frame such as the beam and column (Oh et al 2009).

Fig. 2.17 shows the new connection system with the steel slit damper as energy absorption element. The slit damper on the bottom flange of the beam is actively plasticized before the main structural members. This system takes post-earthquake repairs into consideration as well as the presence of concrete slabs. High- strength bolts are used to connect all columns and beams. That is, the upper split-T is connected with high-strength bolts at the top of the beam to serve as the rotational center of the connection, while the lower split-T is connected with high-strength bolts to concentrate the deformation to the slit dampers of the bottom flange (Oh et al. 2009).

As shown in Fig. 2.18, since the rotation points on the left and right sides stay at the top flange, damage to the split-T on the top flange, which is difficult to exchange, is avoided. It is expected that deformation of a structure is concentrated on the slit dampers at the bottom flange if the slit dampers show the same behaviors in positive bending (when the

top flange is under compression) and negative bending (when the top flange is under tension) (Oh et al.2009).

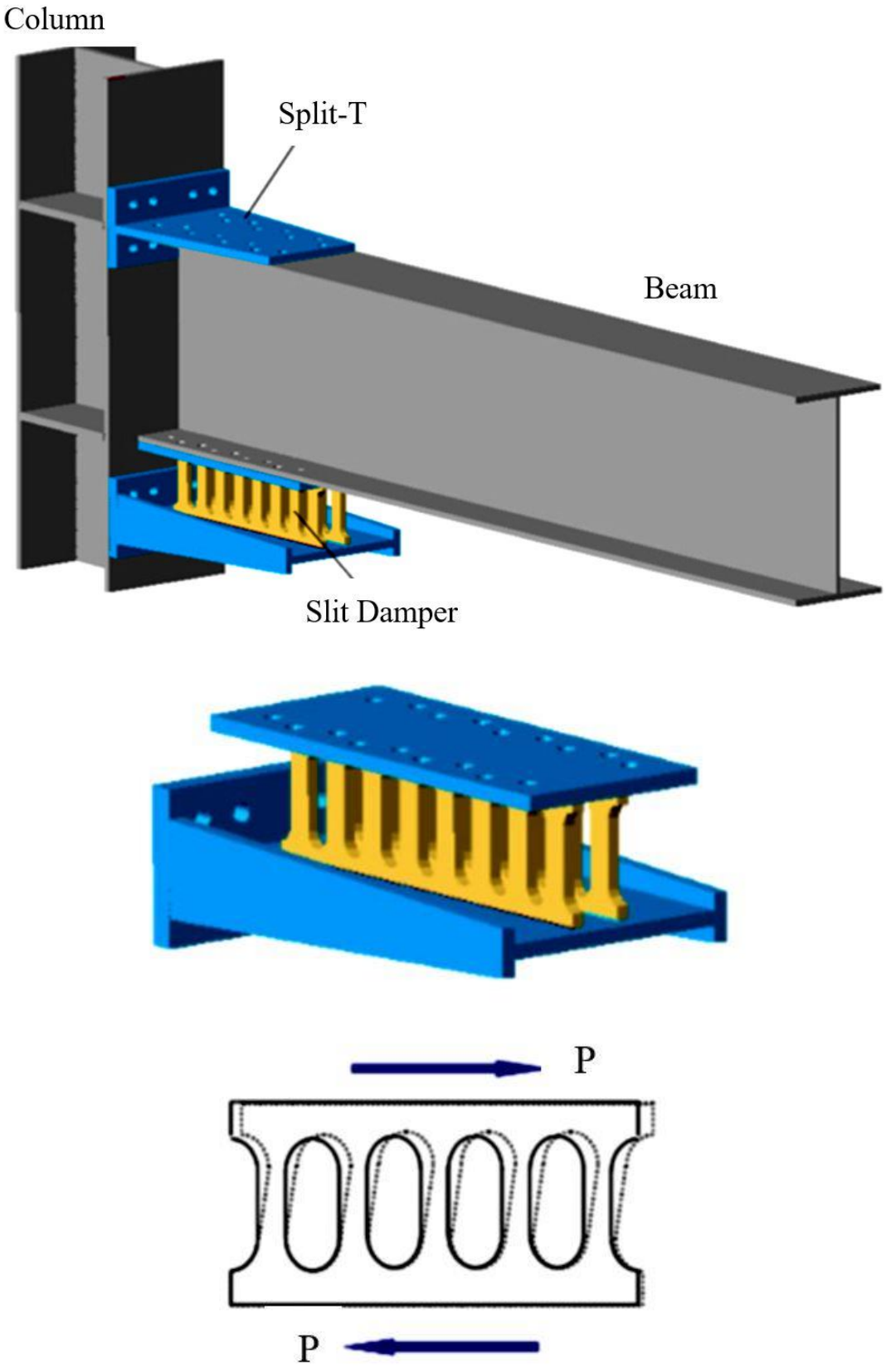

Fig. 2.17: Beam-to-column connection detail with slit damper (Oh et al. 2009)

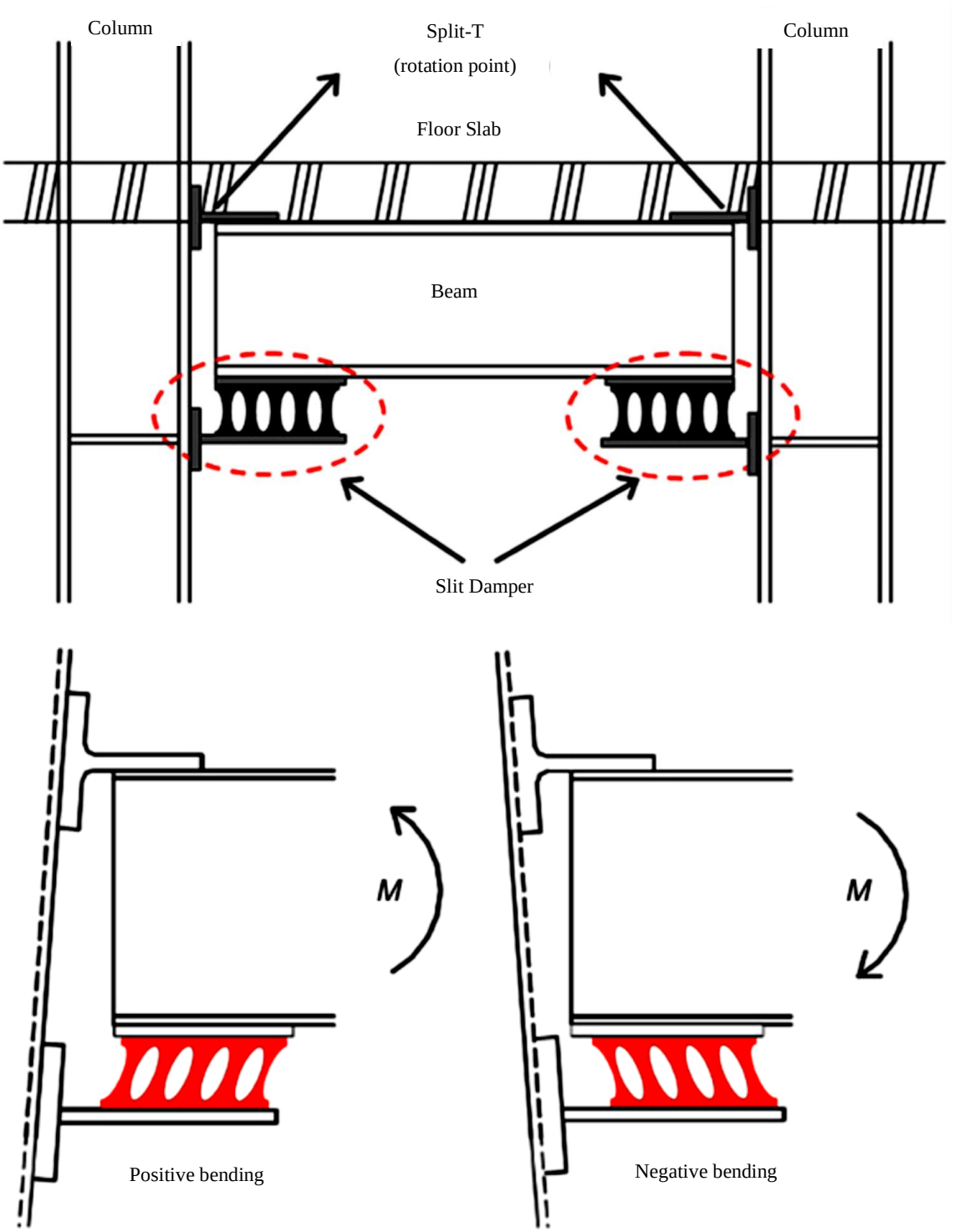

Fig. 2.18: Steel slit damper connection system and deformation (Oh et al. 2009)

As a result, the dampers can freely deform at the bottom flange of the beam without causing significant damage to the concrete slab under large story drifts. This design permits the simple replacement of slit dampers as connection elements of the bottom flange, allowing the continued use of buildings after an earthquake. Since the major retrofit work after an

earthquake is performed near the bottom flange, the slabs do not need to be removed. Furthermore, it is not necessary to consider the influence of the resulting uplift of the neutral axis position due to the constraint effect of the floor slabs. This structural system employs the connection between the beam top flange and the column flange as a means of transferring gravity loads from the beams to the columns. Also, the split-T at the top flange can be kept in an elastic range because the center of rotation stays at the top flange of the beam. Thus, using this system, when the structure suffers compulsory deformation under an earthquake, the deformation is concentrated on the dampers at the bottom flange. Because the plastic deformation of the proposed structural system is concentrated on the dampers in the beam-ends, this system can be regarded as a "strong column-weak beam" when considering the plastic hinge of beam-ends (Oh et al. 2009).

2.5 DIFFERENT TYPES OF DAMPERS

2.5.1 TADAS Damper

A steel Triangular-plate Added Damping and Stiffness (TADAS) device is developed to withstand earthquake forces. This device consists of several triangular plates welded to a common base plate as shown in Fig. 2.19. Experimental results performed by Tsai et al. (1993) indicate that TADAS can sustain a large number of yielding reversals without any stiffness or strength degradation (Aghlara et al. 2015).

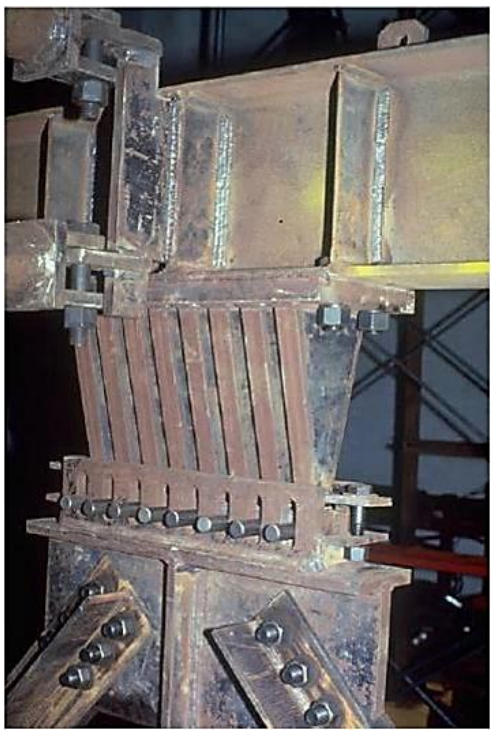

Fig. 2.19: TADAS damper (Tsai et al. 1993)

2.5.2 Cast Steel Yielding Brace

The cast steel Yielding Brace System (YBS) is a hysteretic damper that was developed at the university of Toronto to enhance the seismic performance of braced frames (Gray et al. 2010). In this system, shown in Fig. 2.20, cast steel connector dissipates seismic energy through inelastic flexural yielding triangular fingers. This device prevents the tensile yielding and inelastic buckling of traditional braces. YBS provides a symmetrical hysteresis with increased energy dissipation (Aghlara et al. 2015).

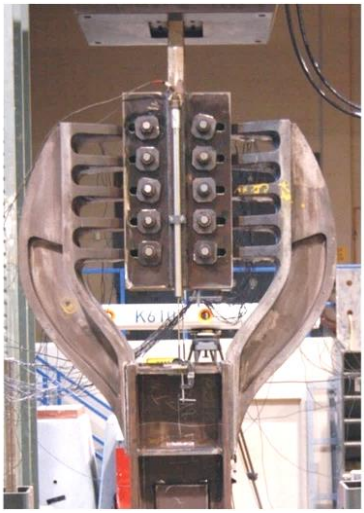

Fig. 2.20: Cast steel yielding brace damper (Gray et al. 2010)

2.5.3 Dual-Pipe Damper

Dual-Pipe Damper (DPD) is made of two pipes welded at selected locations and withstand shear load as shown in Fig. 2.21 (Maleki and Mahjoubi 2013). The mechanism of energy dissipation is flexural of pipe body. However, tension forms at large displacement in the device, leading to increased stiffness and strength (Aghlara et al. 2015).

Fig. 2.21: Dual-pipe damper (Maleki and Mahjoubi 2013)

2.5.4 Infilled-Pipe Damper

Infilled-Pipe Damper (IPD) consists of two welded pipes which have two smaller pipes inside them. The spaces between the pipes are filled with metals such as lead or zinc as shown in Fig. 2.22 (Maleki and Mahjoubi 2014). The device was loaded in shear. The energy absorption mechanism in the device is the plastification of the outer pipes, the inner pipes, infilled metals and the friction between metals (Aghlara et al. 2015).

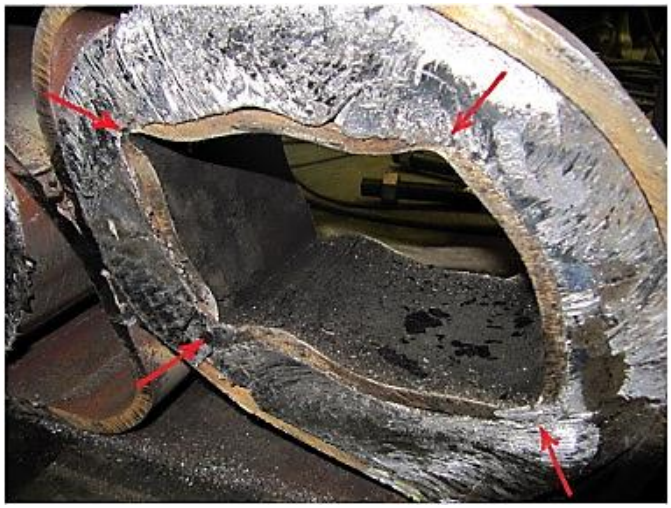

Fig. 2.22: Infilled-pipe damper (Maleki and Mahjoubi 2014)

2.5.5 Yielding Shear Panel Device

The Yielding Shear Panel Device (YSPD) dissipates energy through plastic shear deformation of a thin steel plate welded inside a square hollow section (SHS), as shown in Fig. 2.23 (Chan et al. 2013). The device has the ability to dissipate energy along with stable behavior. Two important variables which influence the performance of the device are plate slenderness and in-plane rigidity of the restraining SHS (Aghlara et al. 2015).

Fig. 2.23: Yielding shear panel device (Chan et al. 2013)

2.5.6 Hysteretic Steel Damper

These types of steel dampers are fabricated from mild steel plate with different geometrical shapes on the side part, as shown in Fig. 2.24 (Teruna et al. 2015). The shapes can be straight, concave or convex. The specimen with convex-shape shows stable hysteretic behavior with desirable energy dissipation capabilities and ductility factor (Aghlara et al. 2015).

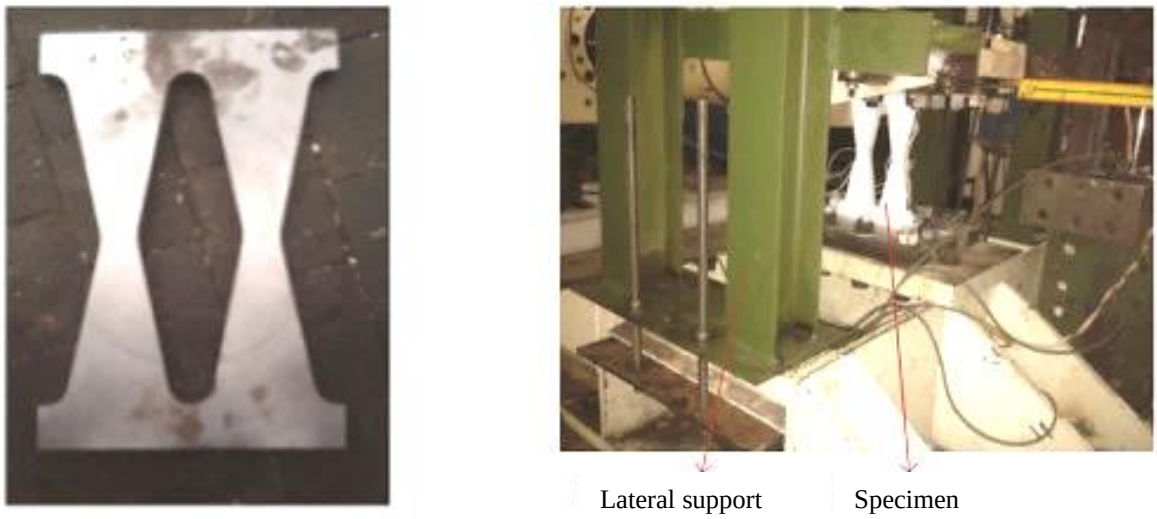

Fig. 2.24: Hysteretic steel damper (Teruna et al. 2015)

2.5.7 Dual Function Metallic Damper

This damper provides additional structural stiffness along with good seismic energy dissipation capabilities. Therefore, they were named as dual function metallic dampers (DFMD) (Li and Li 2007). The dampers are made of mild steel plate with two specific geometric shapes on it, single round-hole (DFMD-O) and double X-shaped (DFMD-X), as shown in Fig. 2.25 (Aghlara et al. 2015).

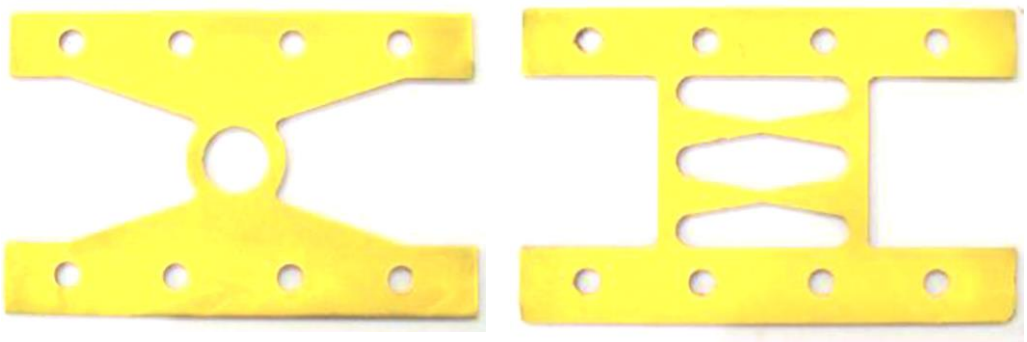

Fig. 2.25: Dual function metallic damper (Li and Li 2007)

2.5.8 Steel Slit Damper

The Steel Slit Damper (SSD) is fabricated from a standard structural wide-flange section with a number of slits cut from the web, in a vierendeel truss arrangement as shown in Fig. 2.26 (Karavasilis et al. 2012). The device is a weld-free design, thereby eliminating the uncertainties and difficulties encountered in in-situ welding. Energy is dissipated through flexural yielding of the vierendeel's web members when the device is subjected to inelastic cyclic deformation. The device yielded at small angular distortion and is thus expected to dissipate energy early in an earthquake. The structural characteristics of the device are readily determined from fundamental engineering principles, thus the design can be easily modified or extended to suit particular structural requirements (Oh et al. 2009).

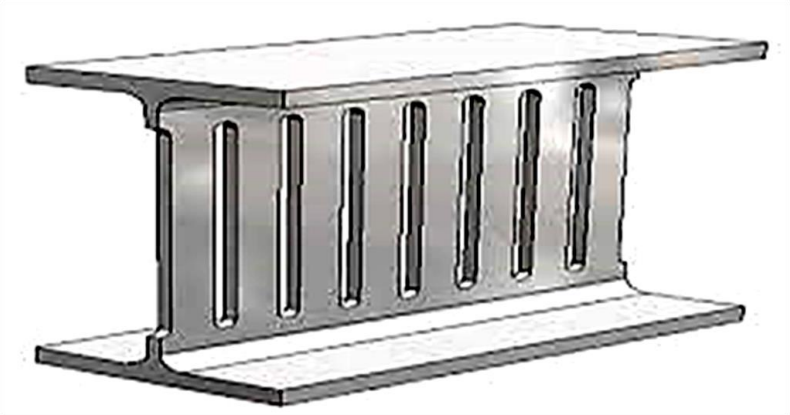

Fig. 2.26: Steel slit damper (Karavasilis et al. 2012)

2.6 OBLONG STEEL SLIT DAMPER

To ensure that the beam-to-column connection system with slit damper operates correctly, it is necessary to have a stable and large energy dissipative capacity at the bottom flange, which can be deformed evenly under repeated loads, i.e. under the tensile and compressive force on the bottom flange. To limit damage to the connection element without causing damage to the main structural members, it is necessary for the connection to have relatively high stiffness that yields ahead of the key structural members.

The energy is dissipated through plastic deformation on the vertical struts of the slit dampers, as shown in Fig. 2.18. It has been previously found that the slit damper has an extremely good energy dissipative capacity as well as high stiffness and is considered appropriate to use as a connection element in the system. For the purpose of predicting the yield strength and deformation of the slit damper, the struts of the damper were idealized

as shown in Fig. 2.27, where the round-shaped ends have been replaced with straight lines (Oh et al. 2009).

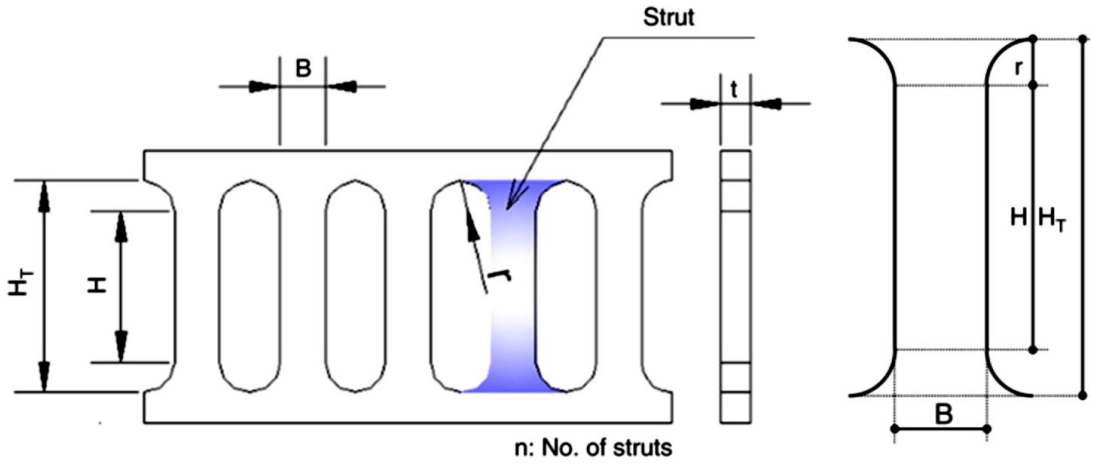

Fig. 2.27: Idealization of slit damper (Oh et al. 2009)

Under small relative displacement between the two supported flanges, the strips behave as a series of partially fixed-ended beams and deform in double curvature. The elastic bending moment in the strips is shown in Fig. 2.28. When movement is sufficiently large, bending moment at the ends of strips causes the extreme fibres to reach yield stress. Under sufficient displacement, plastic hinges form at both ends of each strip. The ultimate force of the device can be determined based on the collapse mechanism when all beam end moment become plastic hinges (Chan and Albermani 2008).

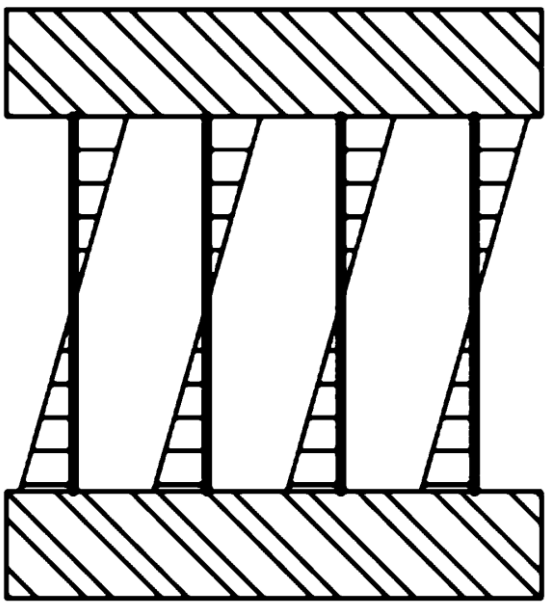

Fig. 2.28: Bending moment in steel slit damper (Chan and Albermani 2008)

By using this simplification, the yielding strength and apparent maximum strength of the slit damper can be obtained analytically as follows: (Oh et al. 2009)

$$P_y = \min\left\{ n\frac{\sigma_y t B^2}{2H'}, n\frac{2\sigma_y t B}{3\sqrt{3}} \right\} \tag{2.1}$$

$$P_u = \min\left\{ n\frac{\sigma_u t B^2}{2H'}, n\frac{2\sigma_u t B}{3\sqrt{3}} \right\} \tag{2.2}$$

In Eqs. (2.1) and (2.2), the first term means that the yielding of the slit damper is governed by the flexural moment, while the second term means that the yielding of the slit damper is governed by shear force. Where *n* = the number of struts on the slit damper; *t* = the thickness of the plate; σ_y = the yield stress*;* σ_u = the maximum stress; *B* = the width of the struts and H' = the equivalent height indicated in Fig. 2.27 ($H' = H + 2r^2/H_T$). The factor 2/3 in the second term of Eqs. (2.1) and (2.2) accounts for the fact that, within the elastic range, when the aspect ratio of the plate *B/H* is less than 1.0, the relationship between the average shear stress and the maximum shear stress is 2/3.

The yield displacement of the slit damper can be analytically expressed and simplified by the following elastic- based equation: (Oh et al. 2009)

$$\delta_y = \frac{1.5 P_y H_T}{nEtB}\left[\left(\frac{H'}{B}\right)^2 + 2.6\right] \tag{2.3}$$

In Eq. (2.3) *E* is the Young's modulus and H_T is the total height of the strut of the slit damper. By using Eq. (2.3) yield deformation of slit damper can be easily calculated.

2.7 ELLIPTICAL STEEL SLIT DAMPER

Steel slit dampers were employed at the connections to prevent brittle failure of the connections and damage of main structural members in the event of an earthquake. It was observed from previous investigations that the use of steel slit dampers with uniform strut width resulted in stress concentration at the end parts of the damper struts and unbalanced distribution of von-Mises stresses along the struts. Furthermore, slit dampers were

commonly fractured in the end parts of its struts. This may be due to the low participation of the strut's middle parts in the energy dissipation. Thus, Shahri and Mousavi (2018) proposed elliptic steel slit damper (ESSD) in such a way that the end parts of struts have more energy absorption area than the struts middle parts. Also, the effect of geometric parameters of elliptic slit damper is investigated on the seismic performance of the beam-to-column connection. They conducted a parametric study to investigate the effects of geometric parameters of elliptic slit damper such as strut width, strut height and plate thickness on the seismic performance of the beam-to-column connection. The stress distribution is improved along the struts in the proposed slit damper with elliptic slits and the stress concentration is decreased in the end parts of struts. The average contributions of elliptic slit dampers, beam and other sections to the energy dissipation are about 97.19%, 2.12% and 0.69%, respectively. The beam-to-column connections equipped with elliptic slit dampers are illustrated in Fig. 2.29.

According to the previous studies, the analytical yielding strength (P_y) and apparent maximum strength (P_u) of the slit damper can be achieved by Eqs. (2.1) and (2.2). By using some simplifications, the effective width of elliptic slit damper (B_{eff}) is defined as follows: (Shahri and Mousavi 2018)

$$B_{eff} = B - \frac{B}{r} \tag{2.4}$$

where r is the minor radius of elliptic slit. By substituting the effective width (B_{eff}) and total height of struts (H_T) in Eqs. (2.1) and (2.2), the analytical yielding strength (P_y) and apparent maximum strength (P_u) of the elliptic slit damper are given by as follows: (Shahri and Mousavi 2018)

$$P_y = \min\left\{n\frac{\sigma_y t B_{eff}^2}{2H_T}, n\frac{2\sigma_y t B_{eff}}{3\sqrt{3}}\right\} \tag{2.5}$$

$$P_u = \min\left\{n\frac{\sigma_u t B_{eff}^2}{2H_T}, n\frac{2\sigma_u t B_{eff}}{3\sqrt{3}}\right\} \tag{2.6}$$

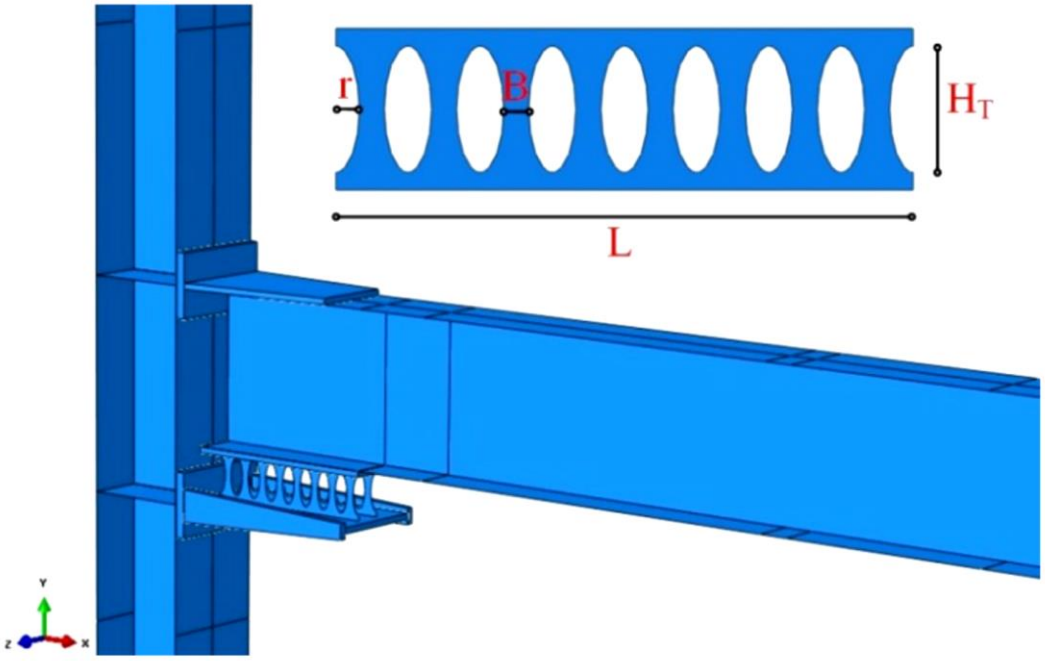

Fig. 2.29: Beam-to-column connection equipped with elliptic slit dampers (Shahri and Mousavi 2018)

Considering the effective width of elliptic slit damper, the yield displacement is expressed as: (Chan and Albermani 2008)

$$\delta_y = \frac{0.5\,\varepsilon_y\,H_T^2}{B_{eff}} \tag{2.7}$$

where ε_y is the yield strain of the steel material. So, the lateral stiffness of the elliptic slit damper (K_{damper}) can be calculated by: (Shahri and Mousavi 2018)

$$K_{damper} = \frac{P_y}{\delta_y} \tag{2.8}$$

In the proposed slit damper with elliptic slits, the stress distribution is improved along the struts of damper. Furthermore, utilizing the elliptic slits results in more participation of the middle part of struts in the energy dissipation. Consequently, stress concentration is decreased at the end parts of damper struts. Decreasing the strut width or plate thickness or increasing the height of elliptic slit dampers leads to decrease of the maximum values of force and moment sustained by the connection. It also results in reduction of von-Mises

stress distribution at the main structural members and increment of the stress concentration at the dampers. Using thin plates for elliptic slit dampers causes the local buckling and low rotational capacity of the beam-to-column connection. To prevent local buckling from occurring, the strut width-to-thickness ratio (*b/t*) of elliptic slit damper should not exceed 2. Elliptic slit dampers can dissipate a significant amount of seismic energy compared to the beam and other sections. So, it can be concluded that elliptic slit dampers contribute to the energy dissipation, effectively (Shahri and Mousavi 2018).

2.8 BUTTERFLY-SHAPED STEEL STRUT DAMPER

Due to the unvarying width and thickness of strips in conventional slit dampers, stress is concentrated at the ends when subjected to external loads. In order to improve ductility and fatigue performance, recent studies attempting to optimize strip shapes have been carried out. In the study by Ghabraie et al. (2010), strips were optimized with diamond-shaped holes derived through the application of a bi-directional evolutionary structural optimization algorithm, and performance was evaluated experimentally. Several types of non-uniform strip shapes (a dumbbell-shaped strip, a tapered strip, and an hourglass-shaped strip) were proposed by Woo et al. (2013) and Lee et al. (2015) for the purpose of simplifying the design and improving performance. The proposed dampers were tested under monotonic and cyclic loadings. They showed superior ductility and energy dissipation capacity compared to a conventional slit damper (Lee et al. 2016).

Xu et al. (2011) presented a a new mild steel slit damper (SSD). The new shape was parabolic according to all the cross section having the same maximal stress, and the elastic stiffness and yield displacement formula were derived. Finite element analysis showed that the parabolic shaped damper had a more reasonable load - displacement curve compared with the previously proposed shape. The theoretical stiffness and yield displacement were consistent with the results by finite element method (FEM), and that indicated the presented design method was simple and feasible. The total plastic energy dissipation was considered as the objective function, which was to be maximized, and the amount of usable material was additional constraint. The optimized shape showed increased energy dissipation capacity and even stress distribution. Experimental study proved that the optimized shape was more resistant to low-cycle fatigue. Taking one strip of mild steel damper which can be seen as a clamped-clamped beam as shown in Fig. 2.30.

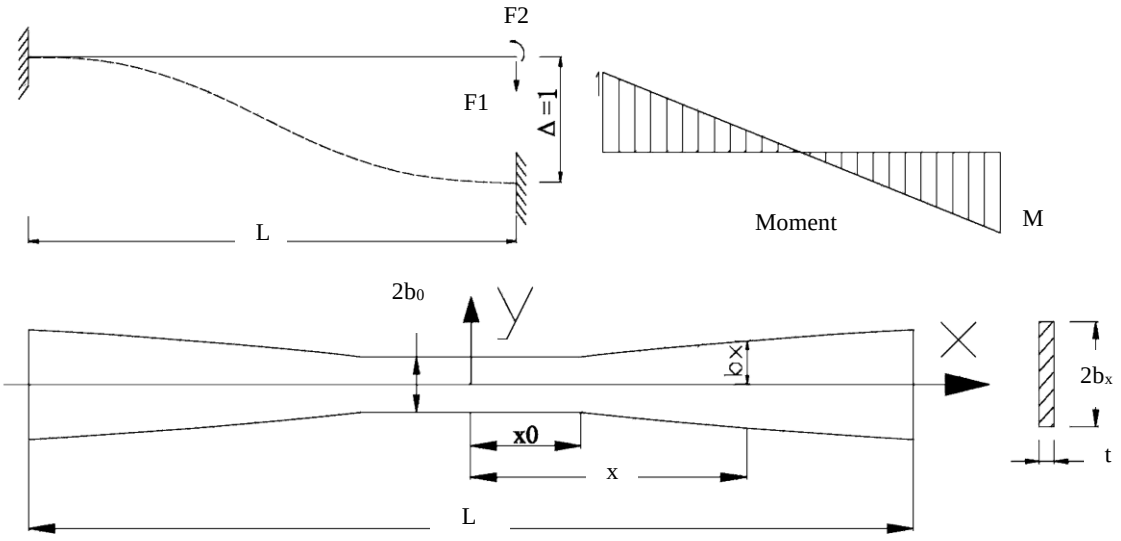

Fig. 2.30: Shape optimization of the damper strip (Xu et al. 2011)

When the height-to-width ratio is greater than 5, the maximum stress can be calculated according to pure bending. By the moment distribution of clamped- clamped beam, if all the cross section having the same maximal stress, the shape of the damper shall meet the following requirements: (Xu et al. 2011)

$$\sigma_{max} = \frac{3M}{tL}\frac{x}{b_x^2} \tag{2.9}$$

where σ_{max} = maximum stress with variable cross section, M = the maximum moment of the cross section, b_x =half width of cross section, t = thickness of section, L = the length of strip. From Eq. (2.9), if the maximum stress for each section are equal, $\frac{x}{b_x^2}$ must be constant, so

$$b_x = a\sqrt{x} \tag{2.10}$$

where a is positive. To satisfy all the cross section having the same maximal stress along length, the section shape should be parabolic (Xu et al. 2011).

The strips each have identical dimensions. After removing unnecessary volume to optimize the shape, the strips have an hourglass shape (Fig. 2.31) in which the cross-section

decreases from the ends to the middle. The shape was designed so that the plastic bending moment (M_p) can be reached at all cross sections simultaneously, and the area of the central part of the strip was decided in order to safely resist shear force (Lee et al. 2015).

Fig. 2.31: The butterfly-shaped damper (Lee et al. 2015)

The typical configuration and geometry of a butterfly-shaped steel strut damper (BSSD) or an hourglass-shaped strip damper is shown in Fig. 2.32.

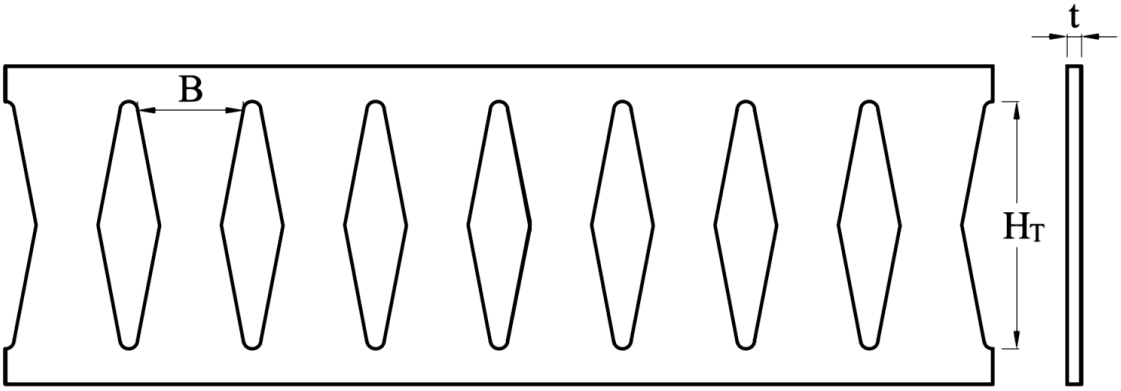

Fig. 2.32: Configuration and geometry of butterfly-shaped steel strut damper

The plastic strength (P_p) of BSSD denotes the horizontal force when the entire cross sections of the strip reach M_p was formulated based on the cross section of the ends as follows: (Lee et al. 2016)

$$P_p = n \frac{\sigma_y t B^2}{2H_T} \tag{2.11}$$

where σ_y is the yield stress, n is the number of the struts, t and B are the thickness and width of the strip at the ends and H_T is the height of the strip. It is observed from the results that BSSD showed substantial load–resistance capacity under monotonic loadings, and excellent ductility and energy dissipation were exhibited under cyclic loadings, with even distribution of damage over the entire height of strips (Lee et al. 2016).

2.9 PINTLE DAMPER

Steel yielding hysteretic devices provide a reliable way to increase the energy dissipation capacity of structures under seismic loading. Steel cylindrical pins with hourglass shape bending parts (called web hourglass shape pins—WHPs) have been recently used as the energy dissipation system of posttensioned connections shown in Fig. 2.33 for self-centering steel moment-resisting frames.

Fig. 2.33: Web hourglass shape pin (Vasdravellis et al. 2014)

Vasdravellis et al. (2014) conducted twenty-six tests using different cyclic loading protocols and different WHP geometries. The tests showed that the WHPs have stable hysteretic behavior and high fracture capacity. Apart from posttensioned connections, WHPs can also be used as energy dissipating fuses in bracing members or column base connections.

Seismic design involving “fuse components” between the superstructure and substructure can improve the seismic performance of bridges during strong earthquakes by ensuring an elastic working state. The mechanical properties of the “fuse components” directly affect the seismic behavior of bridges, and many theoretical and experimental studies of isolation devices to achieve the controlled seismic behavior of continuous girder bridges have been carried out, and some devices are in use in large-scale construction projects. However, there is a lack of evidence from structures that have been subject to earthquakes. The pintle damper is used as a fuse element in the Bangabandhu Bridge of Bangladesh which is illustrated in Fig. 2.34.

Fig. 2.34: Pintle damper in the Bangabandhu Bridge

The pintle damper (PD) is introduced at beam-column connection in this study to dissipate seismic energy. The PD consists of a cylindrical strip of diameter D and length L with a solid circular part at top and bottom of it. The cylindrical part is connected to the circular part with a radius r to avoid stress concentration in the region of abrupt diameter change. The assumed static system of cylindrical part is that of a fixed-ends bar provided that the external supporting plates are thick enough to prevent end rotation.

Fig. 2.35 depicts the geometry and configuration of the pintle damper.

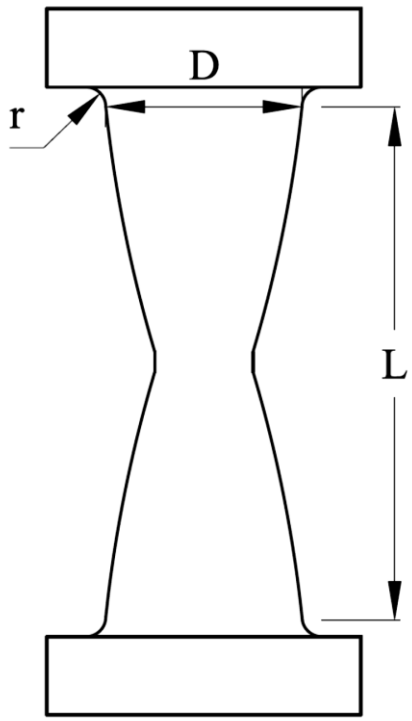

Fig. 2.35: Configuration and geometry of pintle damper

As shown in Fig. 2.35, the pintle dampers are designed to have an hourglass shape to provide enhanced energy dissipation and fracture capacity. The shape of the cylindrical part follows the profile of the bending moment diagram (i.e., is minimum at the mid-length and maximum at the ends) to achieve a uniform distribution of plastic deformations along PD, and so, to increase displacement ductility and delay fracture. The deflected shape and bending moment diagram of PD are illustrated in Fig. 2.36.

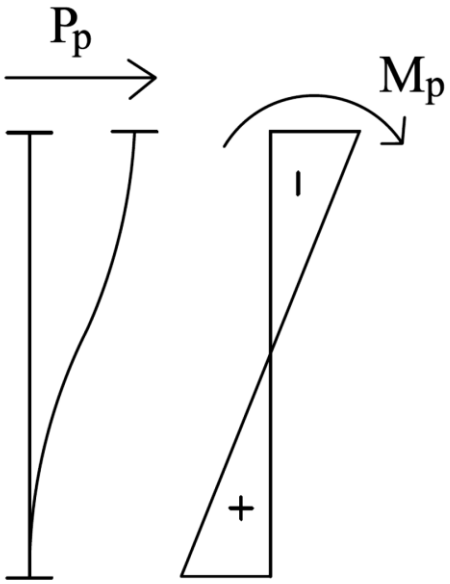

Fig. 2.36: Internal forces diagram of pintle damper

The plastic strength of the pintle damper can be obtained analytically as follows: (Vasdravellis et al. 2014)

$$P_p = 2\frac{M_p}{L} \tag{2.12}$$

$$M_p = \sigma_y Z_x \tag{2.13}$$

So by combining Eqs. (2.12) and (2.13),

$$P_p = n\frac{\sigma_y D^3}{3L} \tag{2.14}$$

where P_p = plastic strength of the PD, M_p = plastic moment capacity, Z_x = section modulus, n = number of pintles, σ_y = yield stress, D = diameter of pintle and L = length of the pintle.

The hysteretic behavior of the pintle damper at moment connection will be investigated in this study so that it can be used as an energy dissipation device to dissipate seismic forces and can be an alternative solution in future for earthquake protection of structures.

2.10 FORMER RESEARCH

After the Northridge and Kobe earthquakes, researchers conducted many experiments to identify the causes of brittle damages in beam-column connections and to be able to test the developed systems that are manufactured to increase the safety of these connections (Engelhardt and Sabol 1998; Shen et al. 2000; Chen and Chao 2001). In these studies, although the plastic moment capacity of the frames is increased, after an extensive earthquake these welded systems cannot be repaired easily or quickly, hence the structure cannot be made serviceable. However, it is critical that a structural system should be repaired and made serviceable as soon as possible after an earthquake.

De et al. (2004) described that a good metallic damper must possess two important characteristics in order for these devices to be used in engineering applications: (1) to have stable and large energy dissipative capability; (2) to have a representative model of its cyclic behaviour. In line with the second aspect, numerous experiment-based and mechanics based models have been developed. While some researchers used the simpler bilinear model for hysteretic response, others adopted models such as the Bouc–Wen model

and Ramberg–Osgood model. These models are capable of capturing the smooth transition from elastic to inelastic regime observed in experiments. The design aspect of structures equipped with passive devices has been considered by many researchers. Nakashima et al. (1995) described that the first yielding, i.e. yielding of the damping mechanism has to be set low, for the purpose of triggering the energy dissipation as early as possible, and to set the yielding level of the parent structure high for the purpose of retarding serious structural damage.

With the advances in technology of the last century, different solutions have been developed. Different structure control mechanisms are manufactured based on the logic of dampening the energy generated by ground movement using structural elements (Rai et al. 2013). The use of the inelastic behavior of metals, with high energy absorption capacity and hysteric behavior, and metallic dampers produced by dampening seismic energy are used more frequently after the Northridge earthquake due to their economic advantages. Utilizing the bending deformations of metals, many dampers such as patented added damping and stiffness damper (ADAS; Tsai et al. 1993), triangular added stiffness and damping damper (TADAS; Kobori et al. 1992), the honeycomb damper (Sabelli et al. 2003), the buckling-restrained brace (BRB; Clark et al. 1999), and the slit damper are used (Chan and Albermani 2008; Lee et al. 2002). On the other hand, slit dampers are also being used on beam to column connections recently (Oh et al. 2009; Koken and Koroglu 2012; Saffari et al. 2013).

Oh et al. (2009) conducted cycling tests on three full-scale samples that three had slit dampers and one specimen had conventional post-Northridge welded connection. They achieved hysteretic behavior and plastic deformations were concentrated on the slit dampers while the beams and columns were on elastic zone. In addition to these studies Saffari et al. (2013) had a parametric study with FEM to find out the best geometric configuration of slit dampers for different beam and column profile length and depth ratios. Koken and Koroglu (2011a, b) studied the mechanical characteristics of different steel damper shapes which is low-cost hysteretic type. They tested nine different slit damper shapes to assess the structural behavior of the slit dampers. Normal shaped slit damper which is also used in the research reported in this paper showed stable hysteresis behavior under shear forces Koken and Koroglu (2011a, b) also studied u-shaped slit dampers that studied waste rubber composites as damper on beam-to column connection. Koken and

Koroglu (2014) performed experimental and theoretical studies on the behavior of beam-to-column connections with slit dampers and compared them with the extended end plate connection. Unlike the extended end plate connection, the connections equipped with slit dampers demonstrated a good hysteretic performance without sustaining any damage to the beam and column.

Benavent-Climent (2010) tested a tube-in-tube brace damper consists of two hollow sections, where the outer hollow section had a series of slits through its wall. The test results showed that the damper exhibited remarkable energy dissipation capacity and stable hysteretic behavior. Furthermore, a hysteretic model has been presented to predict the ultimate energy dissipation capacity of the damper. The shape of slit dampers presented by Chan and Albermani (2008) has been optimized by Ghabraie et al. (2010) using modified BESO algorithm. Total plastic energy dissipation was maximized to reach a high energy dissipation per unit volume. It was concluded that optimized shape of slit damper dissipated 37% more energy compared to the former specimen. Karavasilis et al. (2012) developed a minimal-damage seismic design approach for steel buildings using slit dampers in parallel to viscous dampers. It was observed that residual drifts and peak total floor accelerations of the steel MRF with slit devices and viscous dampers were lower than those of the conventional MRF. Thus, the MRF with slit devices and viscous dampers were suffered less damage compared to the conventional MRF. Safari et al. (2013) conducted a parametric study to figure out the best configuration of slit dampers with respect to different beam length-beam depth ratios. They used steel slit dampers as energy dissipation element to increase the ductility of beam-to-column connections. Their suggested connections was intended to cause a delay in failure using a complicated load transferring system which utilized some additional plates through load transferring path from beam to column.

Lima et al. (2015) studied the behavior of steel slit devices which were utilized as a link in eccentric bracings for seismic retrofitting of RC frames. Nonlinear time history analyses of an existing RC frame with the mentioned bracings have been carried out by taking into account the low-cycle fatigue. It was found that the top displacement demand of the structure was effectively decreased by using the slit devices. Lee and Kim (2015) investigated the seismic performance of hybrid slit-friction dampers by nonlinear dynamic analysis. The analysis results demonstrated that the damage and residual displacements of main structural members are decreased in the structure equipped with

hybrid passive dampers. Hedayat (2015) performed a parametric study to predict the force-displacement behavior of unbuckled slit dampers with different types and geometries. For this purpose, he suggested some formulas for each type of slit dampers based on the finite element results. Tagawa et al. (2016) proposed a seesaw energy dissipation system equipped with steel slit dampers in order to remain the bracing members in tension state and to improve damper stiffness and energy dissipation characteristics. They presented the lateral story stiffness and strength formulas for the mentioned system. In addition, a tri-linear model has been introduced to predict the cyclic behavior of the system.

2.11 REMARKS

Many researchers worked with different types of steel shear dampers at seismic moment connections to improve the seismic performance of steel structures. Therefore, we need to correlate and compare the dampers behavior with respect to each other so that we can use any damper type in replacement of others. Besides, steel shear dampers are not still widely used and its provisions are not included in the codes. Further regularizations of existing dampers are also needed. Experimental research related to the application of steel shear dampers on beam-to-column connections of steel frame structures is too much expensive for our country. As an alternative, a numerical analysis by finite element method has been carried out in this thesis based on the experimental investigation of past researches. If it is possible to show that numerical model can adequately simulate the experimental results than it would be really helpful in the design and construction of steel structure. The more detailed description of experimental study performed by past researches is given in Chapter four. This thesis will report the results from numerically modeled beam-column connection with steel shear damper of different geometry under static cyclic loading to assess its hysteretic behavior, deformation, plastic strength, energy dissipation, equivalent damping ratio etc. and to find an equivalency among them. Limitations of the study will also to be stated.

CHAPTER 3
METHODOLOGY FOR FINITE ELEMENT MODELING

3.1 INTRODUCTION

The Finite Element Analysis (FEA) is the simulation of any given physical phenomenon used for modeling complex products and system. FEA is a computer-based process which simulates using the numerical technique called Finite Element Method (FEM). These simulations occur in a virtual environment for the purpose of 'solving' or finding a series of solutions to potentially complex performance issues. It is useful for all degrees of science and engineering disciplines. Typical problem areas of interest include the traditional fields of structural analysis, heat transfer, fluid flow, mass transport and electromagnetic potential. Specifically, as applied to material sciences and engineering, it is used to calculate the strength and behavioural characteristics of a material under conditions such as stress, vibration and deflection. FEA software is now faster and easier to use than ever before (Erdogan and Ibrahim 2015).

3.2 FINITE ELEMENT ANALYSIS

FEA works by breaking down a large structure, with high degrees of physical complexities and mathematical discontinuities, into smaller, more manageable sections. Each section represents the material properties of its local domain. By slicing the structure into smaller and smaller sections, the simulator gains an understanding of how the larger structure will respond to external or internal stimuli. (Erdogan and Ibrahim 2015)

The start of this process begins by determining the placement of a theoretical array of 'nodes' on the structure:

a) The NODE is a single point within the 2D or 3D structure. Each node is programmed with the material and structural data of its immediate location.
b) The addition of lines between the nodes creates a MESH structure. The meshing encloses smaller, simpler sections of the full part. The denser the mesh, the more precise the results will be for the full system, but the more complex the computations.
c) The regions that are enclosed by the mesh structure are a collection of finite ELEMENTS, hence, Finite Element Analysis.

Each element is defined by more simple equations concerning stress, force, inertia, thickness, strength, acceleration, temperature, etc. pertaining to the border conditions along that unique mesh and those conditions within the element. The computer software keeps a listing of the individual elements, their neighboring elements, and the internal and border conditions. All of the mesh equations within the system are solved simultaneously and the results are used to determine how each node responds when external stimulus is applied to it, or to its neighboring elements. When a simulation program is executed and stressors are applied to the system, each element begins to adjust its equations. These adjustments will either relieve or create additional stresses throughout the mesh, changing border conditions for its neighbors, just as its neighbors will change its own border conditions. If the nodes and meshes have been programmed properly, the system will eventually work all the stresses out of the equations and begin to settle. This is called "convergence" and a solution is created. The computer then applies this solution to each individual node and from this, gets a theoretical stress and deflection function for each section of the structure. This result can be analyzed graphically or numerically within the program software. The solution is compared to the tolerances of the system to determine if the structure is strong enough for the application, even before the part is manufactured (Erdogan and Ibrahim 2015).

The key benefits of the FEA process are:

a) Comprehensive result sets, generating the physical response of the system at any location, including some which might have been neglected in an analytical approach.
b) Safe simulation of potentially dangerous, destructive or impractical load conditions and failure modes.
c) Optimal use of a model. Often, several failure modes or physical events can be tested within a common model.
d) The simultaneous calculation and visual representation of a wide variety of physical parameters such as stress or temperature, enabling the designer to rapidly analyse performance and possible modifications.
e) Extrapolation of existing experimental results via parametric analyses of validated models.
f) Relatively low investment and rapid calculation time for most applications.
g) Availability of large number of computer software packages and literature makes FEM a versatile and powerful numerical method.

3.3 ANSYS: FEM SOFTWARE USED FOR PRESENT ANALYSIS

Among all finite element packages, ANSYS has been chosen for its versatility, reliability and relative ease of use. It is a general-purpose finite-element modeling package for numerically solving a wide variety of mechanical problems. These problems include static/ dynamic, structural analysis (both linear and nonlinear), heat transfer, and fluid problems, as well as acoustic and electromagnetic problems. Structural analysis is the determination of the effects of loads on physical structures and their components. Structures subject to this type of analysis include all that must withstand loads, such as buildings, bridges, vehicles etc. (Erdogan and Ibrahim 2015).

There are three main steps in a typical ANSYS analysis:

- Model generation: (Pre-processor)
  - − Simplifications, idealizations
  - − Define materials/material properties
  - − Generate finite element model (mesh)
- Solution: (Solution Processor)
  - − Specify boundary conditions
  - − Obtain the solution
- Review results: (Post-processor)
  - − Plot/list results
  - − Check for validity

For accomplishing the finite element analysis of seismic moment connections with steel shear dampers of different geometry in steel frame structure related to this thesis paper, the finite element modeling has been performed in this package.

3.4 MODELING OF MOMENT CONNECTION WITH STEEL SHEAR DAMPER OF DIFFERENT GEOMETRY

The aim of this section is to construct nonlinear models of moment connection with steel shear damper of different geometry made of mild steel subjected to a reversible cyclic loading, such as an earthquake, using Ansys Student 2020 R2 software. Through this process it becomes possible to compare the experimental results with numerical analysis

results. In order to predict the hysteretic responses of moment connections with steel shear damper, a few numerical models has been developed. This chapter presents a reliable modeling procedure that can be used to accurately simulate a moment connection with steel shear damper. This modeling procedure is developed based on the effort of reproducing the experiments conducted by Chan and Albermani (2008), Oh et al. (2009) and Koken and Koroglu (2014). These models account for both material and geometric nonlinearities. Each of the following sections will describe the modeling of the tests.

3.4.1 Modeling Parameters

To perform the modeling, the necessary physical and mechanical properties of the material and specimen are taken as mentioned by the researchers. The connection system with steel shear damper as proposed in the studies in general consists of elements like wide flange beam and column, damper upper and lower plate, upper and lower split-T and the shear damper. Experimental specimen SL-3 tested by Chan and Albermani (2008), W and D1 tested by Oh et al. (2009) and N12 tested by Koken and Koroglu (2014) are modeled to verify the accuracy of the finite element modeling. The modulus of elasticity is considered same for other sections as damper and Poisson ratio of steel is assumed 0.3 for all sections.

3.4.2 Element Modeling

SOLID185 element is used to model all the components of the connection system. SOLID185 is used for 3-D modeling of solid structures. It is defined by eight nodes having three degrees of freedom at each node: translations in the nodal x, y, and z directions. The element has plasticity, hyperelasticity, stress stiffening, creep, large deflection, and large strain capabilities. It also has mixed formulation capability for simulating deformations of nearly incompressible elastoplastic materials, and fully incompressible hyperelastic materials (ANSYS, Inc. 2018).

3.4.3 Material Modeling

3.4.3.1 Chaboche Kinematic Hardening

The nonlinear kinematic hardening model have both rate-independent and rate-dependent version of the kinematic hardening model proposed by Chaboche (1989). The model allows the superposition of several independent back-stress tensors and can be combined with any

of the available isotropic hardening models. It can be useful in modeling cyclic plastic behavior such as cyclic hardening or softening and ratcheting or shakedown. The Chaboche kinematic hardening material model can be defined with respect to temperature and allows up to five kinematic models for each temperature. It is required that all kinematic models be defined for each temperature (ANSYS, Inc. 2018).

The Chaboche nonlinear kinematic hardening model was added in ANSYS to complement the existing isotropic and kinematic hardening rules that users relied on. The yield function of the nonlinear kinematic hardening model is shown below: (Imaoka 2008)

$$F = \sqrt{\frac{3}{2}(\{s\} - \{\alpha\})^T [M] (\{s\} - \{\alpha\})} - R = 0 \tag{3.1}$$

In the Eq. (3.1), *{s}* is the deviatoric stress, *{α}* refers to the back stress and *R* represents the yield stress. The back stress is related to the yield surface and can be calculated as follows: (Imaoka 2008)

$$\{\alpha\} = \sum_{i=1}^{n} \{\alpha_i\} \tag{3.2}$$

$$\{\Delta\alpha\}_i = \frac{2}{3} C_i \{\Delta\varepsilon^{pl}\} - \gamma_i \{\alpha_i\} \Delta\varepsilon^{pl} + \frac{1}{C_i}\frac{dC_i}{d\theta} \Delta\theta \{\alpha\} \tag{3.3}$$

where ε^{pl} is the accumulated plastic strain, θ is temperature, and C_i and γ_i are the Chaboche material parameters for *n* number of points. In Eq. (3.3), the first term is the hardening modulus. On the other hand, the second term of the evolution of the back stress is a 'recall term' that produces a nonlinear effect and the third term considers the temperature effect.

The input consists of defining the elastic properties (e.g. elastic modulus, Poisson's ratio) via MP, EX and MP, NUXY, then issuing TB, CHABOCHE, ,ntemp, n, where *ntemp* is the number of temperature sets and n is the number of kinematic models. Any temperature-dependent group of constants are preceded with the TBTEMP command defining the temperature, while the material parameters for that temperature are entered via the

TBDATA command. The first constant is *R*, or the yield stress of the material – this value may be overridden if an isotropic hardening model is added. The second and third material constants are C_1 and γ_1 – these may be followed by additional pairs of C_i and γ_i, depending on the number *n* of kinematic models requested. The Chaboche model uses equivalent plastic strain and this approach is preferable as the elastic modulus and Poisson's ratio completely describe the elastic behavior, while the nonlinear constitutive model fully defines the plastic behavior (Lemaitre and Chaboche 1990).

In the present study, the rate independent version of Chaboche is followed and isotropic hardening is not considered. The Chaboche kinematic hardening parameters are used for three kinematic models with no temperature change. The Chaboche material constants are applied according to the material properties of the experiments and varied for different models based on the materials strength. So for the finite element modeling of this study, the Eqs. (3.1) - (3.3) become:

$$F = \sqrt{\frac{3}{2}(\{s\} - \{\alpha\})^T [M] (\{s\} - \{\alpha\})} = 0 \tag{3.4}$$

$$\{\alpha\} = \sum_{i=1}^{3} \{\alpha_i\} \tag{3.5}$$

$$\{\Delta\alpha\}_i = \frac{2}{3} C_i \{\Delta\varepsilon^{pl}\} - \gamma_i \{\alpha_i\} \Delta\varepsilon^{pl} \tag{3.6}$$

3.4.4 Volume Generation

The moment connection system with steel shear damper in general consists of elements like wide flange beam and column, damper upper and lower plate, upper and lower split-T and the shear damper. All the volumes of the model are formed following the same procedure. At first key points are defined for the element. Then areas of the element are generated with necessary holes for bolts where needed. After that the solid volume of the element is generated by dragging the areas.

Volume formations of the I-beam, column, damper and split-T are shown in Figs. 3.1-3.4 respectively.

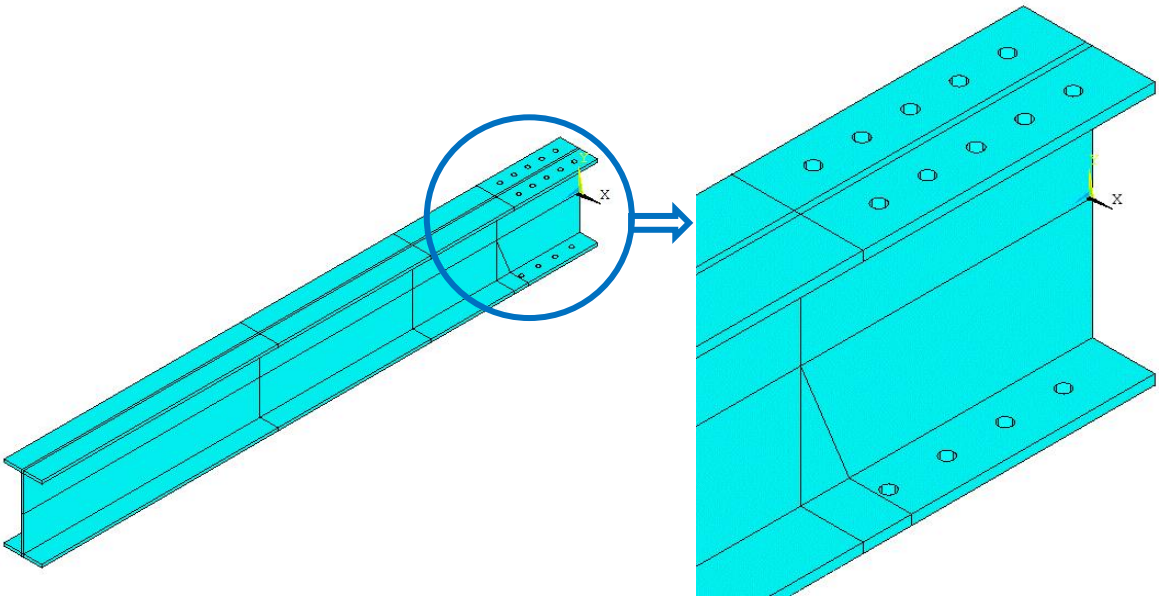

Fig. 3.1: Formation of I-beam with solid volumes

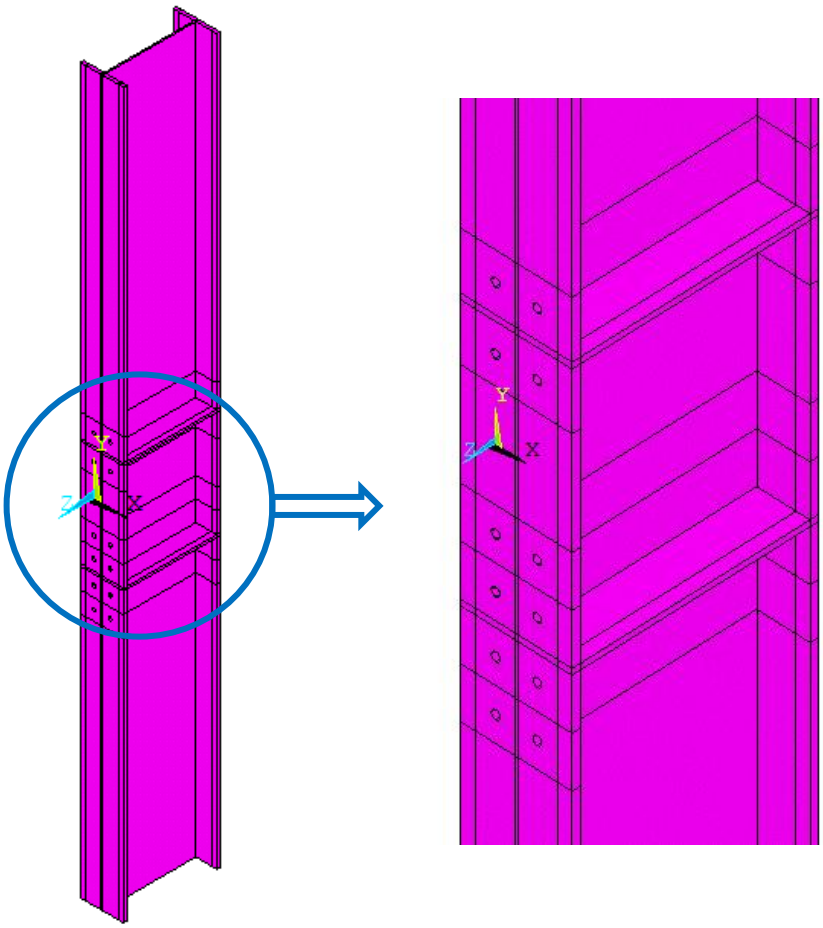

Fig. 3.2: Formation of column with solid volumes

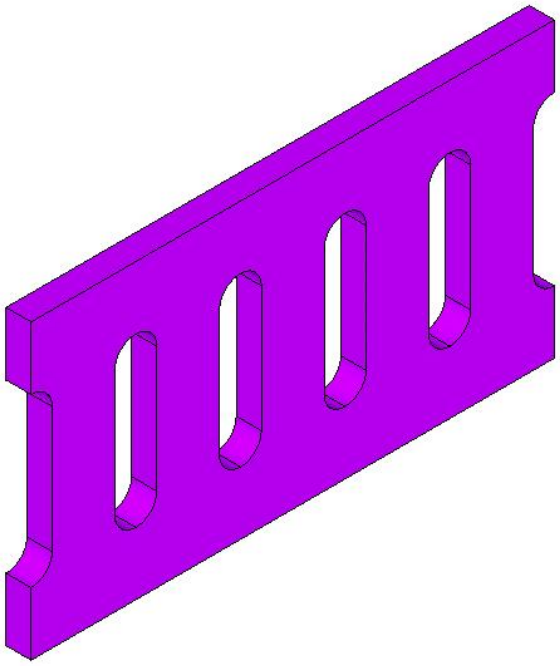

Fig. 3.3: Formation of damper with solid volumes

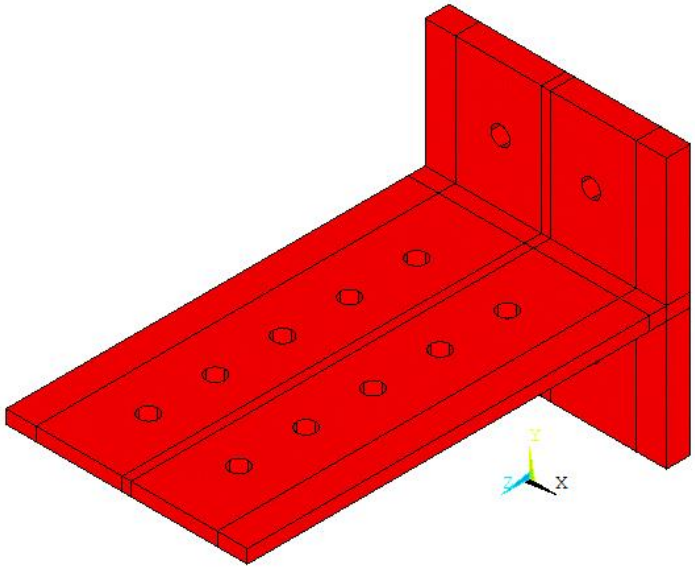

Fig. 3.4: Formation of split-T with solid volumes

3.4.5 Meshing

Meshing is an integral part of the FE simulation process where complex geometries are divided into simple elements that can be used as discrete local approximations of the larger domain. The mesh influences the accuracy, convergence and speed of the simulation. Furthermore, since meshing typically consumes a significant portion of the time it takes to get simulation results, the better and more automated the meshing tools, the faster and more accurate the solution (ANSYS, Inc. 2018).

The VSWEEP command is used for meshing all elements in the modeling. This command fills an existing unmeshed volume with elements by sweeping the mesh from an adjacent area through the volume. The beam and column is divided into several parts along their span and height. The split-T and the damper are meshed in a manner so that the meshing matches the beam-column and split-T respectively. All the parts at the connection region are modeled with a finer mesh to achieve more accuracy. The meshing size is tried to keep reasonable based on the analysis type and geometry of the model for reducing computational time and getting almost accurate result. Figs. 3.5 and 3.6 show the close view of the model before and after meshing, respectively.

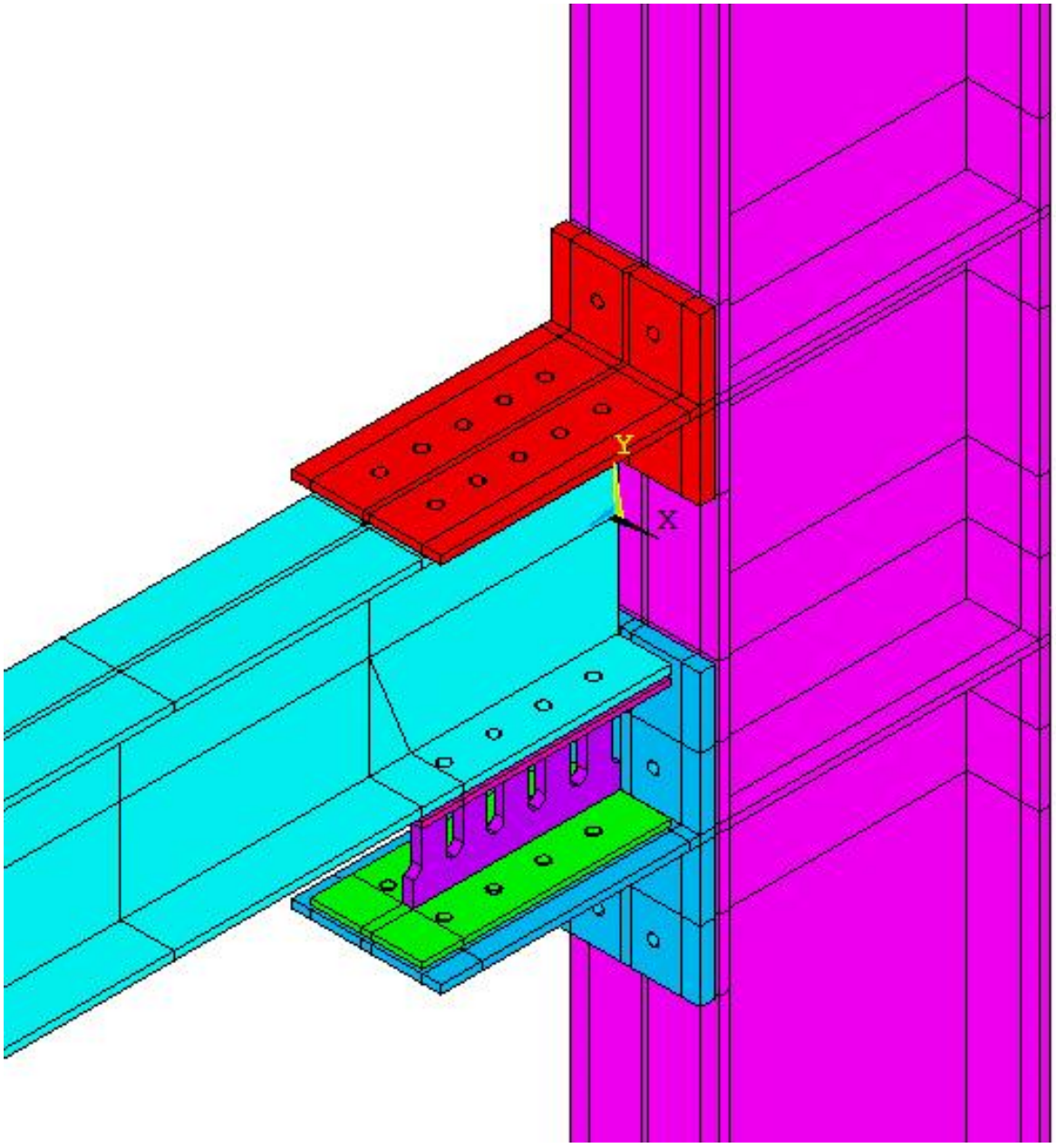

Fig. 3.5: Close view of the model before meshing

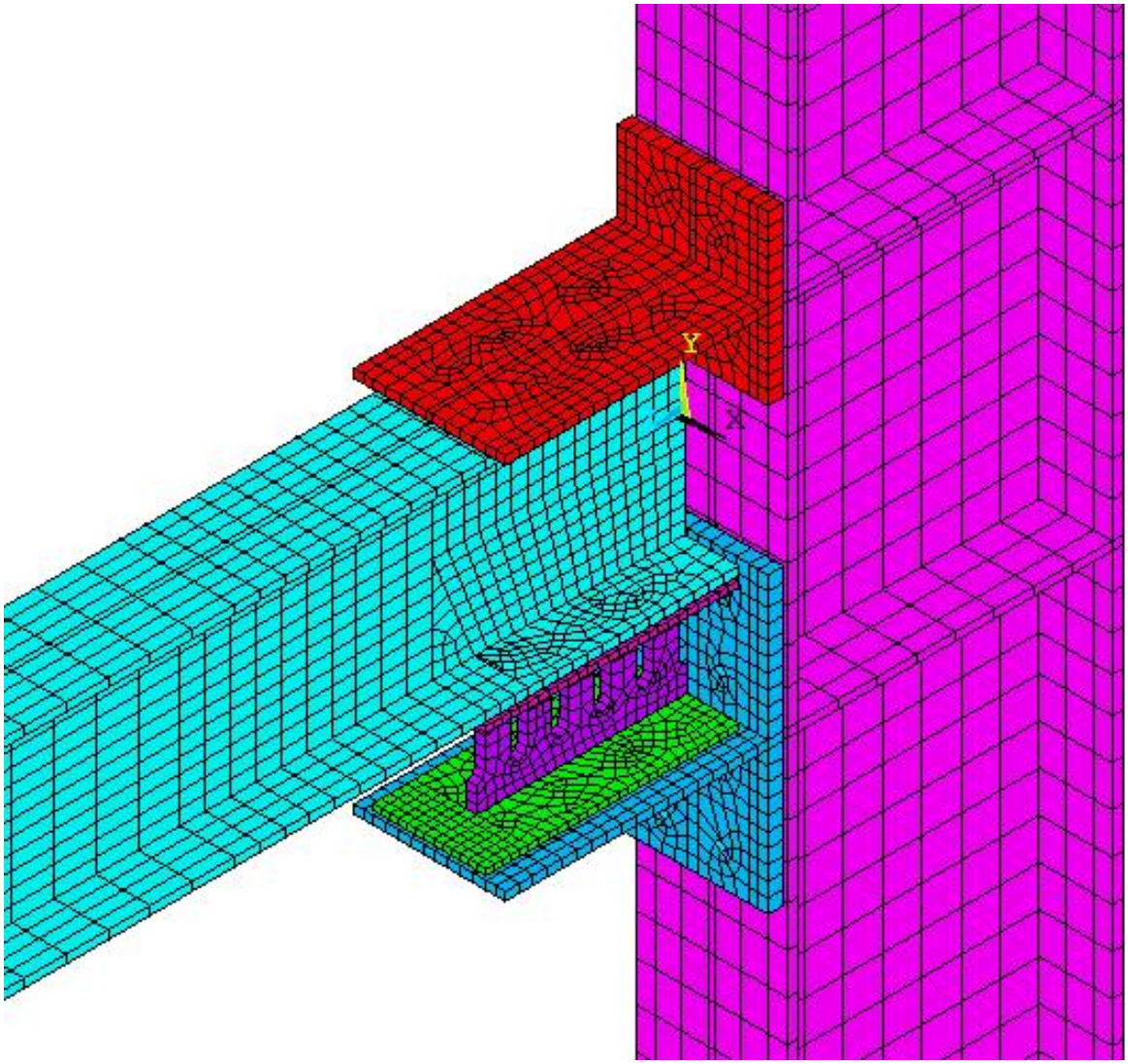

Fig. 3.6: Close view of the model after meshing

3.4.6 Boundary Conditions

3.4.6.1 Restraints

Restraints are provided in the model considering the test setup of the cyclic test as mentioned by the studies. The pin boundary conditions are applied at both ends of a column to simulate the behavior of a moment resisting frame. To prevent an out-of-plane deformation of the beam during loading, lateral supports are also given by providing constraints perpendicular to the span.

3.4.6.2 Coupling

Coupling can be used to model various joint and hinge effects. A more general form of coupling can be done with constraint equations. For structural analyses, a list of nodes is

defined along with the nodal directions in which these nodes are to be coupled. As a result of this coupling, these nodes are forced to take the same displacement in the specified nodal coordinate direction. The amount of the displacement is unknown until the analysis is completed. A set of coupled nodes which are not coincident, or which are not along the line of the coupled displacement direction, may produce an applied moment which will not appear in the reaction forces. The actual degrees of freedom available for a particular node depends upon the degrees of freedom associated with element types at that node. For scalar field analysis, this command is used to couple nodal temperatures, pressures, voltages, etc. A set of coupled nodes which are not coincident, or which are not along the line of the coupled displacement direction, produce an artificial moment constraint. If the structure rotates, a moment may be produced in the coupled set in the form of a force couple. This moment is in addition to the real reaction forces and may make it appear that moment equilibrium is not satisfied by just the applied forces and the reaction forces (ANSYS, Inc. 2018).

In view of a finite element analysis, two primary characteristics of a bolted joint are a pretension and a mating part contact. The pretension can generally be modeled with a thermal deformation, a constraint equation, or an initial strain. For a thermal deformation method, the pretension is generated by assigning virtual different temperatures and thermal expansion coefficients to the bolt and the flange. In the case of the constraint equation method, the pretension is a special form of coupling, with which equations can be applied to govern the behavior of the associated nodes. Initial strain method is more direct approach, in which the initial displacement is considered as a portion of the pretension on the structure with a bolted joint. A contact modeling can be addressed using point-to-point, point-to-surface, or surface-to-surface elements (Kim et al. 2007).

In the modeling coupling is used between the element and bolt location using CP command. Here slip-critical connection is assumed between the plates coupled by bolts. In the coupled bolt model as shown in Fig. 3.7, it is much simpler than the solid bolt model. As a result of the coupling condition, its associated nodes are forced to take the same displacement in the specified nodal coordinate direction so that the structure with bolted joints can be influenced by the pretension effect. In this approach, the number of finite elements is significantly reduced compared to the solid bolt model. Though the solid bolt model

provides the best accurate responses, the coupled bolt model shows the best effectiveness and usefulness in view of computational time and memory usage

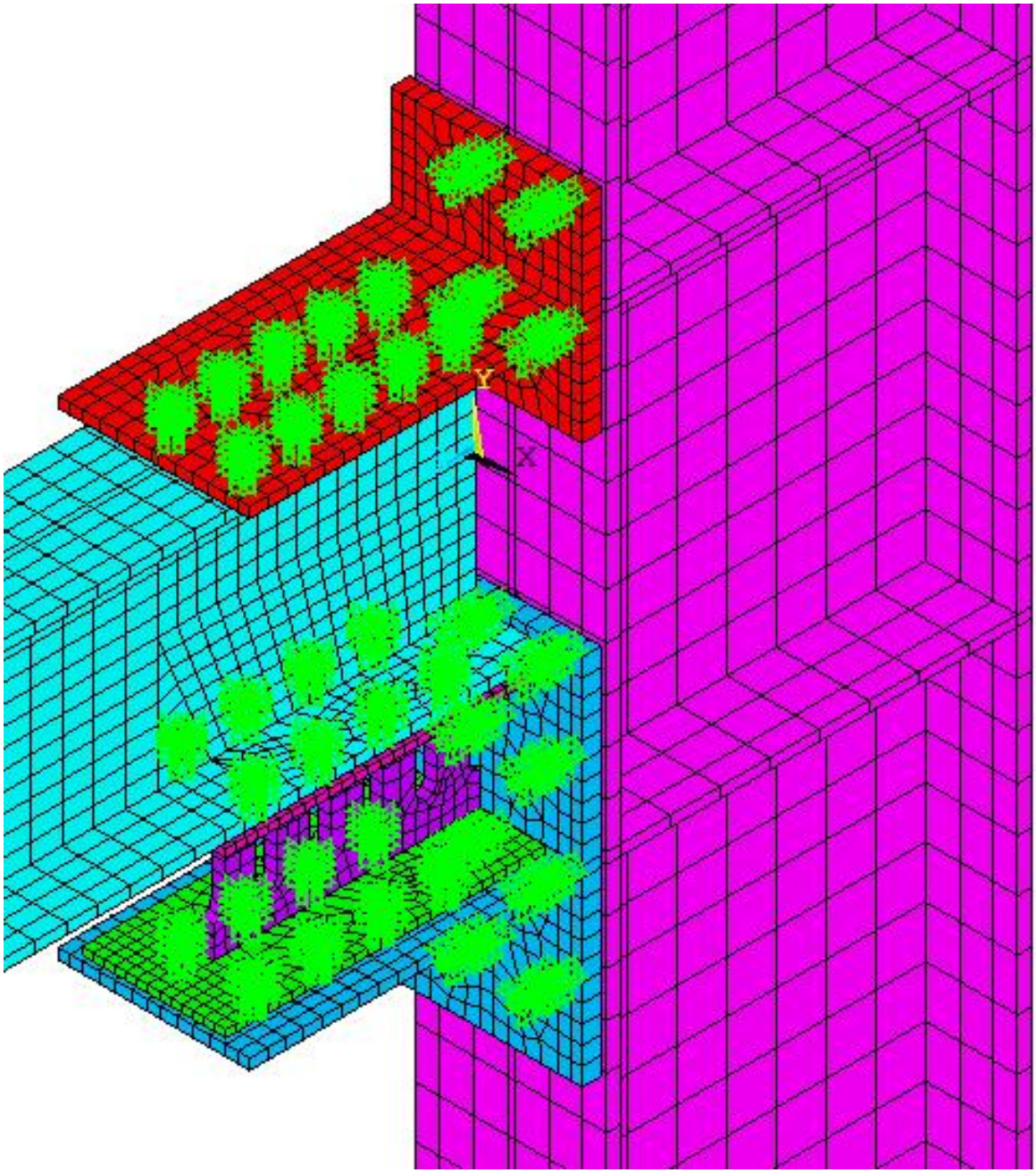

Fig. 3.7: Coupling in the model

3.4.7 Loading

For obtaining the load deflection diagram, we can perform nonlinear analysis either by applying load or deflection. If we want to continue the nonlinear analysis using Newton-Raphson method deflection application is more preferable since with load application, we might be unable to draw load deflection diagram after the peak due to unavailability of data.

Displacement is applied instead of load to prevent instability and also decremental load cannot be applied. But in RIKS method decremental load can be applied. Here static cyclic load is applied on both positive and negative direction by applying displacements as stated in the tests and rate-dependency is not considered.

3.5 ISOMETRIC VIEW OF THE DEVELOPED MODELS

The isometric views of the experimental specimen SL-3 tested by Chan and Albermani (2008), W and D1 tested by Oh et al. (2009) and N12 tested by Koken and Koroglu (2014) are illustrated in Figs. 3.8-3.11 respectively.

3.5.1 Chan and Albermani (2008) Model

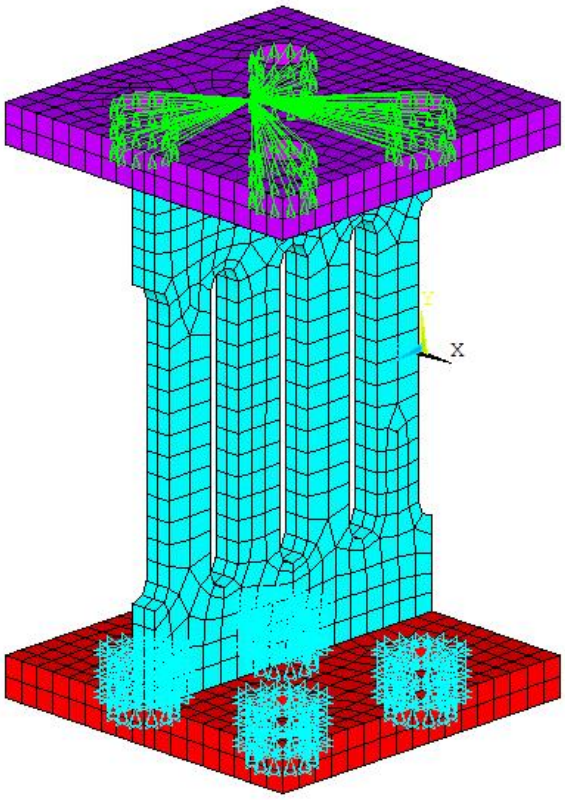

Fig. 3.8: The final model of specimen SL-3 (Chan and Albermani 2008)

To simulate the test setup, the specimen with an upper and a lower plate with necessary bolt holes are modeled. The bolt holes in the lower plate are restrained in all directions and the bolt holes in the upper plate are coupled together in vertical direction so that the upper plate remains perfectly horizontal during the load application. The entire model of Chan and Albermani (2008) specimen SL-3 includes approximately 2000 elements.

3.5.2 Oh et al. (2009) Model

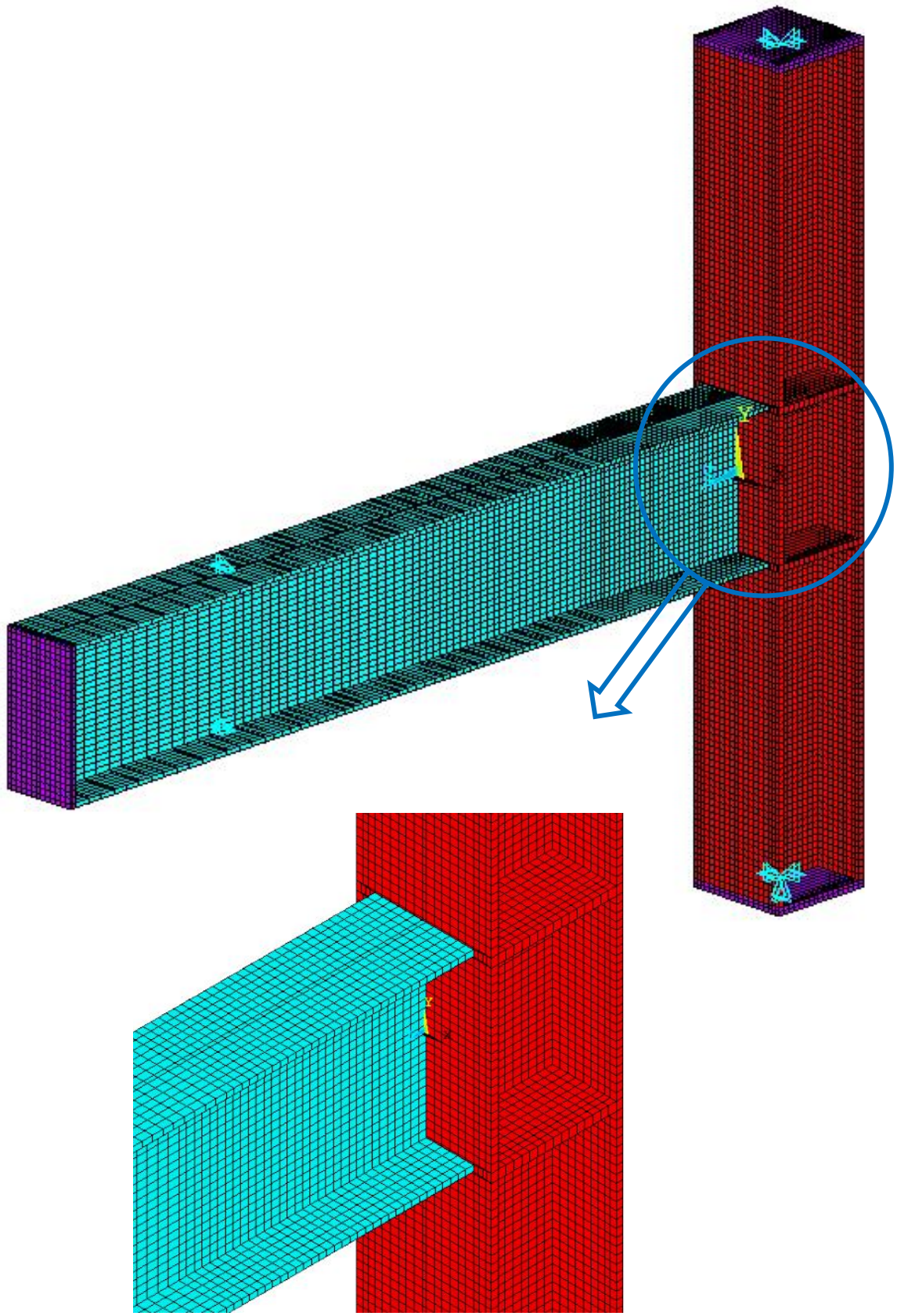

Fig. 3.9: The final model of specimen W (Oh et al. 2009)

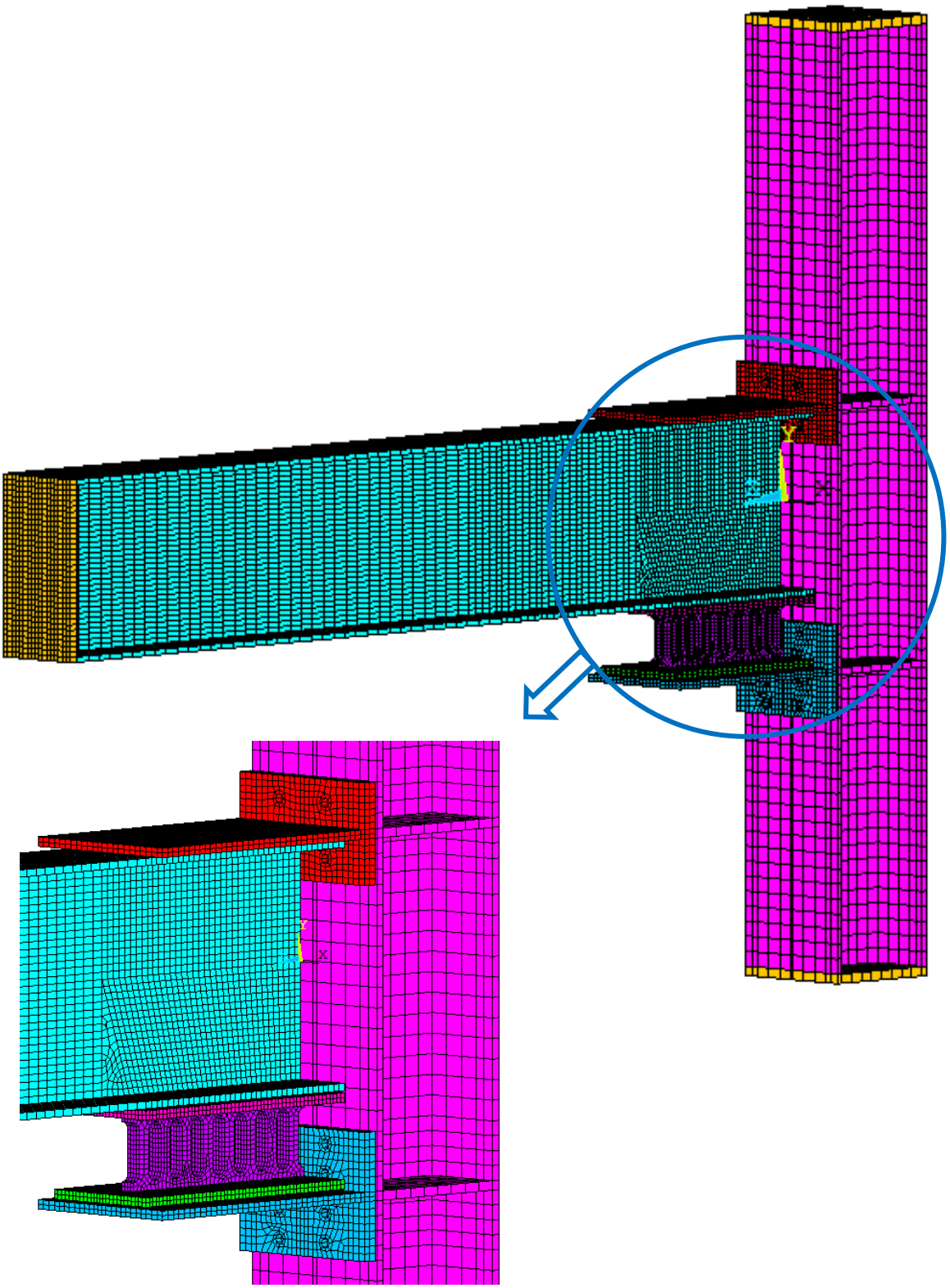

Fig. 3.10: The final model of specimen D1 (Oh et al. 2009)

The entire model of Oh et al. (2009) specimen W and D include approximately 16000 and 24000 elements, respectively.

3.5.3 Koken and Koroglu (2014) Model

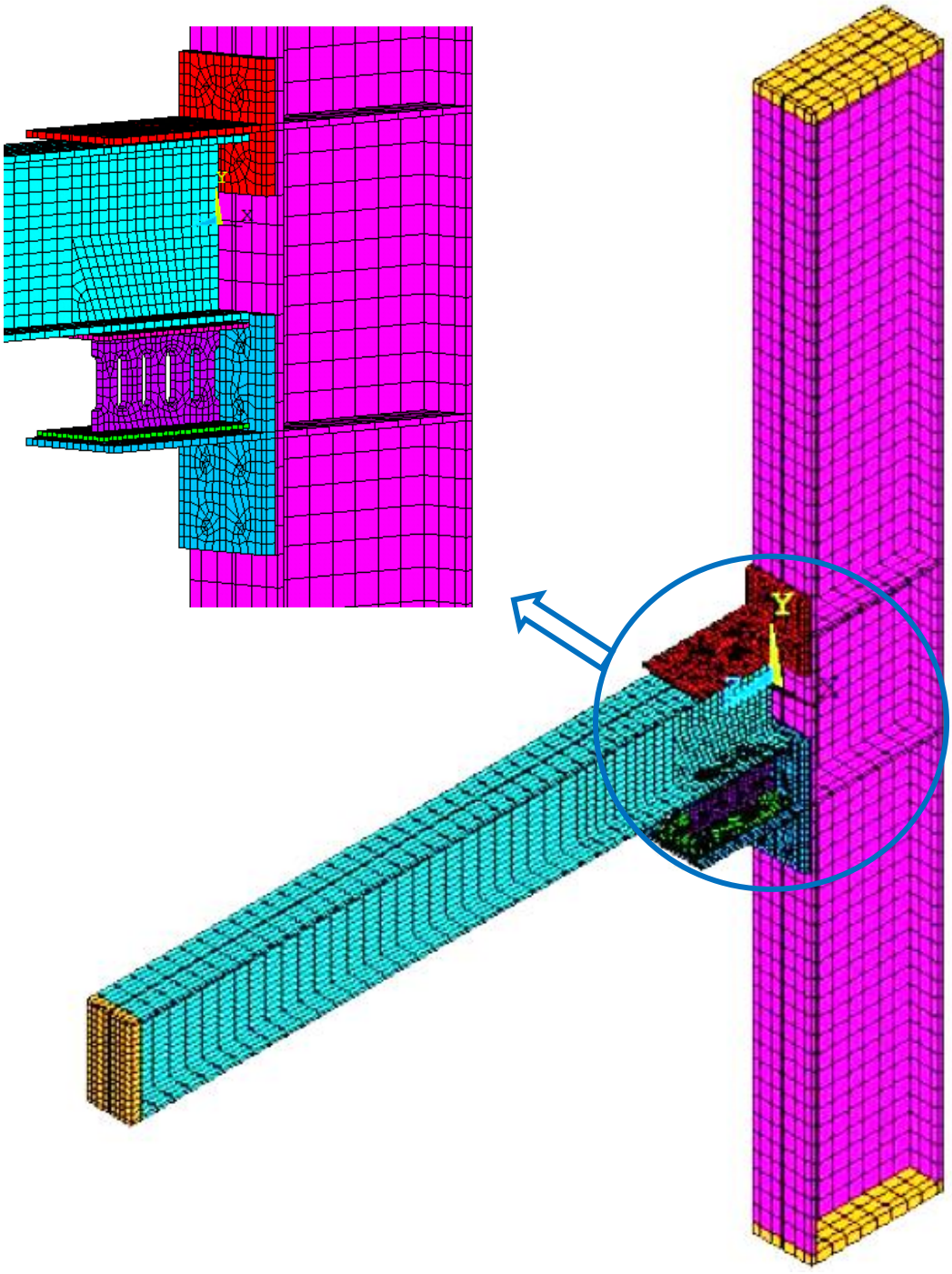

Fig. 3.11: The final model of specimen N12 (Koken and Koroglu 2014)

The entire model of Koken and Koroglu (2014) specimen N12 includes approximately 6000 elements.

3.6 REMARKS

The three-dimensional finite element models developed in this Chapter using finite element software need to be verified to carry on further numerical investigation to simulate the practical conditions. If it is possible to show that numerical model can adequately simulate the experimental results than it would be really helpful for practical problematic situations. In this regard, experimental models used by past researchers and their investigation are considered as reference for model verification which are described in Chapter 4 in details.

CHAPTER 4
EXPERIMENTAL MODEL VERIFICATION

4.1 INTRODUCTION

The finite element models developed in Chapter 3 using finite element method need to be verified to carry on further numerical investigation to simulate the practical conditions. On account of this, the experimental models used by Chan and Albermani (2008), Oh et al. (2009) and Koken and Koroglu (2014) are considered as reference in this chapter.

4.2 DEVELOPMENT OF NUMERICAL MODEL

Using the sectional geometric and material properties given by the mentioned studies, the models are generated almost similar to the way described in Chapter 3 only for experimental specimen SL-3 tested by Chan and Albermani (2008), W and D1 tested by Oh et al. (2009) and N12 tested by Koken and Koroglu (2014). Both material and geometric non-linearity are incorporated while developing the models. The developed models using SOLID185 elements are to be verified by comparing the load-deflection curves or moment-rotation curves obtained from the numerical analysis and the corresponding information obtained from the experimental results only for the specimens of the tests considered in this study.

4.3 VERIFICATION OF CHAN AND ALBERMANI (2008) MODEL

4.3.1 Experiment (Chan and Albermani 2008)

The objective of the experiment was to verify the structural characteristics as well as the cyclic performance of the proposed device. The basic design of the proposed device is shown in Fig. 4.1. It is fabricated from a short length of a standard structural wide flange section made of mild steel with several slits cut from the web, leaving a number of strips between the two flanges in a vierendeel truss arrangement. The slits are rounded at their ends, thereby reducing stress concentration in re-entrant corners. Four bolt holes are drilled on each flange for the connection to the parent structure. The device is a weld-free design, thus eliminating the uncertainties and imperfections associated with welding. The device can be installed on top of an inverted-V brace of a framed structure or at the connection of a beam-column joint.

Attempts were made to identify the key geometric parameters for largest energy dissipation. Particular attention was paid to the change in stiffness and equivalent damping ratio. It was assumed that the device is used as a retrofit option where axial force in the device is less significant; hence no axial force was applied to the specimens in the experiment. The structural behaviour of the proposed SSD is evaluated theoretically, followed by experimental verifications. Eight cyclic tests and one monotonic test were conducted. A total of nine specimens similar to Fig. 4.1 were fabricated at the City University of Hong Kong. To simplify the fabrication process, all specimens (each 100 mm long) in this study were cut from a single segment of a structural wide-flange section 152 x 152 x 37 Universal Column to BS4449 (depth x flange width x web thickness x flange thickness is 161.8 x 152.2 x 8 x 11.5 mm respectively). Consequently, the web thickness t is identical and material strengths of all specimens may be assumed equal. Four 16 mm diameter holes were drilled on each flange. Two standard test coupons were taken from the web of the section. Coupon tests gave an average tensile yield stress of 316.5 N/mm^2 and an average Modulus of Elasticity of 206.1 kN/mm^2. The details of specimens, test setup, loading history, instrumentation and test results with discussion are narrated in Chan and Albermani (2008).

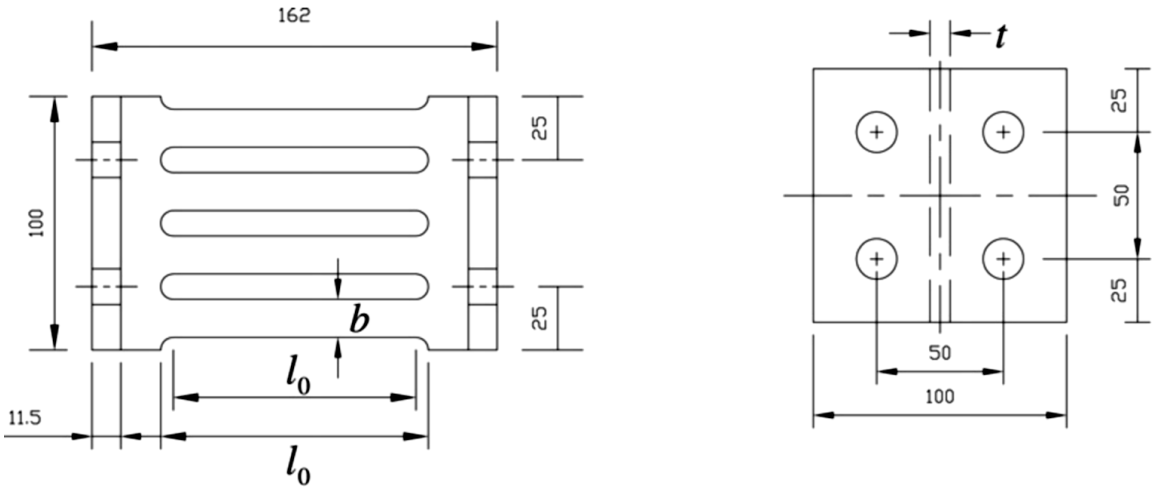

Fig. 4.1: Geometric design of specimens (Chan and Albermani 2008)

Based on the existing laboratory conditions, the test setup shown in Fig. 4.2 was developed. The test specimens were installed between a ground beam and an L-beam, securely fastened by four M16 bolts (snug tight) on each side. Forced displacement was applied by an MTS 100 kN capacity computer-controlled actuator quasi-statically to the specimen via the L-beam. To ensure the verticality of the applied load, a pantograph system was welded to the

right-hand side of the L-beam. The test setup was robust and repeatable, and no visible damage occurred after all tests were carried out.

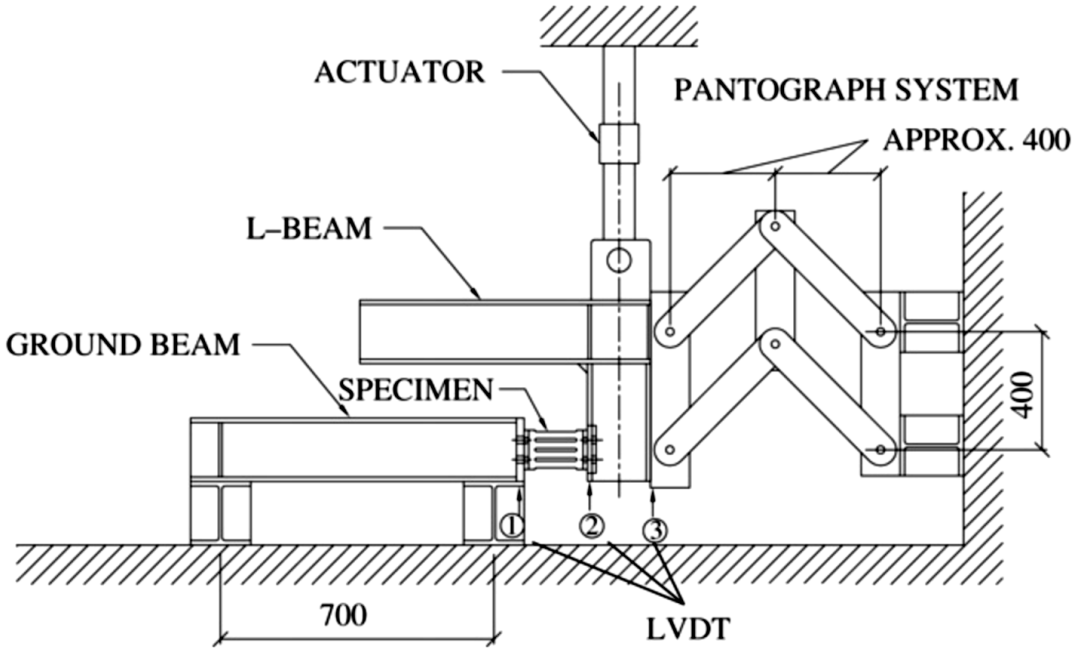

Fig. 4.2: Test setup (Chan and Albermani 2008)

4.3.2 Modeling Parameters (Chan and Albermani 2008)

The geometry of the specimen SL-3 and other sections are taken as mentioned in Chan and Albermani (2008). The elastic properties of the material are directly found from the study and the time independent plastic properties of the material are obtained by calibrating the Chaboche material constants based on the material strength which are listed in Table 4.1.

The element key options keypot,1,2,1 and keyopt,1,6,1 are used in the modeling using the ET command.

Table 4.1: Material model parameters (Chan and Albermani 2008)

Specimen	Elastic parameters		Plastic parameters (Chaboche kinematic hardening)						
	E (MPa)	υ	σ_y (MPa)	C_1 (MPa)	γ_1	C_2 (MPa)	γ_2	C_3 (MPa)	γ_3
SL-3	206000	0.3	316.5	7000	100	2000	50	1500	0

4.3.3 Loading History (Chan and Albermani 2008)

The static cyclic loading is applied both positive and negative direction based on the displacement history given in the study which is shown in Fig. 4.3. The loading is performed at each amplitude of 1.5, -1.5, 3, -4, 5, -6.5, 7.5, -8.5, 9.5, -11, 12 and -13.5 mm.

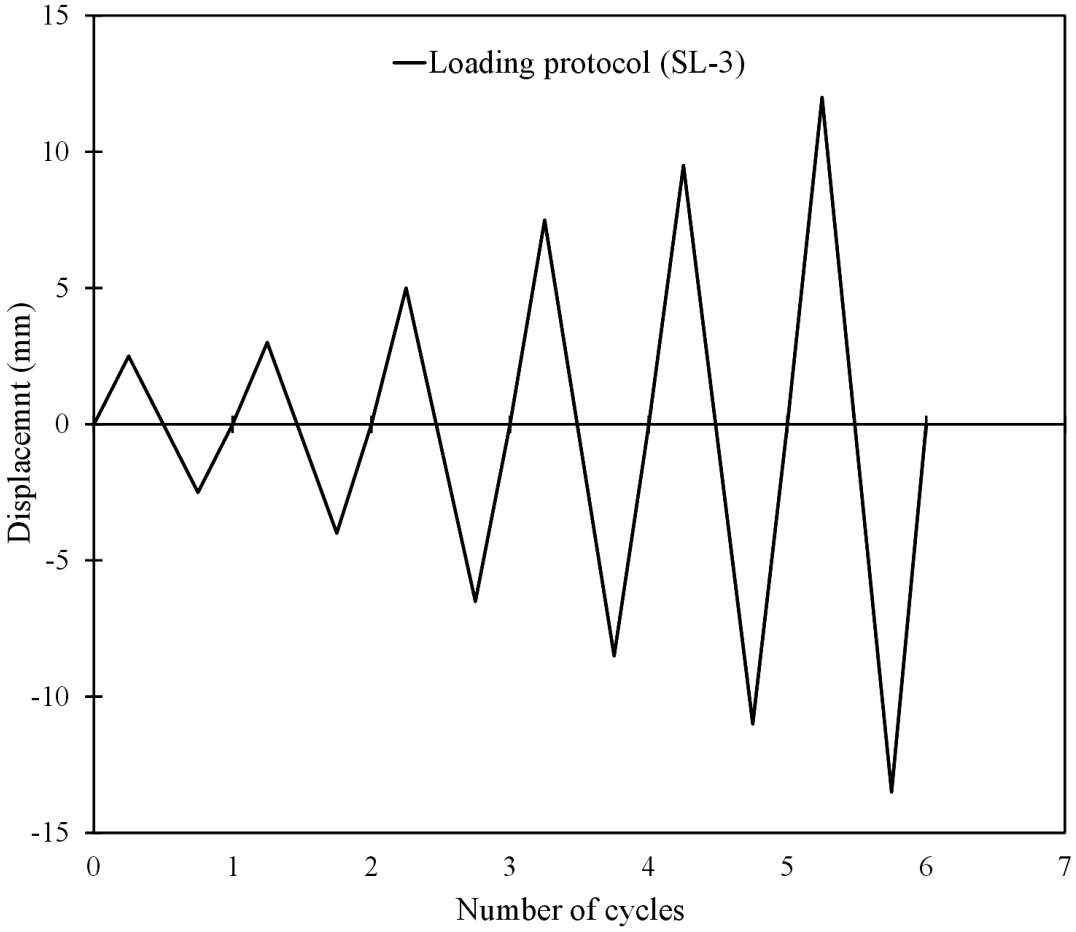

Fig. 4.3: Displacement history for static cyclic loading of the SL-3 model

4.3.4 Deformed Shape (Chan and Albermani 2008)

Fig. 4.4 shows the final deformed shape of the system. It shows significant shear deformation in damper. The deformed shapes from the finite element analysis have resemblance with the actual deformed shapes of the system.

4.3.5 von-Mises Stress Contour (Chan and Albermani 2008)

The von-Mises stress contour of the connection which is shown in Fig. 4.5 clearly indicates that the slit damper reaches the yield strength before other sections and stress is concentrated at end parts of the struts.

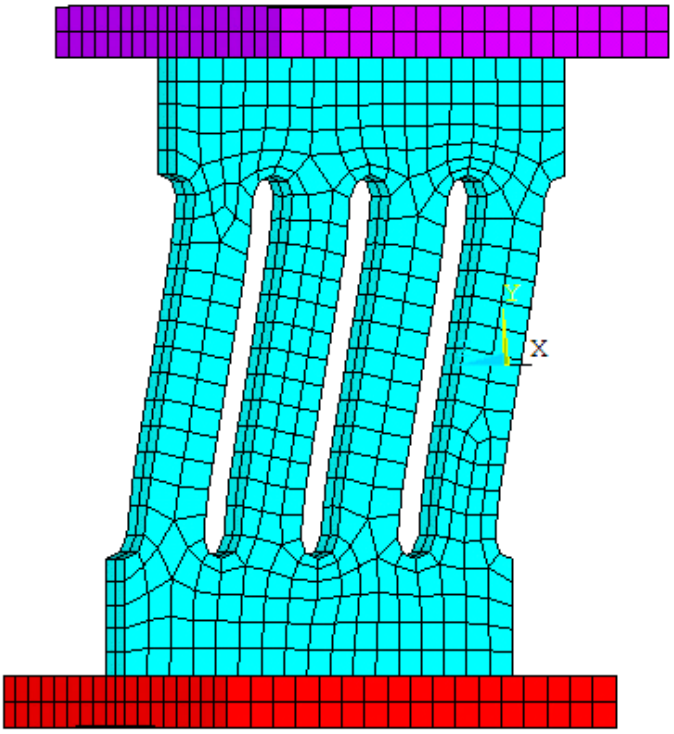

Fig. 4.4: Deformed shape of the SL-3 model

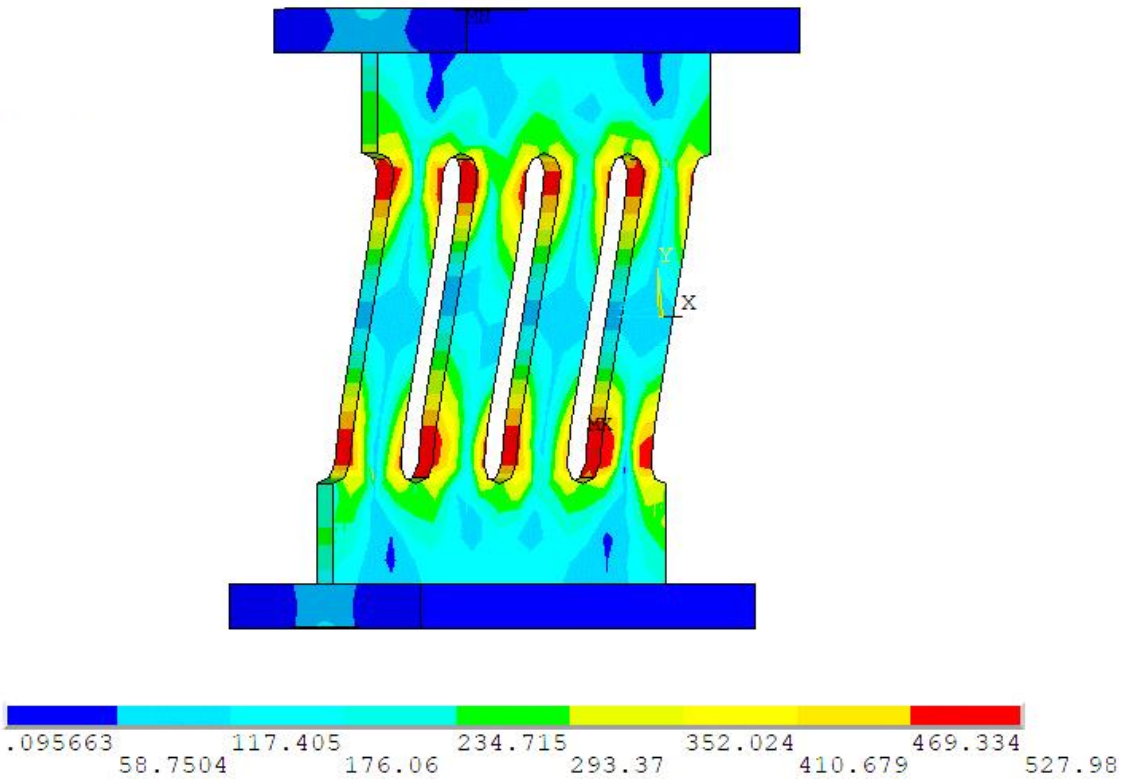

Fig. 4.5: von-Mises stress contour (MPa) of the SL-3 model

4.3.6 Verification of Load vs. Displacement Behavior (Chan and Albermani 2008)

As observed in Fig. 4.6, the load vs. displacement curves obtained from finite element modeling have a good agreement with experimental ones presented by Chan and Albermani (2008) for specimen SL-3. So this numerical model can be used for further studies.

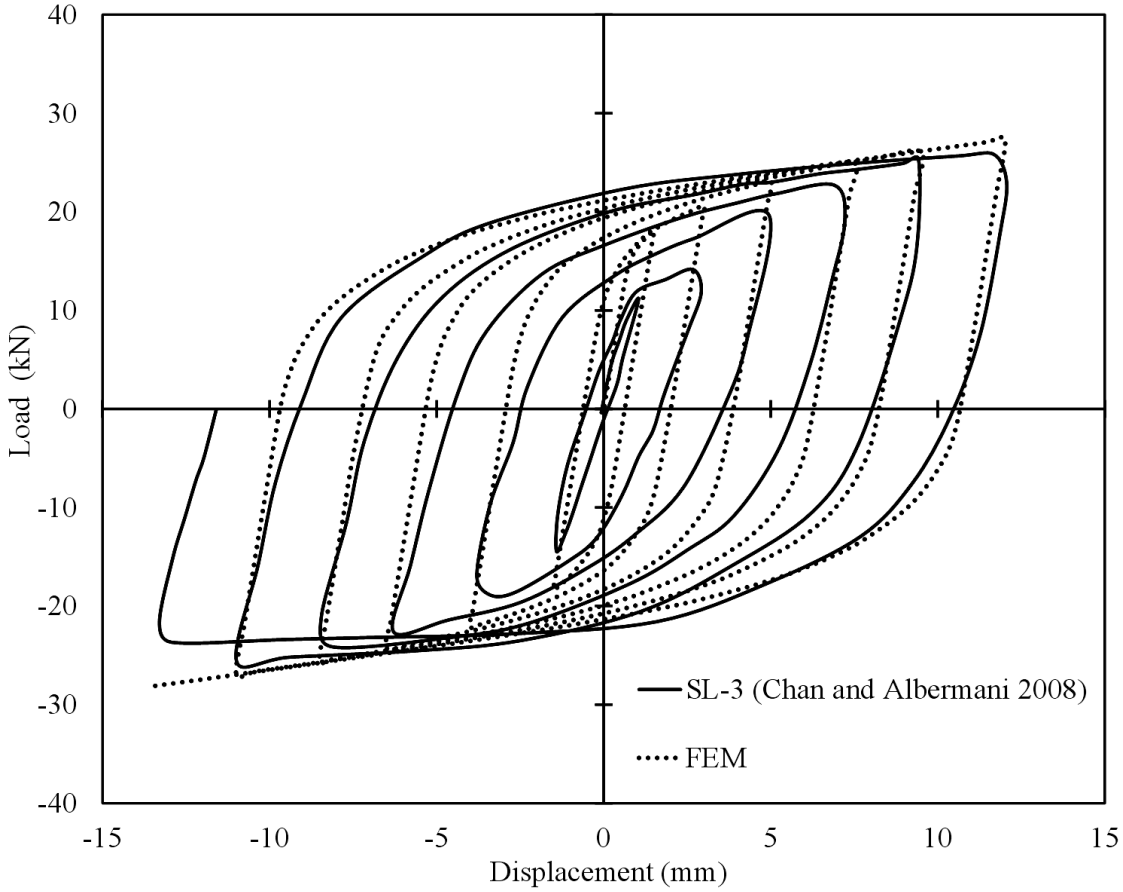

Fig. 4.6: Comparison between experimental and FEM results of specimen SL-3 following loading protocol SL-3

4.4 VERIFICATION OF OH ET AL. (2009) MODEL

4.4.1 Experiment (Oh et al. 2009)

This study proposed a new steel structure that achieves structural performance and is easily repairable after an earthquake. The main feature of this system is that plastic deformation is limited to the slit dampers at the bottom flange of the beam ends. The structural configuration and mechanical characteristics of the proposed structural system are addressed Oh et al. (2009). In the proposed structural system, the mechanical joint was adopted that was equipped with a metallic damper as the beam-to-column connection. Cyclic tests were conducted quasi-statically on three full-scale subassemblages that had slit

dampers and on one specimen that had a conventional post-Northridge welded connection. The mechanical behavior of the entire connection system was also evaluated theoretically and mathematical models were formulated to provide stiffness and strength predictions. Fig. 4.7 shows the specimens details of which there were three that had slit dampers attached and one was a welded moment connection.

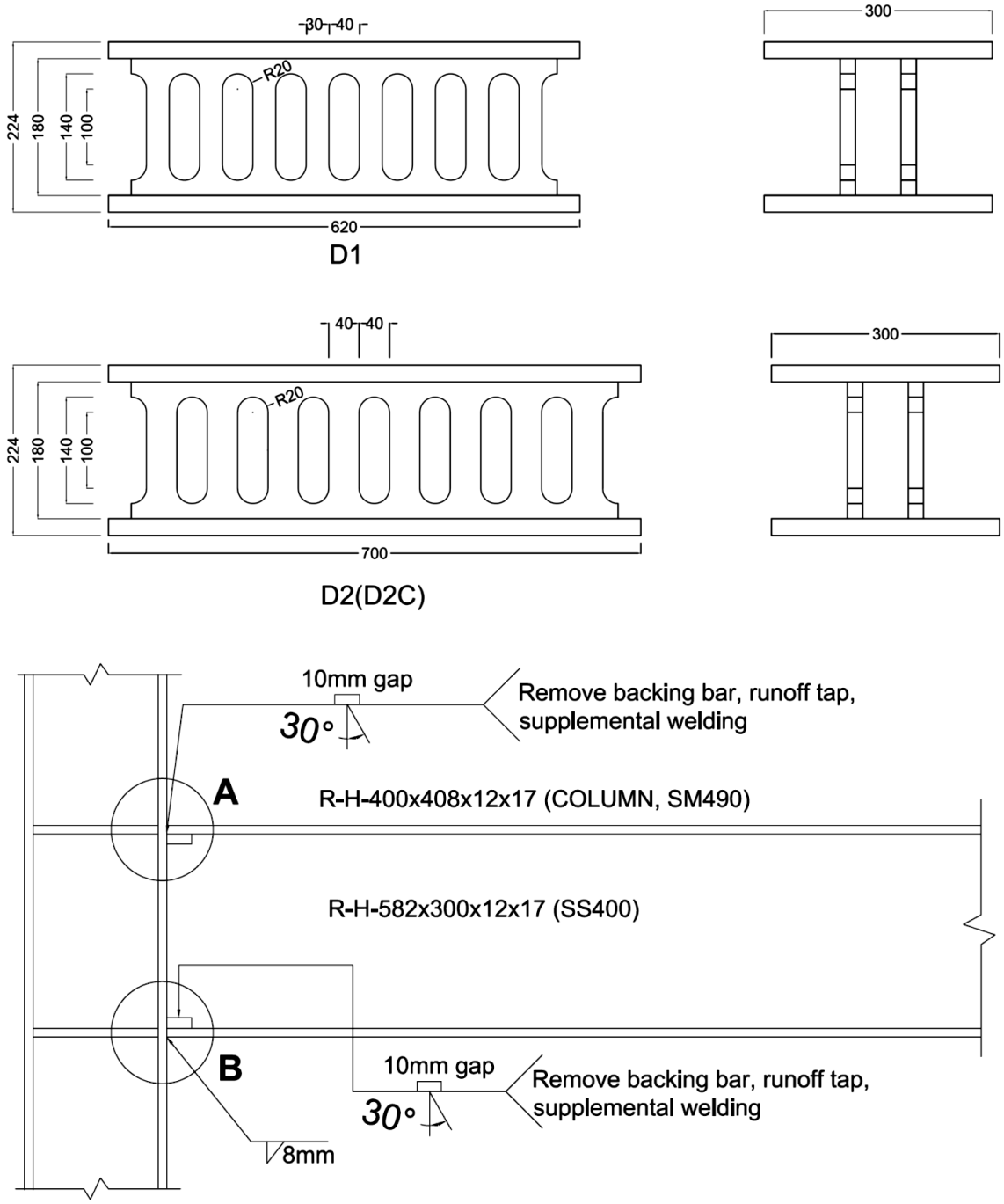

Fig. 4.7: Details of specimens (Oh et al. 2009)

Large-scale structural testing was performed to investigate a comparison of the cyclic performance between the proposed steel structures that have slit dampers and that of a

conventional welded moment resisting frame. A total of four specimens of beam-to-column connections were fabricated.

The test specimen is an external T-shaped model composed of a wide flange beam and column. The beam was an H-582x302x12x17 and the column was an H-400x400x21x21. In terms of the proposed connection between the beam and column, a split-T connection element was used on the top of the beam, and the energy absorption elements constructed by welding the steel slit plate to the split-T was used at the bottom of the beam. High-strength bolts were used to facilitate installation and removal. The frictional connection and the tensile connection of the test specimens constructed with high-strength bolts (F10T) had sufficient connection strength so that the connection would not separate or slip until the slit plate of each test specimen demonstrated maximum strength. Steel grades KS SS400 and SM490 were selected for the beams and columns, respectively. For the slit dampers, the slit plate was manufactured of mild steel KS SS400. The mechanical properties of these steel materials are summarized in Table 4.2.

In Oh et al. (2009) the details of test specimens, loading device, loading method and test results with discussion are described. The test setup developed for this experiment is shown in Fig. 4.8.

Table 4.2: Mechanical properties of steel materials (Oh et al. 2009)

Test Specimen	Thickness (mm)	Steel grade	σ_y (MPa)	σ_u (MPa)	Elongation (%)
Beam	Web (t = 12mm)	SS400	339	488	27
	Flange (t = 17mm)	SS400	318	480	30
Column	Web (t = 20mm)	SM490	395	554	27
	Flange (t = 20mm)	SM490	378	551	24
Split-T	Web (t = 22mm)	SM490	388	577	25
	Flange (t = 35mm)	SM490	386	573	24
Damper	t = 38 mm	SS400	208	464	30

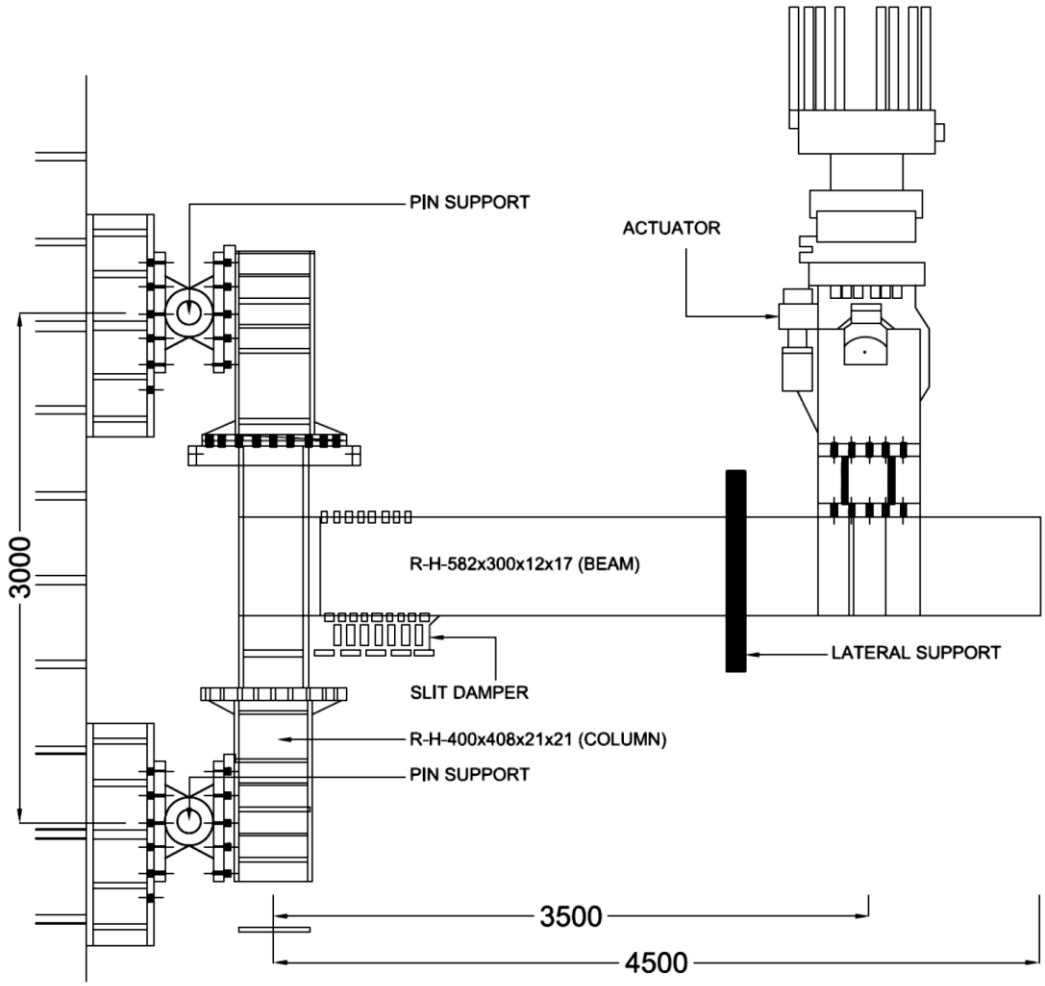

Fig. 4.8: Test setup (Oh et al. 2009)

The proposed structural system employs the connection between the beam top flange and the column flange as a means of transferring gravity loads from the beams to the columns. Also, the split-T at the top flange can be kept in an elastic range because the center of rotation stays at the top flange of the beam.

Thus, using this system, when the structure suffers compulsory deformation under an earthquake, the deformation is concentrated on the dampers at the bottom flange. As a result, the dampers can freely deform at the bottom flange of the beam without causing significant damage to the concrete slab under large story drifts. This design permits the simple replacement of slit dampers as connection elements of the bottom flange, allowing the continued use of buildings after an earthquake. Since the major retrofit work after an earthquake is performed near the bottom flange, the slabs do not need to be removed.

4.4.2 Modeling Parameters (Oh et al. 2009)

The sectional properties of the specimens and other parts of the system are found from Oh et al. (2009). The elastic properties of the material are taken from the study and the time independent plastic properties of the material are set by calibrating the Chaboche material constants based on material which are listed in Table 4.3.

Table 4.3: Material model parameters (Oh et al. 2009)

Specimen	Elastic parameters		Plastic parameters (Chaboche kinematic hardening)						
	E (MPa)	υ	σ_y (MPa)	C_1 (MPa)	γ_1	C_2 (MPa)	γ_2	C_3 (MPa)	γ_3
W	200000	0.3	318	14000	750	4500	60	2000	0
D1	200000	0.3	208	45000	5000	25000	2000	15000	150

4.4.3 Loading History (Oh et al. 2009)

The static cyclic loading is applied both positive and negative direction at beam end based on the loading protocol given in the study which is shown in Figs. 4.9 and 4.10 for specimen W and D1, respectively.

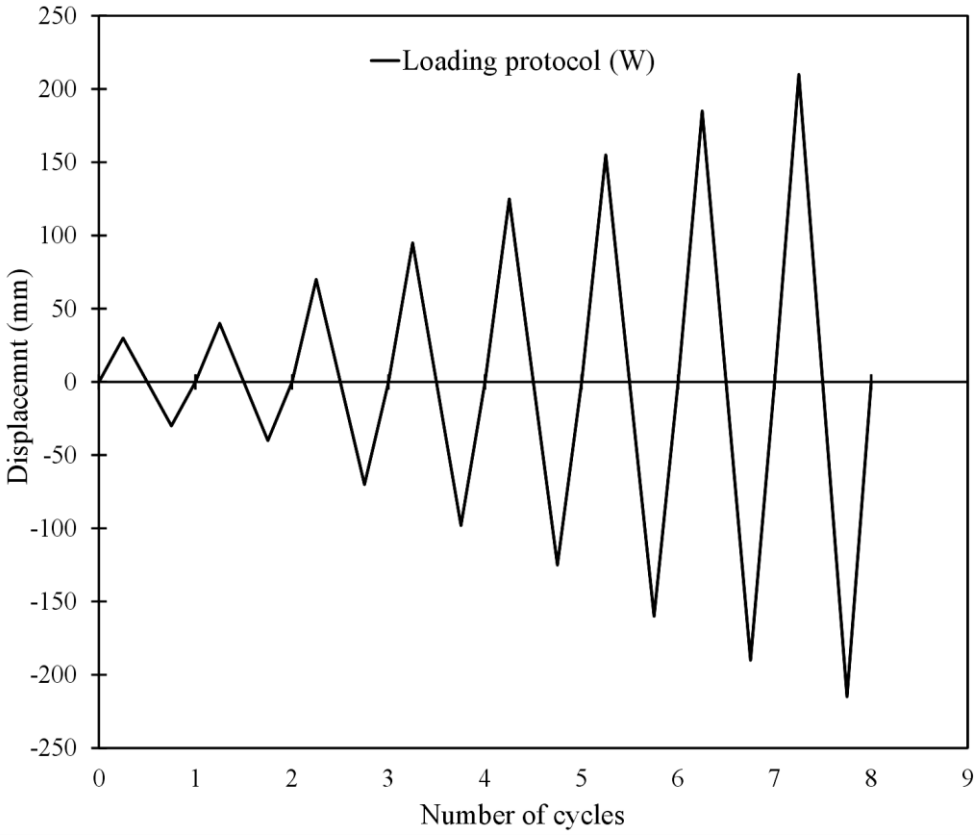

Fig. 4.9: Displacement history for static cyclic loading of the W model

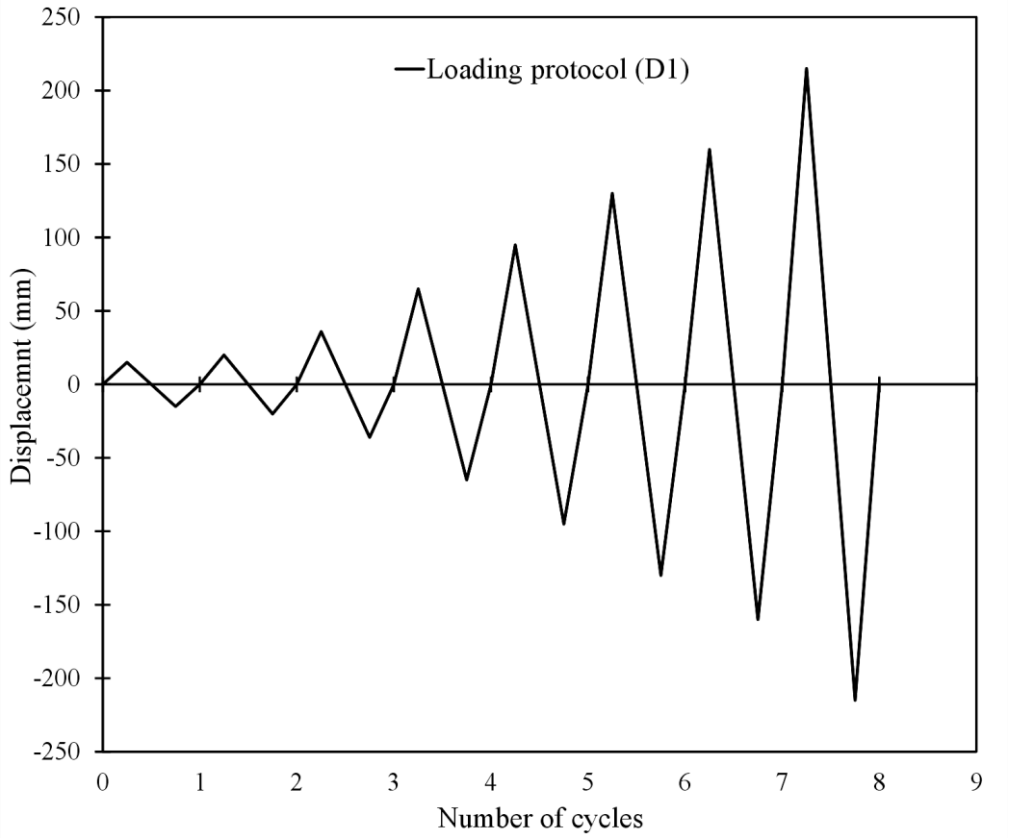

Fig. 4.10: Displacement history for static cyclic loading of the D1 model

4.4.4 Deformed Shape (Oh et al. 2009)

Fig. 4.11 illustrates the actual deformed shape of specimen W which have resemblance with deformed shape of the specimen W model shown in Fig. 4.12. It is observed that the entire plastic deformation originated from the local buckling of the beam. Therefore, it is ineffective to repair these conventional welded connections after an earthquake.

Figs. 4.13 and 4.14 show the actual and model deformed shape of the specimen D1, respectively. The deformed shapes from the finite element analysis have similarity with the actual deformed shapes of the system. It is clear that the energy absorption is concentrated only at the slit dampers rather than at the beams. Thus, the slit dampers can be replaced after an earthquake more readily than can beams and columns.

Coupling is used in the model to simulate the high-strength bolts behavior which were used in test setup to facilitate installation and removal. The frictional connection and the tensile connection of the test specimens constructed with high-strength bolts had sufficient

connection strength so that the connection would not separate or slip until the slit plate of each test specimen demonstrated maximum strength.

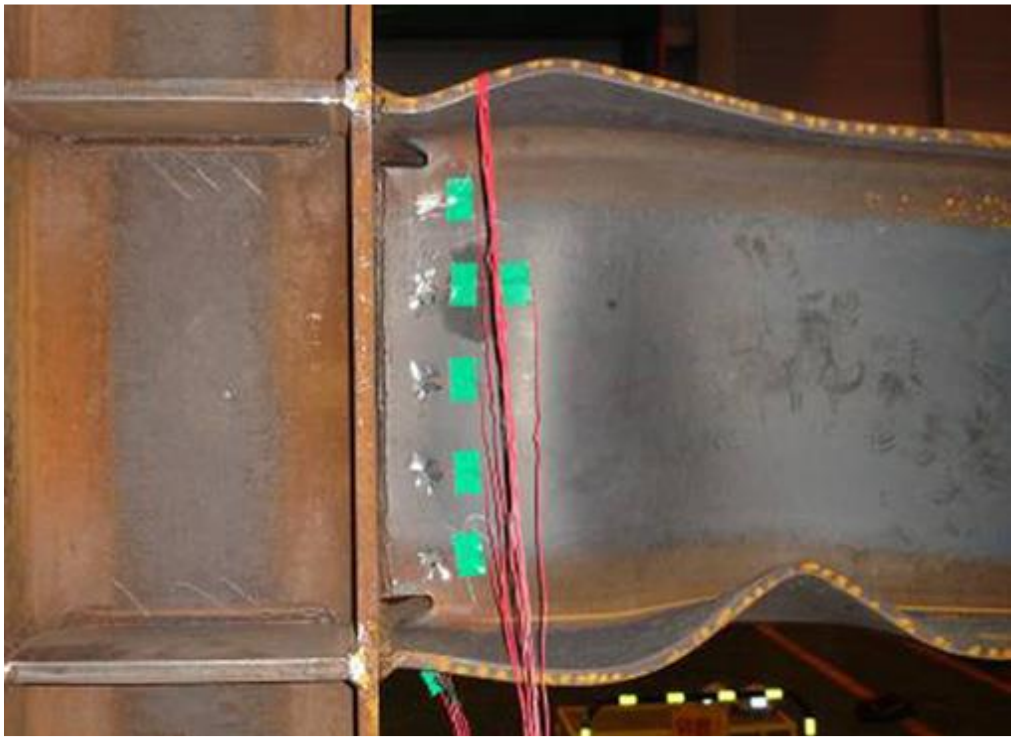

Fig. 4.11: Beam local buckling of specimen W (Oh et al. 2009)

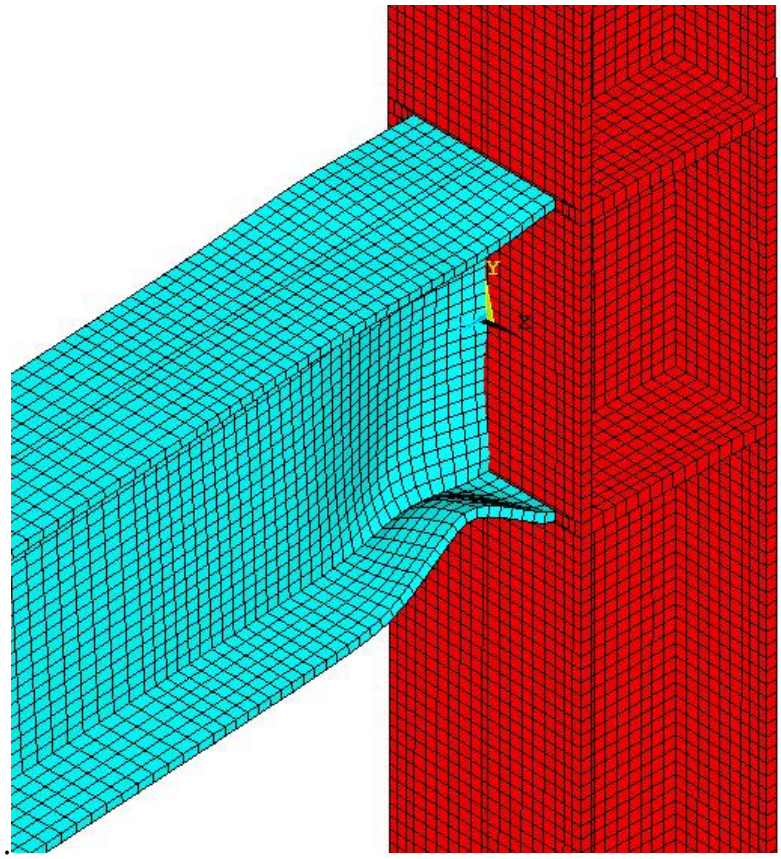

Fig. 4.12: Deformed shape of the W model

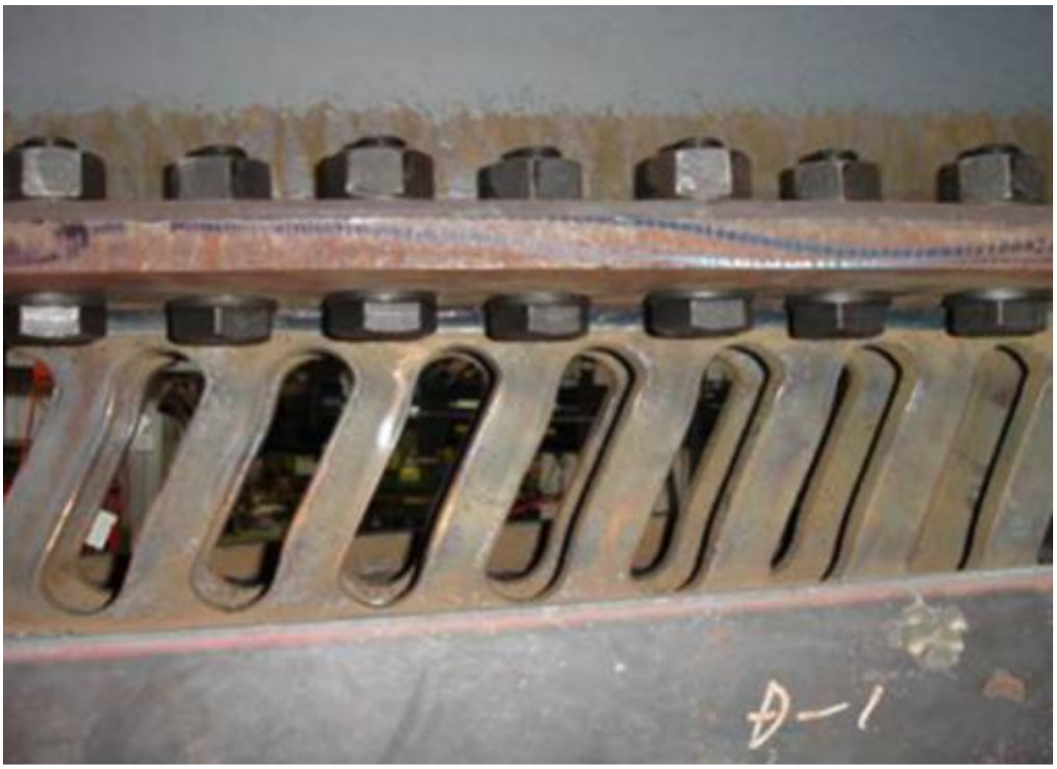

Fig. 4.13: Damper deformation of specimen D1 (Oh et al. 2009)

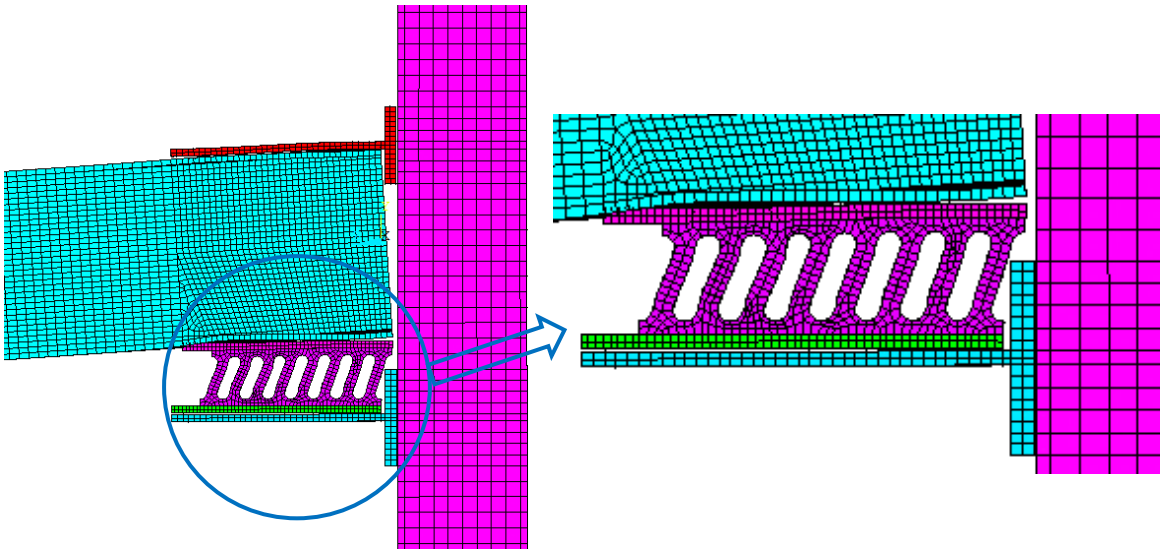

Fig. 4.14: Deformed shape of the D1 model

As illustrated in Fig. 4.14, slight separation of the connection occurs during the extreme deformation of the damper. This is may be due to the gap maintained between the connection while generating the model. Since slippage failure of a slip-critical connection is not necessarily a catastrophic failure, the effect of this separation will not create much deviation in the analysis results.

4.4.5 von-Mises Stress Contour (Oh et al. 2009)

The von-Mises stress contour of the W model which is illustrated in Fig. 4.15 clearly indicates that the conventional welded moment connections fractured prematurely in a brittle manner at the bottom flange of the beam.

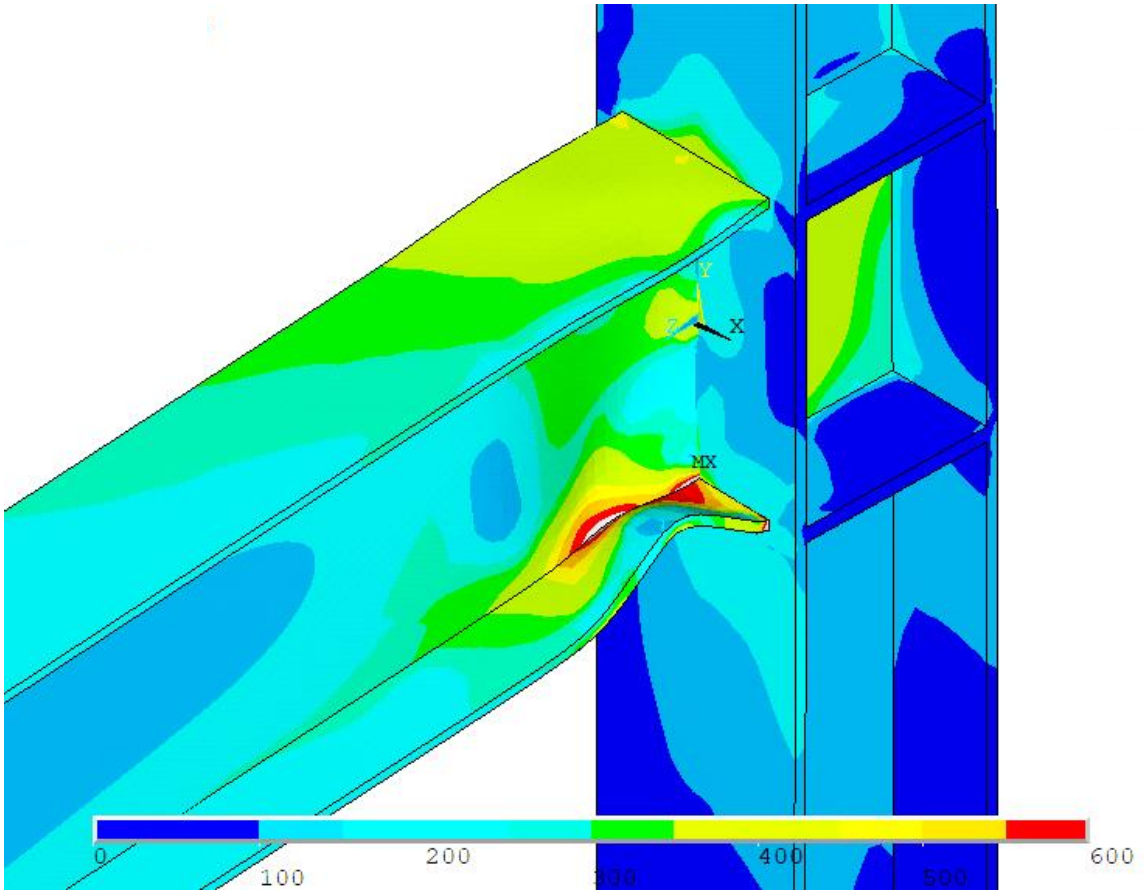

Fig. 4.15: von-Mises stress contour (MPa) of the W model

Fig. 4.16 shows the von-Mises stress contour of the specimen D1 clearly exhibits that the slit damper reaches the yield strength before the other members and plastic deformation is sustained only at the slit dampers.

4.4.6 Verification of Moment vs. Rotation Behavior (Oh et al. 2009)

Figs. 4.17 and 4.18 illustrate the moment vs rotation curves attained from finite element modeling and experiments performed by Oh et al. (2009) for specimens W and D1. In both cases, the numerical results show a fair agreement with the experimental ones.

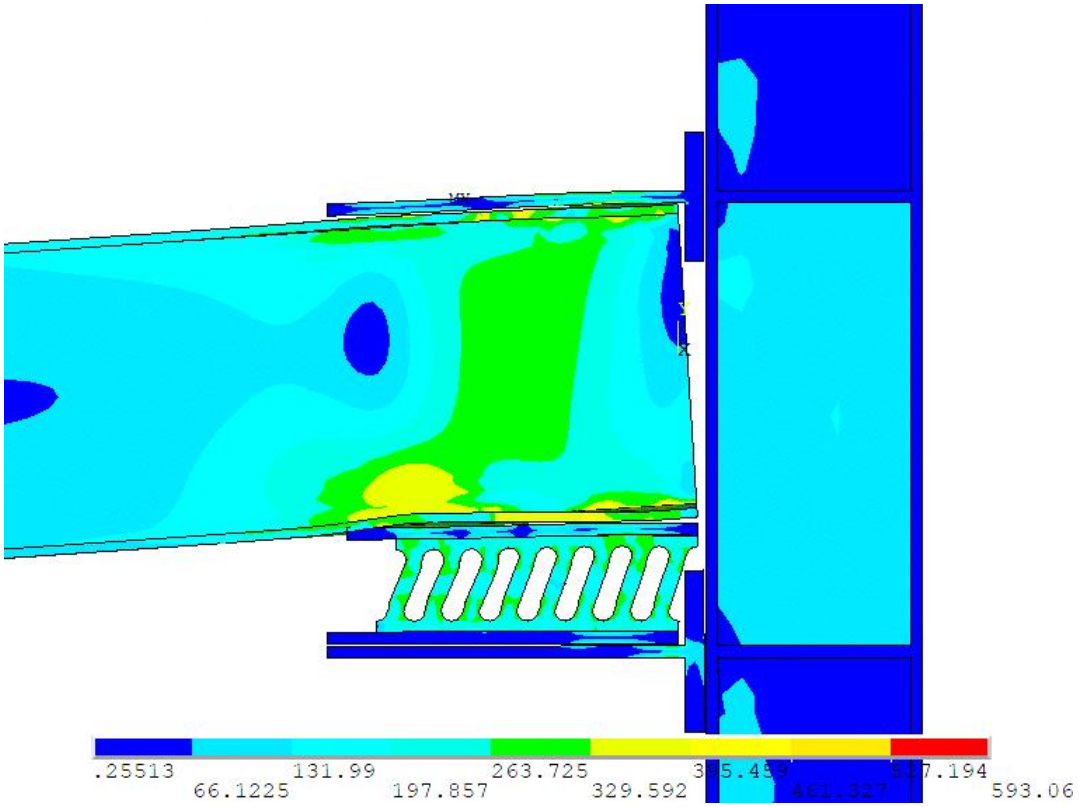

Figure 4.16: von-Mises stress contour (MPa) of the D1 model

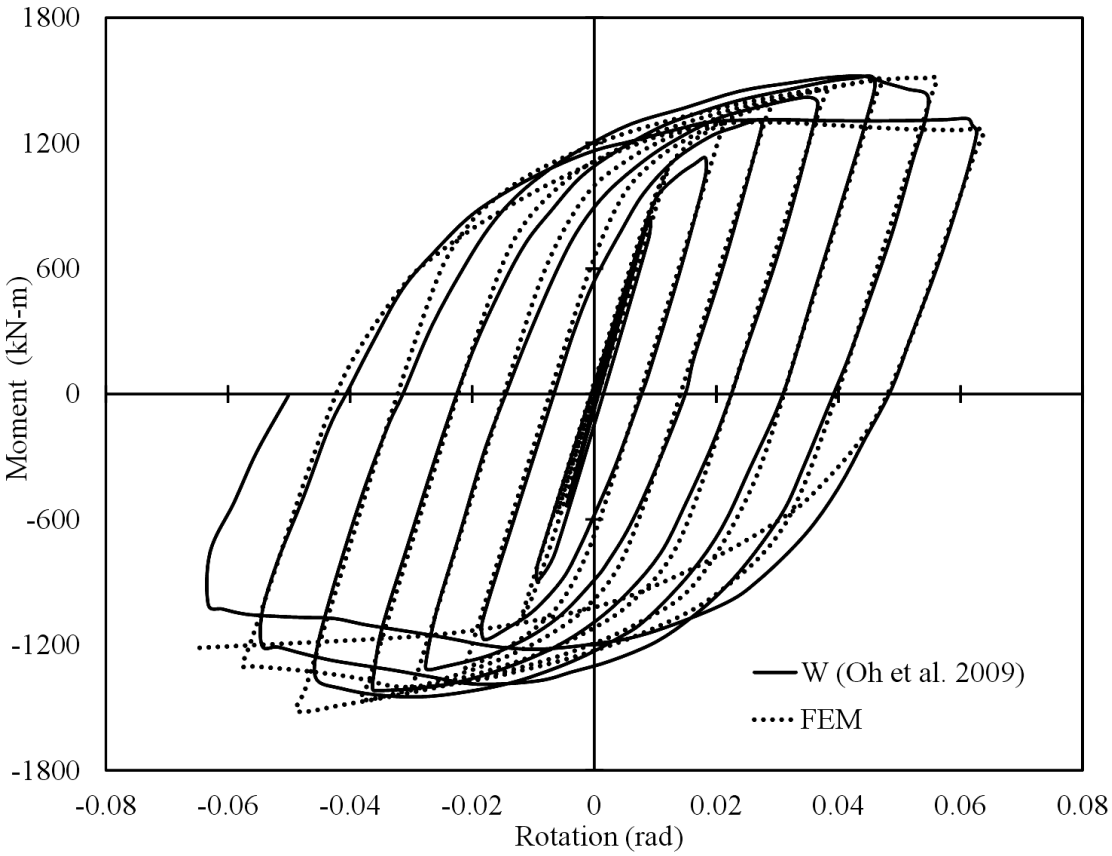

Fig. 4.17: Comparison between experimental and FEM results of specimen W following loading protocol W

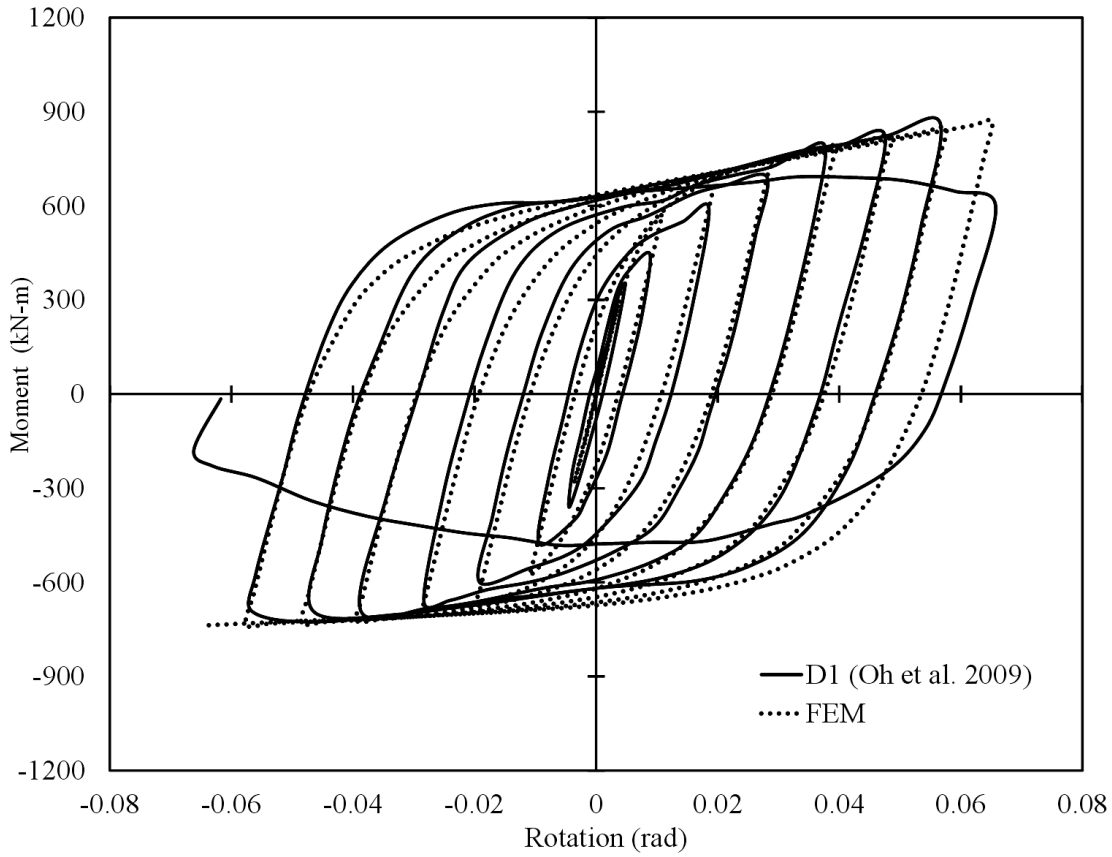

Fig. 4.18: Comparison between experimental and FEM results of specimen D1 following loading protocol D1

4.5 VERIFICATION OF KOKEN AND KOROGLU (2014) MODEL

4.5.1 Experiment (Koken and Koroglu 2014)

The main idea of the study was to prevent damage to the beam or column by dissipating the loads in the dampers that were placed in beam-column connections when earthquake strength is provided by moment transferring frame systems. By this means, after a damage inflicting earthquake, by simply replacing the dampers in the beam-column connections of a structure the structure can be made serviceable as there would be no damage to the beams or columns. Thus, using damper elements will not only prevent serious damage to the structure and loss of lives and property, but also it will ensure that the structure can be repaired and made serviceable as soon as possible with minimal cost.

In this context, three full size beam-column connection experiments, using two dampers and one traditional extended end plate connection, were conducted under reversible cyclic loading. In order to obtain the strength of the connections, theoretical and mathematical

models were generated and compared with the experimental results. In all experiments, IPE400 and IPE270 profiles were used for columns and beams, respectively. In full-scale beam-column connection experiments, test setup was designed to simulate the real boundary conditions of the frame beam-column connection region. An IPE400 column, which has a hinge-to-hinge length of 3,000 mm, and an IPE270 beam, which has a 2,000-mm length measured from the face of the column to the application point of reversible cyclic loading, were used. In order to compare the behavior of the specimens, an extended end plate connection was manufactured as a frame of reference. In full-scale experiments, the connection where the dampers were used was slightly different than the extended end plate connection. The upper split-T that connects the upper flange of the beam to the column was made of HEA600 profile and the gusset plate (lower split-T), which connects the beam to the column through the damper, was made of HEA800. The HEA800 gusset plate was strengthened using welded elements in upper and lower parts of both corners. While the IPE270 profiles, IPE400 profiles, gusset plate, and split-T elements were St 44 which has 440 MPa yielding strength, the extended end plate and continuity plate for the dampers were St 37 standard- compliant. All IPE profiles were cut from same-length profiles, and samples were taken from upper and lower flange, as well as the web of the profile. Table 4.4 shows mechanical properties of the materials that were obtained from the tension tests and the test program of this experiment is illustrated in Fig. 4.19.

Table 4.4: Mechanical properties of steel materials (Koken and Koroglu 2014)

Test Specimen	Thickness (mm)	Steel grade	σ_y (MPa)	σ_u (MPa)	Elongation (%)
Beam	Web (t = 6.6 mm)	St44	319.4	458.22	27.4
	Flange (t = 10.2 mm)	St44	298.75	444.30	29.3
Column	Web (t = 8.6 mm)	St44	305.45	435.40	28.3
	Flange (t = 13.5 mm)	St44	308.40	443.50	29.4
Split-T	Web (t = 10 mm)	St44	322.40	457.45	26.3
	Flange (t = 18 mm)	St44	329.35	465.10	25.9
Damper	t = 12 mm	St37	314.10	402.20	31

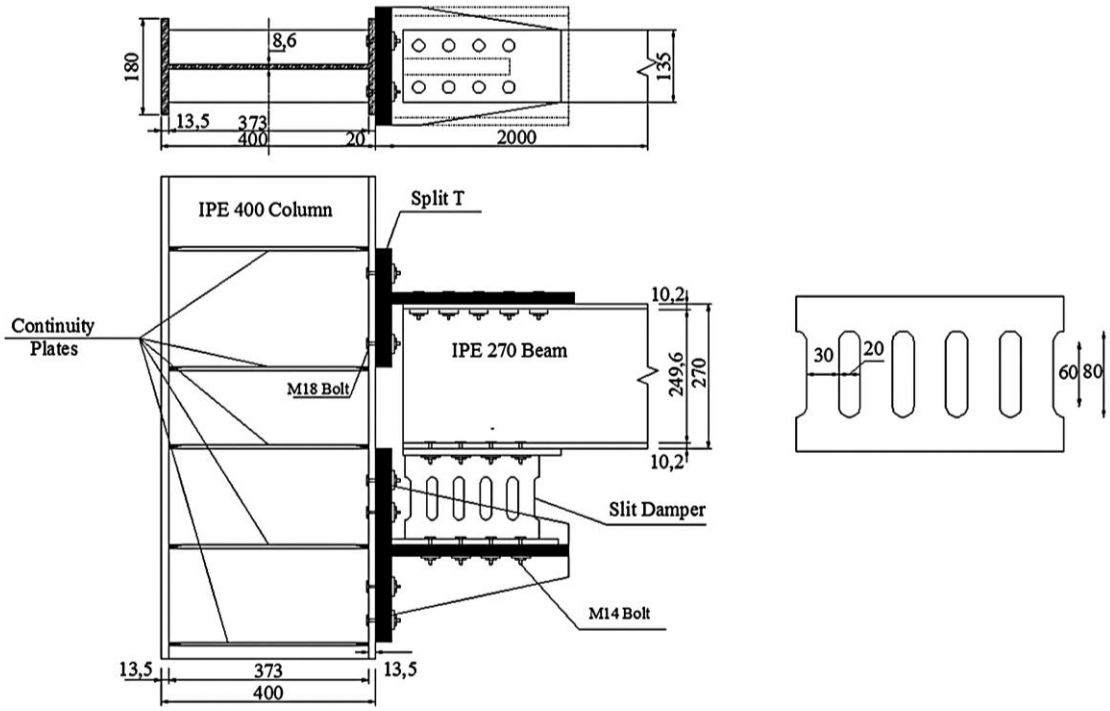

Fig. 4.19: Details of the test program (Koken and Koroglu 2014)

In light of the experimental and analytical studies, the use of dampers in the beam-column connections prevented damage to the structural elements and exhibited expected behavior. During the design process of dampers, in order to concentrate the earthquake loads on the damper, it was manufactured intentionally with a lower strength than the beams and columns. The details of test program and results of the research are narrated in Koken and Koroglu (2014).

4.5.2 Modeling Parameters (Koken and Koroglu 2014)

The details of the specimen N12 and other members are obtained as mentioned in Koken and Koroglu (2014). Table 4.5 list the elastic properties of the material which are directly taken from the study and the time independent plastic properties of the material which are found by calibrating the Chaboche material constants based on the materials strength.

Table 4.5: Material model parameters (Koken and Koroglu 2014)

Specimen	Elastic parameters		Plastic parameters (Chaboche kinematic hardening)						
	E (MPa)	υ	σ_y (MPa)	C_1 (MPa)	γ_1	C_2 (MPa)	γ_2	C_3 (MPa)	γ_3
N12	200000	0.3	314	2000	800	1000	400	500	100

4.5.3 Loading History (Koken and Koroglu 2014)

The static cyclic loading is applied both positive and negative direction by applying displacements at beam end in accordance with FEMA-351 given in the study which is illustrated in Fig. 4.20. The loading is performed at each amplitude of 8, -7.6, 10, -10, 15.6, -15.6, 20, -20, 30, -30, 40, -40, 60, -60, 80, -80, 100 and -100 mm.

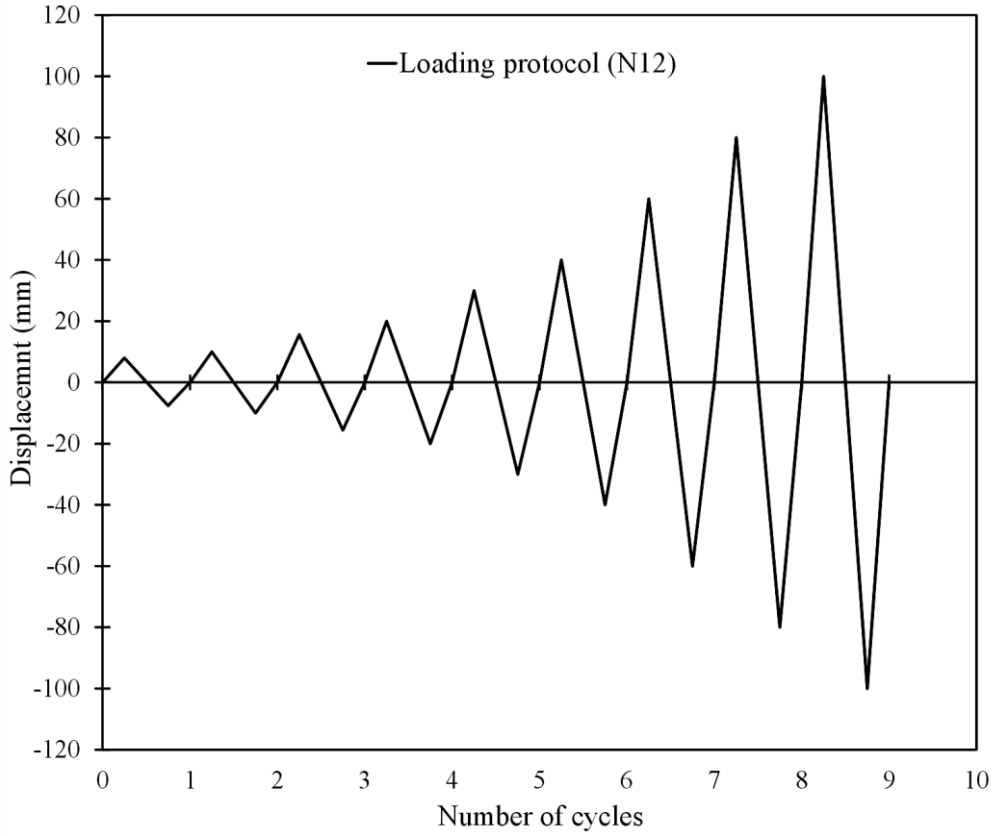

Fig. 4.20: Displacement history for static cyclic loading of the N12 model

4.5.4 Deformed Shape (Koken and Koroglu 2014)

Fig. 4.21 shows the actual deformed shape of the system. It shows prominent shear deformation in damper. The deformed shapes from the finite element analysis shown in Fig. 4.22 have likeness with the actual deformed shapes of the system.

As depicted in Fig. 4.22, slight separation of the connection occurs during the extreme deformation of the damper which is may be due to the gap maintained between the connection while generating the model. The effect of this separation will not create much deviation in the analysis results as slippage failure of is not necessarily a ruinous failure.

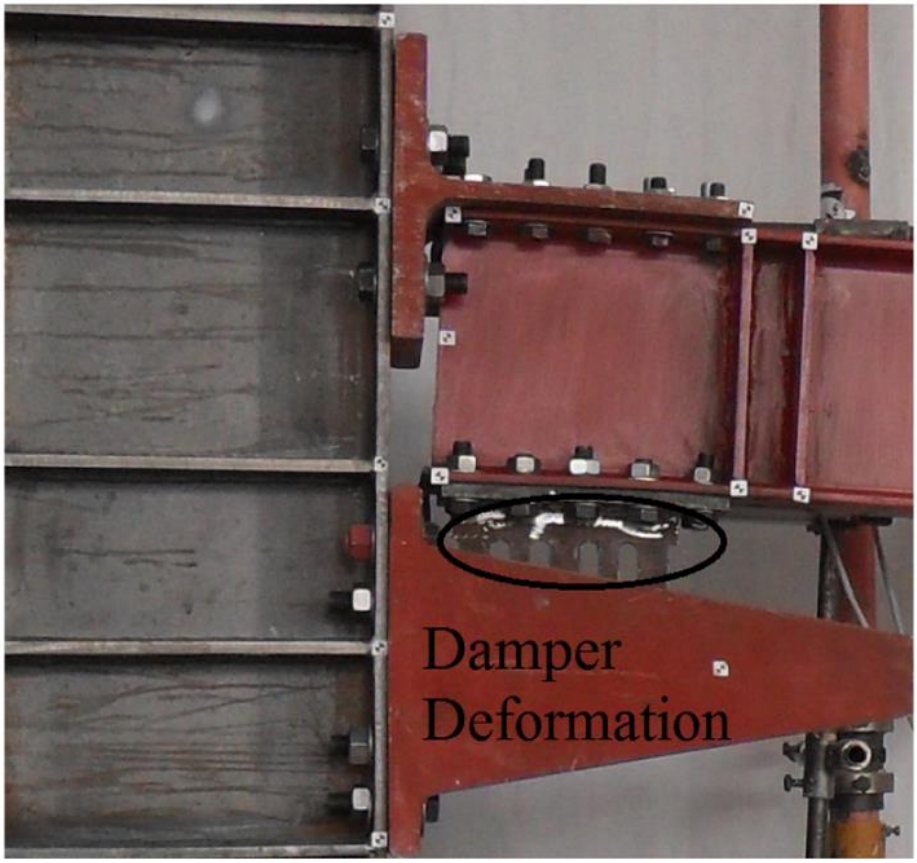

Fig. 4.21: Damper deformation in N12 specimen (Koken and Koroglu 2014)

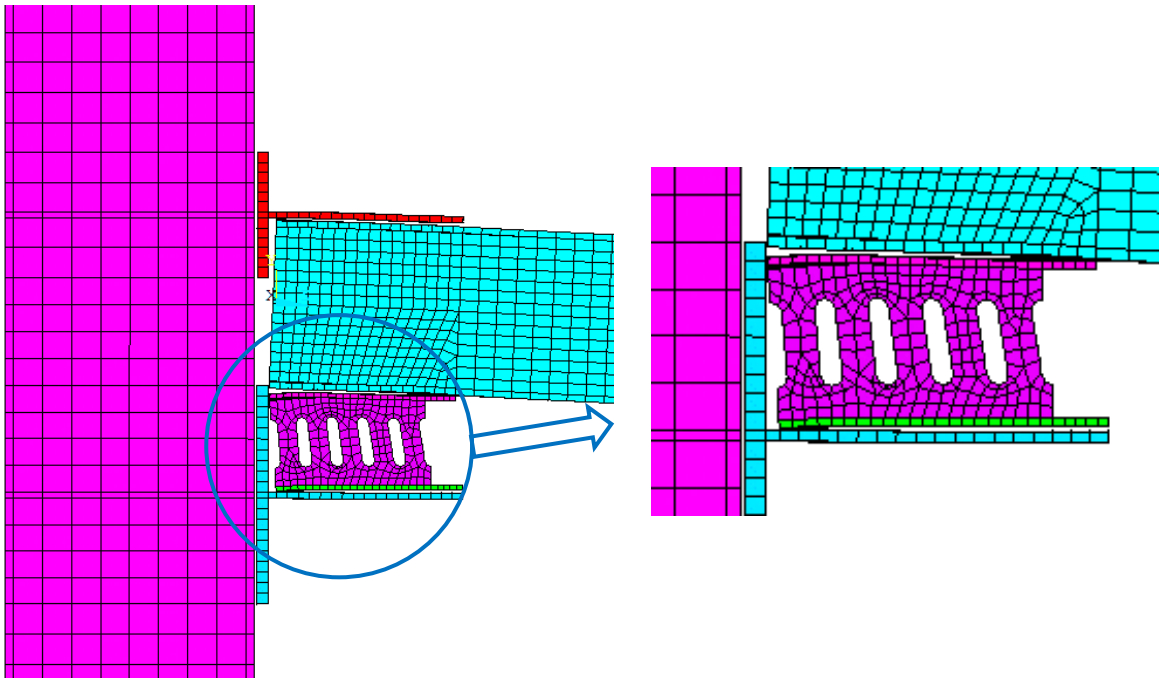

Fig. 4.22: Deformed shape of the N12 model

4.5.5 von-Mises Stress Contour (Koken and Koroglu 2014)

The von-Mises stress contour of the specimen N12 which is shown in Fig. 4.23 clearly indicates that the slit damper first yielded and then reached the ultimate boundary conditions, hence preventing damage to the beam or column and exhibiting the expected behavior.

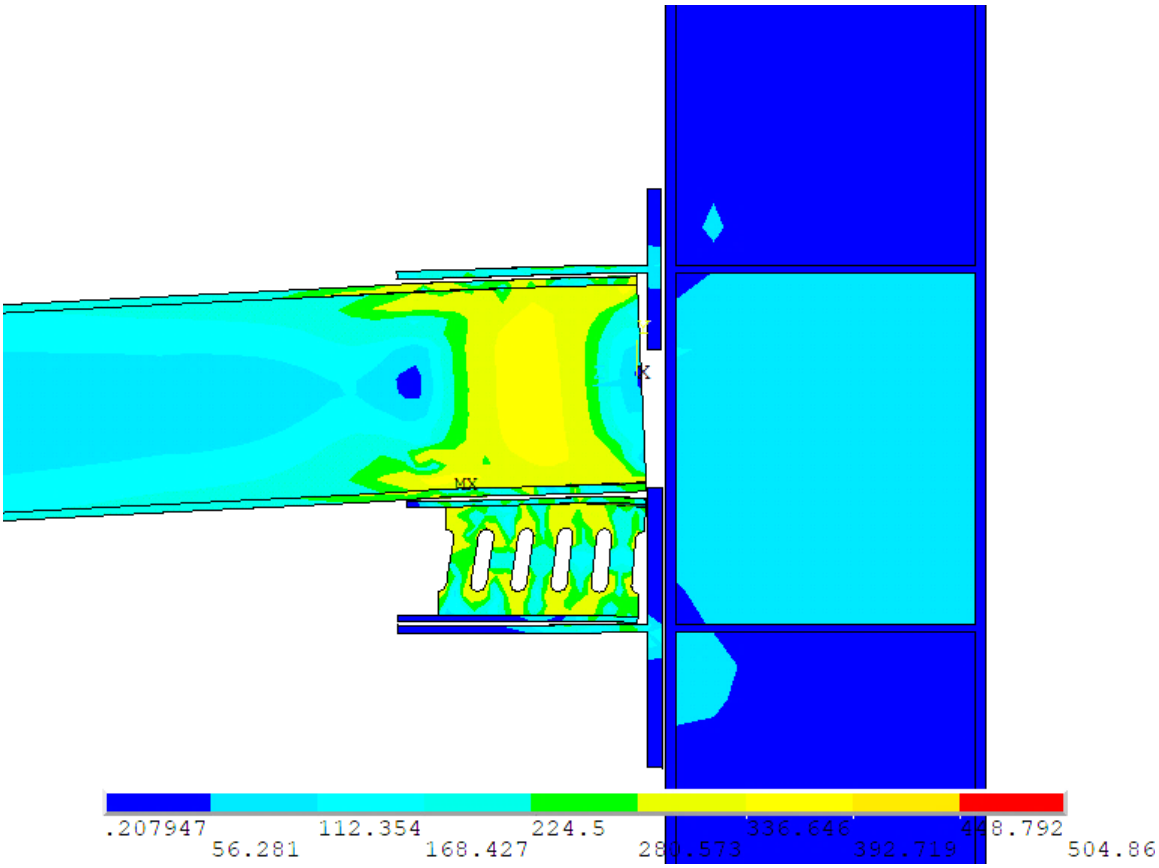

Fig. 4.23: von-Mises stress contour (MPa) of the N12 model

4.5.6 Verification of Moment vs. Rotation Behavior (Koken and Koroglu 2014)

Comparison between numerical and experimental results of specimen N12 tested by Koken and Koroglu 2014 is shown in Fig. 4.24 where it can be seen that FEM results almost match with the test results as isotropic hardening is not considered in the material modeling and may be the model does not match the experimental behavior absolutely.

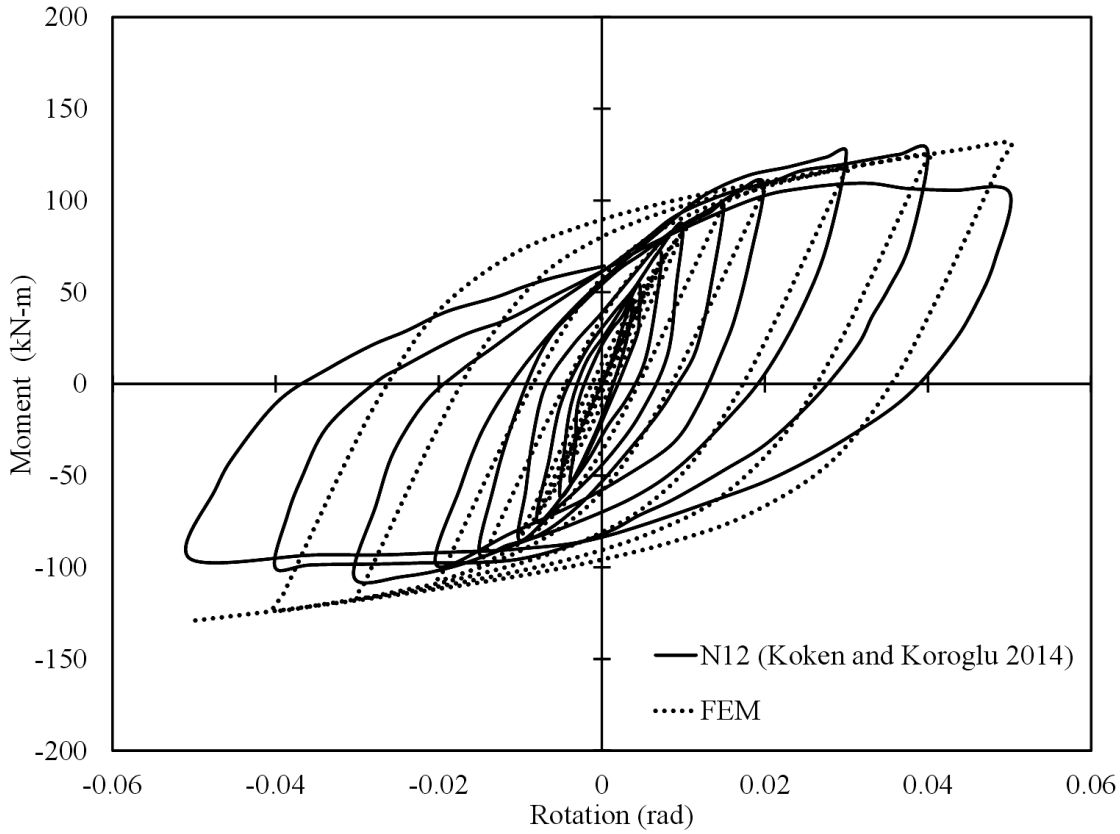

Fig. 4.24: Comparison between experimental and FEM results of specimen N12 following loading protocol N12

4.6 REMARKS

As a summary of this Chapter, it can be said that the finite element models developed in Chapter 3 are adequate enough to simulate the experimental test results done by Chan and Albermani (2008), Oh et al. (2009) and Koken and Koroglu (2014) and establish the reliability of finite element analysis scheme. Therefore the same models can be used for further numerical study instead of performing experimental research works. The numerical study using these models has been carried out in the following Chapter 5.

CHAPTER 5
NUMERICAL STUDY WITH DISCUSSIONS

5.1 INTRODUCTION

The finite element models developed in Chapter 3 using finite element software has been verified with reference to the experimental studies performed by Chan and Albermani (2008), Oh et al. (2009) and Koken and Koroglu (2014) in Chapter 4 to conclude whether the models are adequate enough for the numerical simulation of practical test results and satisfactory results have been obtained. Now using these proposed finite element models comparative and parametric studies on moment connection with steel shear dampers of different geometry will be carried out in this chapter.

5.2 EQUIVALENCE OF DIFFERENT TYPES OF SHEAR DAMPERS

As the numerical models give satisfactory results, shear dampers of different geometry such as oblong steel slit damper (OSSD), elliptical steel slit damper (ESSD), butterfly-shaped steel strut damper (BSSD), pintle damper (PD) etc. made of mild steel are compared with each other based on the plastic strength to find the equivalency among them by observing the hysteretic behavior on moment connection. To determine the plastic strength of the dampers more accurately, some analytical formulae are also developed observing the finite element results. The model setup, material elastic and plastic parameters, Chaboche material constants and loading cycles are kept constant throughout this study. The elastic properties and the time independent plastic properties of the material followed in the numerical study are listed in Table 5.1.

Table 5.1: Material model parameters (Numerical Study)

Specimen	Elastic parameters		Plastic parameters (Chaboche kinematic hardening)						
	E (MPa)	υ	σ_y (MPa)	C_1 (MPa)	γ_1	C_2 (MPa)	γ_2	C_3 (MPa)	γ_3
Damper	200000	0.3	208	7000	100	2000	50	1500	0

The static cyclic loading is applied both positive and negative direction following the ATC24 protocol which is shown in Fig. 5.1. The loading is performed at each amplitude of 2.5, -2.5, 5, -5, 7.5, -7.5, 10, -10, 12.5, -12.5, 15, -15, 17.5 and -17.5 mm.

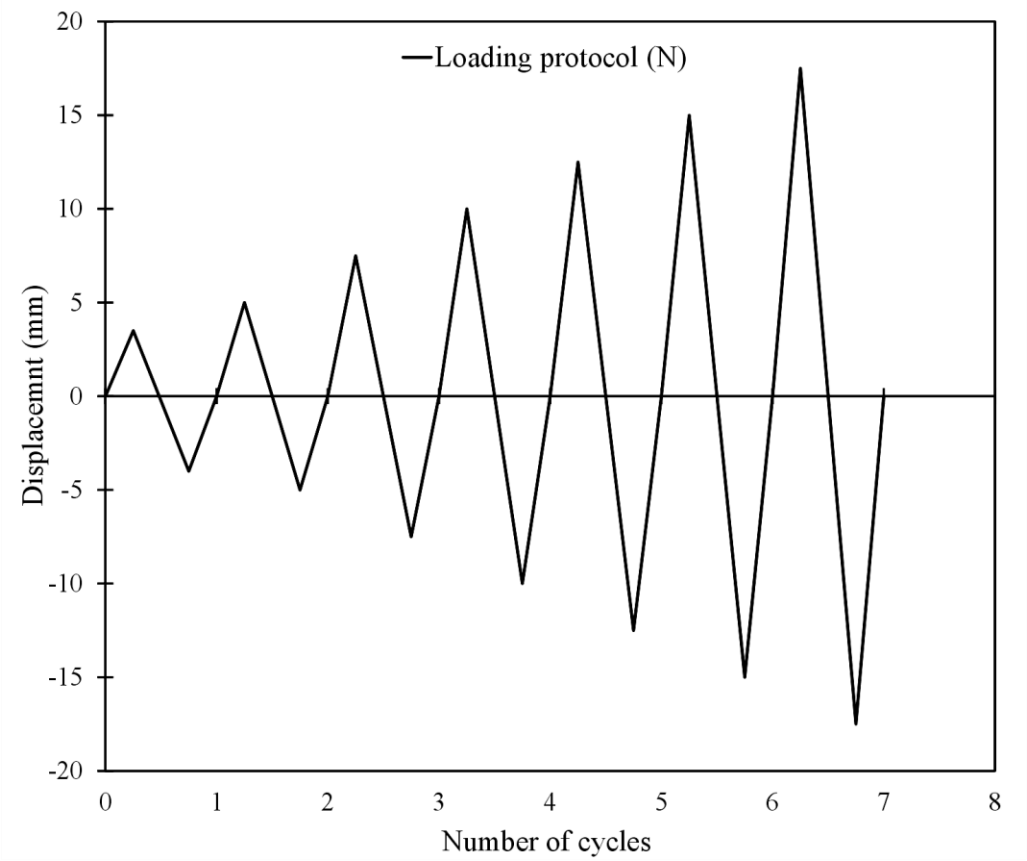

Fig. 5.1: Displacement history for static cyclic loading of the numerical study

5.2.1 Equivalency of Oblong Steel Slit Damper (OSSD) and Elliptical Steel Slit Damper (ESSD)

5.2.1.1 OSSD Plastic Strength Calculation

The Oblong Steel Slit Damper (OSSD) is fabricated with a number of oblong slits cut from a structural wide-flange section. For calculating the plastic strength of the oblong slit damper it can be idealized as shown in Fig. 2.27. The energy dissipation is mainly occurred through the vertical struts of the OSSD. The steel strips of the damper dissipate energy with in-plane flexural behavior.

Since the horizontal force is uniformly distributed to each strip, the strengths of a damper with multiple strips can be obtained by multiplying the number of the strips (n) to the theoretical strengths for one strip. When a strip damper is subjected to horizontal in-plane force, bending moment and shear force occur simultaneously in the strips. However, in cases where the height-to-width ratio of the strips (which is defined as the aspect ratio)

becomes large, the behavior of the damper is governed by flexure. The yield strength of the OSSD can be obtained analytically as follows: (Oh et al. 2009)

$$P_y = n \frac{\sigma_y t B^2}{2H'} \tag{5.1}$$

This formula gives satisfactory results and has widely used in many studies. There is a little scope for changing this equation. The specimen D1 of Oh et al. (2009) is taken as a reference for OSSD which is illustrated in Fig. 5.2.

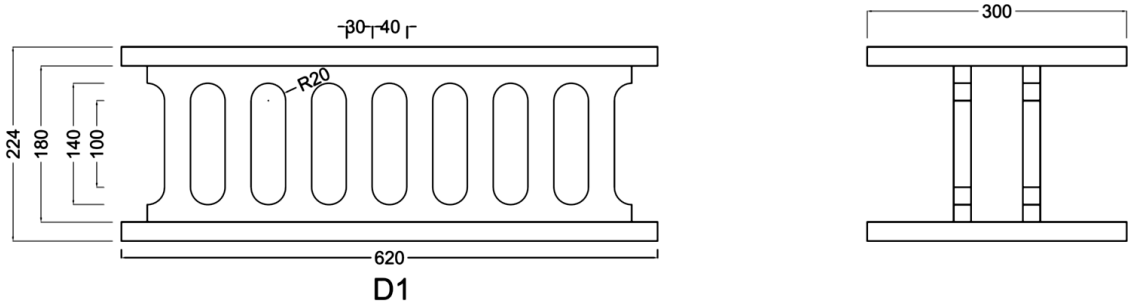

Fig. 5.2: Specimen D1 (Oh et al. 2009)

Here,

Number of struts, n =8

Yield stress, σ_y = 208 MPa

Thickness, t = 38 mm

Strut width, B = 30 mm

Strut height, H = 100 mm

Fillet radius, r = 20 mm

Total strut height, H_T = 140 mm

Net strut height, $H' = H + 2r^2/H_T$ = 105.7 mm

Solving Eq. (5.1),

$$\boldsymbol{P_y = 269.2 \times 10^3 \text{ N}}$$

5.2.1.2 Equivalent ESSD Modeling

The Elliptical Steel Slit Damper (ESSD) is a structural wide-flange section with a number of elliptical slits cut from the web part. In ESSD energy is dissipated uniformly along the strut heights.

To find the equivalency between OSSD and ESSD, an equivalent ESSD model is developed for the same plastic strength as OSSD of section 5.2.1.1 which is depicted in Fig. 5.3.

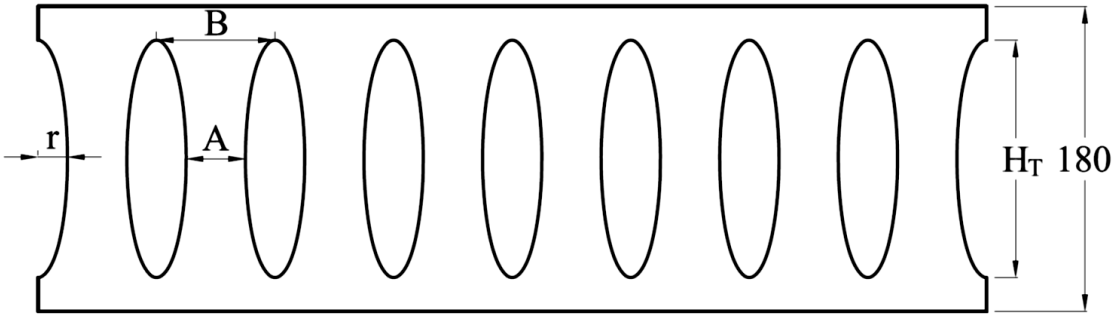

Fig. 5.3: Equivalent elliptical steel slit damper

From specimen D1 of Oh et al. (2009),

P_y = 269.2 x 10^3 N

n =8

σ_y = 208 MPa

H_T = 140 mm

Let,

B = 70 mm [Strut width at end]

A= B/2 mm [Strut width at middle]

r = (B-A)/2 = 17.5 mm [Slit radius]

The analytical yield strength (P_y) of ESSD is given by: (Shahri and Mousavi 2018)

$$P_y = n \frac{\sigma_y t B_{eff}^2}{2H_T} \tag{5.2}$$

where

$$B_{eff} = A - \frac{A}{r} \tag{5.3}$$

For simplification, the number of struts and the total strut height in ESSD are kept same as OSSD. Initially the strut width of ESSD is assumed according to the geometry of OSSD and the *A/B* ratio is taken 0.5 for simplicity.

Solving Eq. (5.2),

***t* = 41.59 mm**

5.2.1.3 Equivalence of OSSD and ESSD

The developed models for equivalency are shown in Fig. 5.4.

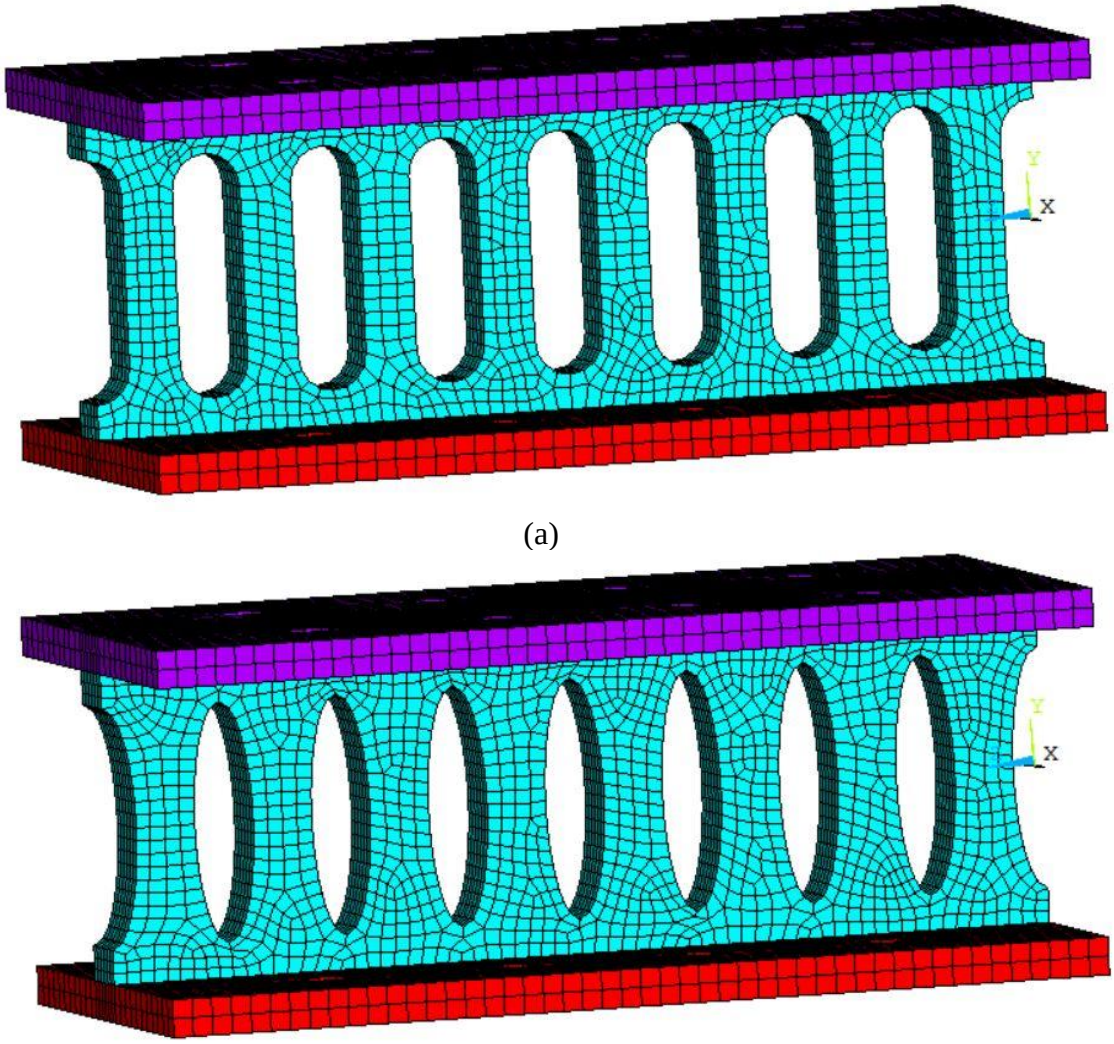

(a)

(b)

Fig. 5.4: Equivalent models of (a) OSSD and (b) ESSD

As illustrated in Fig. 5.5, the hysteretic responses of ESSD having a thickness of 41.59 mm which is found by solving Eq. (5.2) does not comply with the responses of OSSD. In fact, it is overestimating the thickness of ESSD. So, this formula may not be appropriate and there can be a scope for modification. After several trials, a thickness of 19.19 mm is found for ESSD based on matching the load vs. deformation response of OSSD which is shown in Fig. 5.5. This is happened because stress distribution is improved along the strut height of the ESSD whereas stress is concentrated at the end parts of the struts in OSSD. Therefore, a thickness of 19.19 mm for ESSD is sufficient to match the responses of OSSD having a thickness of 38 mm.

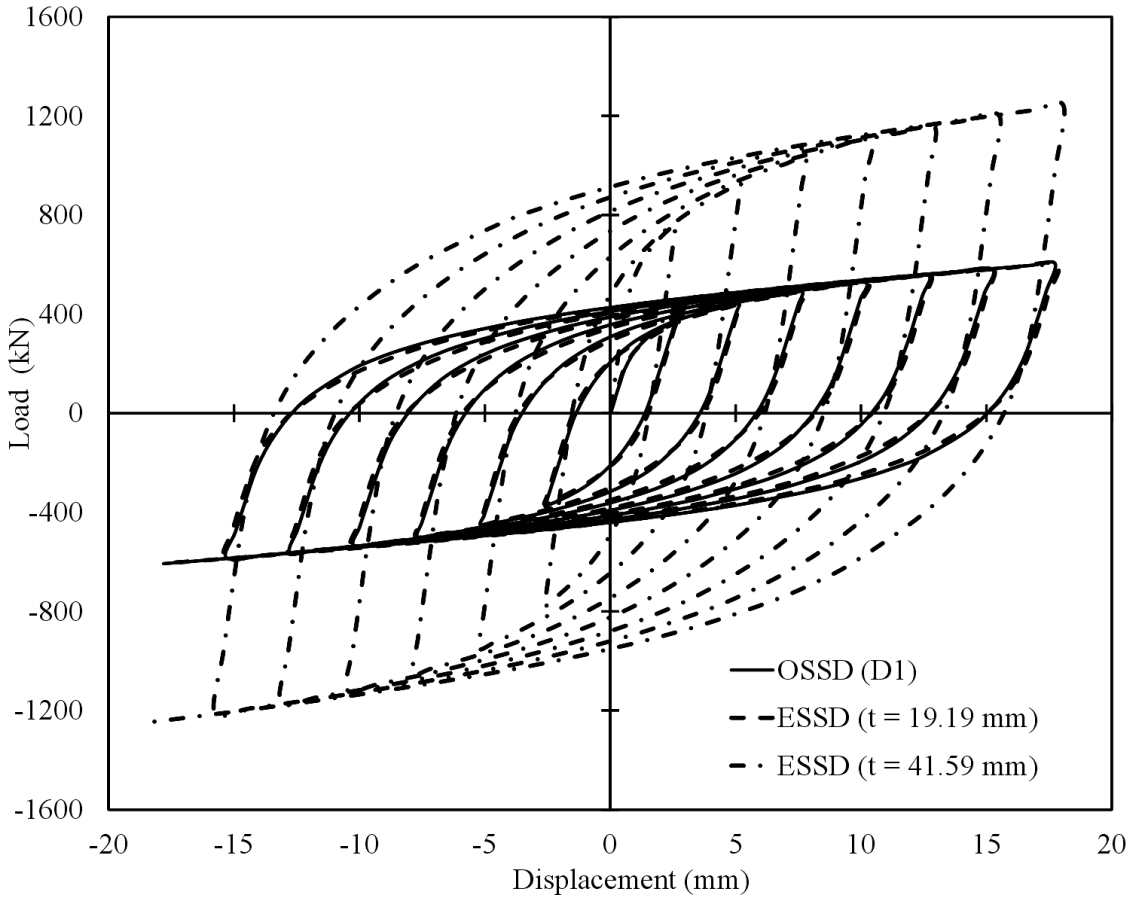

Fig. 5.5: Comparison of numerical results for equivalent models of OSSD and ESSD following loading protocol N

So, Eq. (5.2) needs to be modified for finding the parameters of equivalent ESSD to match with a particular strength of OSSD by observing and analyzing the finite element results.

5.2.1.4 Development of Plastic Strength Formula for ESSD

In the previous section, it is observed that Eq. (5.2) does not provide the same hysteretic responses of ESSD for the same plastic strength of OSSD. So in this section, some parametric studies have been performed to observe the effects of different parameters of ESSD for different plastic strengths of OSSD. Therefore, the hysteretic responses of ESSD are compared with the OSSD of different strengths by changing the parameters such as strut width, strut height, thickness etc.

At first, the height of strut is varied in both OSSD and ESSD for A/B = 0.5 ratio. The geometry for different strut heights of OSSD and ESSD are shown in Table 5.2.

Table 5.2: Geometry of OSSD and ESSD for different strut heights [*A/B* = 0.5]

OSSD					ESSD				
Specimen	H_T (mm)	H' (mm)	t (mm)	B (mm)	Specimen	H_T (mm)	B (mm)	A (mm)	t (mm)
OSSD1	120	86.67	38	30	ESSD1	120	70	35	21.09
OSSD2	130	96.15	38	30	ESSD2	130	70	35	20.08
OSSD3	140	105.7	38	30	ESSD3	140	70	35	19.19
OSSD4	150	115.3	38	30	ESSD4	150	70	35	18.35
OSSD5	160	125	38	30	ESSD5	160	70	35	17.67

For every pair of OSSD and ESSD specimens in Table 5.2, the equivalent thickness of ESSD is found by matching the load vs. displacement responses. The load vs. displacement curves for OSSD1 and ESSD1 specimens are shown in Fig. 5.6. For simplicity, the load vs. displacement responses of other specimens are not shown.

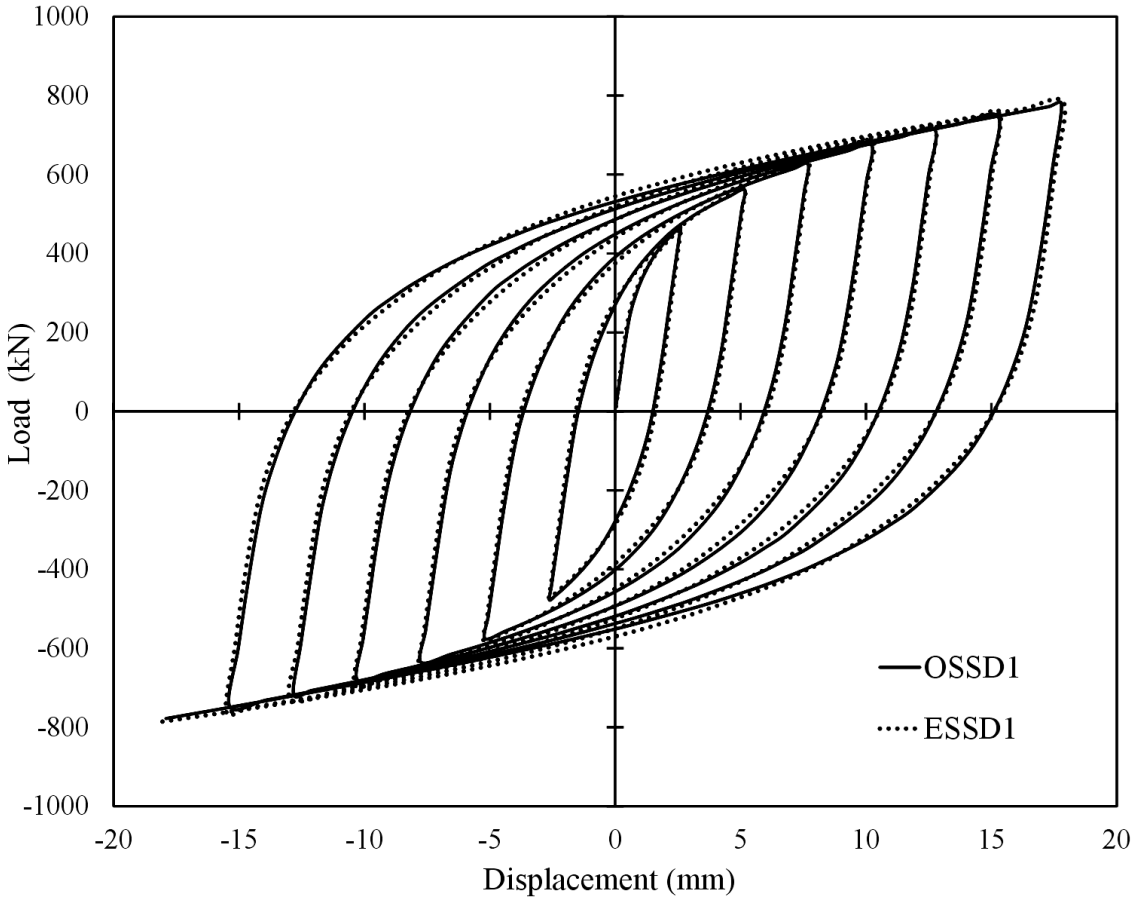

Fig. 5.6: Comparison of hysteretic curves between OSSD1 and ESSD1 following loading protocol N [*A/B* = 0.5]

Energy dissipation capacity is one of the substantial seismic features of any structure which can be achieved from the area within the force-displacement loop. The amounts of energy

dissipated by the specimens for different strut heights are mentioned in Fig. 5.7 which is obtained using software.

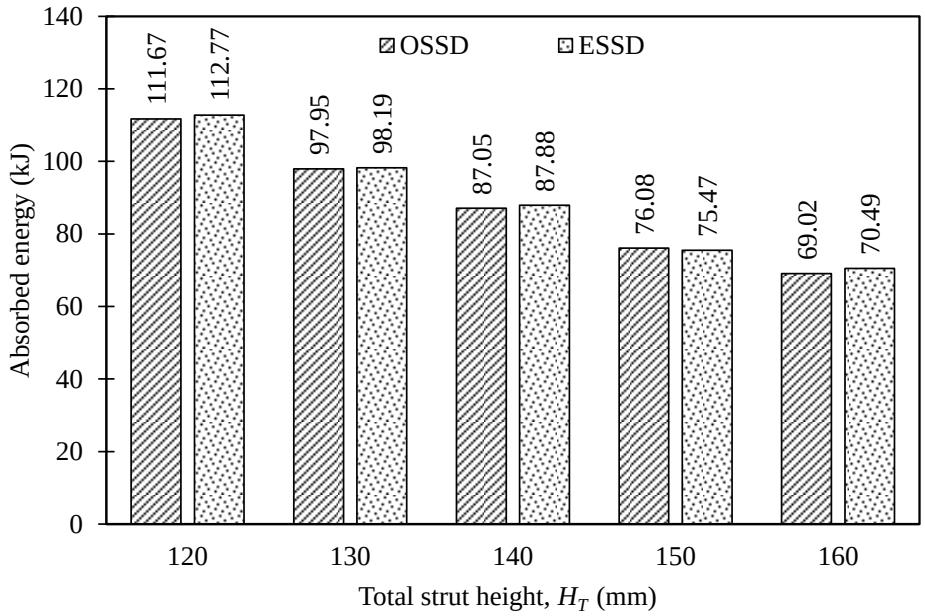

Fig. 5.7: Comparison of absorbed energy between OSSD and ESSD for different strut heights [*A/B* = 0.5]

Fig. 5.7 shows an increase in the height of ESSD results in a slightly reduction of the maximum force suffered by the connections as flexibility increases. As observed in Fig. 5.8, increasing the strut height decreases the thickness of equivalent ESSD. This is happened because of the reduction in stiffness.

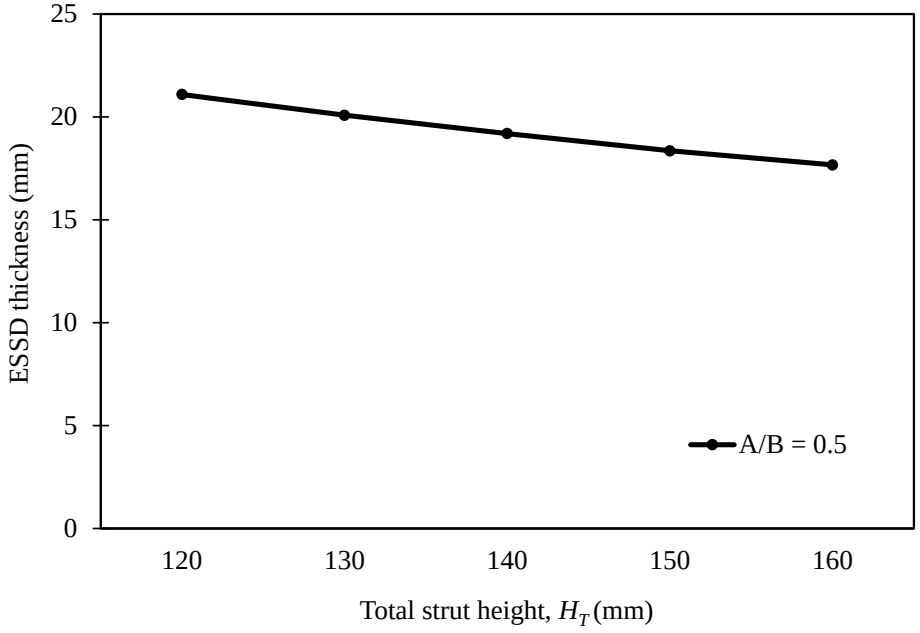

Fig. 5.8: Comparison of ESSD thickness for different strut heights [*A/B* = 0.5]

Similar studies are carried out for different strut widths of OSSD and ESSD. The geometry of OSSD and ESSD for different strut widths are listed in Table 5.3.

Table 5.3: Geometry of OSSD and ESSD for different strut widths [*A/B* = 0.5]

OSSD					ESSD				
Specimen	*B* (mm)	H_T (mm)	*H'* (mm)	*t* (mm)	Specimen	H_T (mm)	*B* (mm)	*A* (mm)	*t* (mm)
OSSD6	20	140	105.7	38	ESSD6	140	70	35	8.53
OSSD7	25	140	105.7	38	ESSD7	140	70	35	13.33
OSSD3	30	140	105.7	38	ESSD3	140	70	35	19.19
OSSD8	35	140	105.7	38	ESSD8	140	70	35	26.12
OSSD9	40	140	105.7	38	ESSD9	140	70	35	34.12

To avoid repeatability, only the load vs. displacement curves for OSSD6 and ESSD6 specimens are shown in Fig. 5.9.

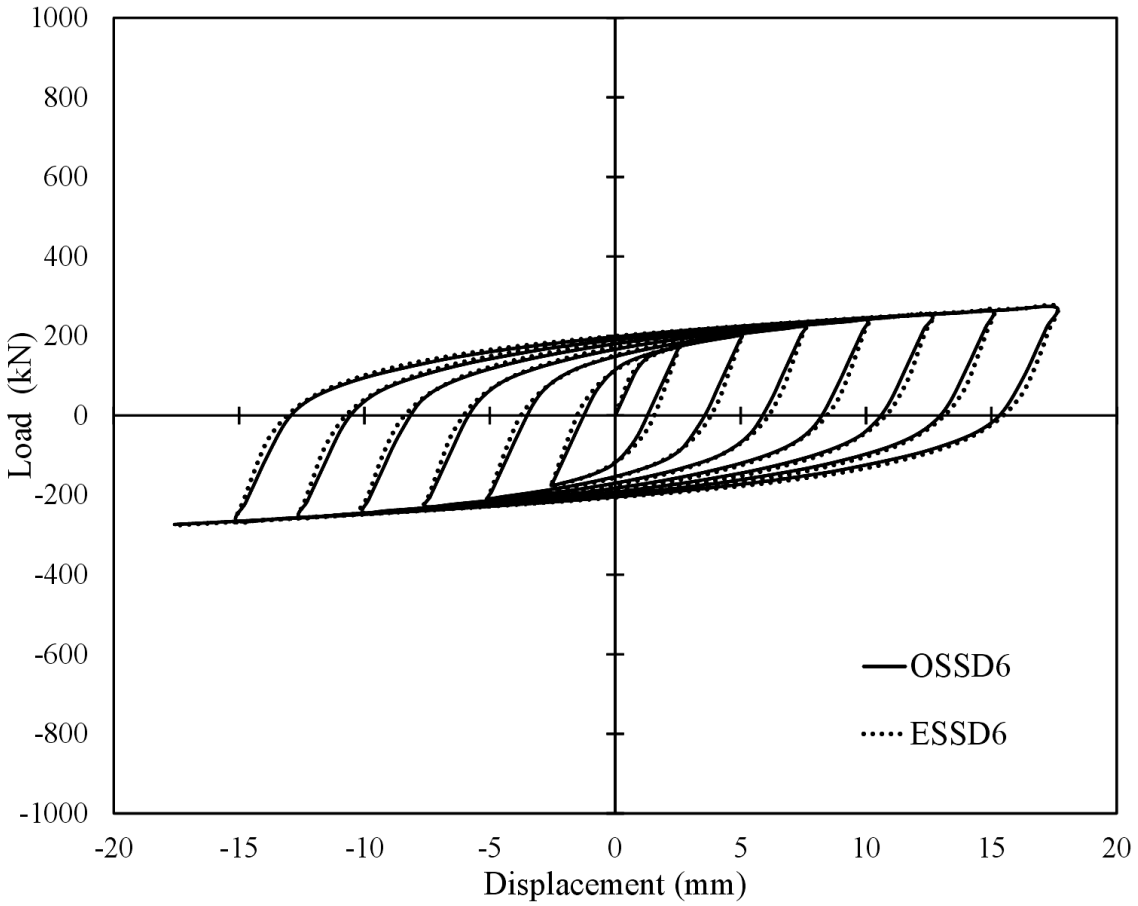

Fig. 5.9: Comparison of hysteretic curves between OSSD6 and ESSD6 following loading protocol N [*A/B* = 0.5]

The energy dissipation and equivalent ESSD thickness comparison for different strut widths are portrayed in Figs. 5.10-5.11 respectively.

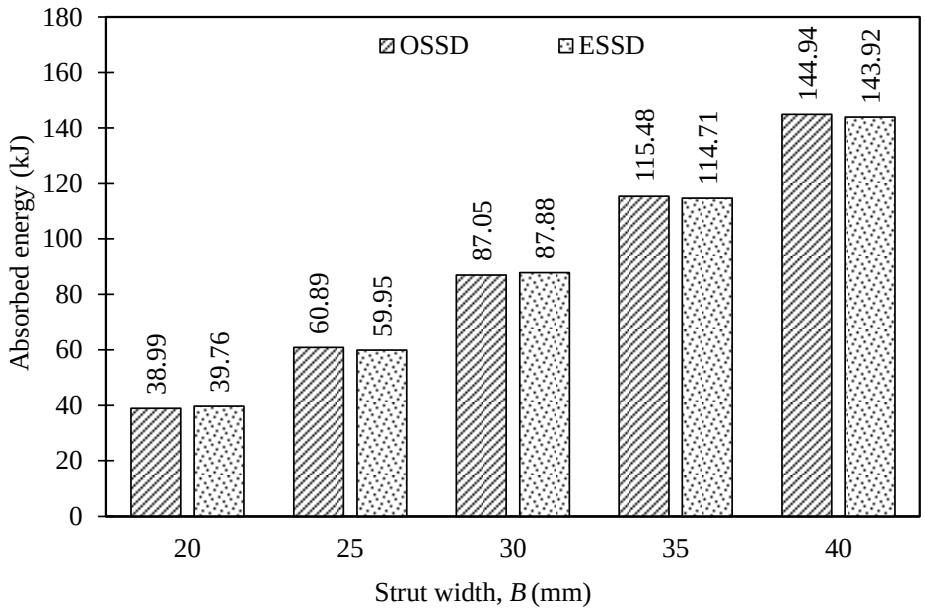

Fig. 5.10: Comparison of absorbed energy between OSSD and ESSD for different strut widths [*A/B* = 0.5]

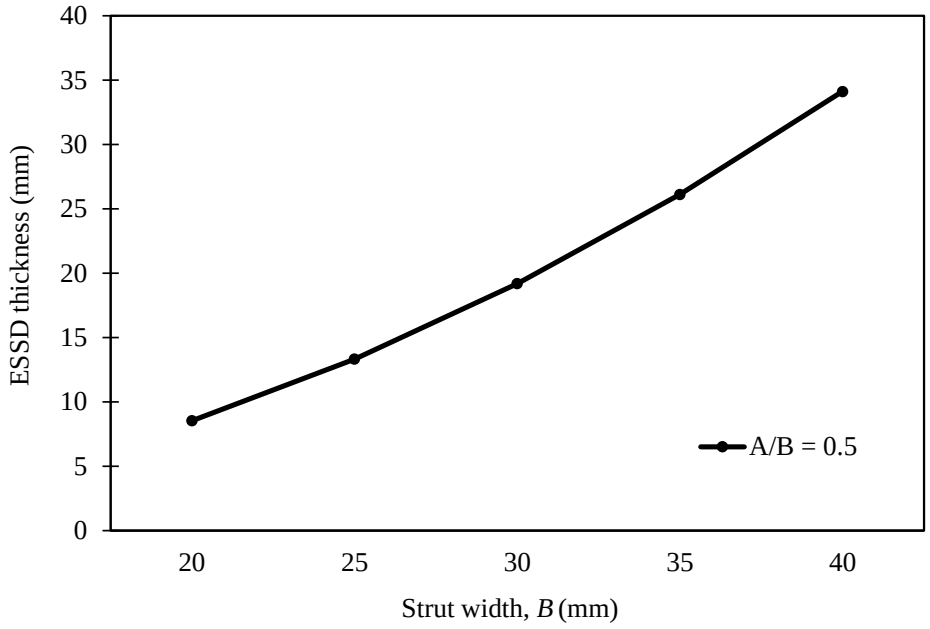

Fig. 5.11: Comparison of ESSD thickness for different strut widths [*A/B* = 0.5]

It is observed from Fig. 5.10 that decreasing the strut width decreases the maximum force in connection and amount of energy dissipation because of increment in stiffness. As observed in Fig. 5.11, increasing the strut width increases the thickness of equivalent ESSD which is happened because of the reduction in flexibility.

Therefore, based on the pattern of parametric study results shown in Figs. 5.8 and 5.11, the yield strength of the ESSD can be modified analytically as follows:

$$P_y = n \frac{\sigma_y t}{2H_T} [0.694B + 0.06(H_T - 140)]^2 \quad [if\ A/B = 0.5] \qquad (5.4)$$

Here,

P_y = Yield strength

n = Number of Struts

σ_y = Yield stress

t = Thickness

H_T = Total strut height

B = Strut width at end

By solving Eq. (5.4), the parameters of the ESSD for an equivalent strength of the OSSD can be obtained for the *A/B* = 0.5 ratio. It can be concluded that the Eq. (5.4) sets good agreement for any strut height and width of ESSD for *A/B* = 0.5 ratio as observed in Figs. 5.7 and 5.10.

Similarly, studies are carried out for different *A/B* ratios analogous to *A/B* = 0.5 ratio. The data and results are shown in Tables 5.4-5.7 and Figs. 5.12-5.23. For simplification, similar types of results are omitted.

Table 5.4: Geometry of OSSD and ESSD for different strut heights [*A/B* = 0.33]

OSSD					ESSD				
Specimen	H_T (mm)	H' (mm)	t (mm)	B (mm)	Specimen	H_T (mm)	B (mm)	A (mm)	t (mm)
OSSD2	130	96.15	38	30	ESSD10	130	70	23.1	31.75
OSSD3	140	105.7	38	30	ESSD11	140	70	23.1	30.78
OSSD4	150	115.3	38	30	ESSD12	150	70	23.1	29.85

Table 5.5: Geometry of OSSD and ESSD for different strut widths [*A/B* = 0.33]

OSSD					ESSD				
Specimen	B (mm)	H_T (mm)	H' (mm)	t (mm)	Specimen	H_T (mm)	B (mm)	A (mm)	t (mm)
OSSD7	25	140	105.7	38	ESSD13	140	70	23.1	21.37
OSSD3	30	140	105.7	38	ESSD11	140	70	23.1	30.78
OSSD8	35	140	105.7	38	ESSD14	140	70	23.1	41.89

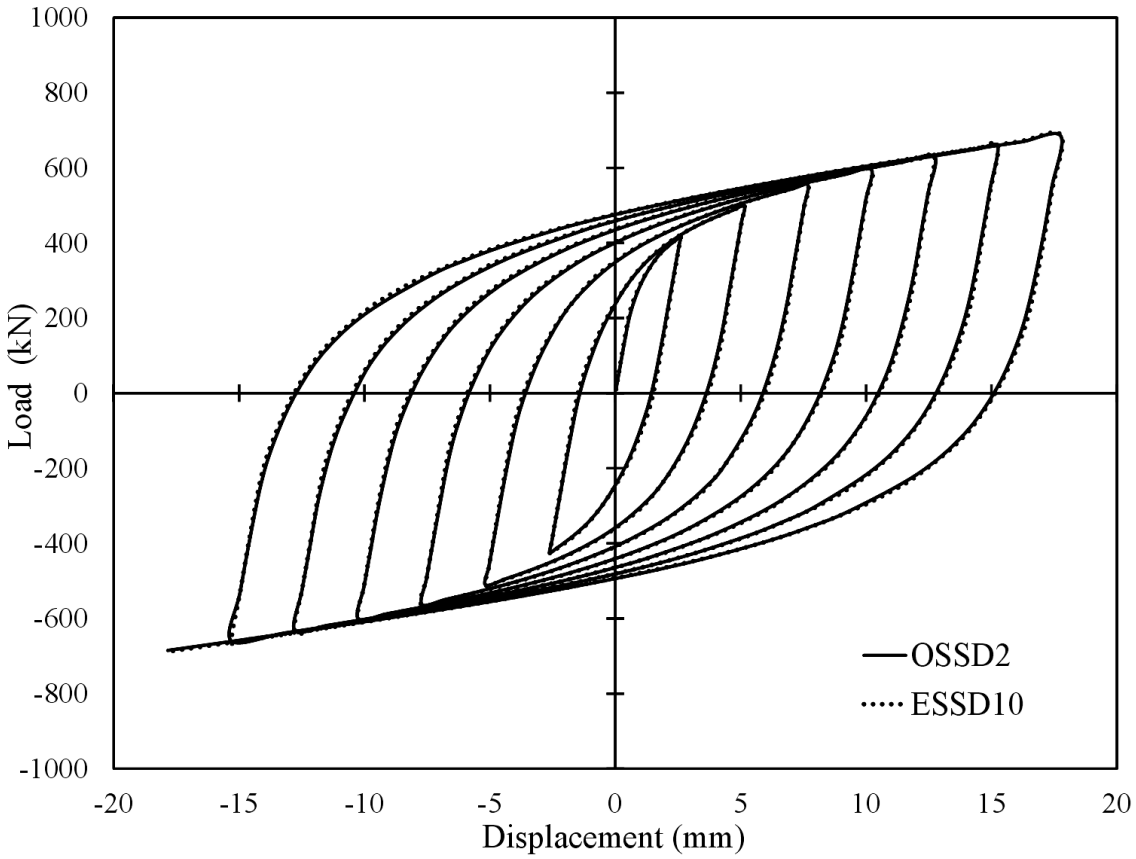

Fig. 5.12: Comparison of hysteretic curves between OSSD2 and ESSD10 following loading protocol N [*A/B* = 0.33]

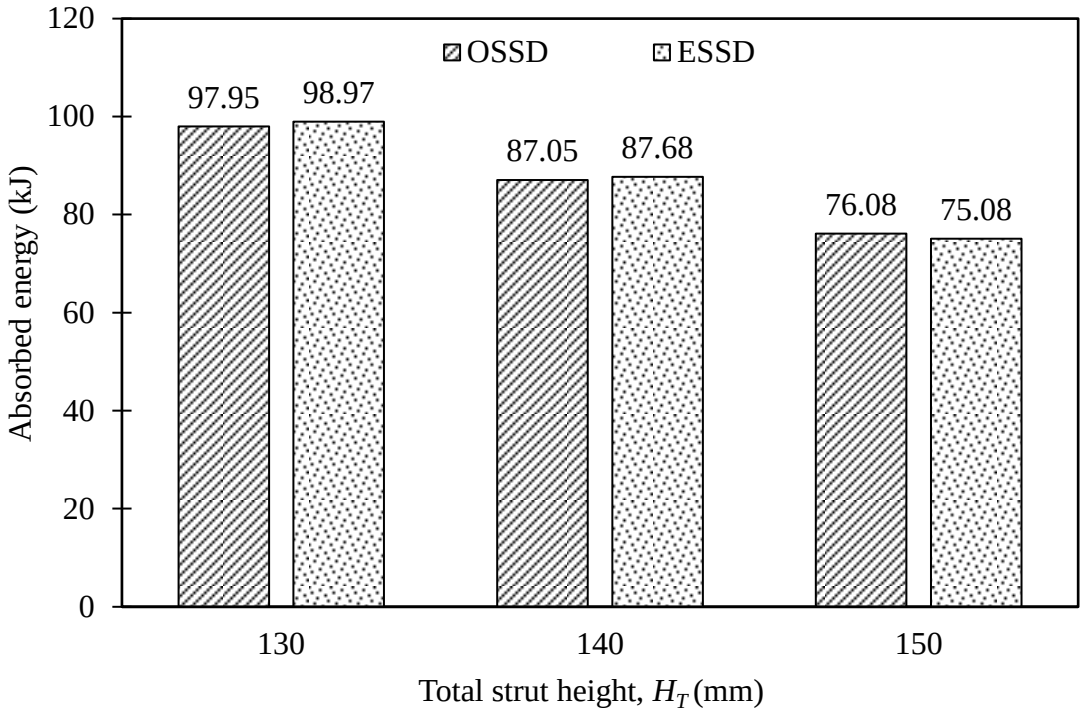

Fig. 5.13: Comparison of absorbed energy between OSSD and ESSD for different strut heights [*A/B* = 0.33]

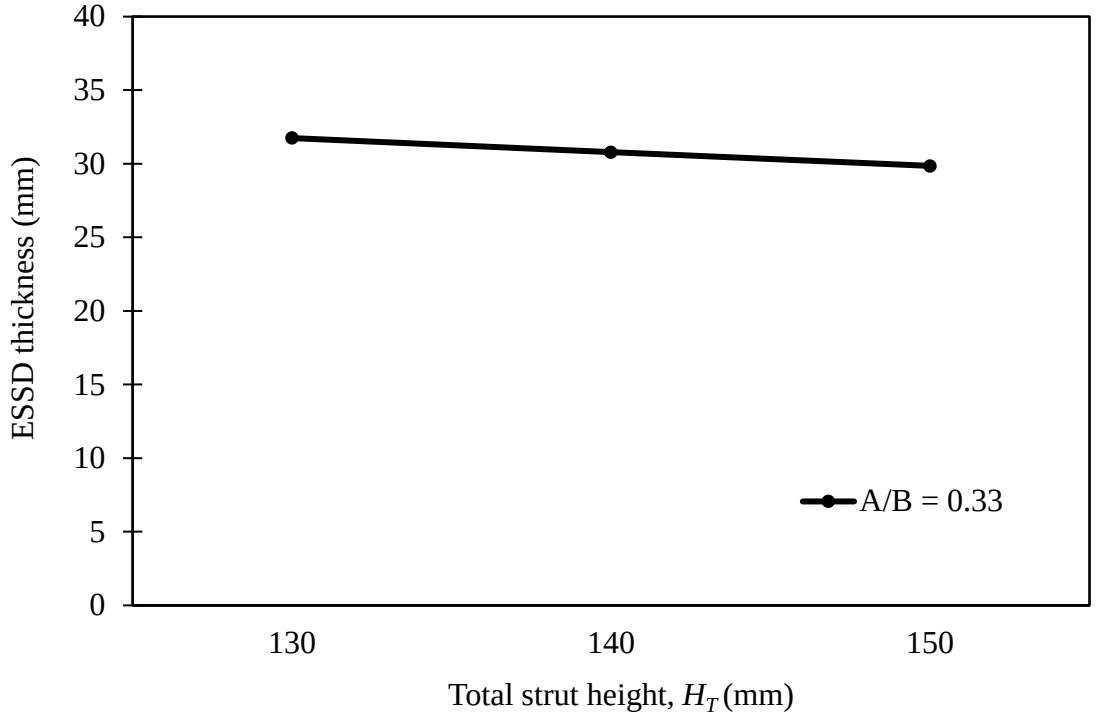

Fig. 5.14: Comparison of ESSD thickness for different strut heights [*A/B* = 0.33]

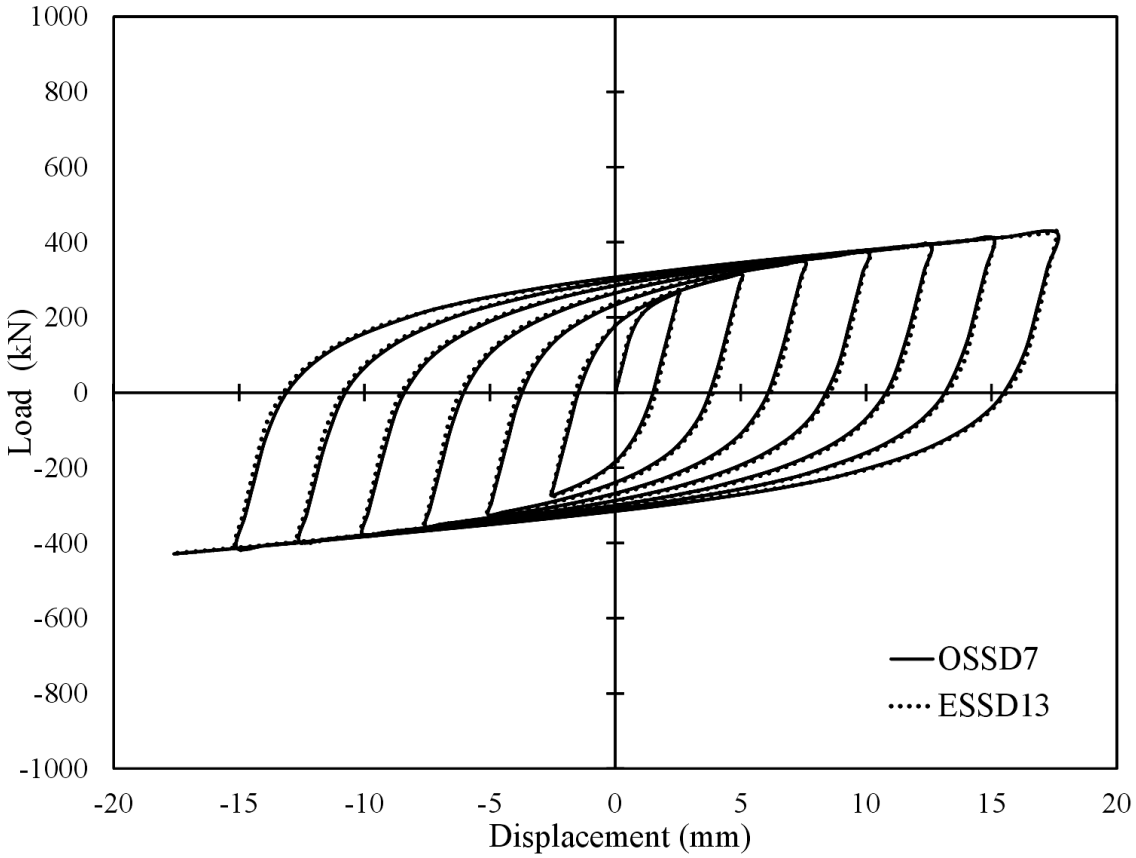

Fig. 5.15: Comparison of hysteretic curves between OSSD7 and ESSD13 following loading protocol N [*A/B* = 0.33]

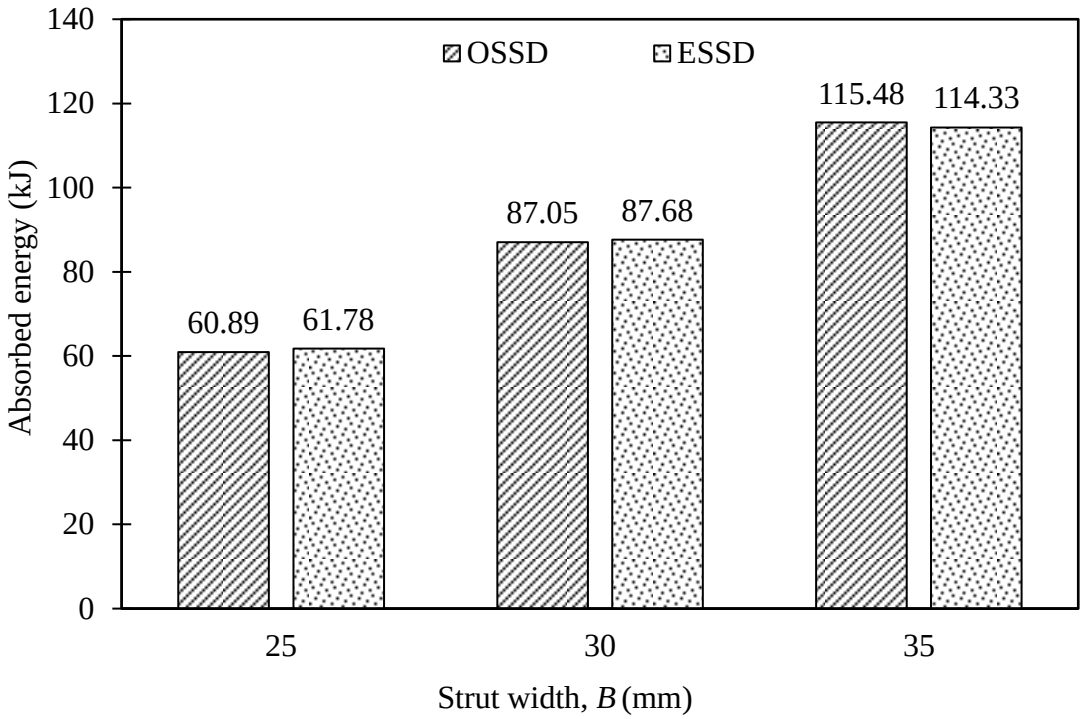

Fig. 5.16: Comparison of absorbed energy between OSSD and ESSD for different strut widths [*A/B* = 0.33]

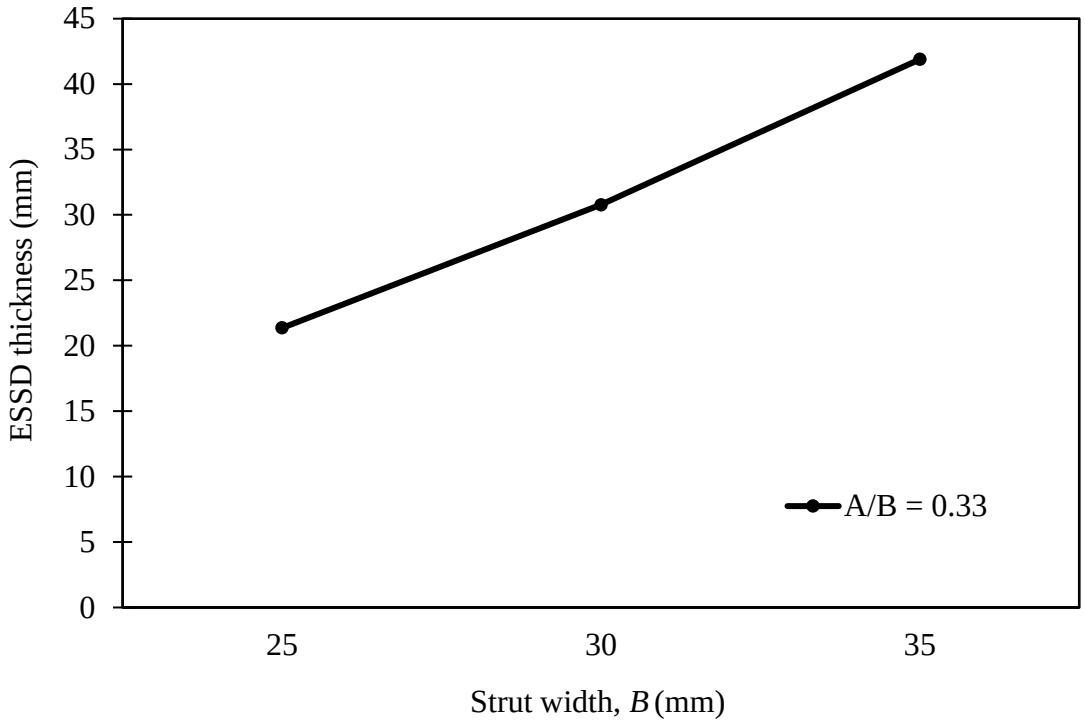

Fig. 5.17: Comparison of ESSD thickness for different strut widths [*A/B* = 0.33]

Table 5.6: Geometry of OSSD and ESSD for different strut heights [*A/B* = 0.67]

	OSSD					ESSD			
Specimen	H_T (mm)	H' (mm)	t (mm)	B (mm)	Specimen	H_T (mm)	B (mm)	A (mm)	t (mm)
OSSD2	130	96.15	38	30	ESSD14	130	70	46.67	15.13
OSSD3	140	105.7	38	30	ESSD15	140	70	46.67	14.30
OSSD4	150	115.3	38	30	ESSD16	150	70	46.67	13.53

Table 5.7: Geometry of OSSD and ESSD for different strut widths [*A/B* = 0.67]

OSSD					ESSD				
Specimen	B (mm)	H_T (mm)	H' (mm)	t (mm)	Specimen	H_T (mm)	B (mm)	A (mm)	t (mm)
OSSD7	25	140	105.7	38	ESSD17	140	70	46.67	9.93
OSSD3	30	140	105.7	38	ESSD15	140	70	46.67	14.30
OSSD8	35	140	105.7	38	ESSD18	140	70	46.67	19.46

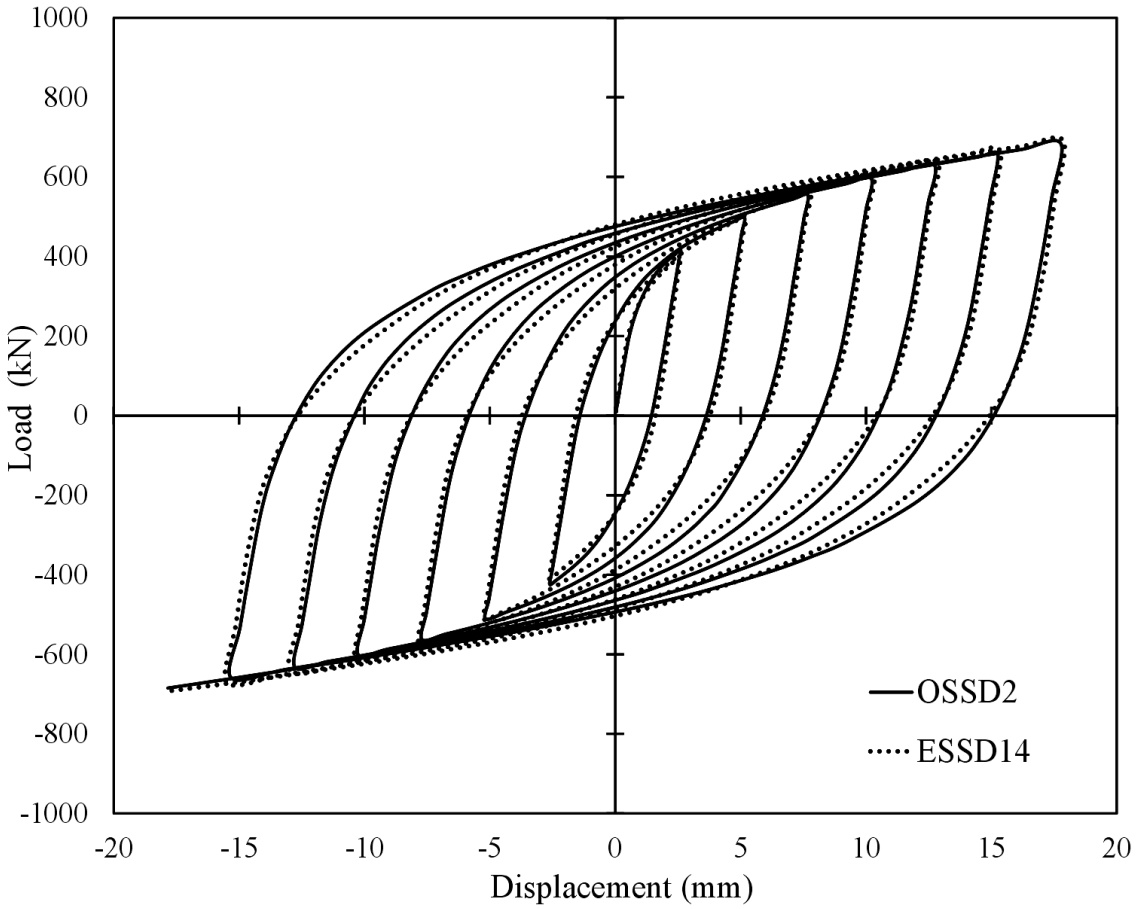

Fig. 5.18: Comparison of hysteretic curves between OSSD2 and ESSD14 following loading protocol N [*A/B* = 0.67]

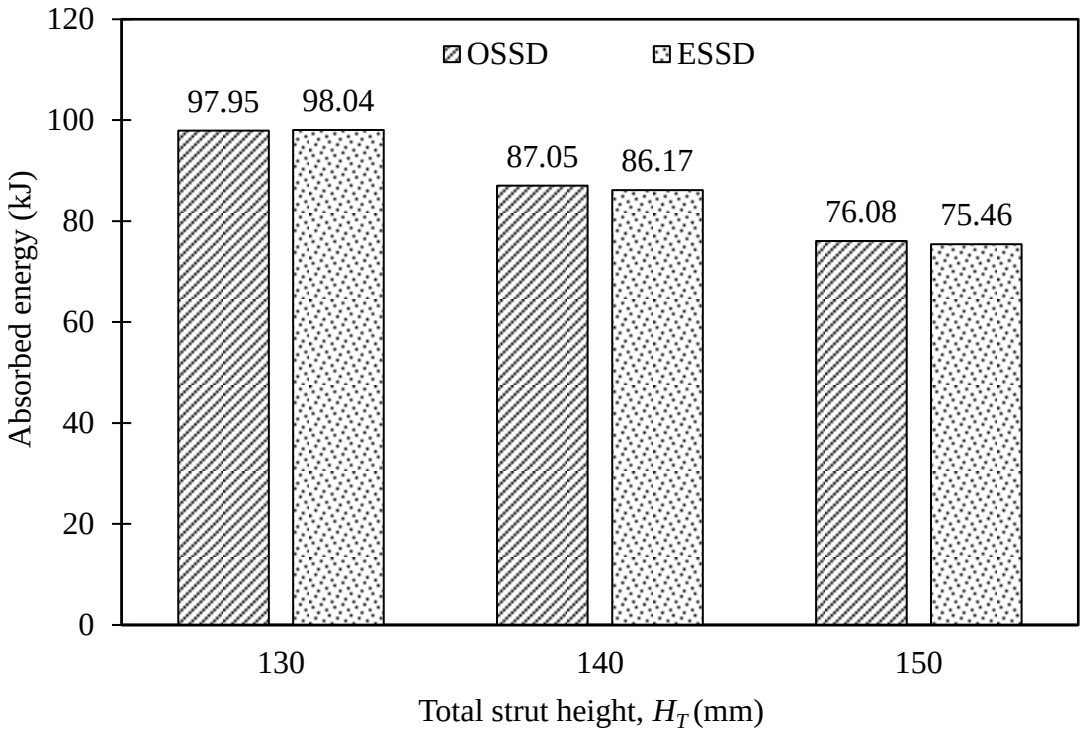

Fig. 5.19: Comparison of absorbed energy between OSSD and ESSD for different strut heights [*A/B* = 0.67]

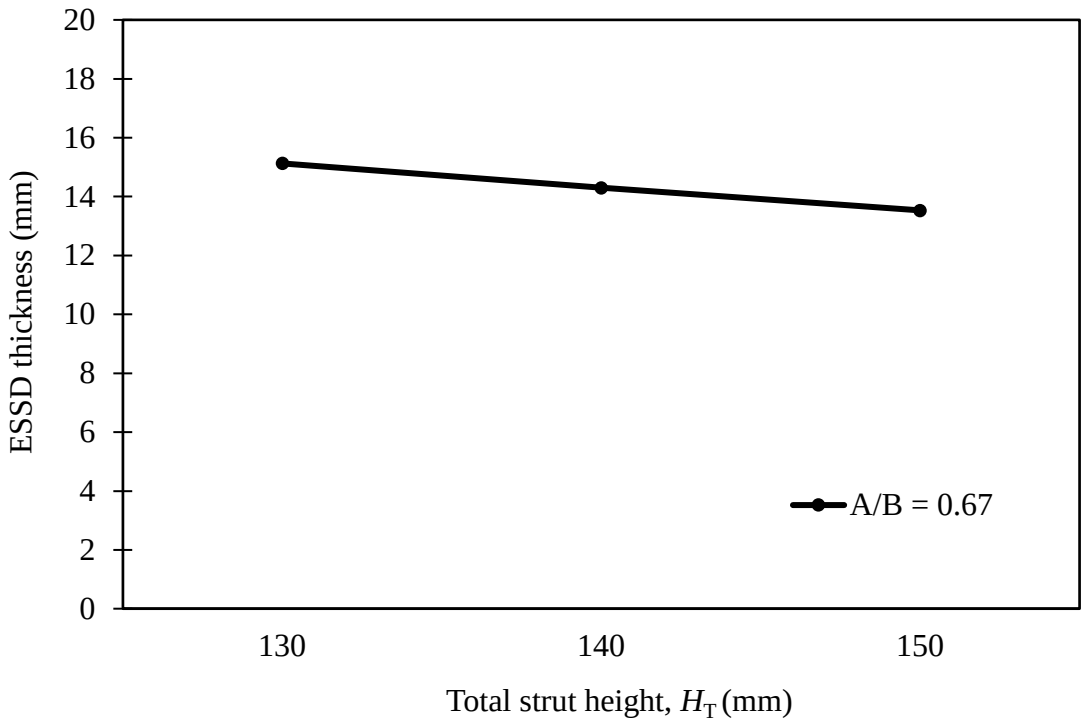

Fig. 5.20: Comparison of ESSD thickness for different strut heights [*A/B* = 0.67]

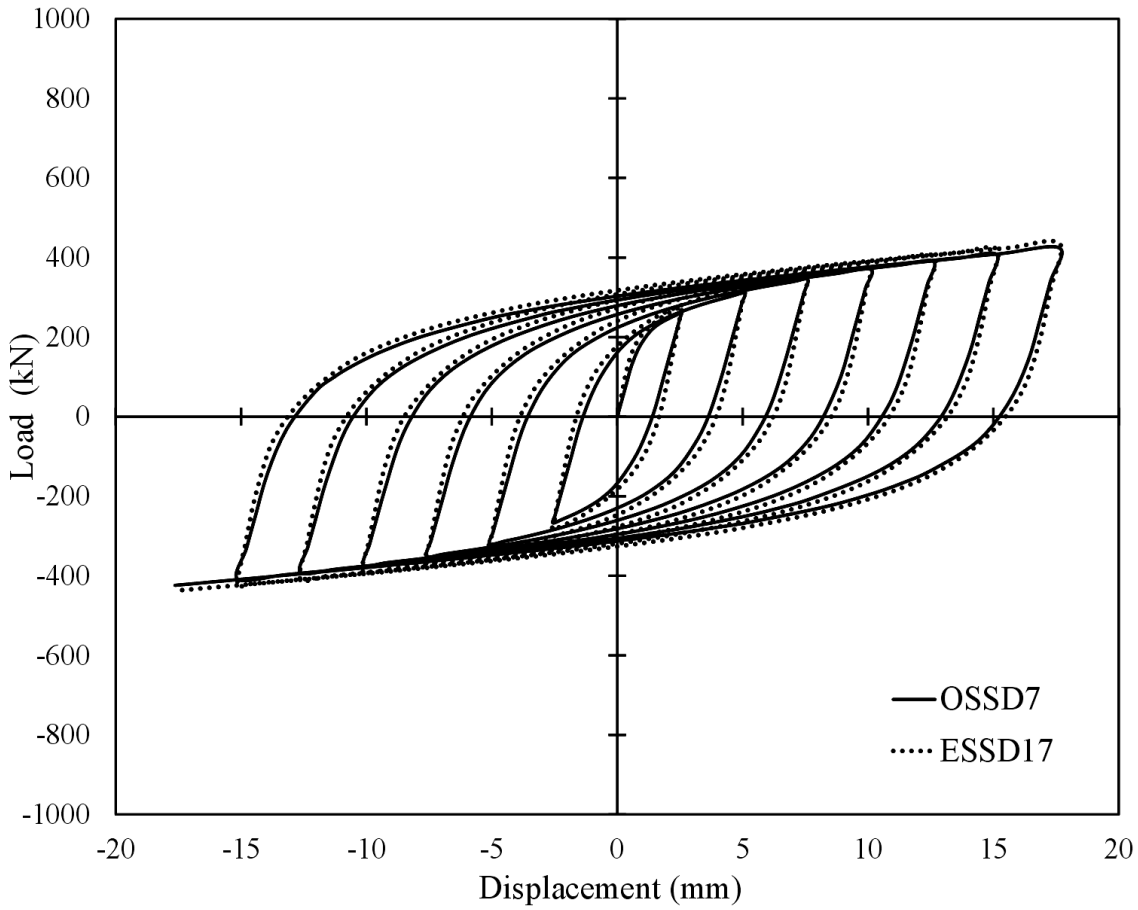

Fig. 5.21: Comparison of hysteretic curves between OSSD7 and ESSD17 following loading protocol N [*A/B* = 0.67]

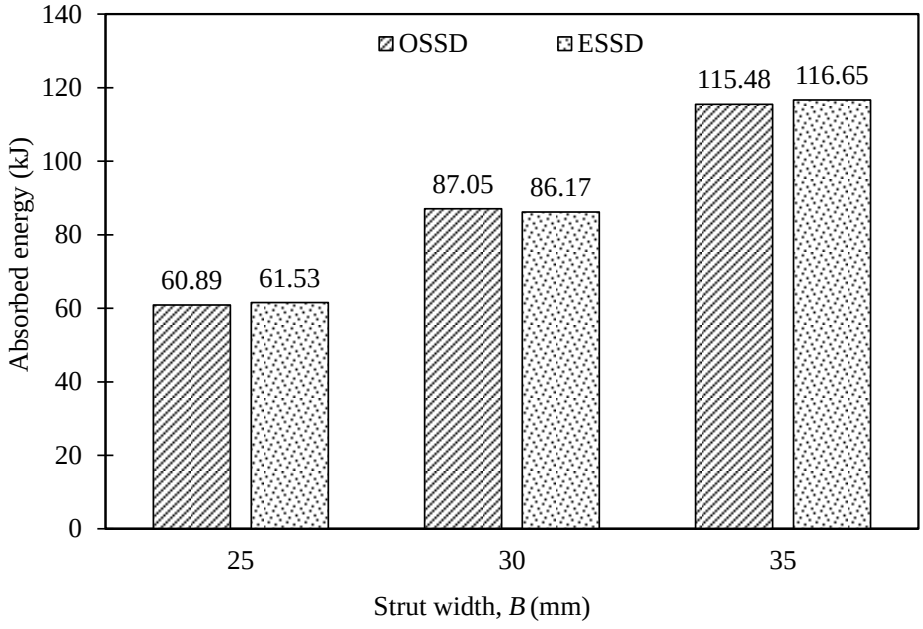

Fig. 5.22: Comparison of absorbed energy between OSSD and ESSD for different strut widths [*A/B* = 0.67]

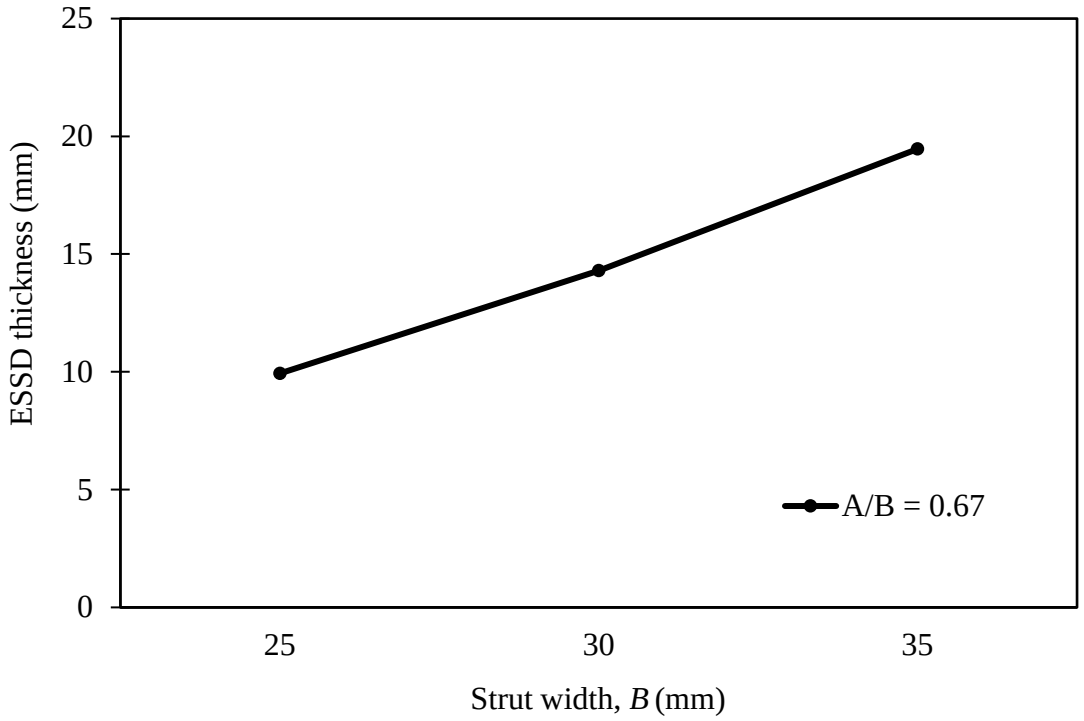

Fig. 5.23: Comparison of ESSD thickness for different strut widths [*A/B* = 0.67]

Similarly, the following equations are developed for ESSD by observing the finite element results pattern for *A/B* ratios of 0.33 and 0.67 respectively.

$$P_y = n \frac{\sigma_y t}{2H_T} [0.548B + 0.02(H_T - 140)]^2 \quad [if\ A/B = 0.33] \qquad (5.5)$$

$$P_y = n \frac{\sigma_y t}{2H_T} [0.804B + 0.1(H_T - 140)]^2 \quad [if\ A/B = 0.67] \qquad (5.6)$$

It can be concluded from Figs. 5.12-5.23 that the Eqs. (5.5) and (5.6) hold perfect for different *A/B* ratios of ESSD.

It is observed from Eqs. 5.4-5.6 that, for different *A/B* ratios of ESSD the coefficient of strut width and strut height varies in the Eqs. which are depicted in Figs. 5.24 and 5.25 named as α and β respectively.

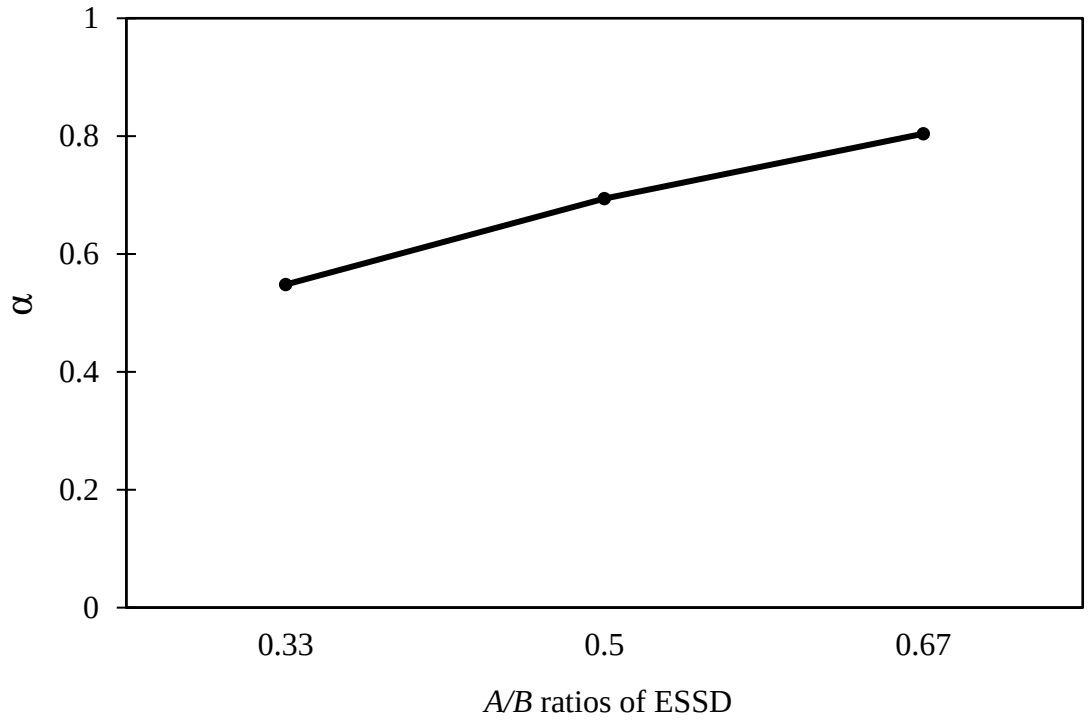

Fig. 5.24: Variation of strut width coefficient for different *A/B* ratios of ESSD

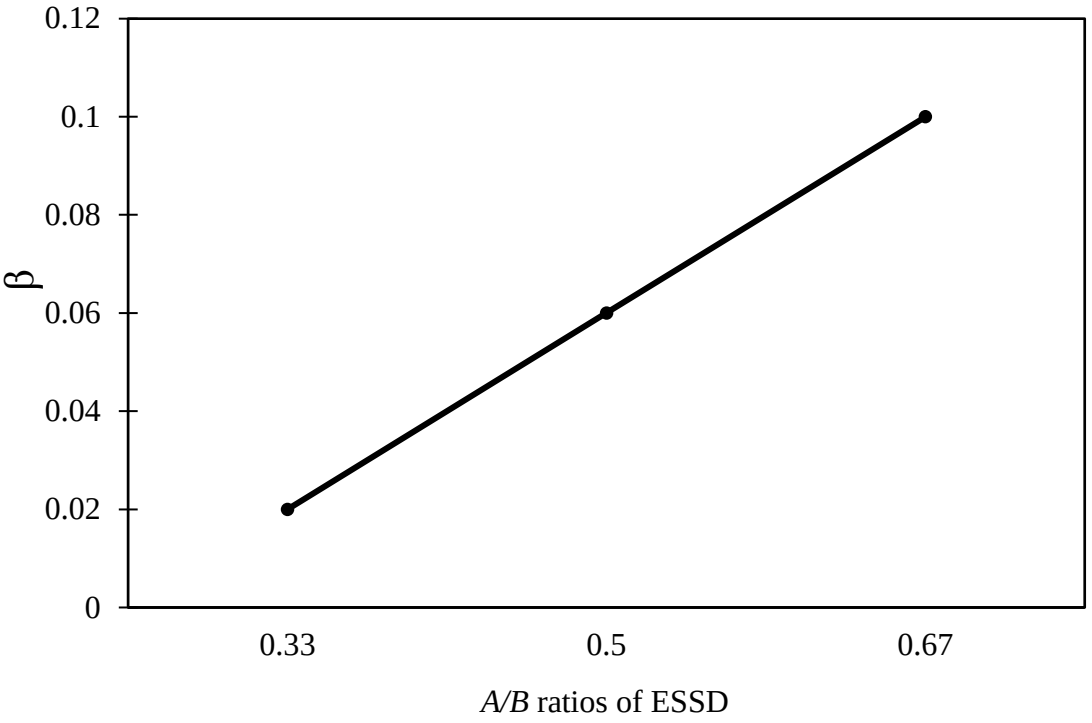

Fig. 5.25: Variation of strut height coefficient for different *A/B* ratios of ESSD

Therefore, by combining Eqs. (5.4), (5.5) and (5.6) the plastic strength formula of the ESSD can be expressed analytically in general as:

$$P_y = n \frac{\sigma_y t}{2H_T} [\alpha B + \beta(H_T - 140)]^2 \quad (5.7)$$

where

$$\alpha = \begin{cases} 0.694 + 0.647\left(\frac{A}{B} - 0.5\right) & [if\ A/B \geq 0.5] \\ 0.694 + 0.858\left(\frac{A}{B} - 0.5\right) & [if\ A/B < 0.5] \end{cases}$$

and

$$\beta = 0.06 + 0.235(\tfrac{A}{B} - 0.5)$$

So, the plastic strength of the ESSD can be determined using the developed Eq. (5.7) for any geometry.

5.2.2 Equivalency of Oblong Steel Slit Damper (OSSD) and Butterfly-shaped Steel Strut Damper (BSSD)

5.2.2.1 Equivalent BSSD Modeling

The butterfly-shaped steel strut damper (BSSD) is fabricated by cutting slits from a structural wide-flange section in such a way that the strips of the damper become an hourglass shape. So the damper has a parabolic shape and having the same maximal stress along all the cross section. An equivalent BSSD model is developed for the same plastic strength as OSSD of section 5.2.1.1 which is depicted in Fig. 5.26 to find the equivalency between OSSD and BSSD.

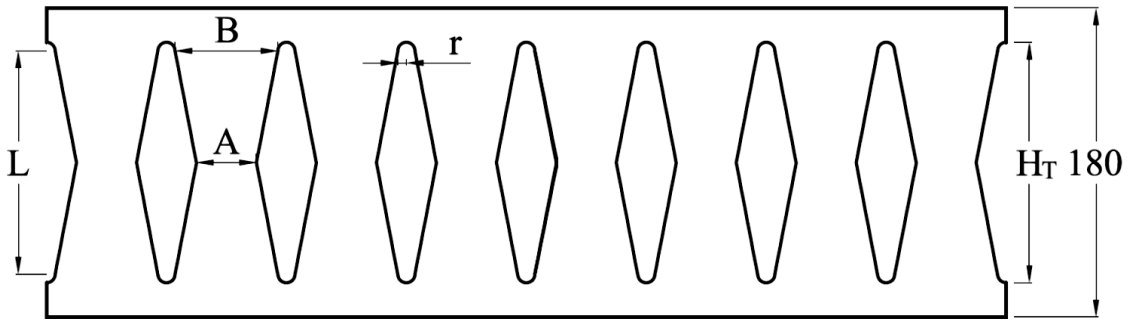

Fig. 5.26: Equivalent butterfly-shaped steel strut damper

The plastic strength (P_p) of BSSD can be calculated according to Eq. (2.11).

From section 5.2.1.1,

P_p = 269.2 x 10^3 N

n =8

σ_y = 208 MPa

H_T = 140 mm

Let,

B = 60 mm

A = b/2 = 30 mm

r = 5 mm

L = H_T – 2*r = 130 mm

The number of struts and the total strut height in BSSD are kept same as OSSD for simplification. Initially the strut width of BSSD is assumed according to the geometry of OSSD and the *A/B* ratio is taken 0.5 for simplicity.

Solving Eq. (2.11),

$$\boldsymbol{t = 12.58 \text{ mm}}$$

To maintain the parabolic profile of the damper struts, shape optimization study mentioned in section 2.8 is followed.

Let,

b_x = B/2 = 30 mm

b_0 = $(B\text{-}A)$/2 = 15 mm

x_0 = H_T /40 = 3.5 mm

x = L/2 = 65 mm

From Eq. (2.10),

$$a = b_x / \sqrt{x} = 3.72$$

5.2.2.2 Equivalence of OSSD and BSSD

The developed models for equivalency are shown in Fig. 5.27.

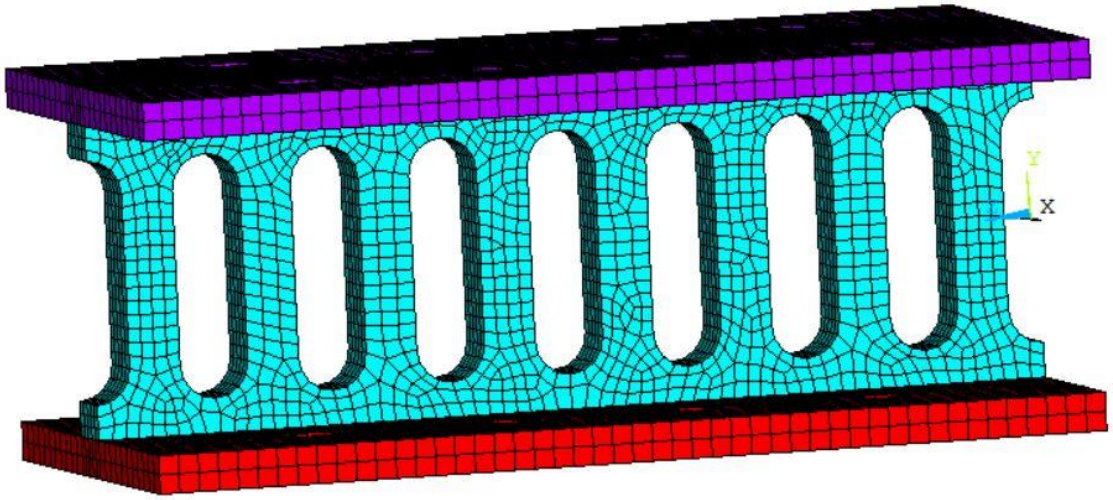

(a)

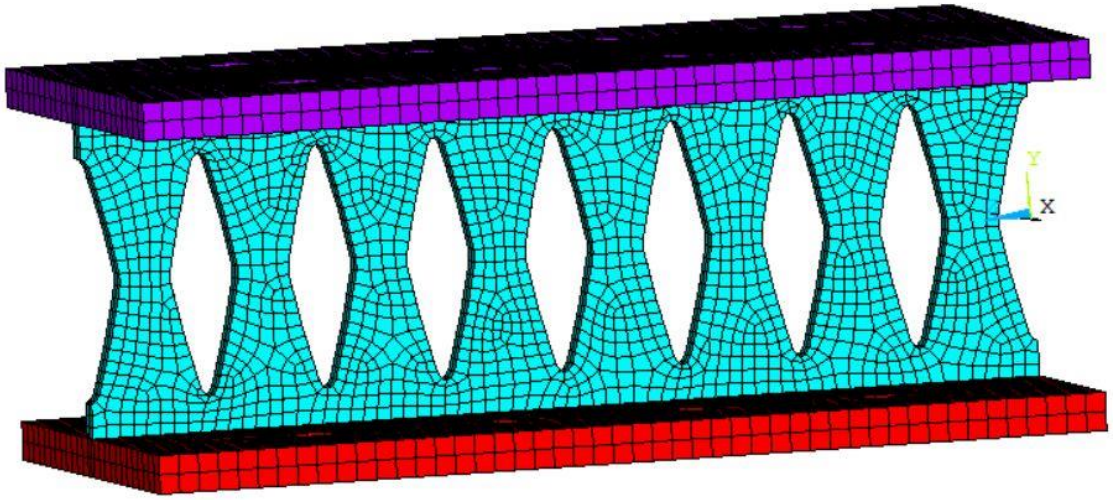

(b)

Fig. 5.27: Equivalent models of (a) OSSD and (b) BSSD

As observed in Fig. 5.28, the hysteretic responses of BSSD having a thickness of 12.58 mm which is found by solving Eq. (2.11) does not comply with the responses of OSSD. Actually, it is underestimating the thickness of BSSD. Therefore, there can be a scope for modification as this formula may not be appropriate. A thickness of 16.25 mm is found for BSSD after several trials, based on matching the load vs. deformation response of OSSD which is shown in Fig. 5.28. This is happened because stress distribution is improved along the strut height of the BSSD which has a parabolic profile whereas stress is concentrated at

the end parts of the struts in OSSD. Hence to match the responses of OSSD having a thickness of 38 mm, a thickness of 16.25 mm for BSSD is enough.

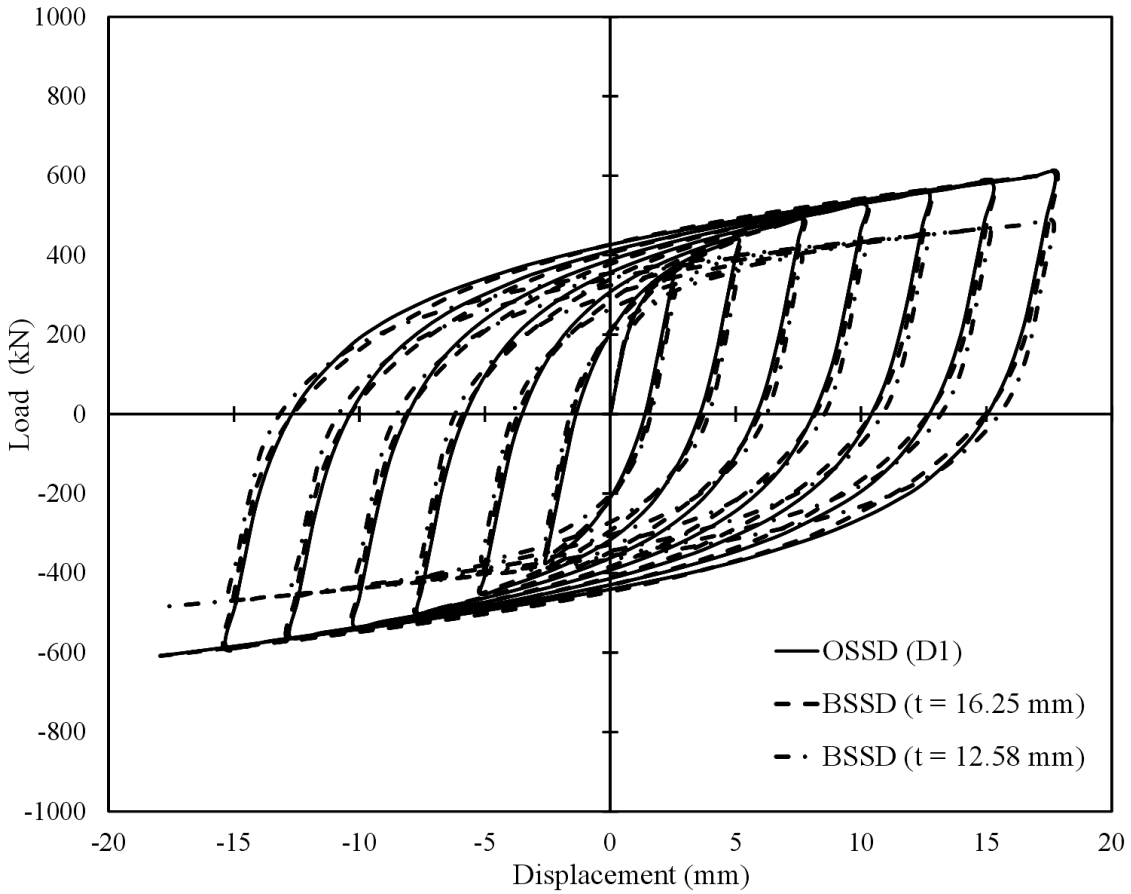

Fig. 5.28: Comparison of numerical results for equivalent models of OSSD and BSSD following loading protocol N

Therefore, for finding the parameters of equivalent BSSD to match with a particular strength of OSSD Eq. (2.11) needs to be modified by observing and analyzing the finite element results.

5.2.2.3 Development of Plastic Strength Formula for BSSD

It is found in the previous section that Eq. (2.11) does not provide the same hysteretic responses of BSSD for the same plastic strength of OSSD. So some parametric studies have been performed in this section to observe the effects of different parameters of BSSD for different plastic strengths of OSSD. Hence, the hysteretic responses of BSSD are compared with the OSSD of different strengths by changing the parameters such as strut width, strut height, thickness etc.

Initially, the height of strut is varied in both OSSD and BSSD for *A/B* = 0.5 ratio. The geometry for different strut heights of OSSD and BSSD are shown in Table 5.8.

Table 5.8: Geometry of OSSD and BSSD for different strut heights [*A/B* = 0.5]

OSSD					BSSD				
Specimen	H_T (mm)	*H'* (mm)	*t* (mm)	*B* (mm)	Specimen	H_T (mm)	*B* (mm)	*A* (mm)	*t* (mm)
OSSD2	130	96.15	38	30	BSSD1	130	60	30	17.07
OSSD3	140	105.7	38	30	BSSD2	140	60	30	16.25
OSSD4	150	115.3	38	30	BSSD3	150	60	30	15.51

In Table 5.8, the equivalent thickness of BSSD is obtained for every pair of OSSD and BSSD specimens by matching the load vs. displacement responses. The load vs. displacement curves for OSSD2 and BSSD1 specimens are shown in Fig. 5.29. The load vs. displacement curves of other specimens are not depicted for simplicity.

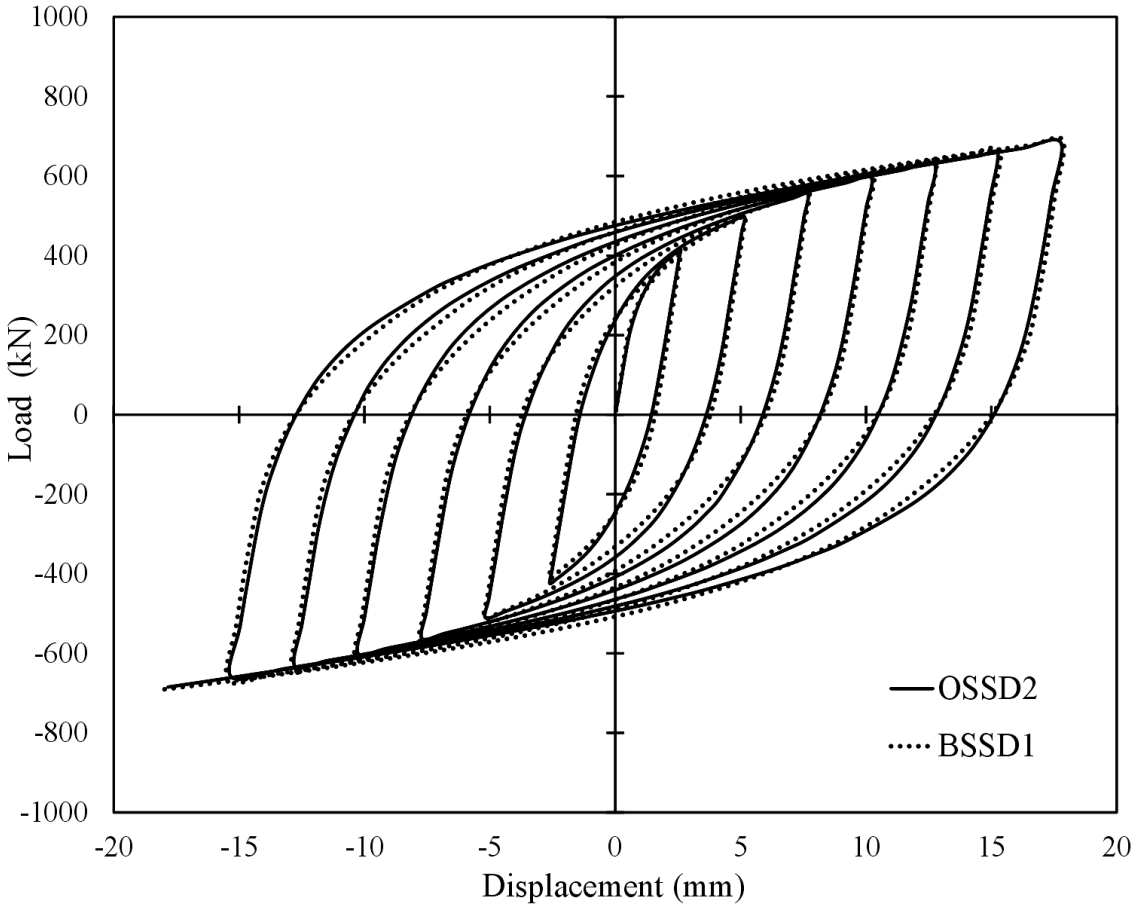

Fig. 5.29: Comparison of hysteretic curves between OSSD2 and BSSD1 following loading protocol N [*A/B* = 0.5]

Area within the force-displacement loop gives energy dissipation which is one of the

substantial seismic features of any structure. The amounts of energy dissipated by the specimens obtained using software for different strut heights are shown in Fig. 5.30.

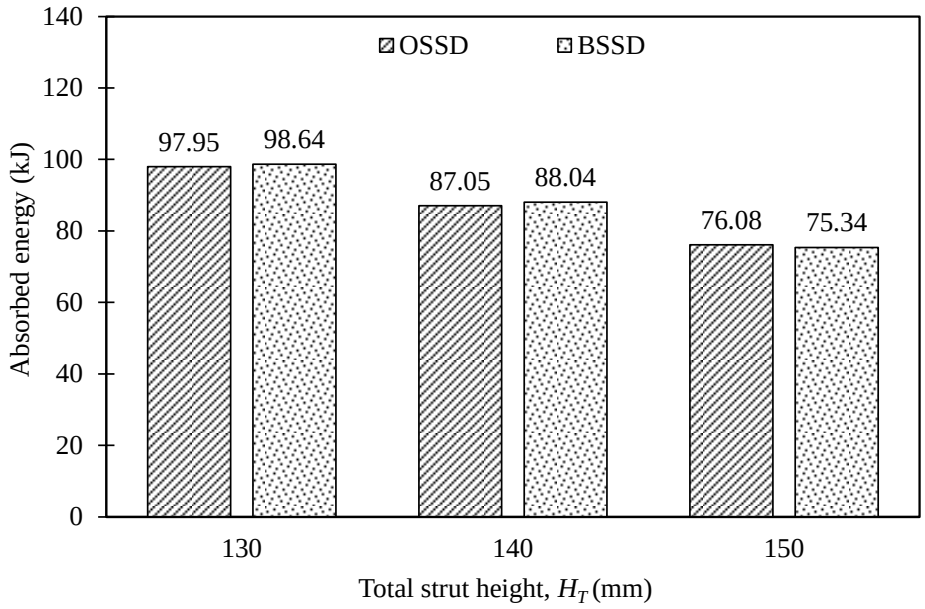

Fig. 5.30: Comparison of absorbed energy between OSSD and BSSD for different strut heights [*A/B* = 0.5]

It is clear from Fig. 5.30 that as flexibility increases an increase in the height of BSSD results in a slightly reduction of the maximum force suffered by the connections. As observed in Fig. 5.31, increasing the strut height decreases the thickness of equivalent BSSD which is happened because of the reduction in stiffness.

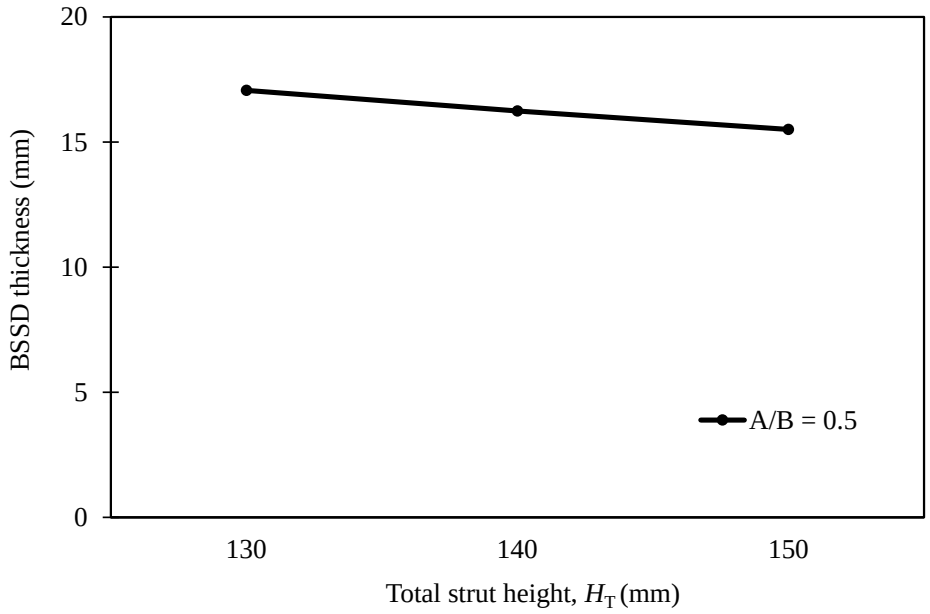

Fig. 5.31: Comparison of BSSD thickness for different strut heights [*A/B* = 0.5]

Identical studies are carried out for different strut widths of OSSD and BSSD. The geometry of OSSD and ESSD for different strut widths are listed in Table 5.9. To avoid repeatability, only the load vs. displacement curves for OSSD7 and BSSD4 specimens are shown in Fig. 5.32.

Table 5.9: Geometry of OSSD and BSSD for different strut widths [A/B = 0.5]

OSSD					BSSD				
Specimen	B (mm)	H_T (mm)	H' (mm)	t (mm)	Specimen	H_T (mm)	B (mm)	A (mm)	t (mm)
OSSD7	25	140	105.7	38	BSSD4	140	60	30	11.28
OSSD2	30	140	105.7	38	BSSD2	140	60	30	16.25
OSSD8	35	140	105.7	38	BSSD5	140	60	30	22.11

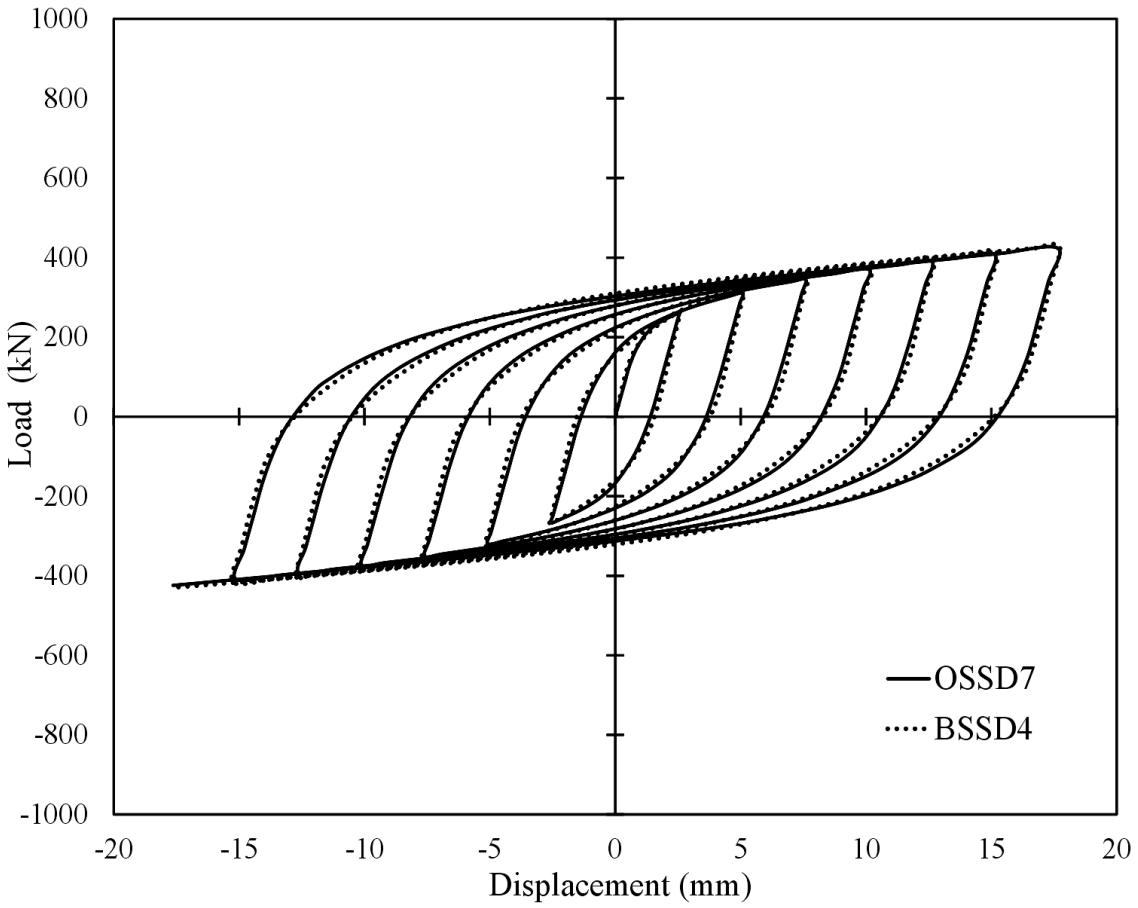

Fig. 5.32: Comparison of hysteretic curves between OSSD7 and BSSD4 following loading protocol N [A/B = 0.5]

In Figs. 5.33-5.34, the energy dissipation and equivalent BSSD thickness comparison for different strut widths are illustrated respectively.

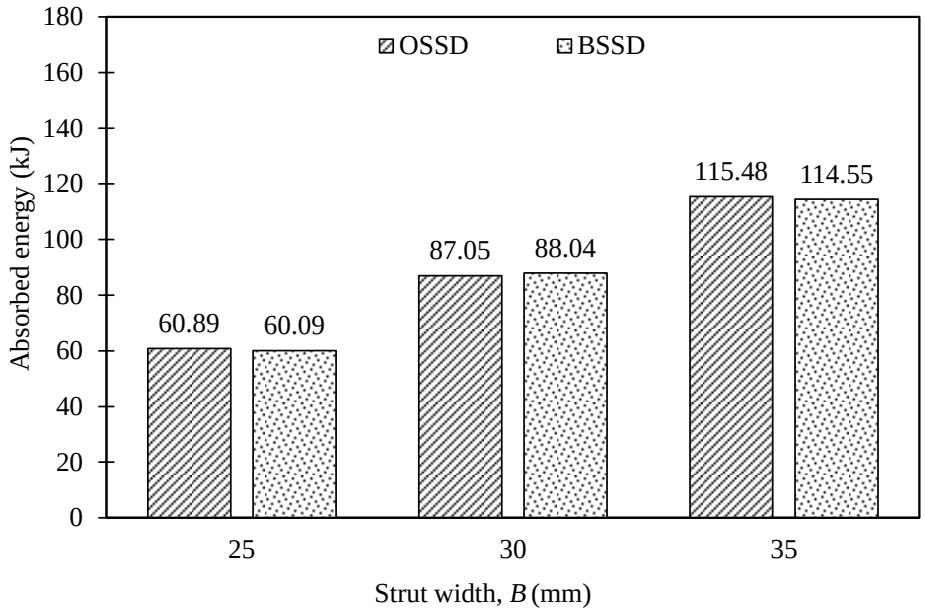

Fig. 5.33: Comparison of absorbed energy between OSSD and BSSD for different strut widths [*A/B* = 0.5]

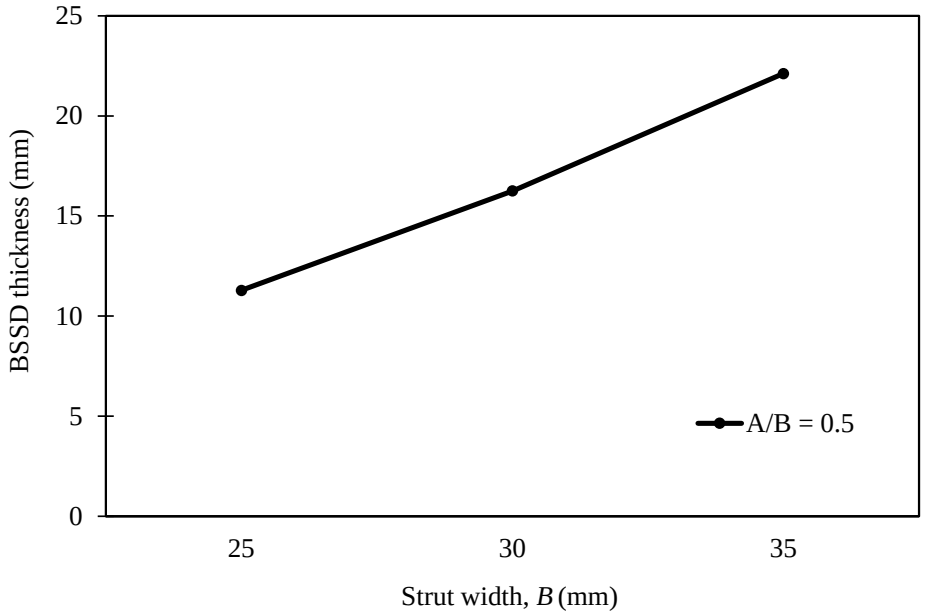

Fig. 5.34: Comparison of BSSD thickness for different strut widths [*A/B* = 0.5]

From Fig. 5.33, it is observed that decreasing the strut width decreases the maximum force in connection and amount of energy dissipation because of increment in stiffness. It is also noticed from Fig. 5.34 that, increasing the strut width increases the thickness of equivalent BSSD which is happened because of the reduction in flexibility.

Therefore, based on the parametric study results pattern depicted in Figs. 5.31 and 5.34, the yield strength of the BSSD can be modified analytically as follows:

$$P_y = n \frac{\sigma_y t}{2H_T} [0.88B + 0.075(H_T - 140)]^2 \quad [if\ A/B = 0.5] \quad (5.8)$$

Here,

P_y = Yield strength

n = Number of Struts

σ_y = Yield stress

t = Thickness

H_T = Total strut height

B = Strut width at end

By solving Eq. (5.8), for *A/B* = 0.5 the parameters of the BSSD for an equivalent strength of the OSSD can be obtained. It can be decided that the Eq. (5.8) sets good agreement for any strut height and width of BSSD for *A/B* = 0.5 ratio as observed in Figs. 5.30 and 5.33.

In a similar manner, studies are carried out for different *A/B* ratios analogous to *A/B* = 0.5 ratio. The data and results are shown in Tables 5.10-5.13 and Figs. 5.35-5.46. Similar types of results are excluded for simplification.

Table 5.10: Geometry of OSSD and BSSD for different strut heights [*A/B* = 0.33]

OSSD					BSSD				
Specimen	H_T (mm)	*H'* (mm)	*t* (mm)	*B* (mm)	Specimen	H_T (mm)	*B* (mm)	*A* (mm)	*t* (mm)
OSSD2	130	96.15	38	30	BSSD6	130	60	20	18.42
OSSD3	140	105.7	38	30	BSSD7	140	60	20	17.41
OSSD4	150	115.3	38	30	BSSD8	150	60	20	16.51

Table 5.11: Geometry of OSSD and BSSD for different strut widths [*A/B* = 0.33]

OSSD					BSSD				
Specimen	*B* (mm)	H_T (mm)	*H'* (mm)	*t* (mm)	Specimen	H_T (mm)	*B* (mm)	*A* (mm)	*t* (mm)
OSSD7	25	140	105.7	38	BSSD9	140	60	20	12.09
OSSD3	30	140	105.7	38	BSSD7	140	60	20	17.41
OSSD8	35	140	105.7	38	BSSD10	140	60	20	23.70

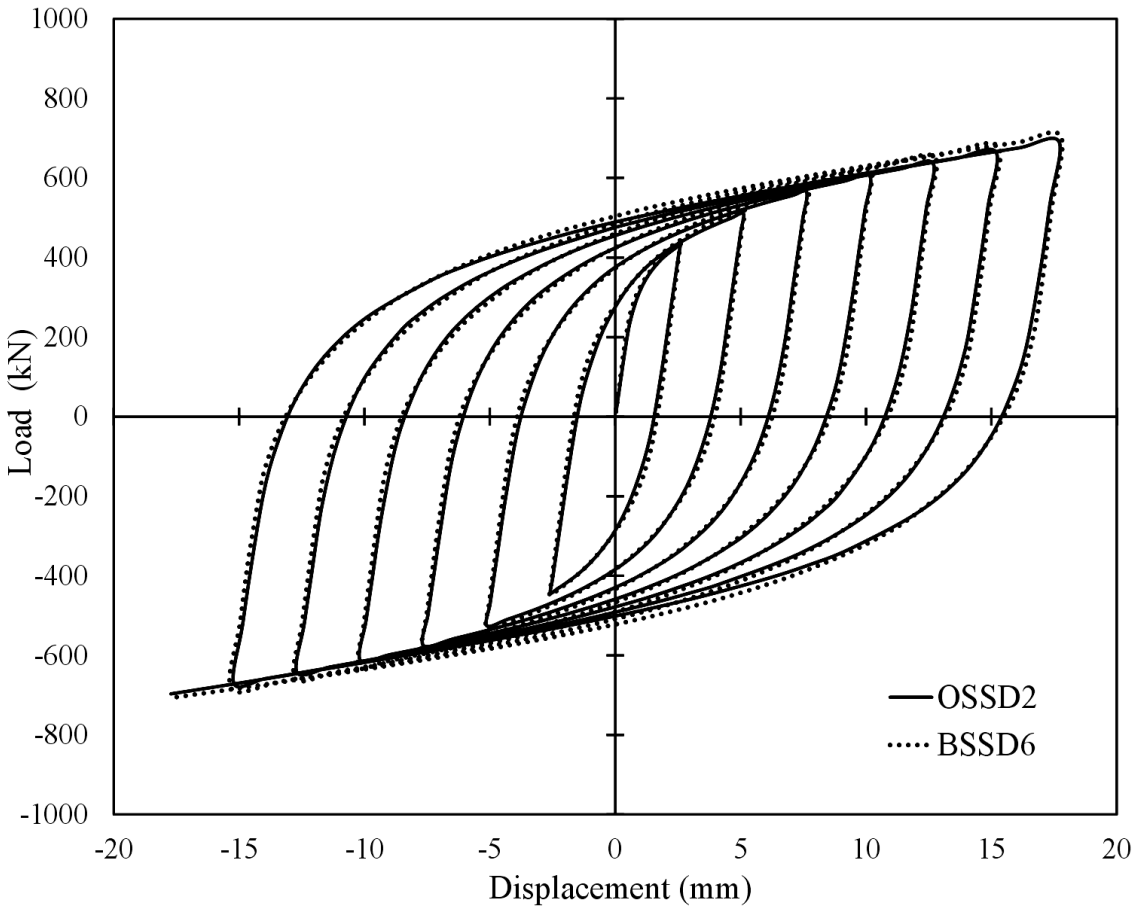

Fig. 5.35: Comparison of hysteretic curves between OSSD2 and BSSD6 following loading protocol N [*A/B* = 0.33]

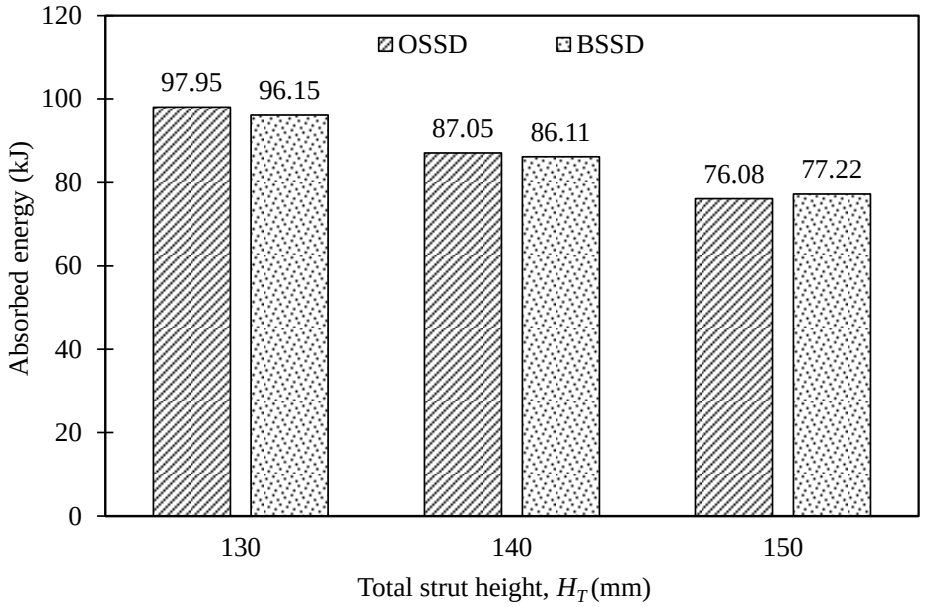

Fig. 5.36: Comparison of absorbed energy between OSSD and BSSD for different strut heights [*A/B* = 0.33]

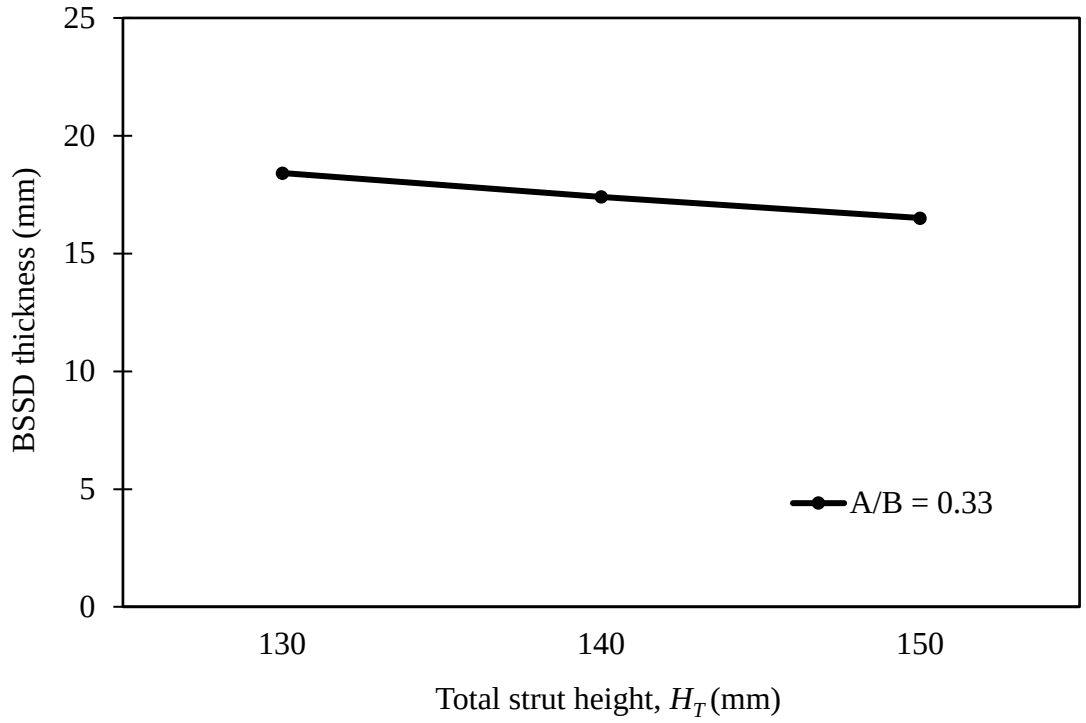

Fig. 5.37: Comparison of BSSD thickness for different strut heights [*A/B* = 0.33]

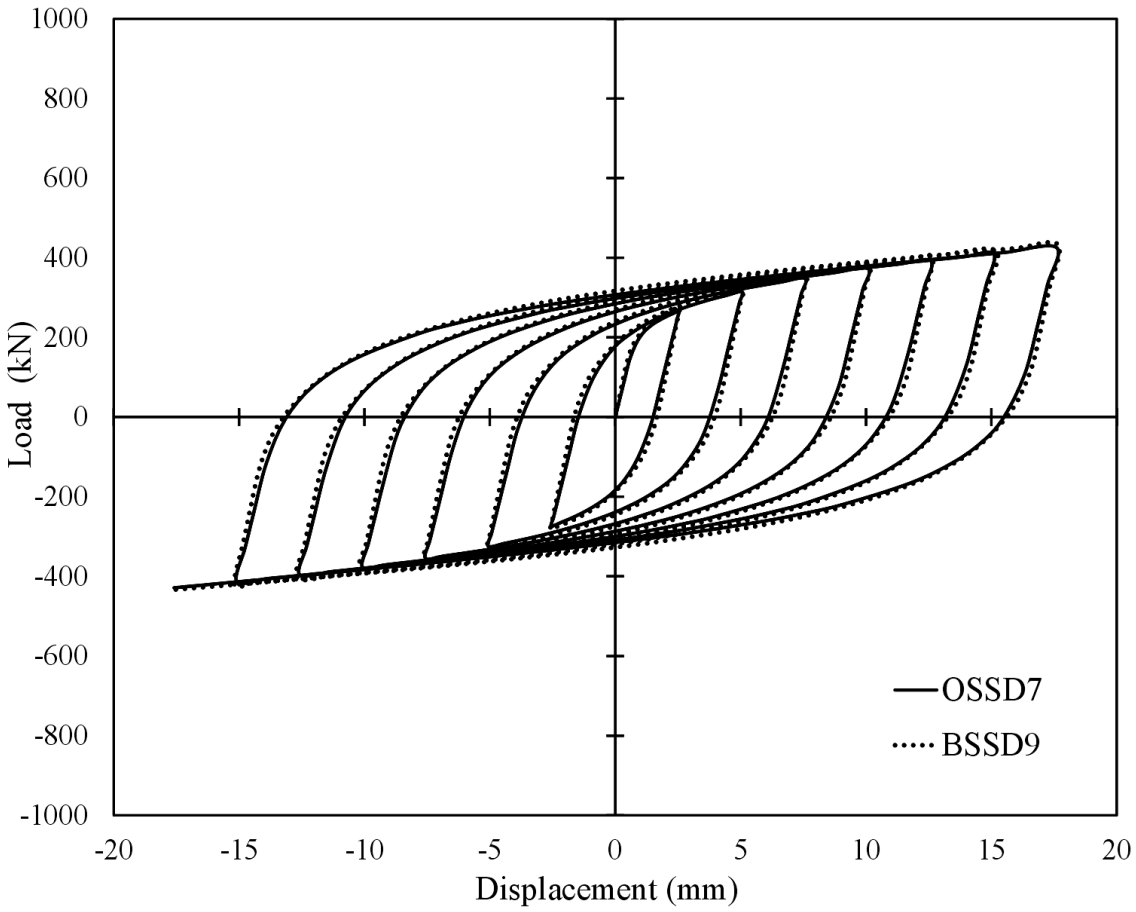

Fig. 5.38: Comparison of hysteretic curves between OSSD7 and BSSD9 following loading protocol N [*A/B* = 0.33]

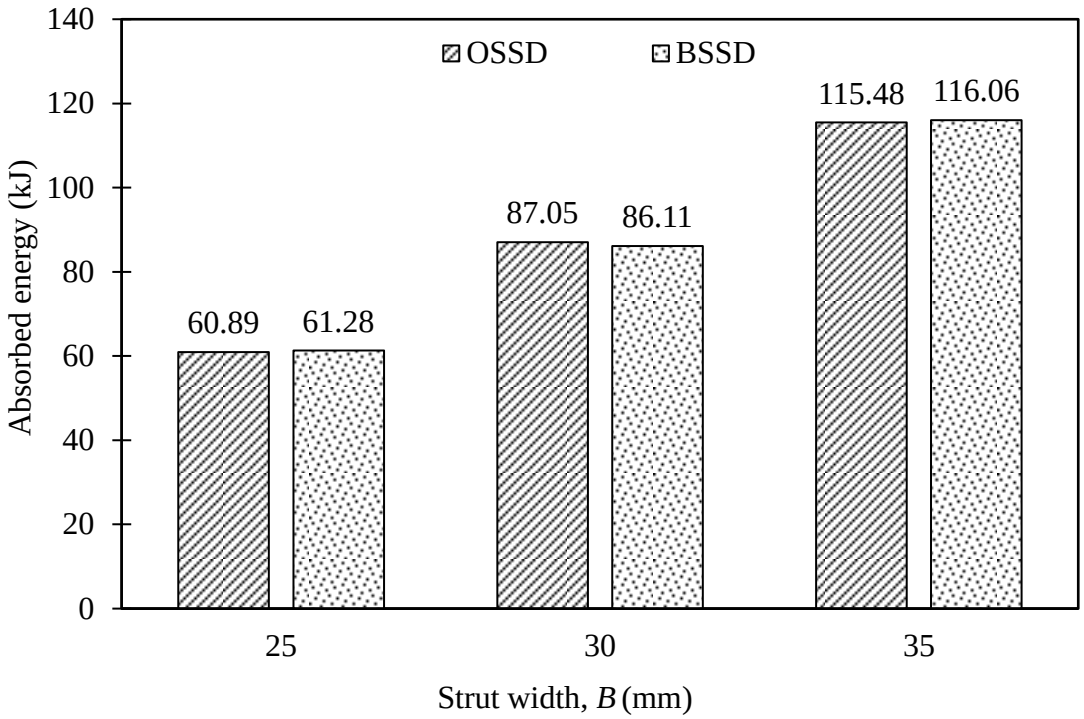

Fig. 5.39: Comparison of absorbed energy between OSSD and BSSD for different strut widths [*A/B* = 0.33]

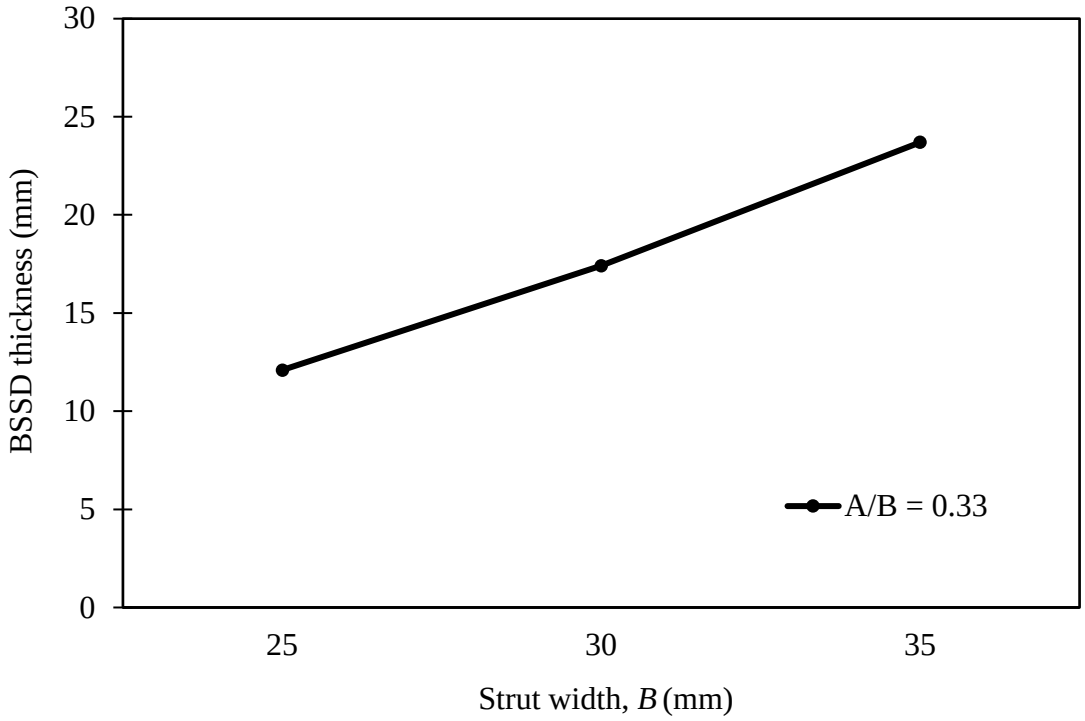

Fig. 5.40: Comparison of BSSD thickness for different strut widths [*A/B* = 0.33]

Table 5.12: Geometry of OSSD and BSSD for different strut heights [*A/B* = 0.67]

OSSD					BSSD				
Specimen	H_T (mm)	H' (mm)	t (mm)	B (mm)	Specimen	H_T (mm)	B (mm)	A (mm)	t (mm)
OSSD2	130	96.15	38	30	BSSD11	130	60	40	16.65
OSSD3	140	105.7	38	30	BSSD12	140	60	40	15.88
OSSD4	150	115.3	38	30	BSSD13	150	60	40	15.19

Table 5.13: Geometry of OSSD and BSSD for different strut widths [*A/B* = 0.67]

OSSD					BSSD				
Specimen	B (mm)	H_T (mm)	H' (mm)	t (mm)	Specimen	H_T (mm)	B (mm)	A (mm)	t (mm)
OSSD7	25	140	105.7	38	BSSD14	140	60	40	11.03
OSSD3	30	140	105.7	38	BSSD12	140	60	40	15.88
OSSD8	35	140	105.7	38	BSSD15	140	60	40	21.62

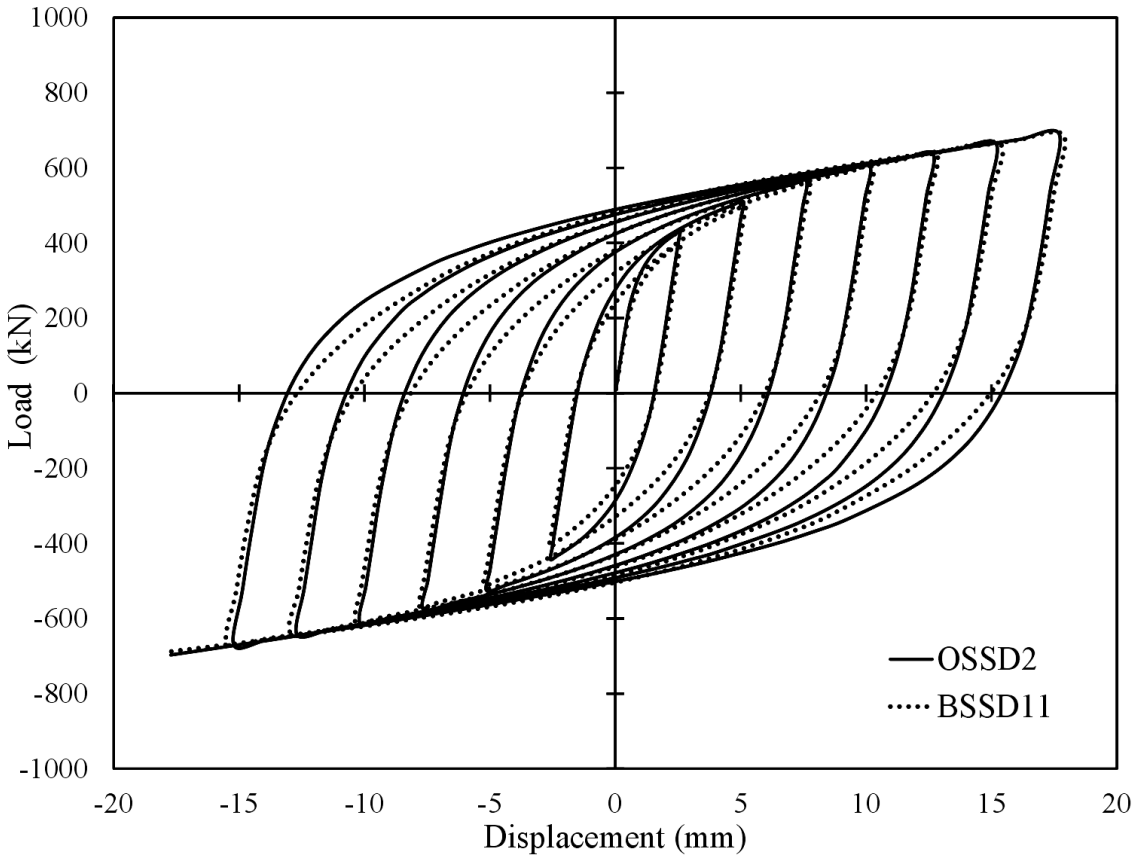

Fig. 5.41: Comparison of hysteretic curves between OSSD2 and BSSD11 following loading protocol N [*A/B* = 0.67

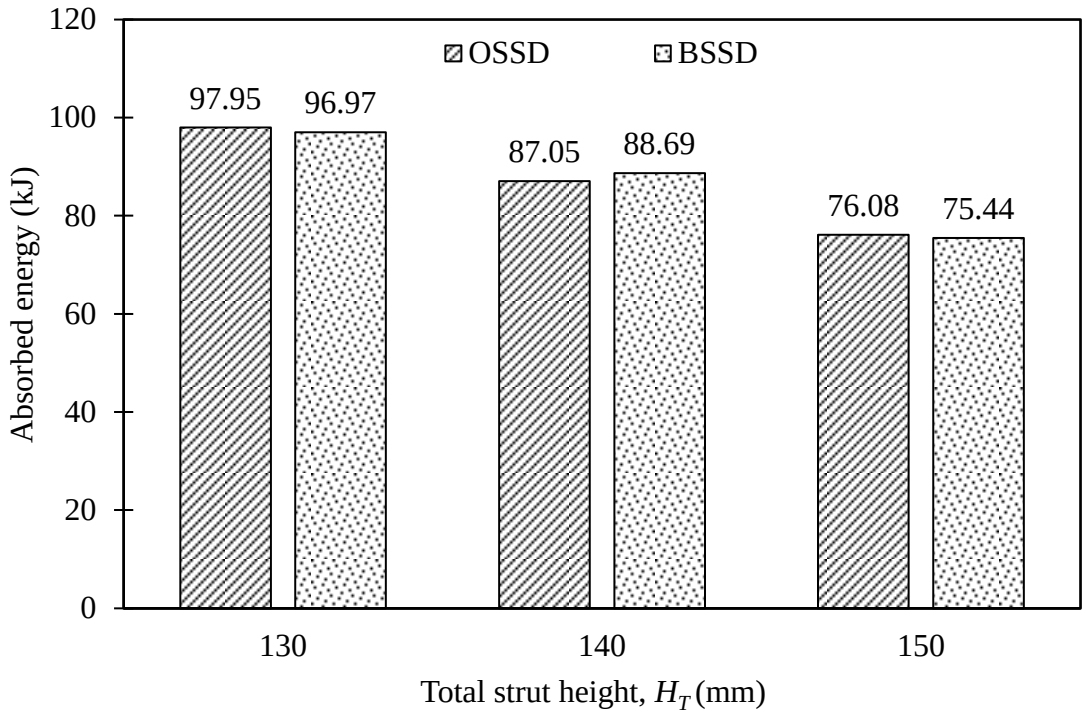

Fig. 5.42: Comparison of absorbed energy between OSSD and BSSD for different strut heights [*A/B* = 0.67]

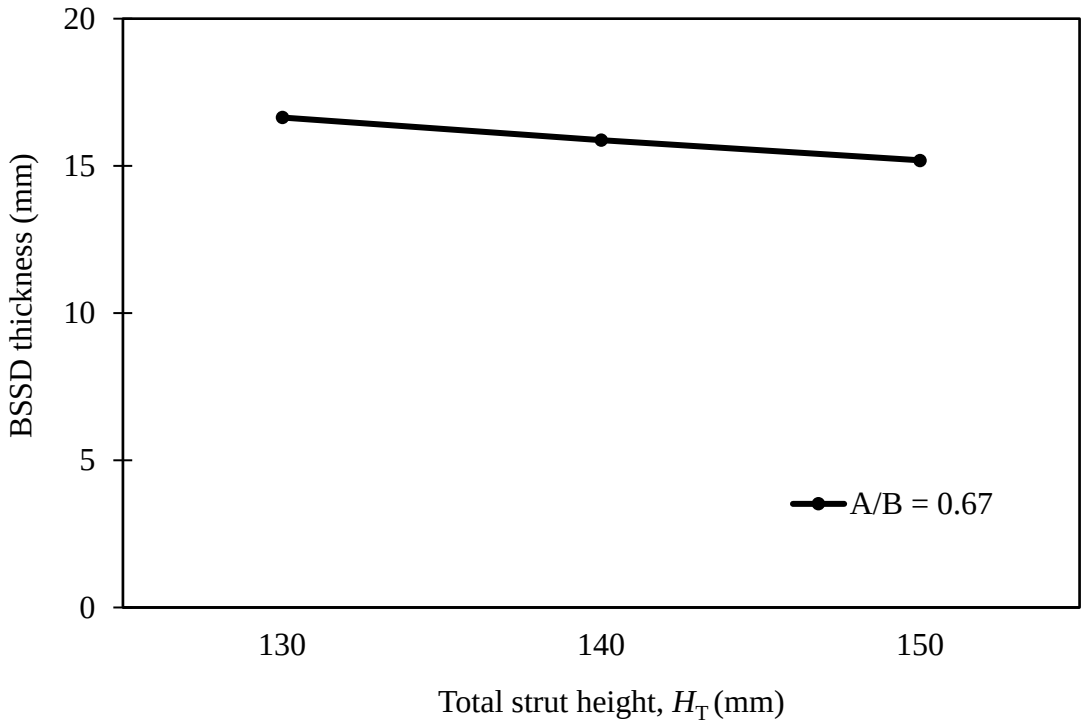

Fig. 5.43: Comparison of BSSD thickness for different strut heights [*A/B* = 0.67]

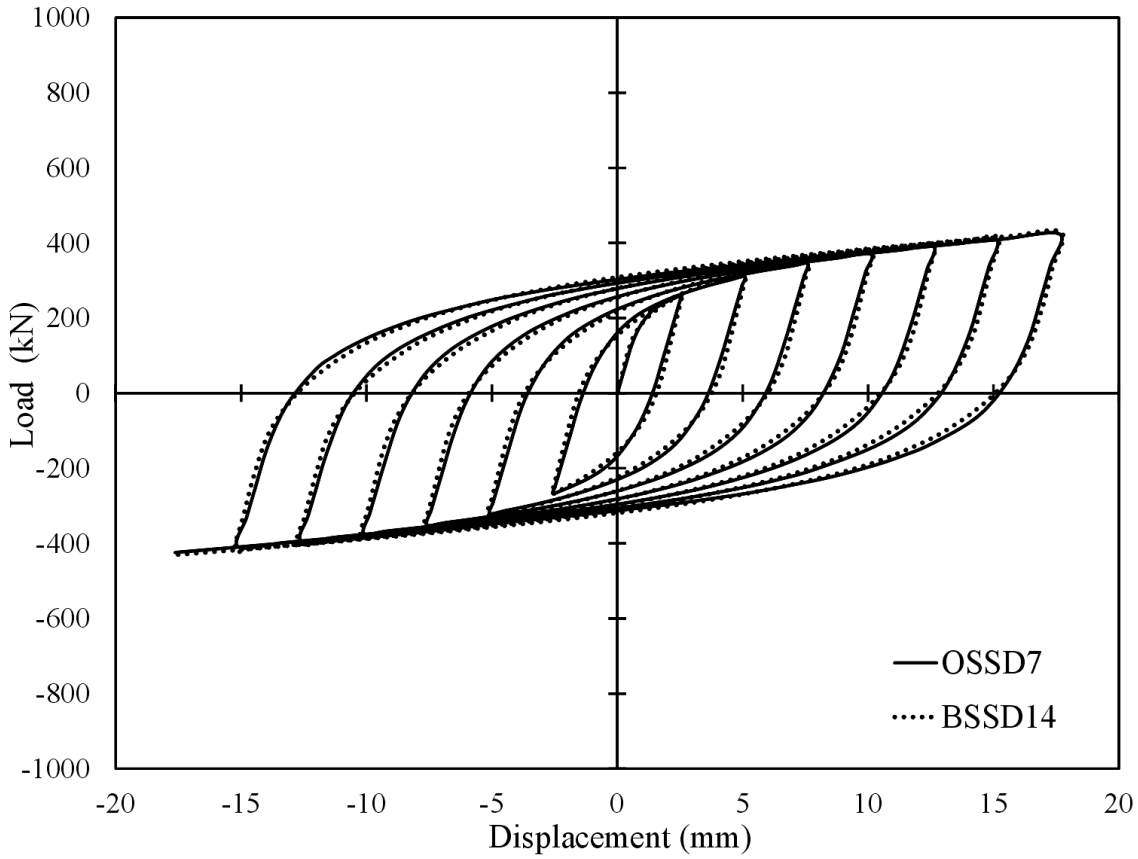

Fig. 5.44: Comparison of hysteretic curves between OSSD7 and BSSD14 following loading protocol N [*A/B* = 0.67]

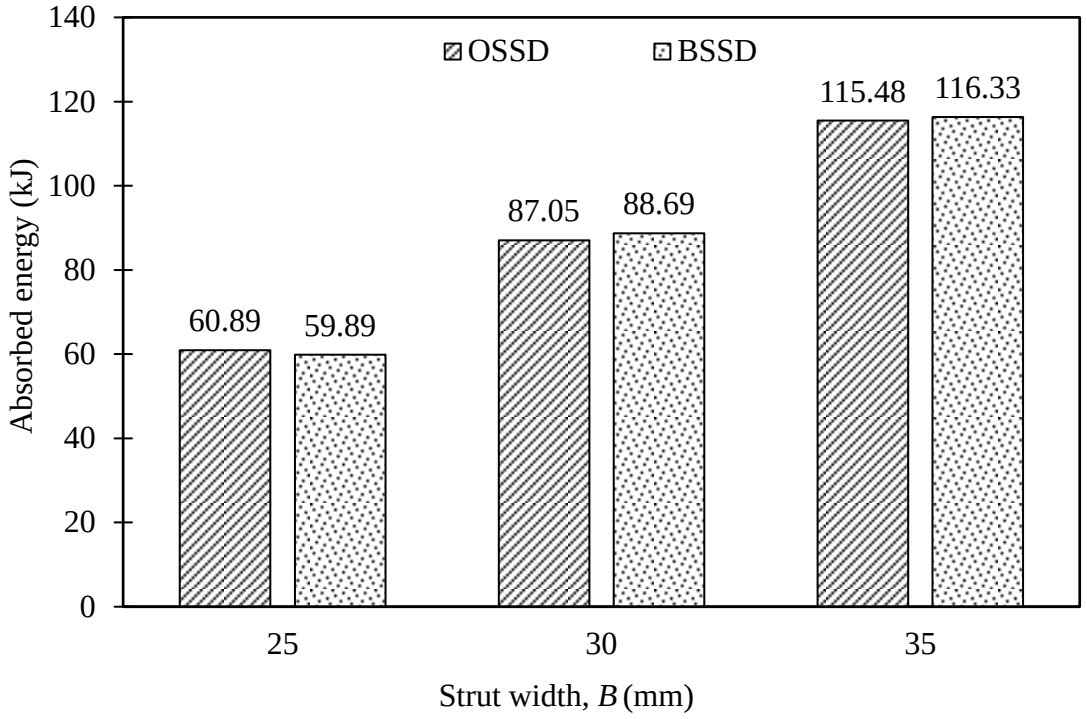

Fig. 5.45: Comparison of absorbed energy between OSSD and BSSD for different strut widths [*A/B* = 0.67]

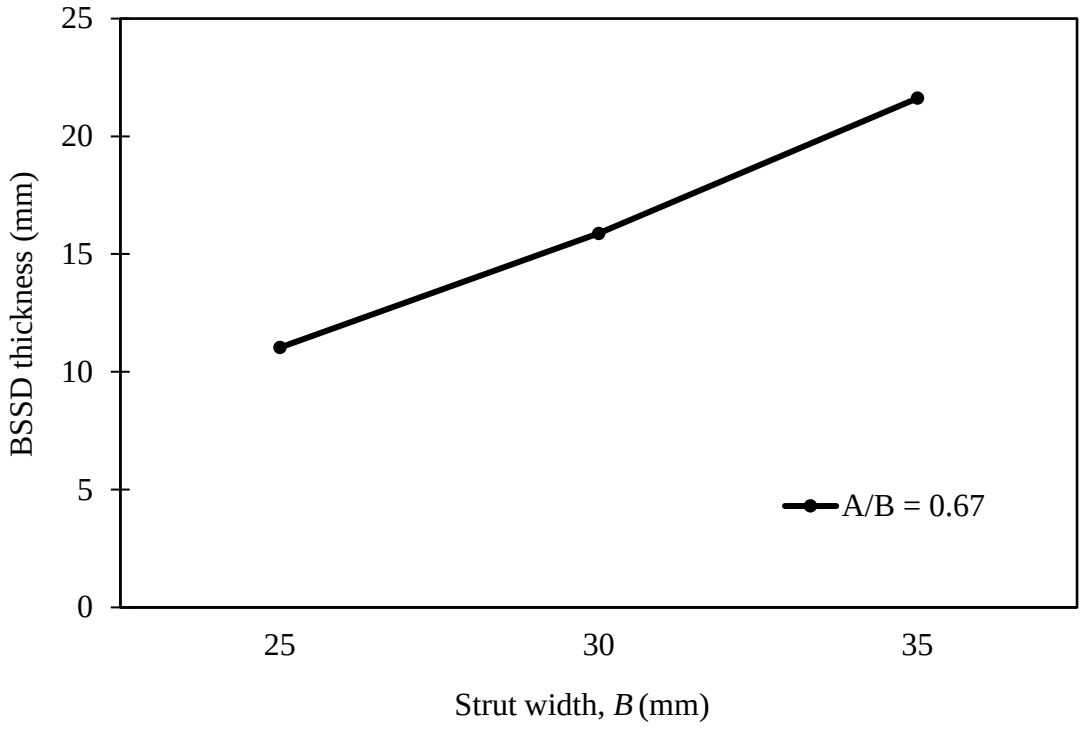

Fig. 5.46: Comparison of BSSD thickness for different strut widths [*A/B* = 0.67]

By observing the finite element results pattern the following equations are developed for BSSD for *A/B* ratios of 0.33 and 0.67 respectively.

$$P_y = n\,\frac{\sigma_y t}{2H_T}\,[0.85B + 0.09(H_T - 140)]^2 \qquad [if\ A/B = 0.33] \qquad (5.9)$$

$$P_y = n\,\frac{\sigma_y t}{2H_T}\,[0.89B + 0.07(H_T - 140)]^2 \qquad [if\ A/B = 0.67] \qquad (5.10)$$

From Figs. 5.35-5.46, it can be concluded that the Eqs. (5.9) and (5.10) hold perfect for different *A/B* ratios of BSSD.

It is observed from Eqs. 5.8-5.10 that, in the Eqs. for different *A/B* ratios of BSSD the coefficient of strut width and strut height varies which are depicted in Figs. 5.47 and 5.48 named as α and β respectively.

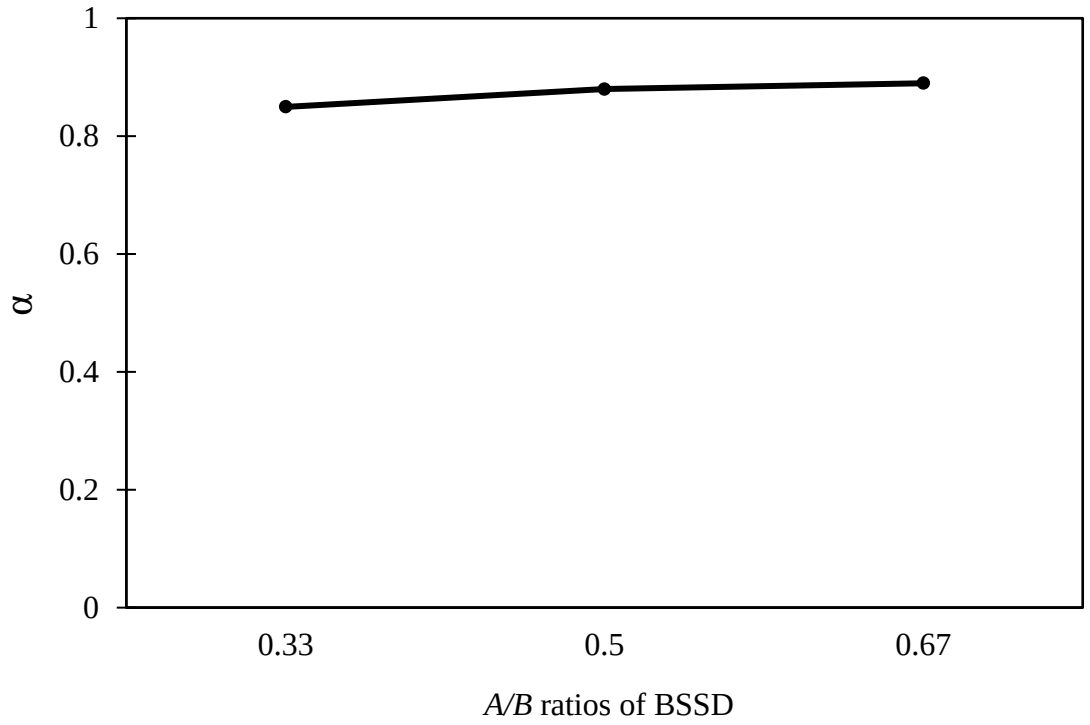

Fig. 5.47: Variation of strut width coefficient for different *A/B* ratios of BSSD

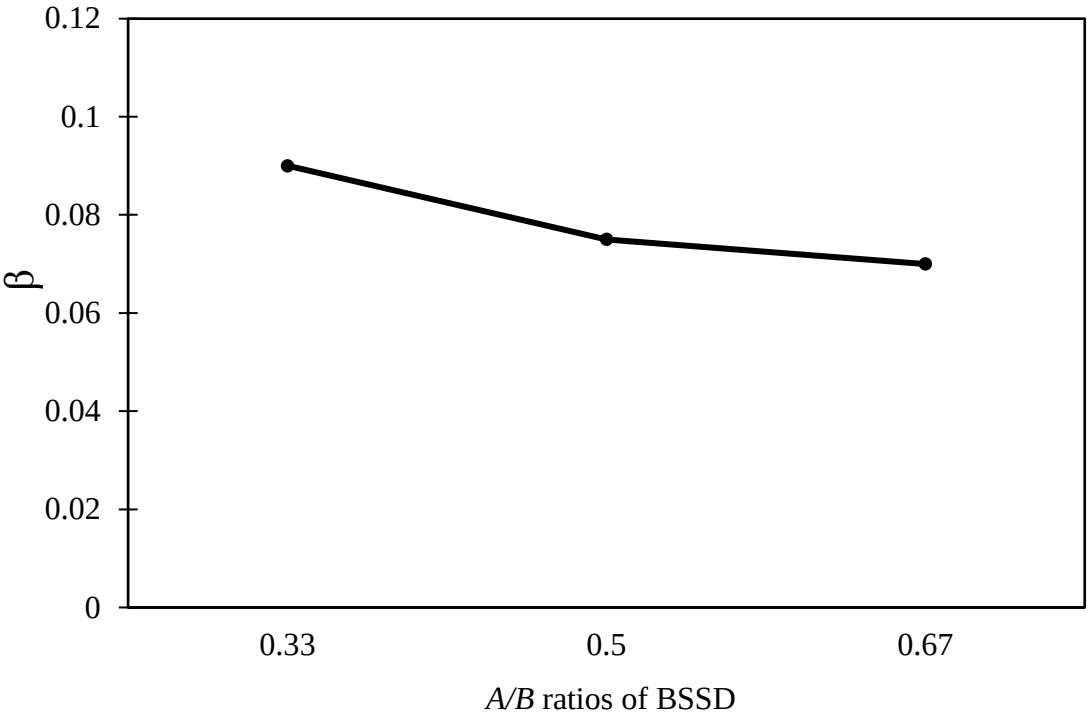

Fig. 5.48: Variation of strut height coefficient for different *A/B* ratios of BSSD

Therefore, by joining Eqs. (5.8), (5.9) and (5.10) the plastic strength formula of the BSSD can be expressed analytically in general as:

$$P_y = n \frac{\sigma_y t}{2H_T} [\alpha B + \beta(H_T - 140)]^2 \quad (5.11)$$

where

$$\alpha = \begin{cases} 0.88 + 0.059\left(\frac{A}{B} - 0.5\right) & [if\ A/B \geq 0.5] \\ 0.88 + 0.176\left(\frac{A}{B} - 0.5\right) & [if\ A/B < 0.5] \end{cases}$$

and

$$\beta = \begin{cases} 0.075 + 0.029\left(0.5 - \frac{A}{B}\right) & [if\ A/B \geq 0.5] \\ 0.075 + 0.088\left(0.5 - \frac{A}{B}\right) & [if\ A/B < 0.5] \end{cases}$$

Hence, for any geometry the plastic strength of the BSSD can be determined using the developed Eq. (5.11).

5.2.3 Equivalency of Oblong Steel Slit Damper (OSSD) and Pintle Damper (PD)

5.2.3.1 Equivalent PD Modeling

In this study, a type of steel shear damper called Pintle Damper (PD) is introduced in the beam-column connection. The PD is generally a solid cylindrical pin of butterfly shape with solid circular parts at top and bottom of it.

In order to find the equivalency between OSSD and PD, an equivalent PD model is developed for the same plastic strength as OSSD of section 5.2.1.1 which is depicted in Fig. 5.49.

The plastic strength of the Pintle damper can be obtained analytically from Eq. (2.14). From section 5.2.1.1,

P_y = 269.2 x 10^3 N

n =8

σ_y = 208 MPa

H_T = 140 mm

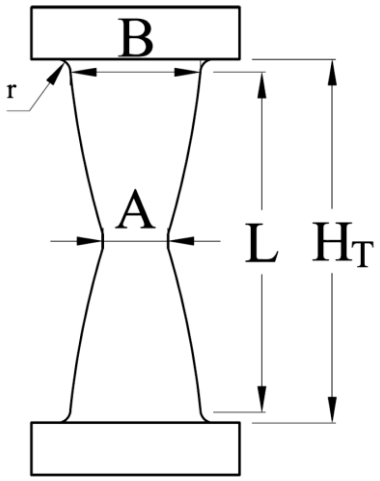

Fig. 5.49: Equivalent pintle damper

Let,

$B = D$ [Pintle diameter at end]

$A = B/2$ [Pintle diameter at middle]

$r = 5$ mm [Fillet radius]

$L = 130$ mm [Length of pintle]

The number and total height of PD are kept same as OSSD and the *A/B* ratio is taken 0.5 for simplicity. Solving Eq. (2.14),

$$\boldsymbol{D = 39.81 \text{ mm}}$$

To satisfy the same maximal stress along length of all the cross section, the section shape should be parabolic which is shown in Fig. 5.50.

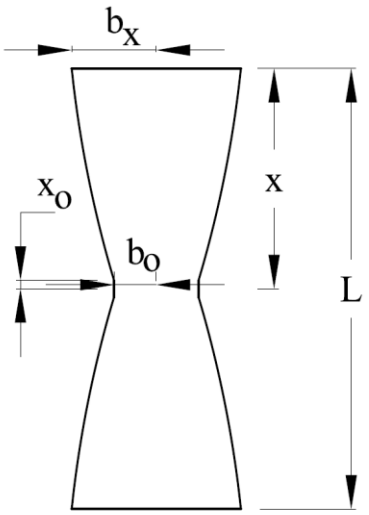

Fig. 5.50: Shape of the pintle damper

Let,

b_x = OD/2 [Outer Radius]

b_0 = (OD-ID) /2 [Inner Radius]

x_0 = L/40

x = L/2 = 65 mm

From Eq. (2.10), a = 4.95

5.2.3.2 Equivalence of OSSD and PD

In Fig. 5.51, the developed models of OSSD and PD for equivalency are shown.

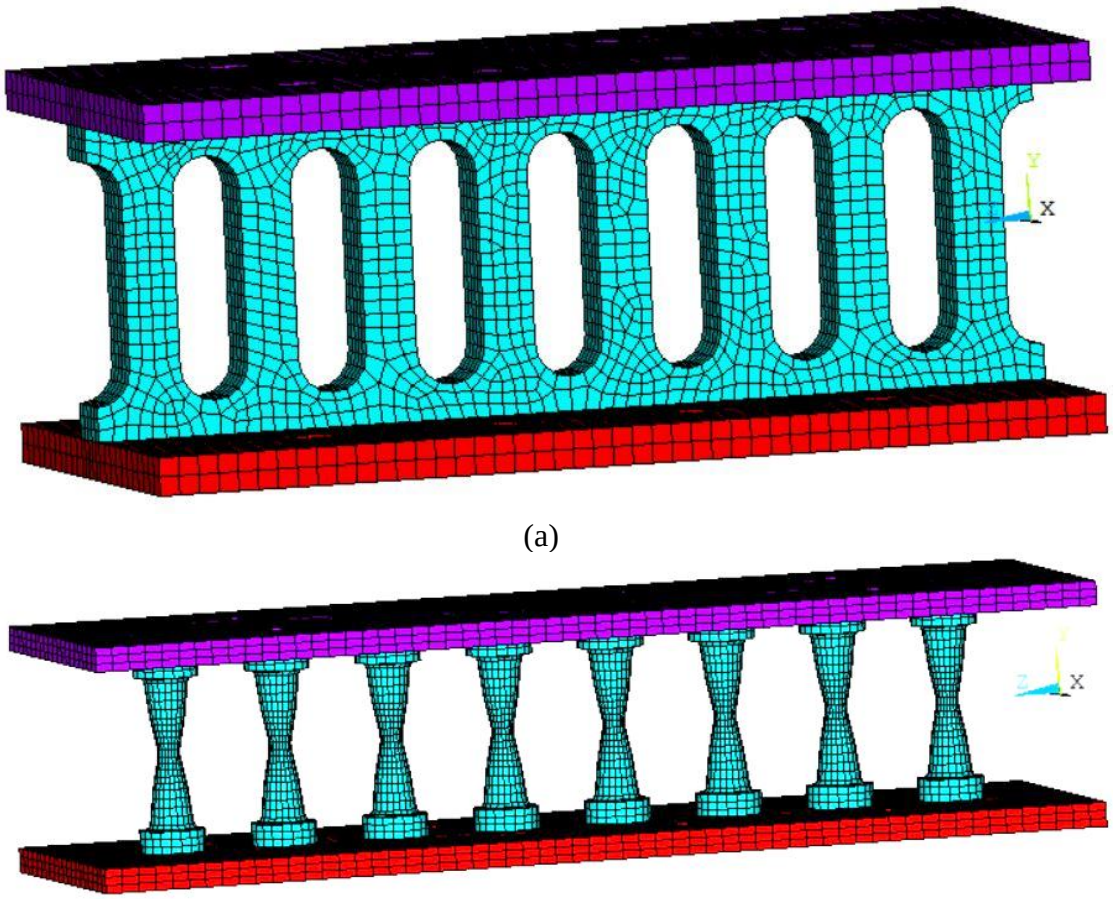

(a)

(b)

Fig. 5.51: Equivalent models of (a) OSSD and (b) BSSD

As noticed in Fig. 5.52, the hysteretic responses of PD having a diameter of 39.81 mm which is found by solving Eq. (2.14) does not comply with the responses of OSSD. In fact, it is underestimating the diameter of PD. So, this formula may not be appropriate and there can be a scope for modification. After several trials, a diameter of 45.03 mm is found for

PD based on matching the load vs. deformation response of OSSD which is shown in Fig. 5.52. This is happened because stress distribution is uniform along the pintle height having hourglass profile whereas stress is concentrated at the end parts of the struts in OSSD. Hence, a diameter of 45.03 mm for PD is sufficient to match the responses of OSSD having a thickness of 38 mm.

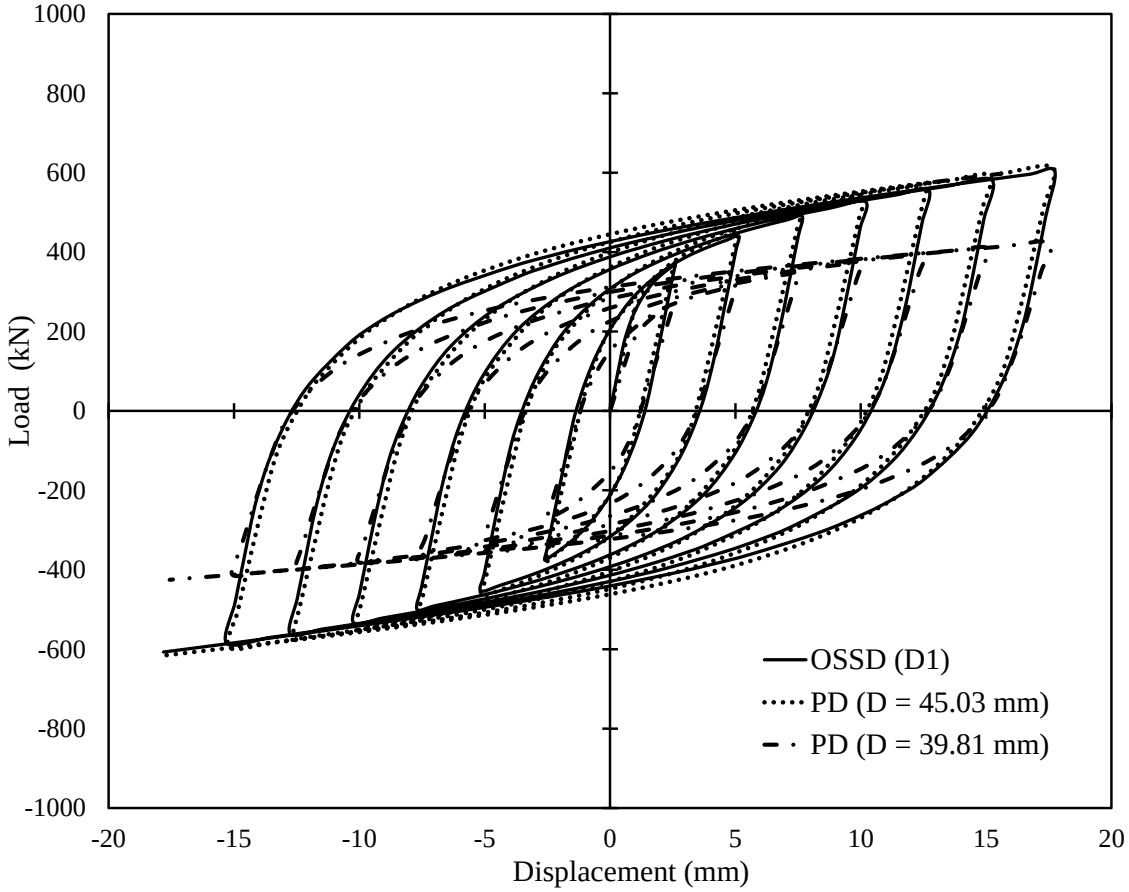

Fig. 5.52: Comparison of numerical results for equivalent models of OSSD and PD following loading protocol N

Therefore, Eq. (2.14) needs to be modified for finding the parameters of equivalent PD to match with a particular strength of OSSD by observing and analyzing the finite element results. The deformed shape of the PD model matches the experimental ones used in posttensioned connections by Vasdravellis et al. (2014) which is illustrated in Fig. 5.53.

5.2.3.3 Development of Plastic Strength Formula for PD

In the previous section, it is observed that Eq. (2.14) does not provide the same hysteretic responses of PD for the same plastic strength of OSSD. So in this section, some parametric

studies have been performed to observe the effects of different parameters of PD for different plastic strengths of OSSD. Therefore, the hysteretic responses of PD are compared with the OSSD of different strengths by changing the parameters such as strut width, strut height, thickness etc. The height of strut is varied at first in both OSSD and PD for *A/B* = 0.5 ratio. The geometry for different strut heights of OSSD and PD are shown in Table 5.14.

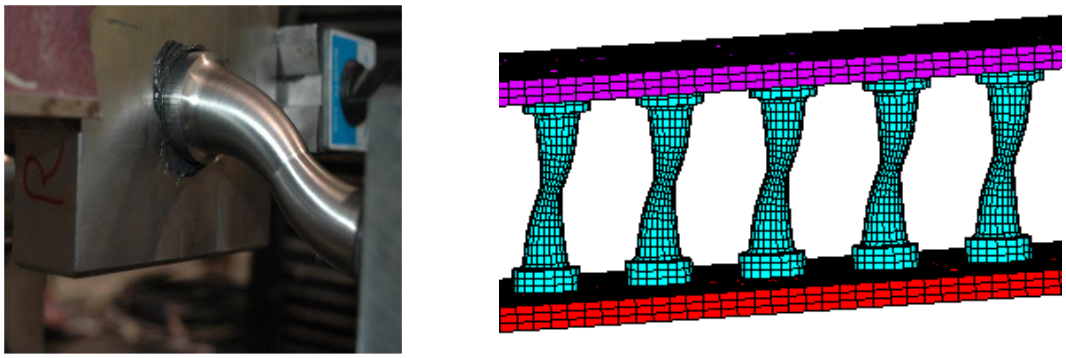

(a) Vasdravellis et al. 2014 (b) PD Model

Fig. 5.53: Deformed shape of the pintle damper

Table 5.14: Geometry of OSSD and PD for different strut heights [*A/B* = 0.5]

OSSD					PD				
Specimen	H_T (mm)	H' (mm)	t (mm)	B (mm)	Specimen	H_T (mm)	L (mm)	A (mm)	B (mm)
OSSD2	130	96.15	38	30	PD1	130	120	22.78	45.56
OSSD3	140	105.7	38	30	PD2	140	130	22.52	45.03
OSSD4	150	115.3	38	30	PD3	150	140	22.27	44.54

For every pair of OSSD and PD specimens in Table 5.14, the equivalent diameter of PD is found by matching the load vs. displacement responses. The load vs. displacement curves for OSSD2 and PD1 specimens are shown in Fig. 5.54. For simplicity, the load vs. displacement responses of other specimens are not included. Energy dissipation capacity is one of the substantial seismic features of any structure which can be obtained from the area within the force-displacement loop. The amounts of energy dissipated by the specimens for different strut heights are mentioned in Fig. 5.55 which is obtained using software. Fig. 5.55 shows an increase in the height of PD results in a slightly reduction of the maximum force suffered by the connections as flexibility increases. As observed in Fig. 5.56, increasing the strut height decreases the diameter of equivalent PD which is happened because of the reduction in stiffness.

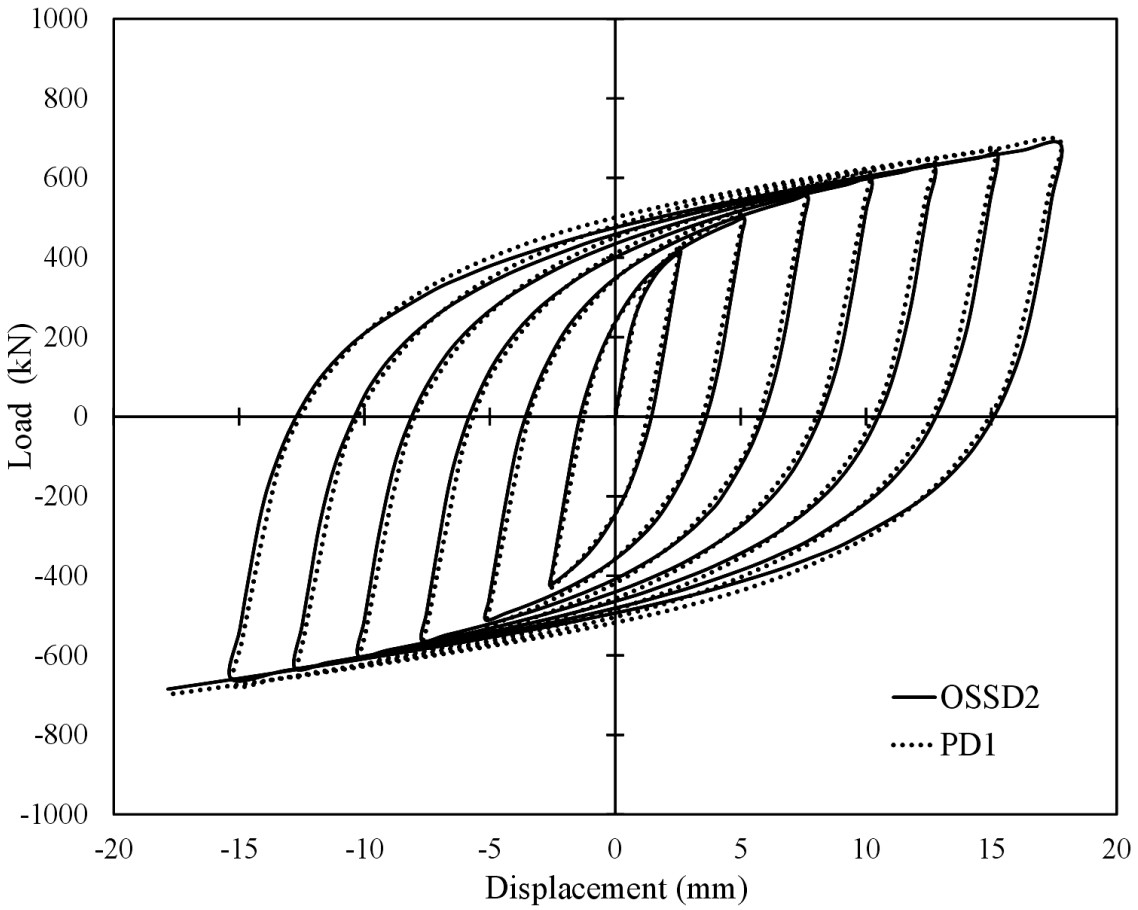

Fig. 5.54: Comparison of hysteretic curves between OSSD2 and PD1 following loading protocol N [*A/B* = 0.5]

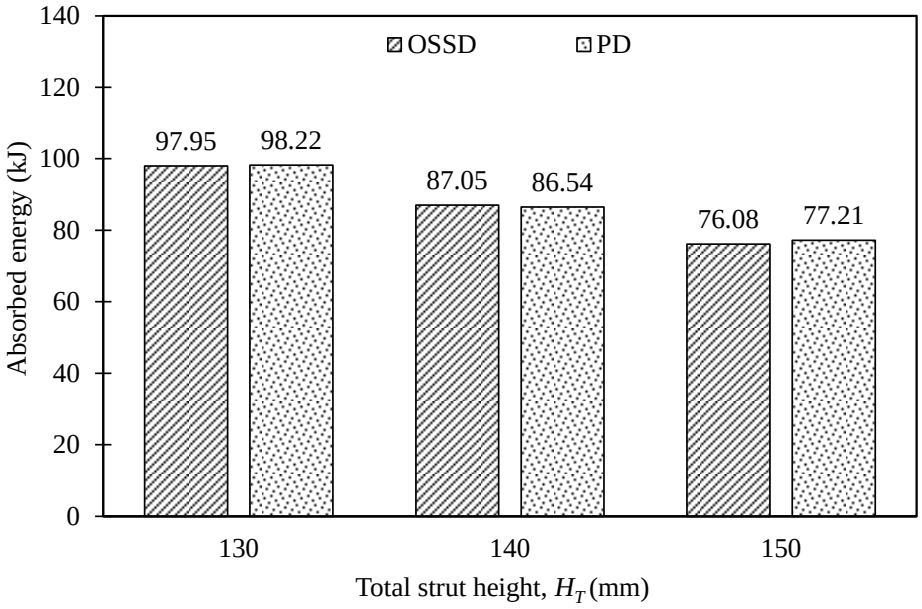

Fig. 5.55: Comparison of absorbed energy between OSSD and PD for different strut heights [*A/B* = 0.5]

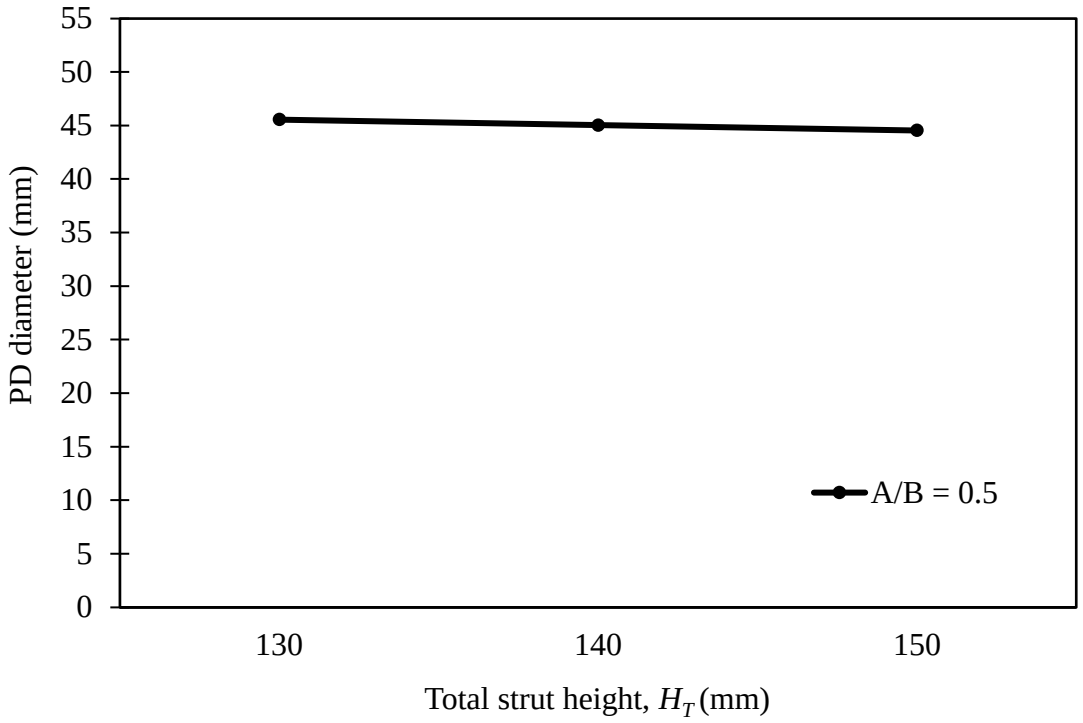

Fig. 5.56: Comparison of PD diameter for different strut heights [*A/B* = 0.5]

Similar studies are carried out for different strut widths and thicknesses of OSSD. The geometry of OSSD and PD for different strut widths and thicknesses are listed in Tables 5.15-5.16. To avoid repeatability, only the load vs. displacement curves for OSSD7 vs. PD4 and OSSD10 vs. PD6 specimens are shown in Figs. 5.57-5.58.

Table 5.15: Geometry of OSSD and PD for different strut widths [*A/B* = 0.5]

OSSD					PD				
Specimen	*B* (mm)	H_T (mm)	*H'* (mm)	*t* (mm)	Specimen	H_T (mm)	*L* (mm)	*A* (mm)	*B* (mm)
OSSD7	25	140	105.7	38	PD4	140	130	19.94	39.88
OSSD3	30	140	105.7	38	PD2	140	130	22.52	45.03
OSSD8	35	140	105.7	38	PD5	140	130	24.96	49.91

Table 5.16: Geometry of OSSD and PD for different strut thicknesses [*A/B* = 0.5]

OSSD					PD				
Specimen	*t* (mm)	H_T (mm)	*H'* (mm)	*B* (mm)	Specimen	H_T (mm)	*L* (mm)	*A* (mm)	*B* (mm)
OSSD10	34	140	105.7	30	PD6	140	130	21.69	43.39
OSSD3	38	140	105.7	30	PD2	140	130	22.52	45.03
OSSD11	42	140	105.7	30	PD7	140	130	23.28	46.56

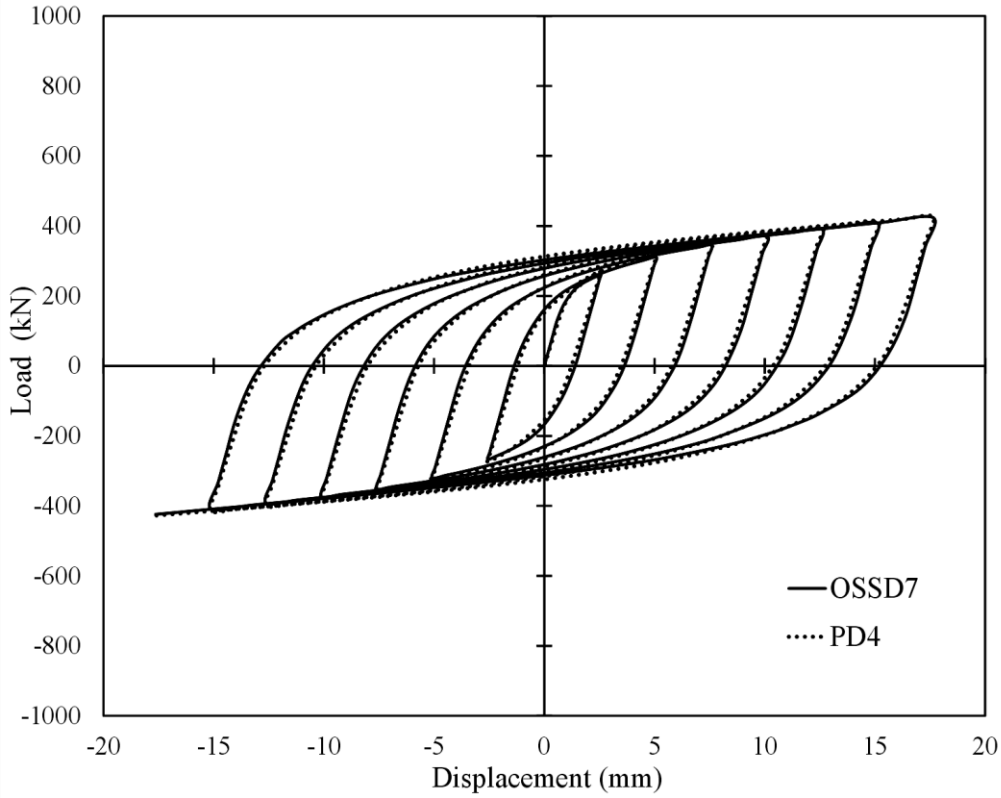

Fig. 5.57: Comparison of hysteretic curves between OSSD7 and PD4 following loading protocol N [*A/B* = 0.5]

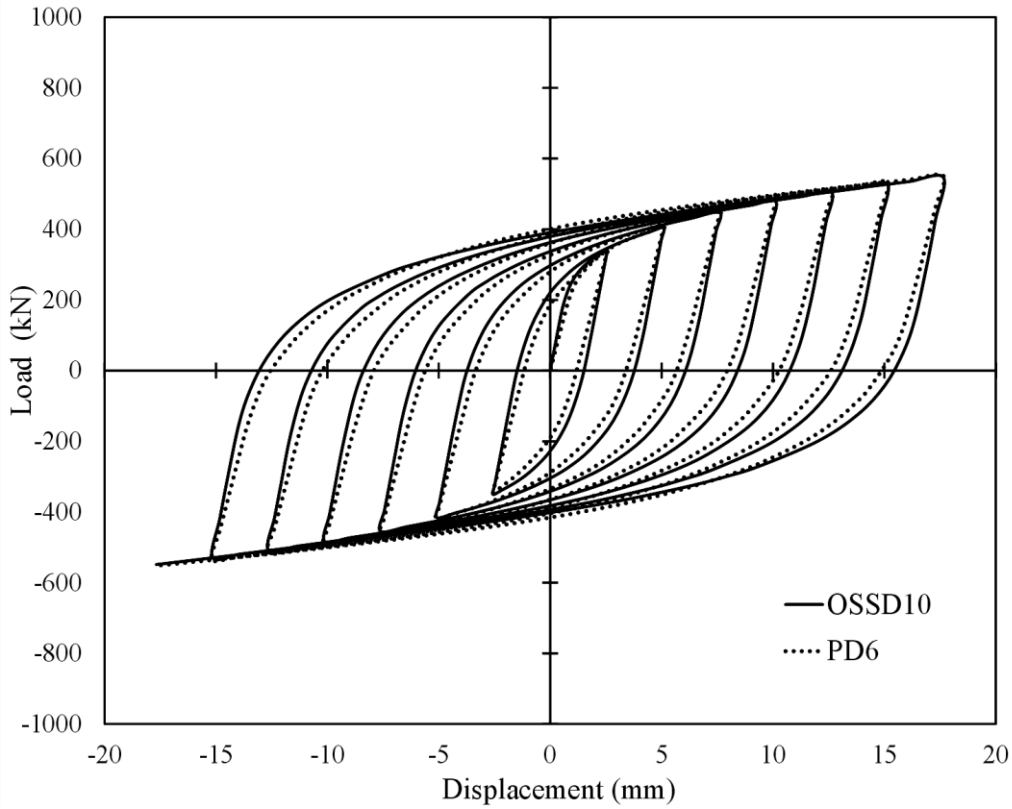

Fig. 5.58: Comparison of hysteretic curves between OSSD7 and PD4 following loading protocol N [*A/B* = 0.5]

The energy dissipation and equivalent PD diameter comparison for different strut widths and thicknesses are illustrated in Figs. 5.59-5.62 respectively.

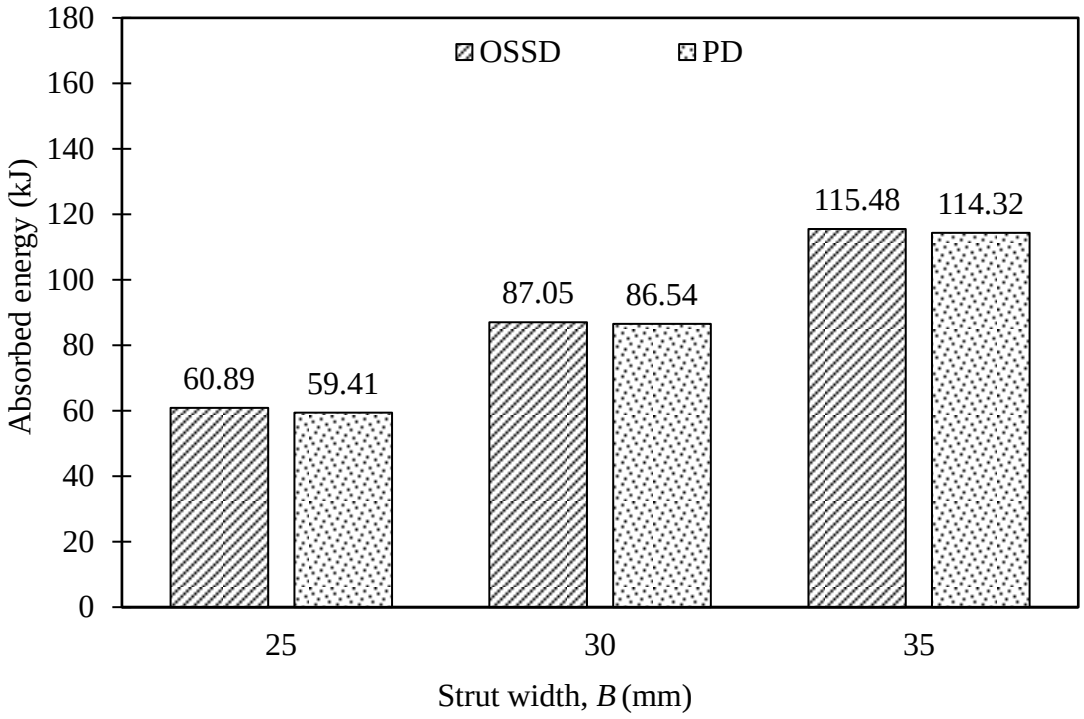

Fig. 5.59: Comparison of absorbed energy between OSSD and PD for different strut widths [*A/B* = 0.5]

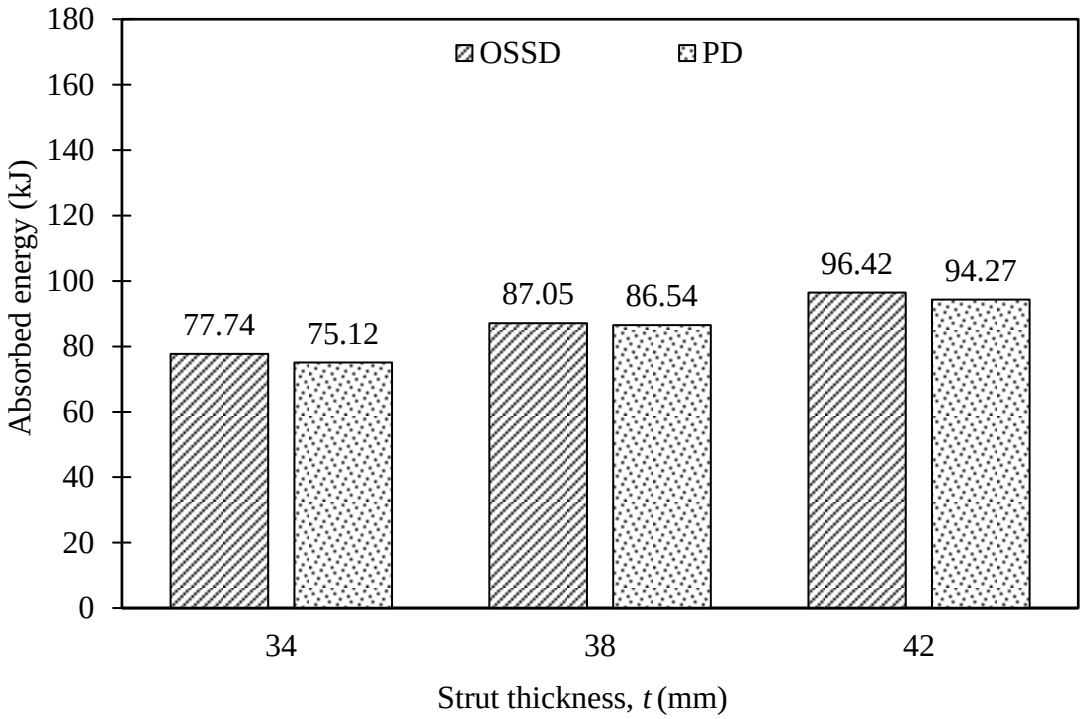

Fig. 5.60: Comparison of absorbed energy between OSSD and PD for different strut thicknesses [*A/B* = 0.5]

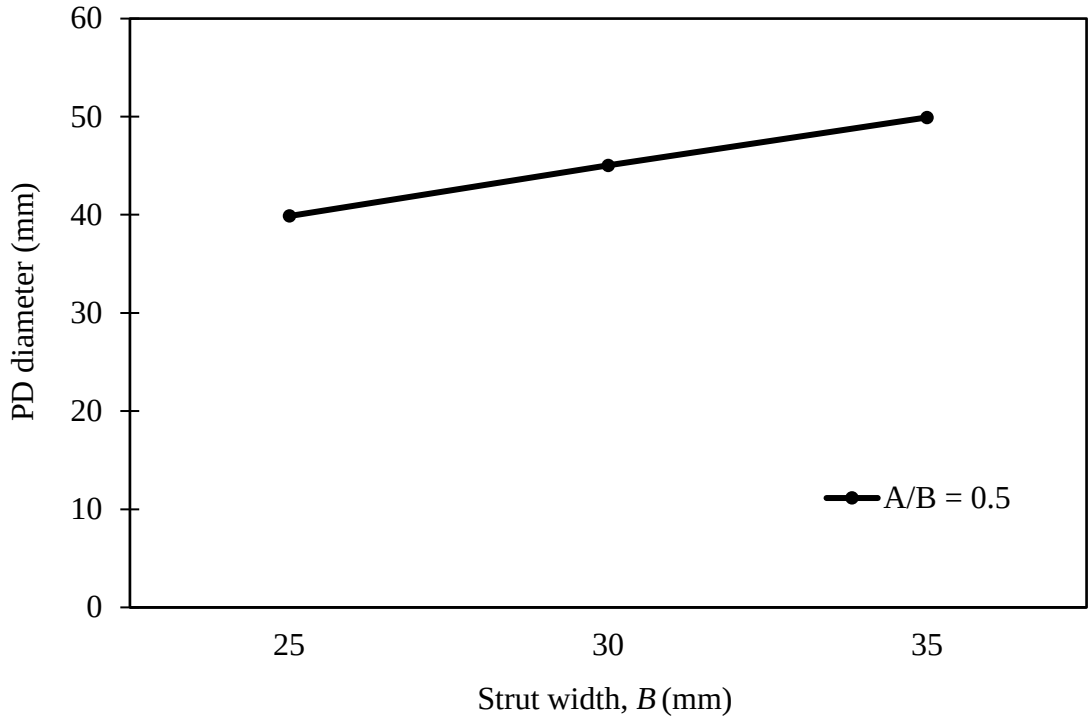

Fig. 5.61: Comparison of PD diameter for different strut widths [*A/B* = 0.5]

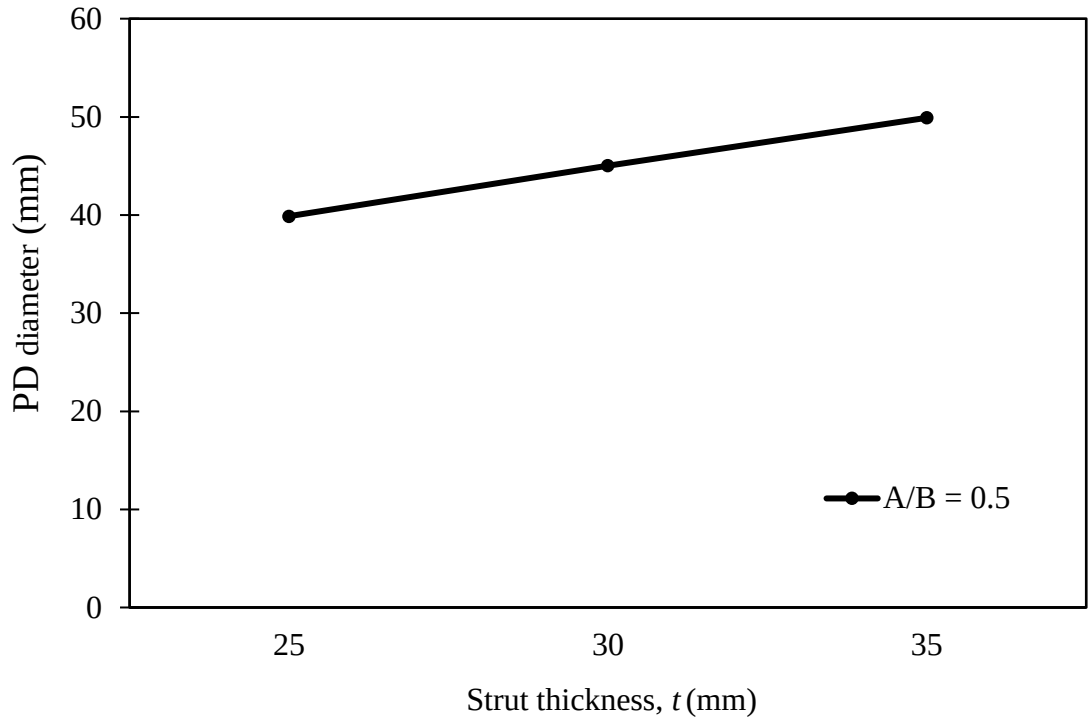

Fig. 5.62: Comparison of PD diameter for different strut thicknesses [*A/B* = 0.5]

It is observed from Figs. 5.59-5.60 that decreasing the strut width and thickness decreases the maximum force in connection and amount of energy dissipation because of increment in stiffness. As observed in Figs. 5.61-5.62, because of the reduction in flexibility increasing the strut width and thickness increases the diameter of equivalent PD.

Therefore, based on the pattern of parametric study results illustrated in Figs. 5.56, 5.61 and 5.62, the yield strength of the PD can be modified analytically as follows:

$$P_y = n \frac{\sigma_y}{3L} [0.884D + 0.0006(L - 130)]^3 \qquad [if\ A/B = 0.5] \qquad (5.12)$$

Here,

P_y = Yield strength

n = Number of Struts

σ_y = Yield stress

t = Thickness

H_T = Total strut height

B = Strut width at end

By solving Eq. (5.12), the parameters of the PD for an equivalent strength of the OSSD can be obtained for the *A/B* = 0.5 ratio. It is clear that Eq. (5.12) sets good agreement for any parameter of PD for *A/B* = 0.5 ratio as observed in Figs. 5.55, 5.59 and 5.60.

Studies are carried out in a similar manner for different *A/B* ratios correspond to *A/B* = 0.5 ratio. In Tables 5.17-5.22 and Figs. 5.63-5.80 the data and results are shown. For simplification, similar types of results are omitted.

Table 5.17: Geometry of OSSD and PD for different strut heights [*A/B* = 0.4]

OSSD					PD				
Specimen	H_T (mm)	*H'* (mm)	*t* (mm)	*B* (mm)	Specimen	H_T (mm)	*L* (mm)	*A* (mm)	*B* (mm)
OSSD2	130	96.15	38	30	PD15	130	120	19.03	47.57
OSSD3	140	105.7	38	30	PD16	140	130	18.78	46.95
OSSD4	150	115.3	38	30	PD17	150	140	18.54	46.36

Table 5.18: Geometry of OSSD and PD for different strut widths [*A/B* = 0.4]

OSSD					PD				
Specimen	*B* (mm)	H_T (mm)	*H'* (mm)	*t* (mm)	Specimen	H_T (mm)	*L* (mm)	*A* (mm)	*B* (mm)
OSSD7	25	140	105.7	38	PD18	140	130	16.63	41.57
OSSD3	30	140	105.7	38	PD16	140	130	18.78	46.95
OSSD8	35	140	105.7	38	PD19	140	130	20.81	52.02

Table 5.19: Geometry of OSSD and PD for different strut thicknesses [*A/B* = 0.4]

OSSD					PD				
Specimen	*t* (mm)	H_T (mm)	*H'* (mm)	*B* (mm)	Specimen	H_T (mm)	*L* (mm)	*A* (mm)	*B* (mm)
OSSD10	34	140	105.7	30	PD20	140	130	18.09	45.24
OSSD3	38	140	105.7	30	PD16	140	130	18.78	46.95
OSSD11	42	140	105.7	30	PD21	140	130	19.42	48.54

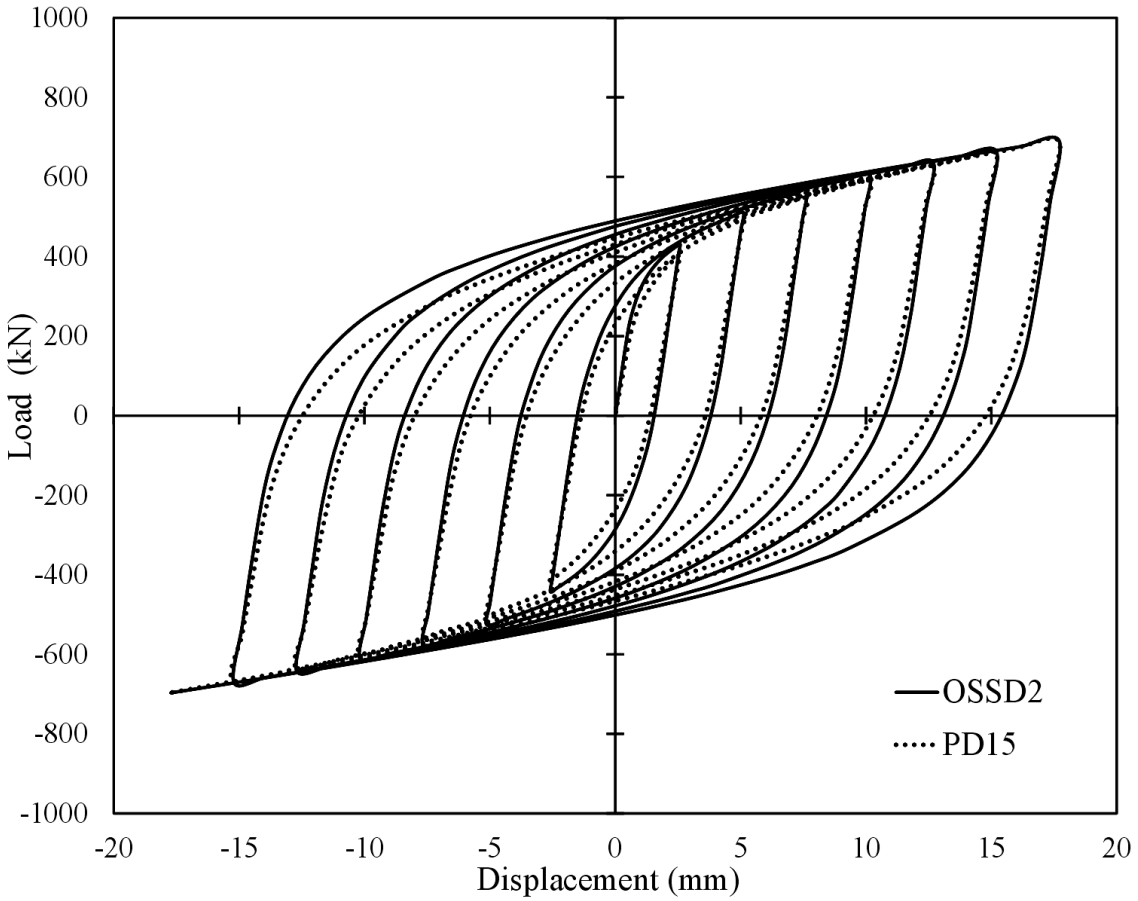

Fig. 5.63: Comparison of hysteretic curves between OSSD2 and PD15 following loading protocol N [*A/B* = 0.4]

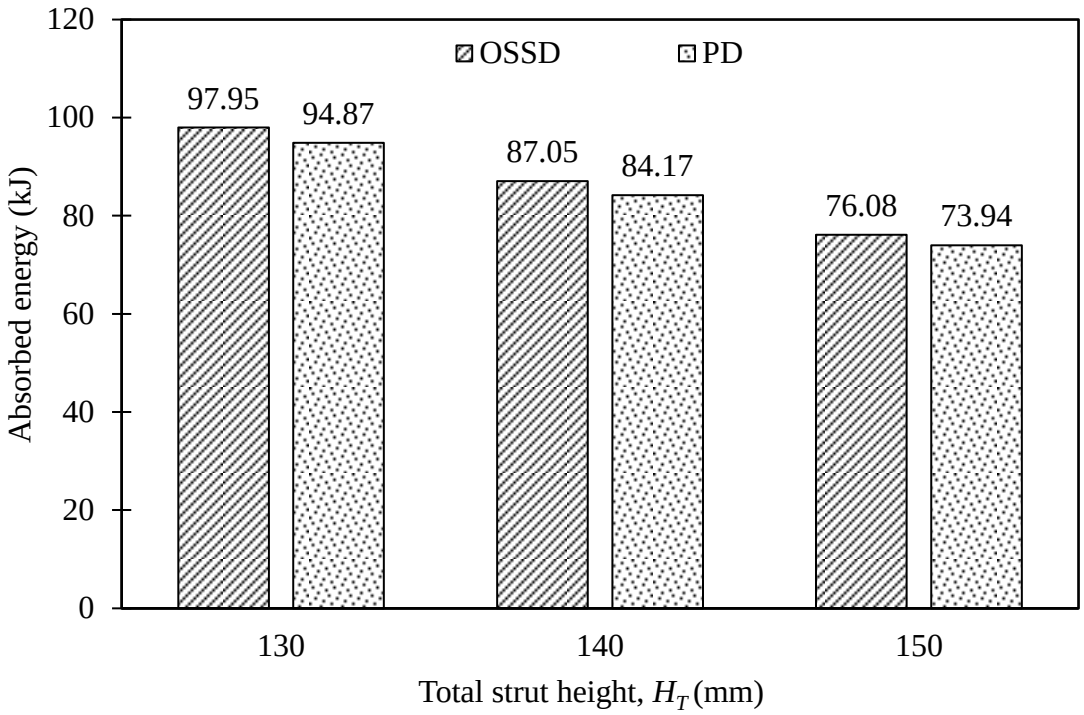

Fig. 5.64: Comparison of absorbed energy between OSSD and PD for different strut heights [*A/B* = 0.4]

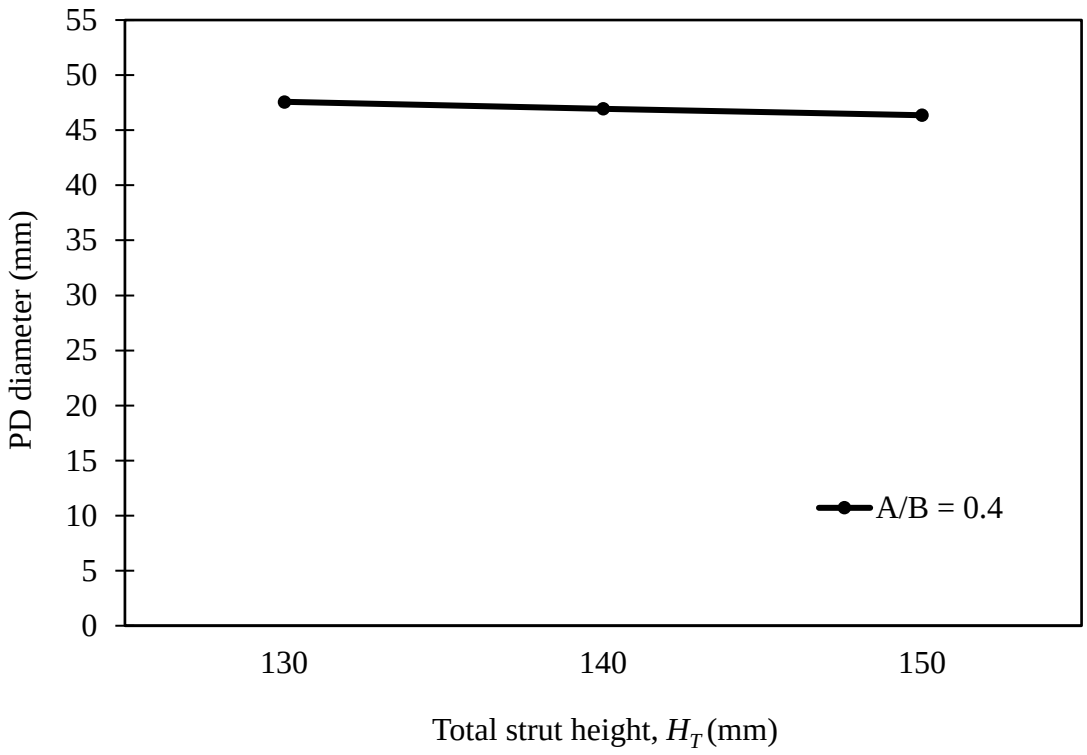

Fig. 5.65: Comparison of PD diameter for different strut heights [*A/B* = 0.4]

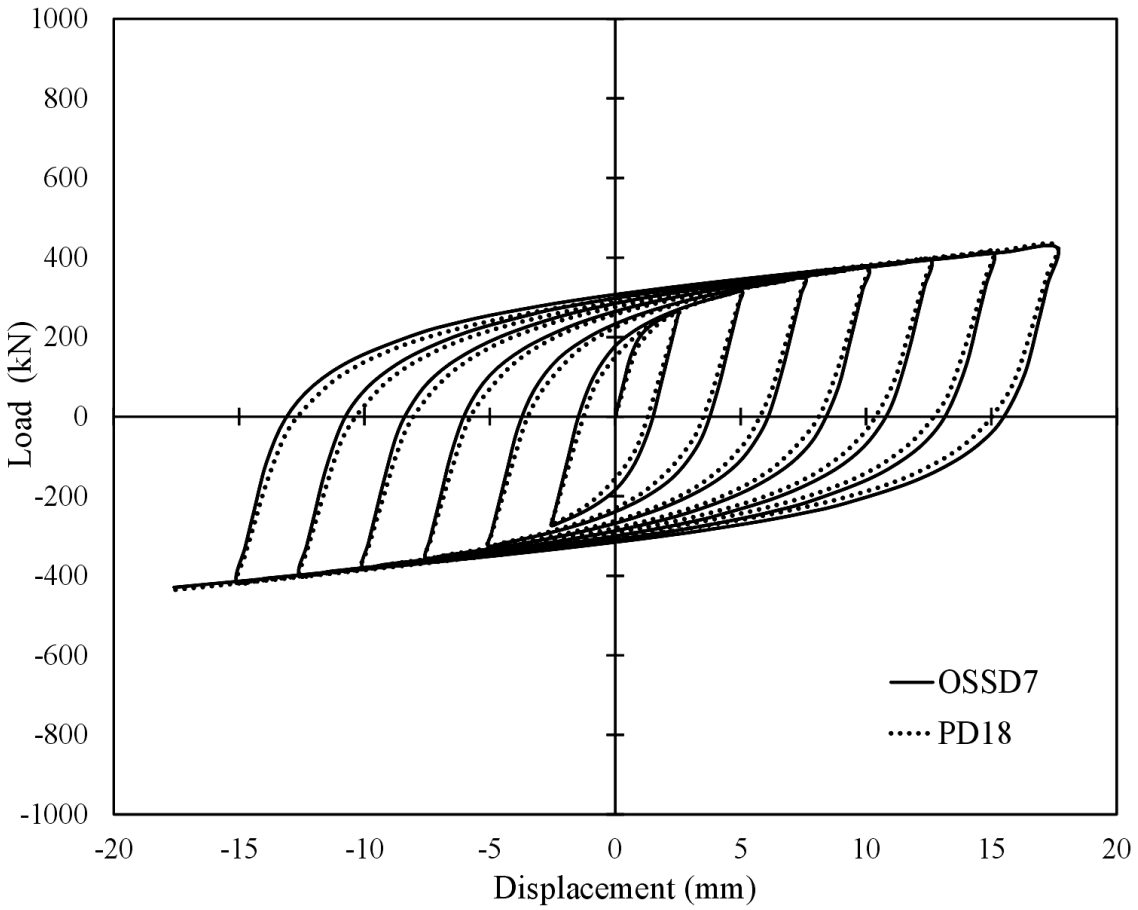

Fig. 5.66: Comparison of hysteretic curves between OSSD7 and PD18 following loading protocol N [*A/B* = 0.4]

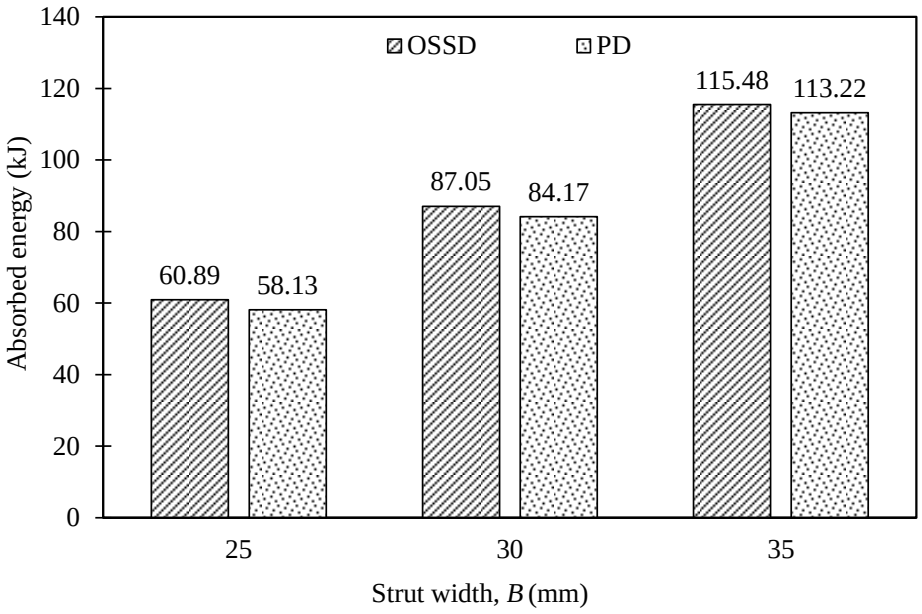

Fig. 5.67: Comparison of absorbed energy between OSSD and PD for different strut widths [*A/B* = 0.4]

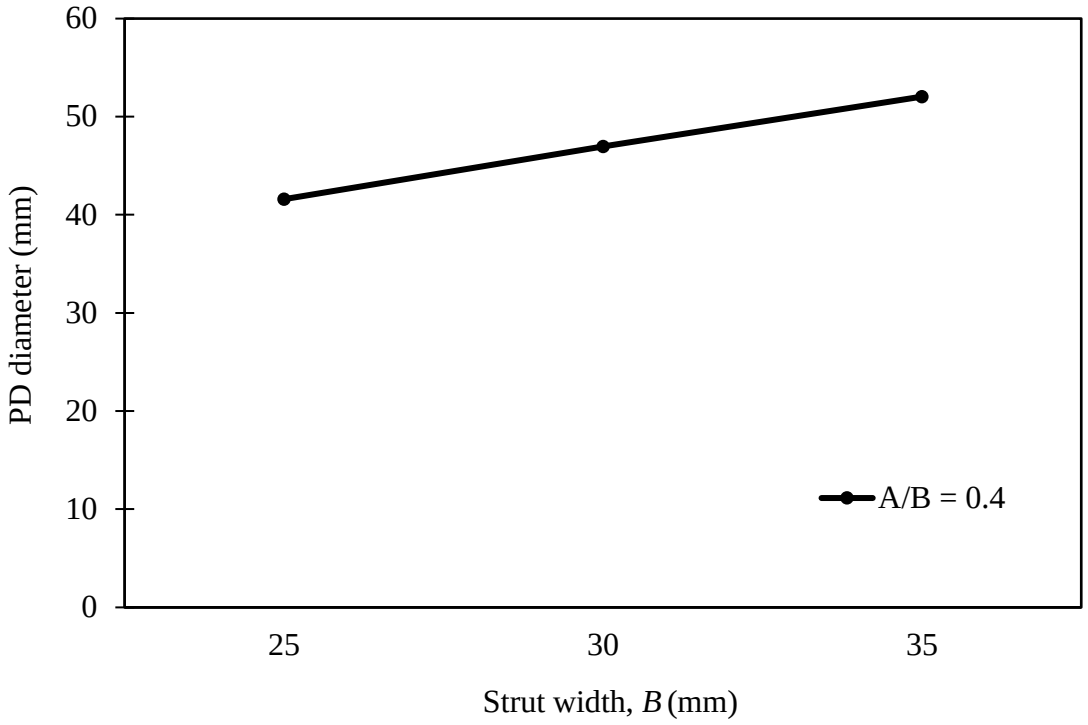

Fig. 5.68: Comparison of PD diameter for different strut widths [*A/B* = 0.4]

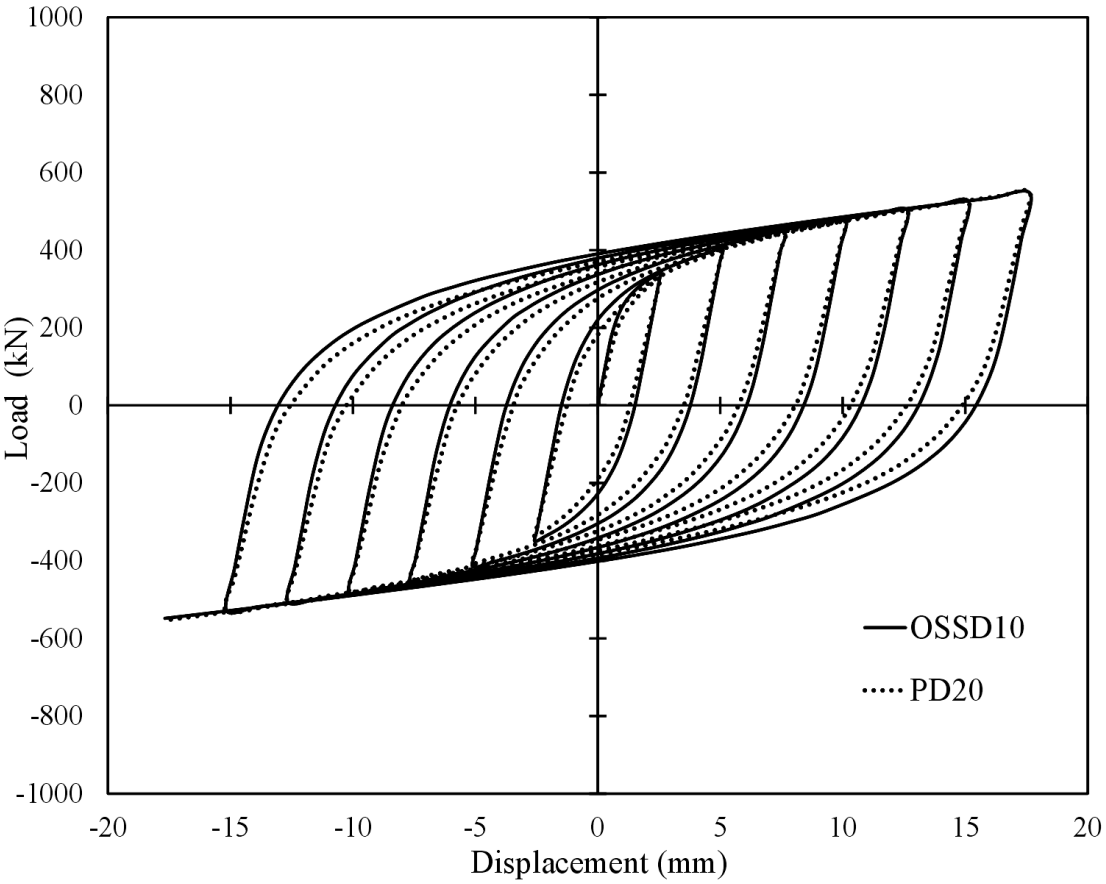

Fig. 5.69: Comparison of hysteretic curves between OSSD10 and PD20 following loading protocol N [*A/B* = 0.4]

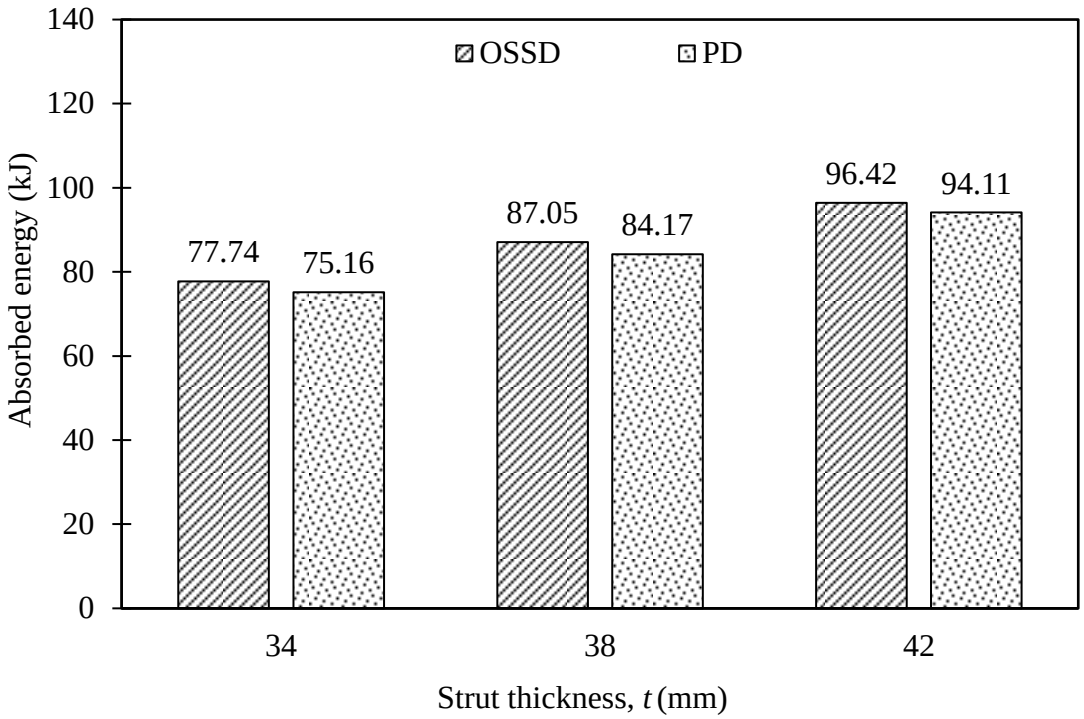

Fig. 5.70: Comparison of absorbed energy between OSSD and PD for different strut thicknesses [*A/B* = 0.4]

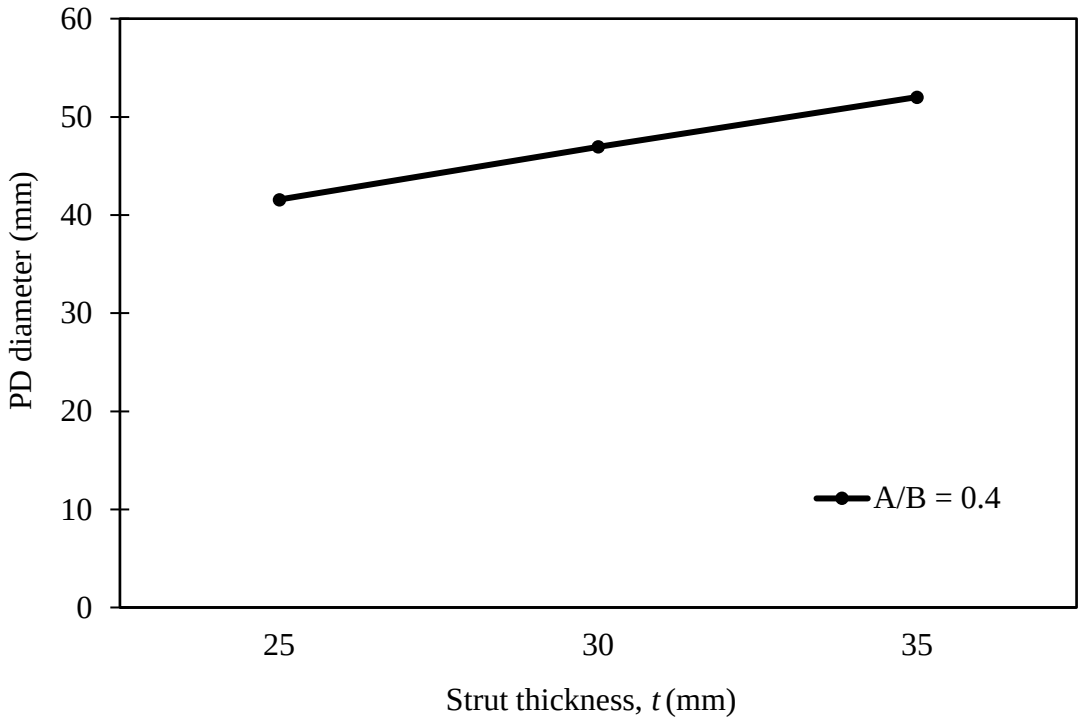

Fig. 5.71: Comparison of PD diameter for different strut thicknesses [*A/B* = 0.4]

Table 5.20: Geometry of OSSD and PD for different strut heights [*A/B* = 0.67]

OSSD					PD				
Specimen	H_T (mm)	H' (mm)	t (mm)	B (mm)	Specimen	H_T (mm)	L (mm)	A (mm)	B (mm)
OSSD2	130	96.15	38	30	PD8	130	120	29.50	44.25
OSSD3	140	105.7	38	30	PD9	140	130	29.26	43.89
OSSD4	150	115.3	38	30	PD10	150	140	29.04	43.56

Table 5.21: Geometry of OSSD and PD for different strut widths [*A/B* = 0.67]

OSSD					PD				
Specimen	B (mm)	H_T (mm)	H' (mm)	t (mm)	Specimen	H_T (mm)	L (mm)	A (mm)	B (mm)
OSSD7	25	140	105.7	38	PD11	140	130	25.91	38.87
OSSD2	30	140	105.7	38	PD9	140	130	29.26	43.89
OSSD8	35	140	105.7	38	PD12	140	130	32.43	48.64

Table 5.22: Geometry of OSSD and PD for different strut thicknesses [*A/B* = 0.67]

OSSD					PD				
Specimen	t (mm)	H_T (mm)	H' (mm)	B (mm)	Specimen	H_T (mm)	L (mm)	A (mm)	B (mm)
OSSD10	34	140	105.7	30	PD13	140	130	28.19	42.29
OSSD3	38	140	105.7	30	PD9	140	130	29.26	43.89
OSSD11	42	140	105.7	30	PD14	140	130	30.25	45.38

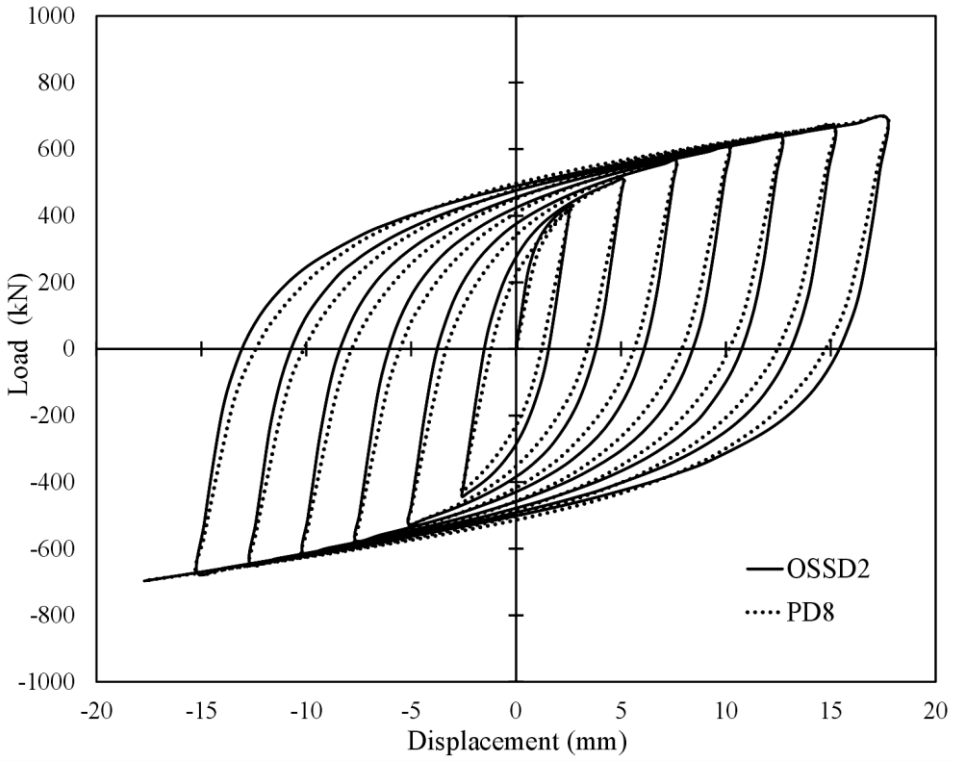

Fig. 5.72: Comparison of hysteretic curves between OSSD2 and PD15 following loading protocol N [*A/B* = 0.67]

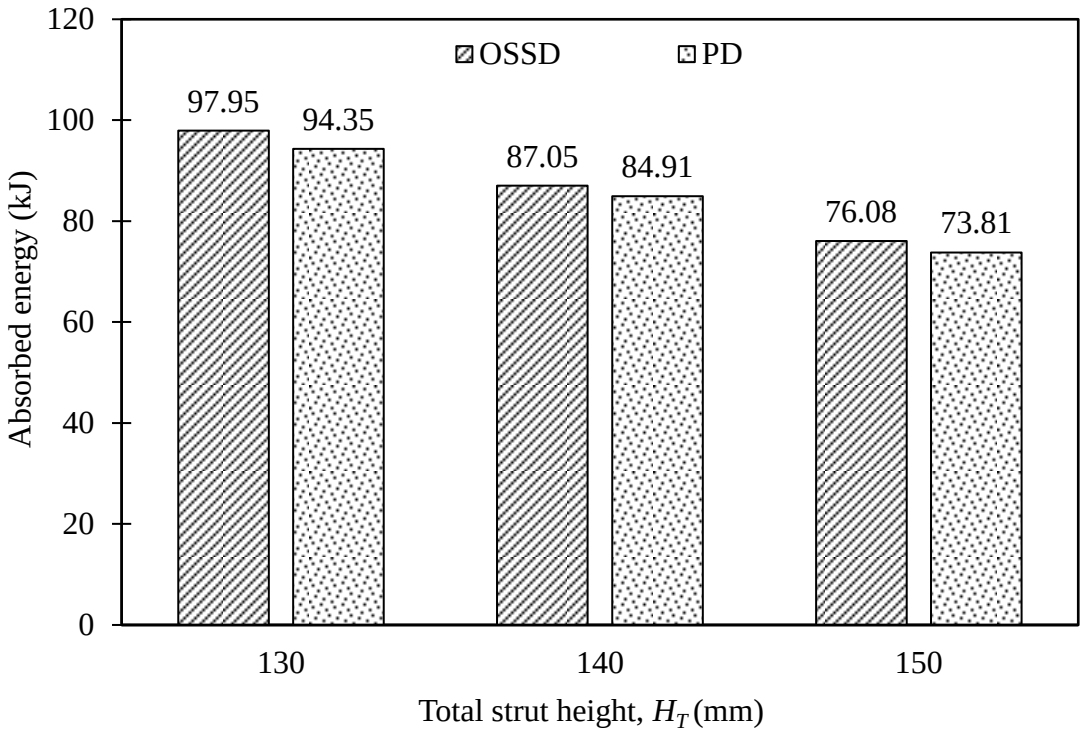

Fig. 5.73: Comparison of absorbed energy between OSSD and PD for different strut heights [*A/B* = 0.67]

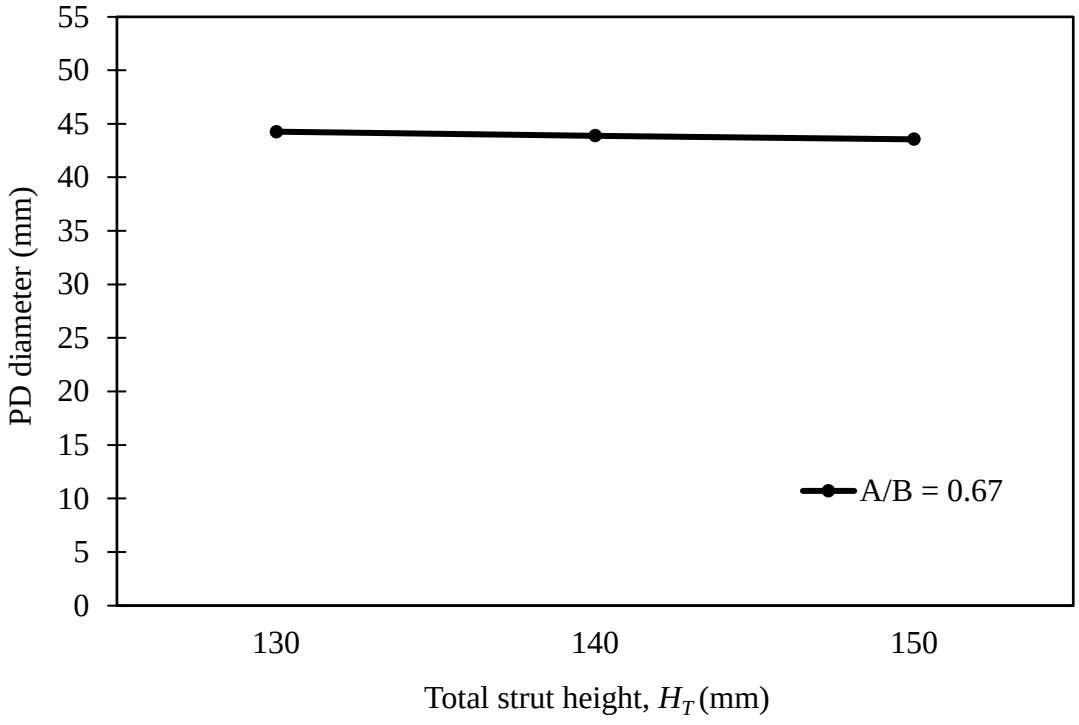

Fig. 5.74: Comparison of PD diameter for different strut heights [*A/B* = 0.67]

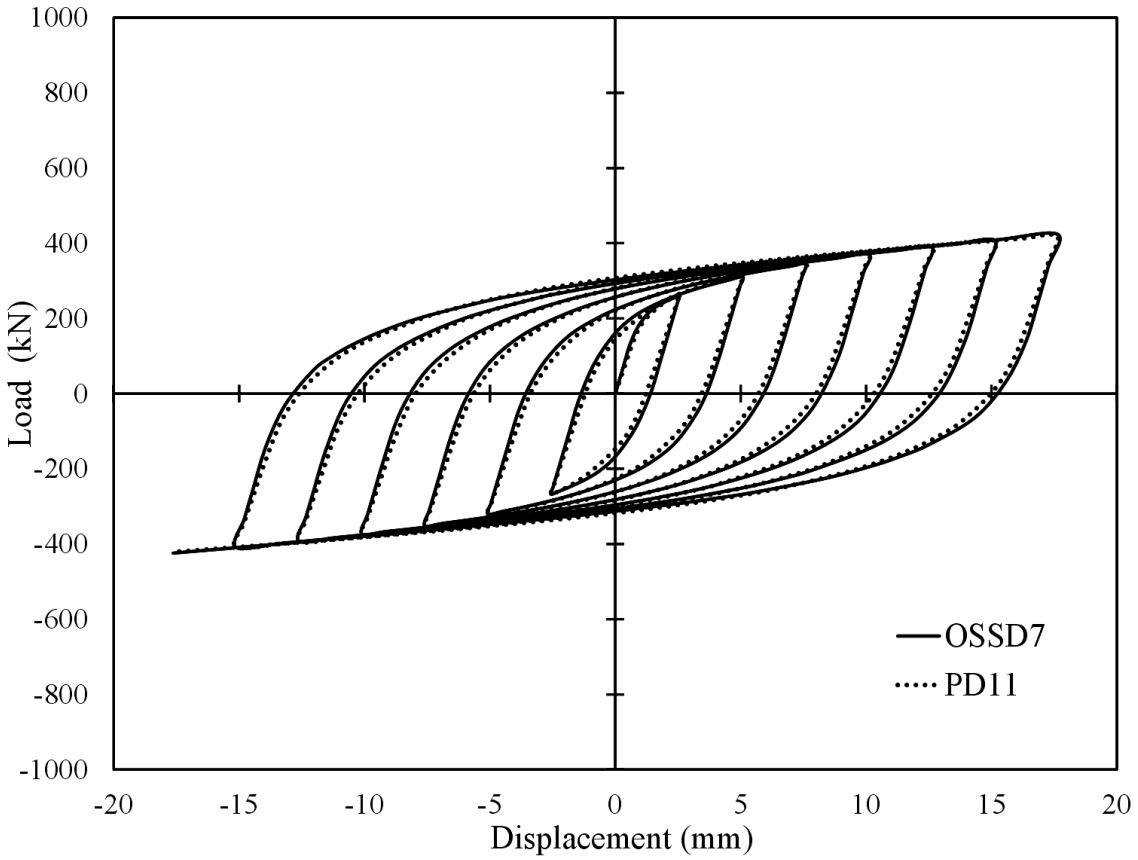

Fig. 5.75: Comparison of hysteretic curves between OSSD7 and PD11 following loading protocol N [*A/B* = 0.67]

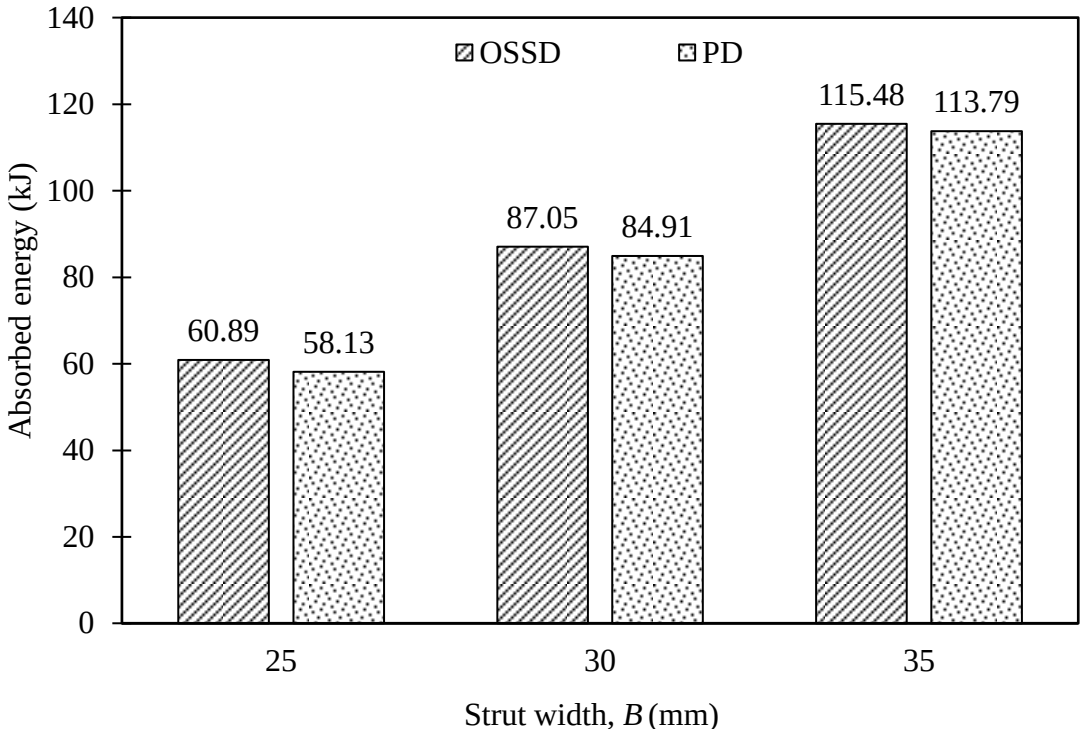

Fig. 5.76: Comparison of absorbed energy between OSSD and PD for different strut widths [*A/B* = 0.67]

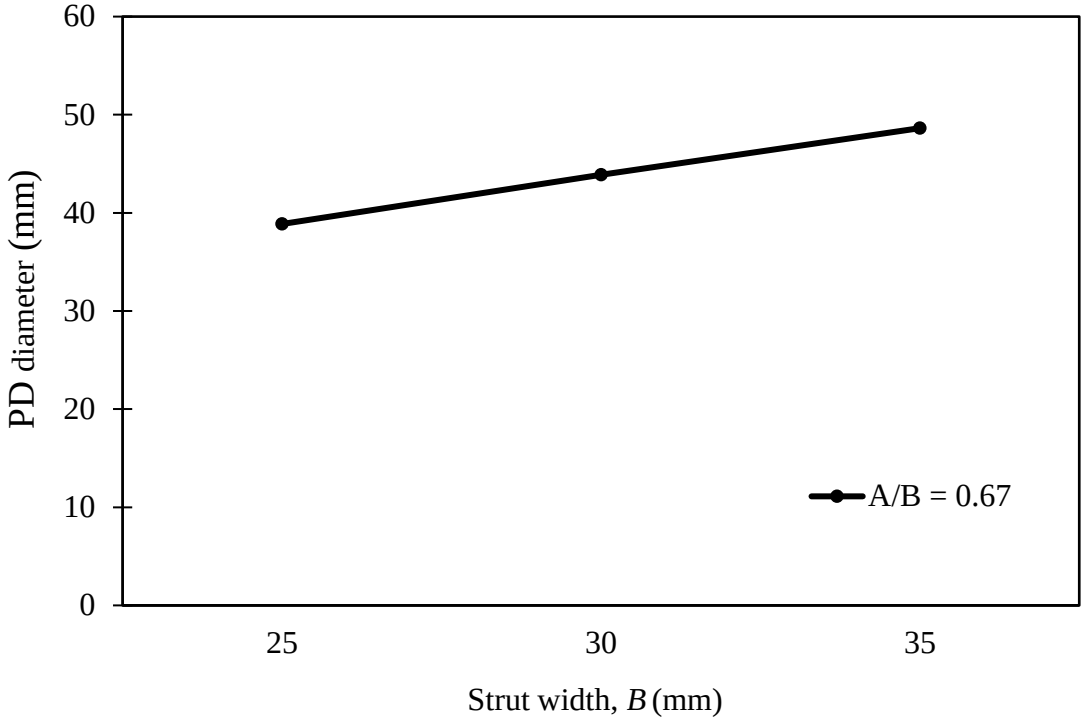

Fig. 5.77: Comparison of PD diameter for different strut widths [*A/B* = 0.67]

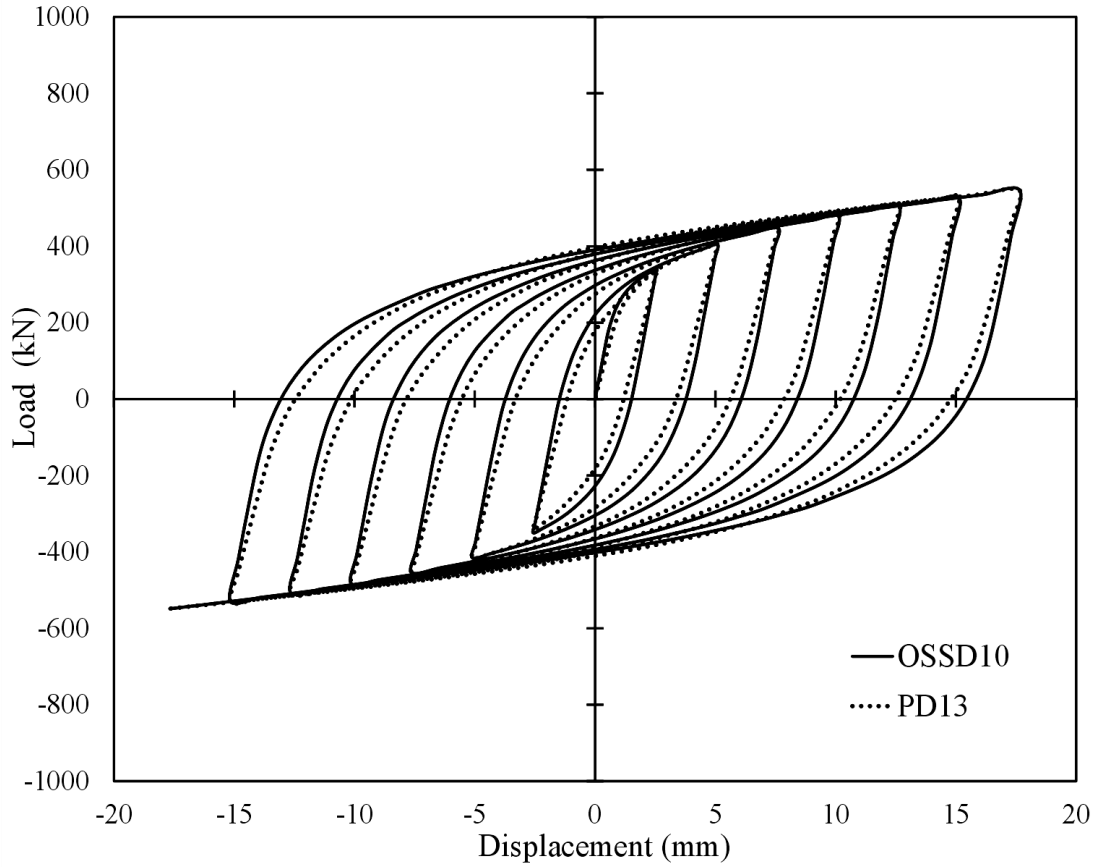

Fig. 5.78: Comparison of hysteretic curves between OSSD10 and PD13 following loading protocol N [*A/B* = 0.67]

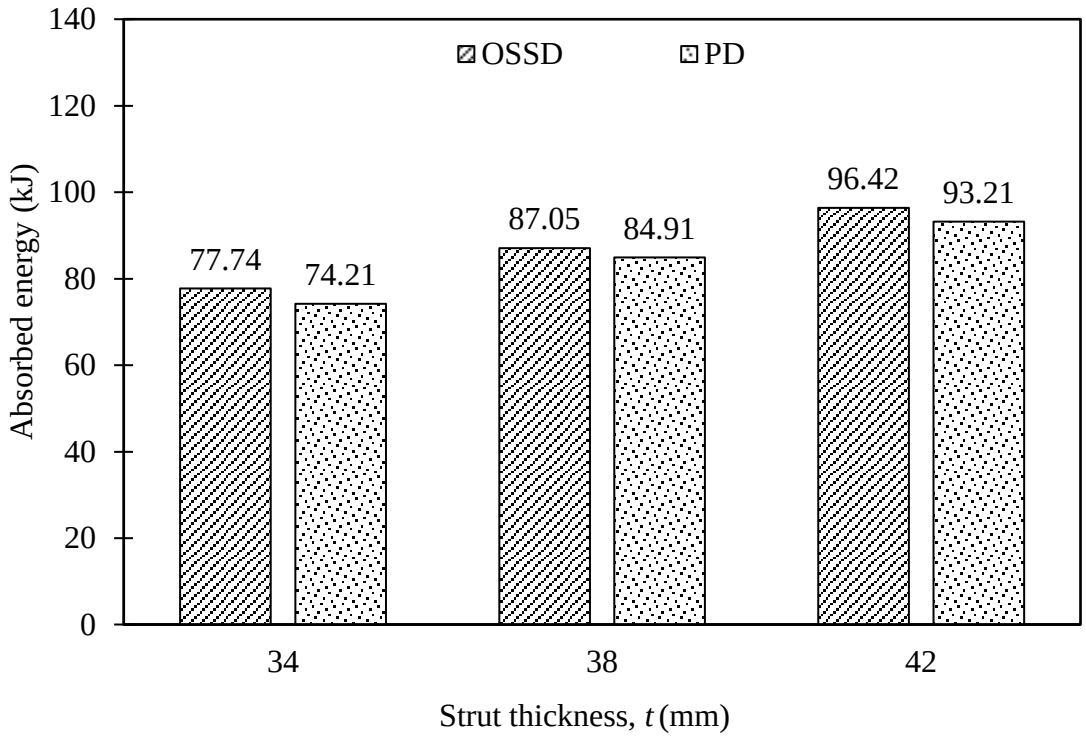

Fig. 5.79: Comparison of absorbed energy between OSSD and PD for different strut thicknesses [*A/B* = 0.67]

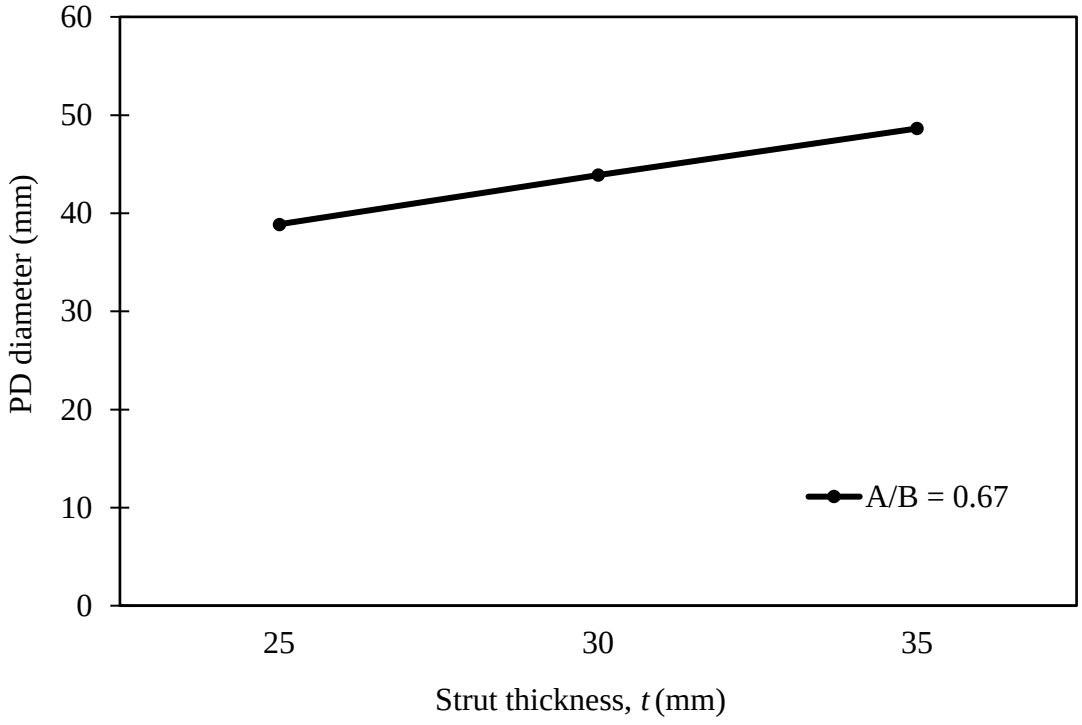

Fig. 5.80: Comparison of PD diameter for different strut thicknesses [*A/B* = 0.67]

Identically, the following equations are developed for PD by observing the pattern of finite element results for *A/B* ratios of 0.4 and 0.67 respectively.

$$P_y = n\,\frac{\sigma_y}{3L}\,[0.848D + 0.0007(L-130)]^3 \qquad [if\ A/B = 0.4] \qquad (5.13)$$

$$P_y = n\,\frac{\sigma_y}{3L}\,[0.907D + 0.0003(L-130)]^3 \qquad [if\ A/B = 0.67] \qquad (5.14)$$

It is distinct from Figs. 5.63-5.80 that the Eqs. (5.13) and (5.14) hold perfect for different *A/B* ratios of PD.

It is noticed from Eqs. 5.12-5.14 that, for different *A/B* ratios of PD the coefficient of pintle diameter and pintle height varies in the Eqs. which are depicted in Figs. 5.81 and 5.82 named as α and β respectively.

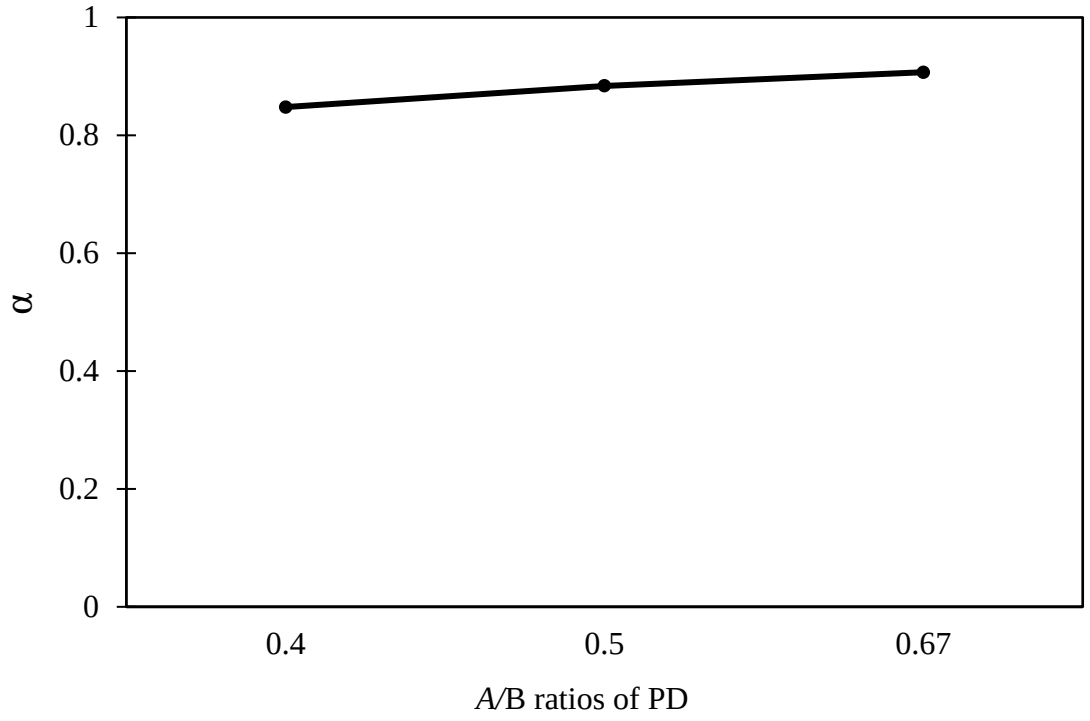

Fig. 5.81: Variation of pintle diameter coefficient for different *A/B* ratios of PD

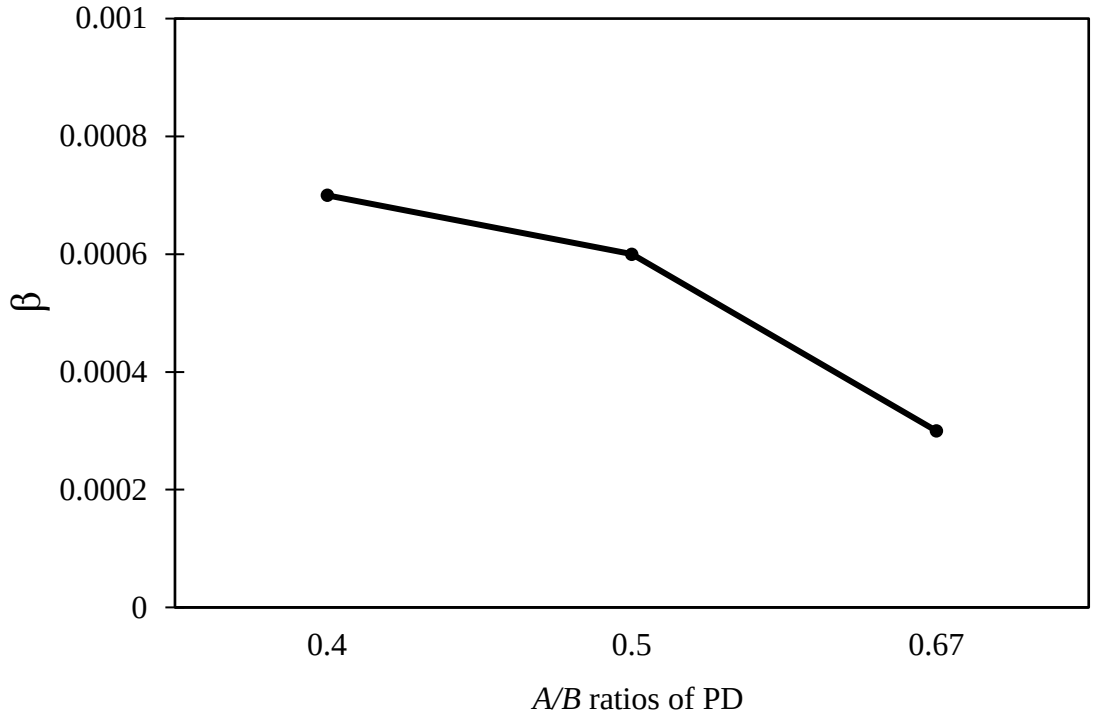

Fig. 5.82: Variation of pintle height coefficient for different *A/B* ratios of PD

Therefore, the plastic strength formula of the PD can be expressed analytically in general by combining Eqs. (5.12), (5.13) and (5.14) as:

$$P_y = n \frac{\sigma_y}{3L} [\alpha D + \beta(L - 130)]^3 \quad (5.15)$$

where

$$\alpha = \begin{cases} 0.884 + 0.135\left(\frac{A}{B} - 0.5\right) & [if\ A/B \geq 0.5] \\ 0.884 + 0.36\left(\frac{A}{B} - 0.5\right) & [if\ A/B < 0.5] \end{cases}$$

and

$$\beta = \begin{cases} 0.0006 + 0.0018\left(0.5 - \frac{A}{B}\right) & [if\ A/B \geq 0.5] \\ 0.0006 + 0.001\left(0.5 - \frac{A}{B}\right) & [if\ A/B < 0.5] \end{cases}$$

Therefore, the plastic strength of the PD for any geometry can be obtained using the developed Eq. (5.15).

5.3 REMARKS

It can be concluded from the study presented in this section that the proposed equations for elliptical steel slit damper (ESSD), butterfly-shaped steel strut damper (BSSD) and pintle damper (PD) can now be used to calculate the plastic strength of these with acceptable accuracy for any geometry. Therefore, oblong steel slit damper (OSSD), elliptical steel slit damper (ESSD), butterfly-shaped steel strut damper (BSSD) and pintle damper (PD) can now be used in replacement of others at seismic moment connections using the developed plastic strength formula.

CHAPTER 6
PERFORMANCE VERIFICATION OF THE PROPOSED EQUATIONS FOR DAMPERS

6.1 PERFORMANCE OF EQUIVALENT DAMPERS ON BEAM-COLUMN CONNECTION

Many researches have been carried out with different types of shear dampers. The main objective of the study described in section 5.2 is to find the equivalency among different types of shear dampers. The equivalent dampers are developed for elliptical steel slit damper (ESSD), butterfly-shaped steel strut damper (BSSD) and pintle damper (PD) with respect to the plastic strength of the oblong steel slit damper (OSSD). To make equivalent, the plastic strength formula of the ESSD, BSSD and PD are modified.

So, by using the developed equation the OSSD, ESSD, BSSD and PD can now be alternately used in seismic moment connection. The dampers are used in moment connection to dissipate energy before other structural members in the event of an earthquake. So the developed equivalent dampers are used in beam-column connection of Oh et al. (2009) to observe the behavior of the dampers.

The equivalent ESSD, BSSD and PD are modeled in the beam-column connection of Oh et al. (2009) replacing the OSSD specimen D1 using finite element software. The finite element models and deformed shapes of the ESSD, BSSD and PD are illustrated in Figs. 6.1-6.6 respectively. It is observed from Figs. 6.2, 6.4 and 6.6 respectively that the ESSD, BSSD and PD yield before the other members of the system and show the expected behavior of an energy dissipation device. It is distinct that the energy dissipation is concentrated only at the shear dampers and nothing is happened to the beam and column.

The moment vs. rotation curves are obtained from finite element analysis of the beam-column connection with the OSSD, ESSD, BSSD and PD which are illustrated in Fig. 6.7. As observed in Fig. 6.7, the equivalent dampers ESSD, BSSD and PD show stable hysteretic behavior like OSSD specimen D1 of Oh et al. (2009) in the beam-column connection.

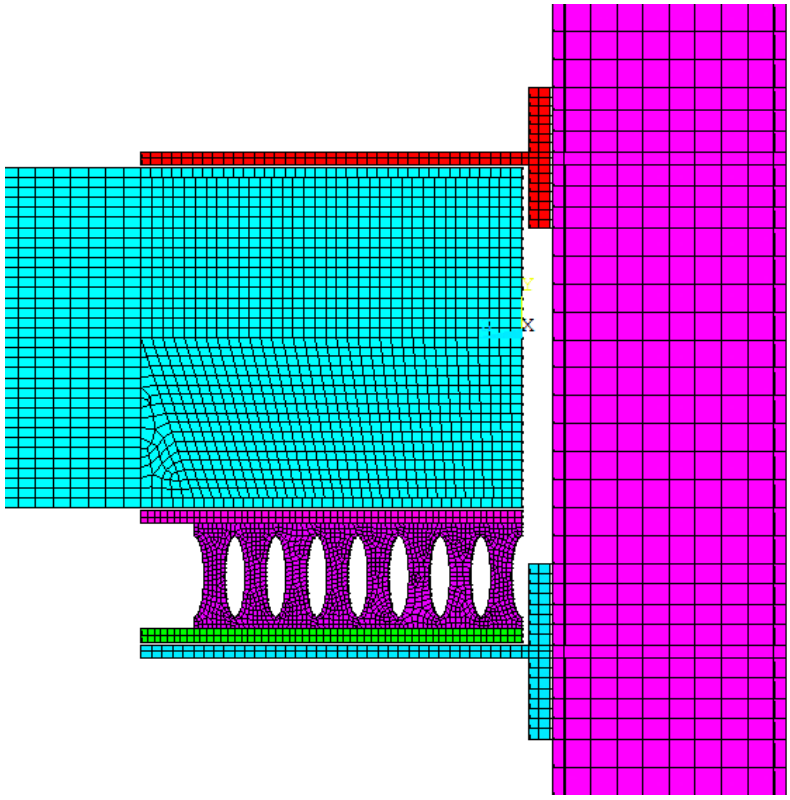

Fig. 6.1: Beam-column connection with elliptical steel slit damper

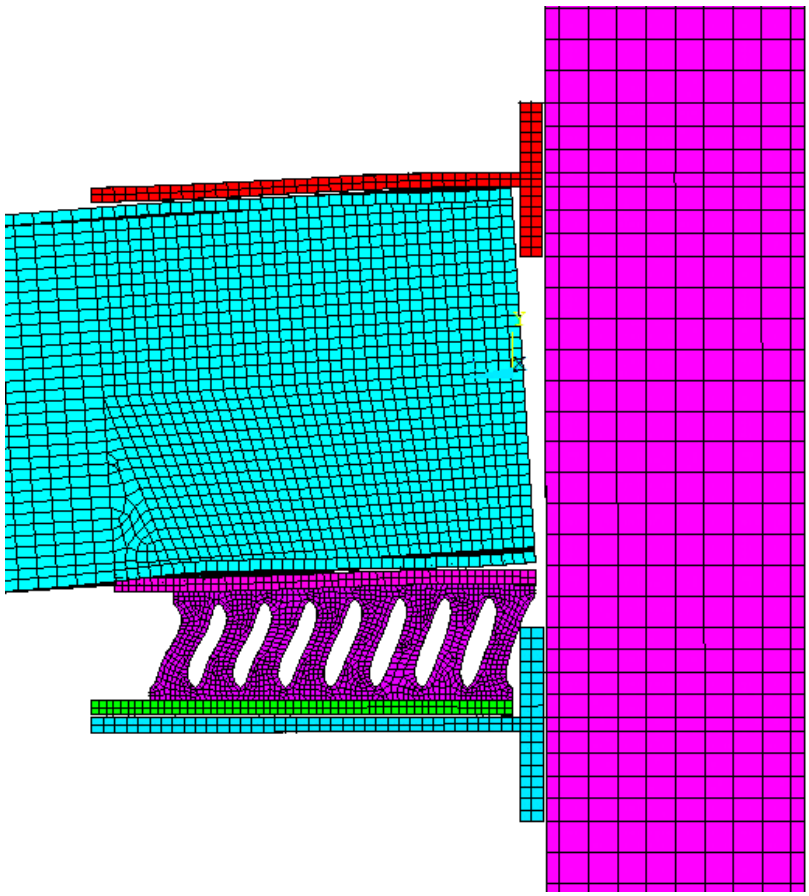

Fig. 6.2: Deformed shape of the elliptical steel slit damper

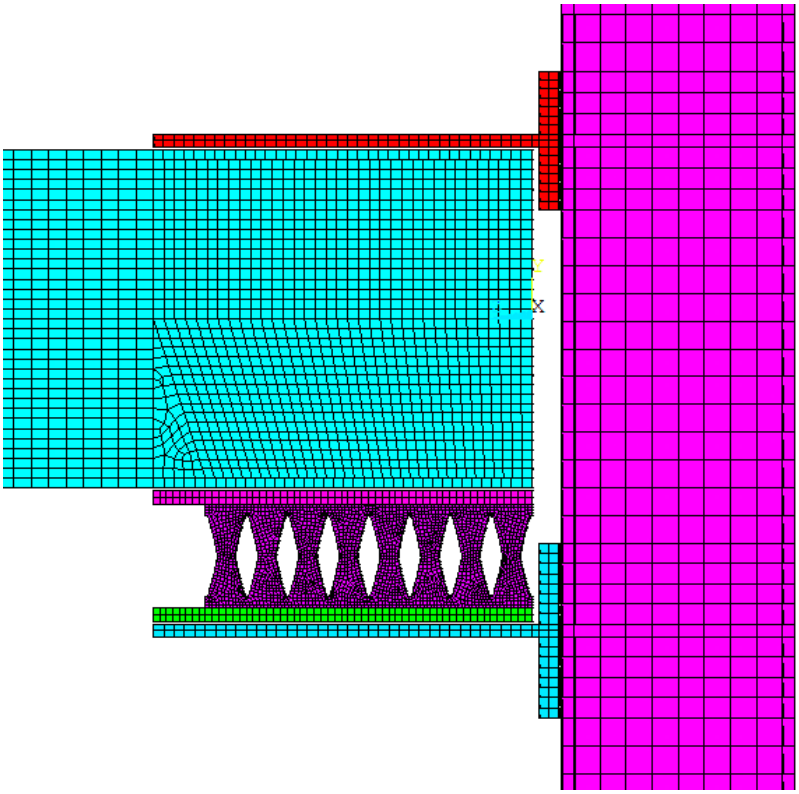

Fig. 6.3: Beam-column connection with butterfly-shaped steel strut damper

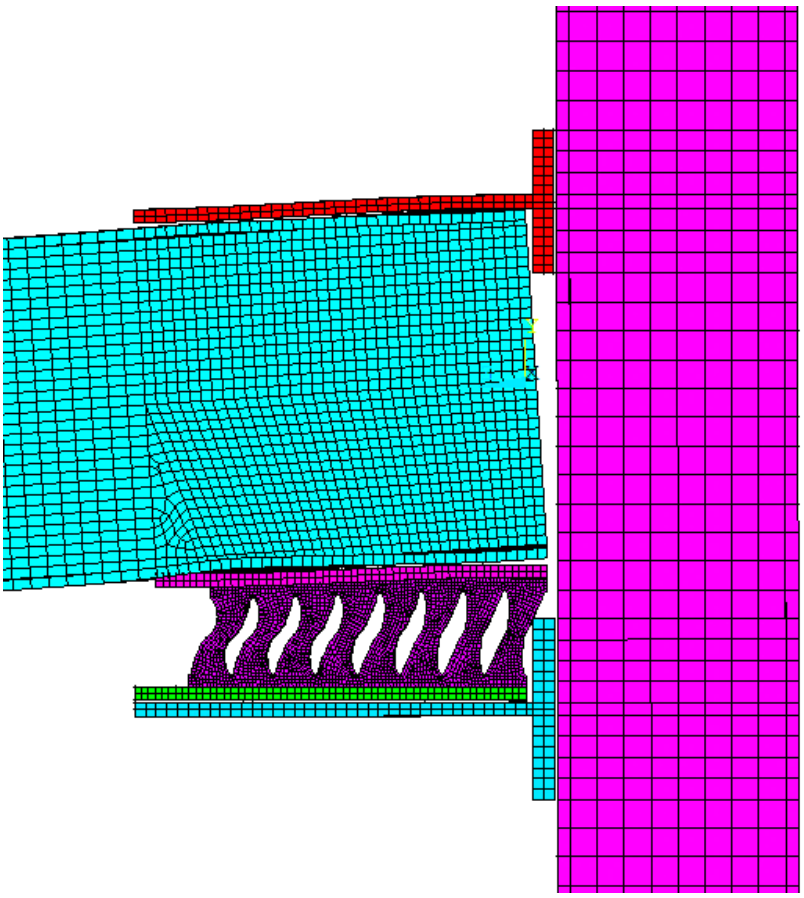

Fig. 6.4: Deformed shape of the butterfly-shaped steel strut damper

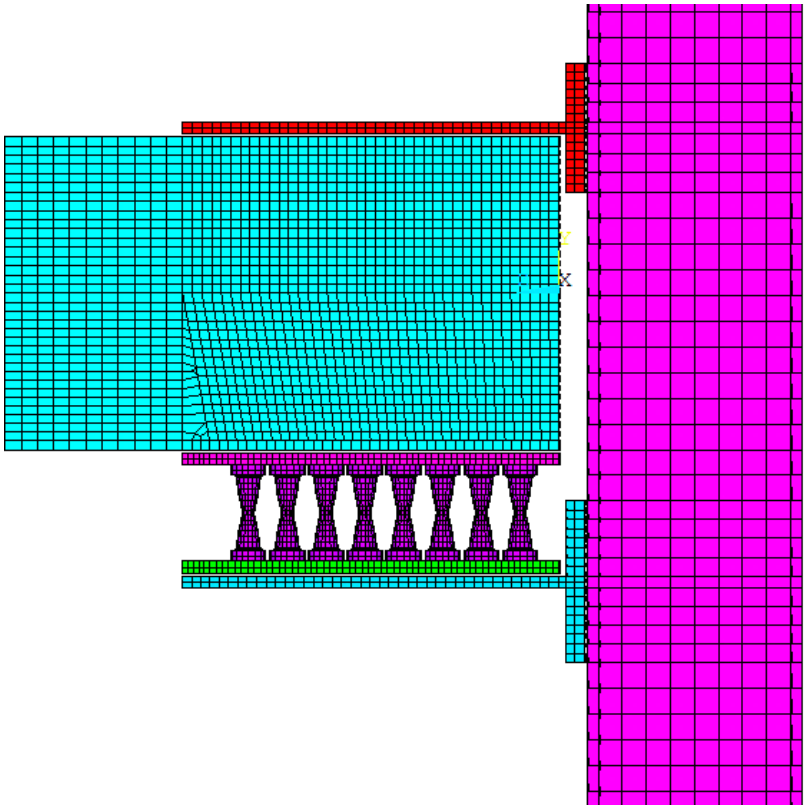

Fig. 6.5: Beam-column connection with pintle damper

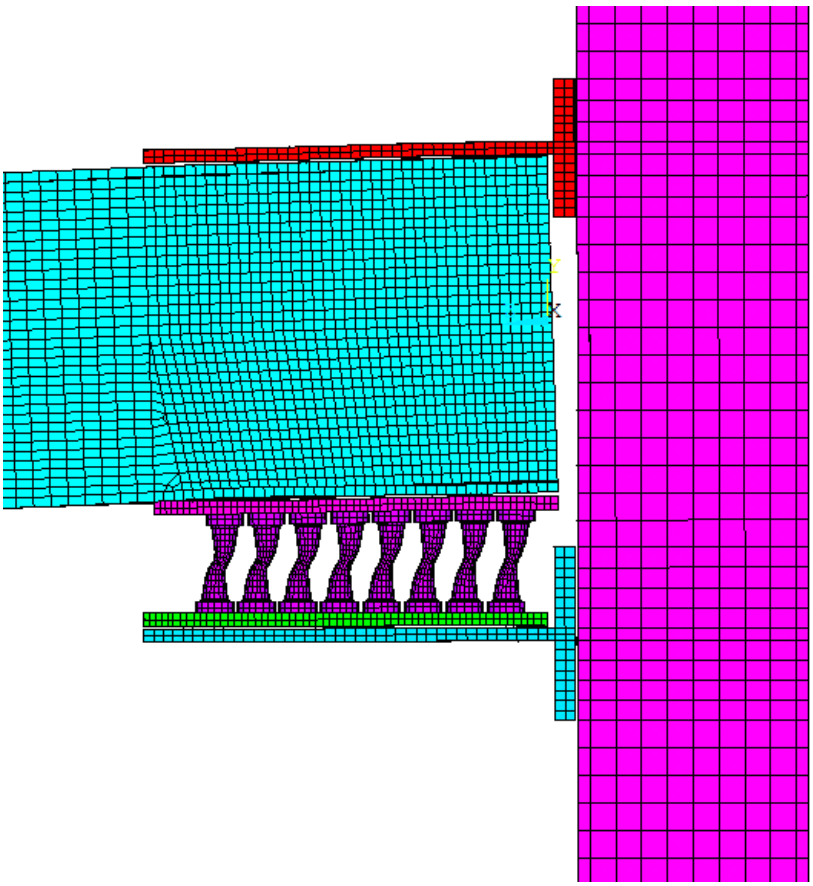

Fig. 6.6: Deformed shape of the pintle damper

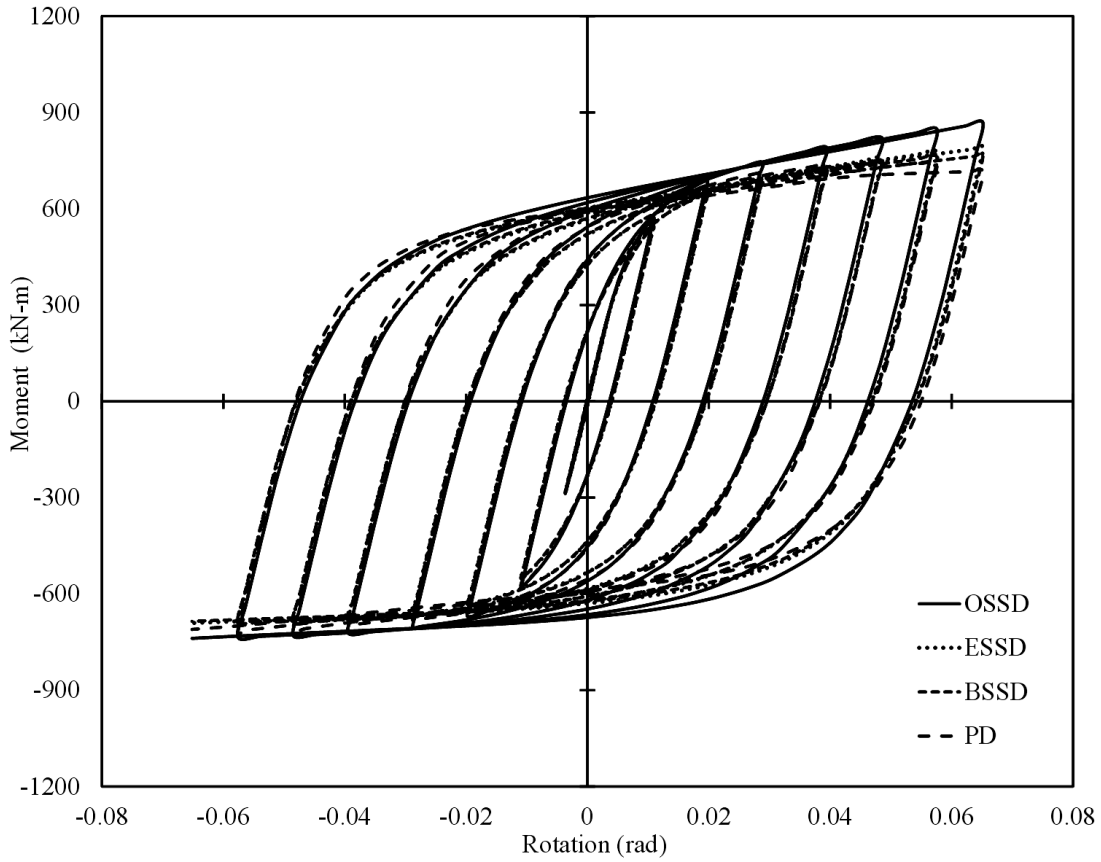

Fig. 6.7: Comparison of hysteretic curves among different steel shear dampers of different geometry in beam-column connection of Oh et al. (2009) following loading protocol D1

Therefore, the equivalent dampers of different geometry can be alternatively used at moment connection design using the developed plastic strength formula to serve the purposes of energy dissipation effectively.

6.2 VERIFICATION OF PROPOSED EQUATIONS FOR DIFFERENT PLASTIC STRENGTH OF DAMPERS

Based on the plastic strength of the oblong steel slit damper (OSSD), the plastic strength equations of elliptical steel slit damper (ESSD), butterfly-shaped steel strut damper (BSSD) and pintle damper (PD) are modified to make equivalency among them so that they can be used alternatively at beam-column connection. In order to validate these formulations, the moment vs. rotation behaviors of the equivalent dampers are investigated in this section for different plastic strength of the dampers in beam-column connection of Oh et al. (2009) following loading protocol D1. For simplification, only the thickness or diameter is varied corresponding to the plastic strength of the dampers and the *A/B* ratio is kept 0.5. The

necessary data are listed in Table 6.1 where the thicknesses of OSSD, ESSD, BSSD are obtained using Eqs. 5.1, 5.7, 5.15 respectively and the diameters of PD are found from Eq. 5.15. The moment vs. rotation curves for different plastic strengths of the dampers are illustrated in Figs. 6.8-6.12.

Table 6.1: Thickness of equivalent dampers for different plastic strengths

Plastic strength of the damper, P_y (kN)	Thickness, t (mm)			Diameter at end, B (mm)
	OSSD	ESSD	BSSD	PD
200	28.23	14.26	12.07	40.79
250	35.29	17.83	15.09	43.94
300	42.35	21.39	18.11	46.69
350	49.41	24.96	21.13	49.15
400	56.46	28.52	24.14	51.39

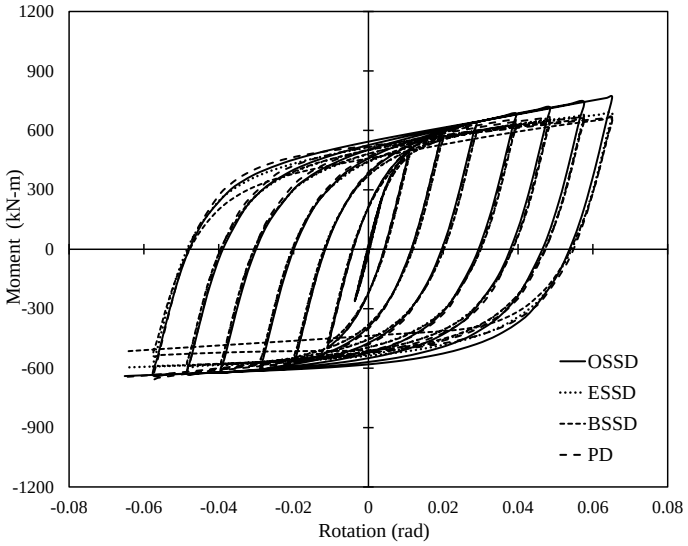

Fig. 6.8: Comparison of hysteretic curves among equivalent dampers for P_y = 200 kN

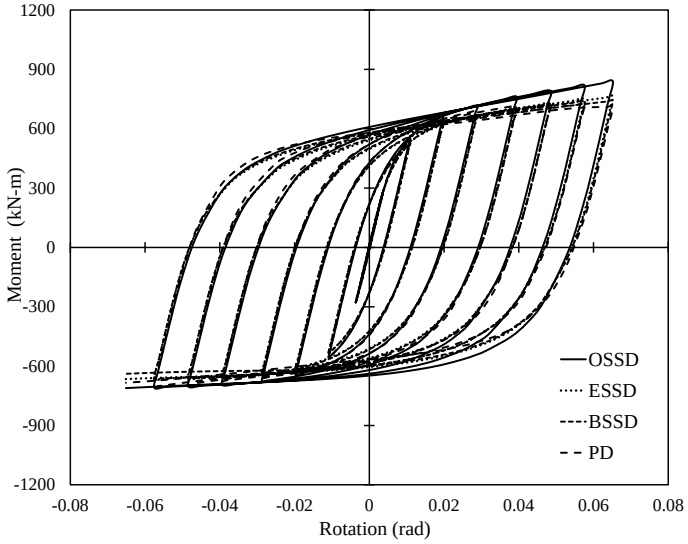

Fig. 6.9: Comparison of hysteretic curves among equivalent dampers for P_y = 250 kN

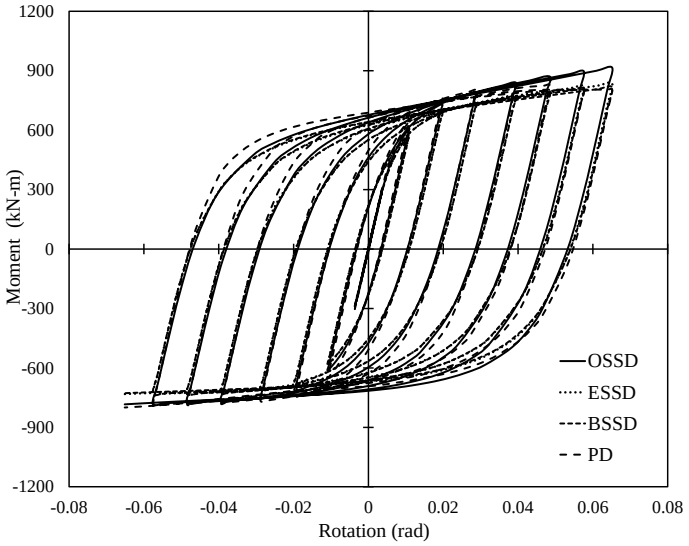

Fig. 6.10: Comparison of hysteretic curves among equivalent dampers for P_y = 300 kN

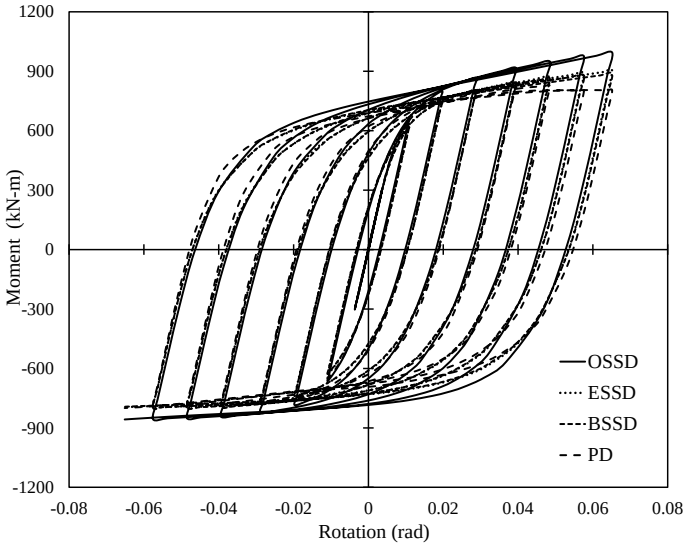

Fig. 6.11: Comparison of hysteretic curves among equivalent dampers for P_y = 350 kN

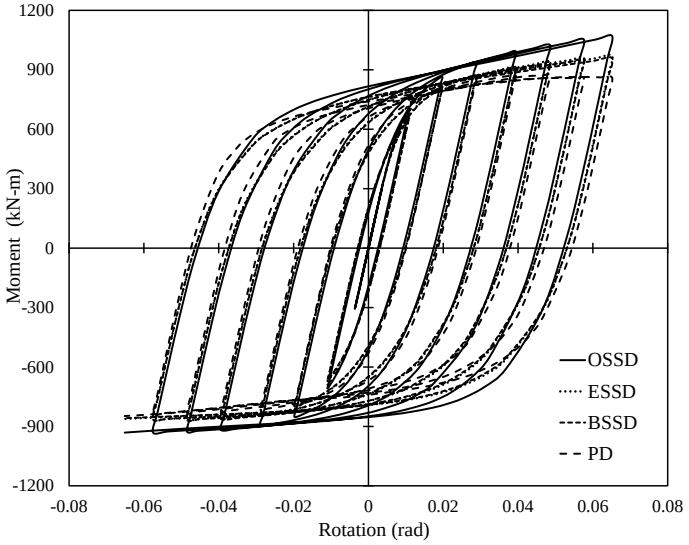

Fig. 6.12: Comparison of hysteretic curves among equivalent dampers for P_y = 400 kN

From Figs. 6.8-6.12, it is distinct that the proposed plastic strength equations for elliptical steel slit damper (ESSD), butterfly-shaped steel strut damper (BSSD) and pintle damper (PD) perform well for different plastic strength since these dampers show stable hysteretic behavior and adequate energy absorption capacity like the oblong steel slit damper (OSSD). Therefore, it can be concluded that the developed equations for elliptical steel slit damper (ESSD), butterfly-shaped steel strut damper (BSSD) and pintle damper (PD) can be used in the design of moment connection to calculate the plastic strength of the dampers with more precision.

6.3 COMPARISON OF EQUIVALENT DAMPING RATIO FOR DIFFERENT TYPES OF SHEAR DAMPERS

6.3.1 Equivalent Damping Ratio

Equivalent damping ratio (ε_{eq}) for the specimens is calculated from the force-displacement hysteretic curves as shown in Fig. 6.13 and as expressed in Eq. (6.1): (Shahri and Mousavi 2018)

$$\varepsilon_{eq} = \frac{E_D}{4\pi E_{S0}} \tag{6.1}$$

where E_D is dissipated energy in the last loading cycle which can be achieved from the area within the closed hysteretic loop, as shown in Fig. 6.13.

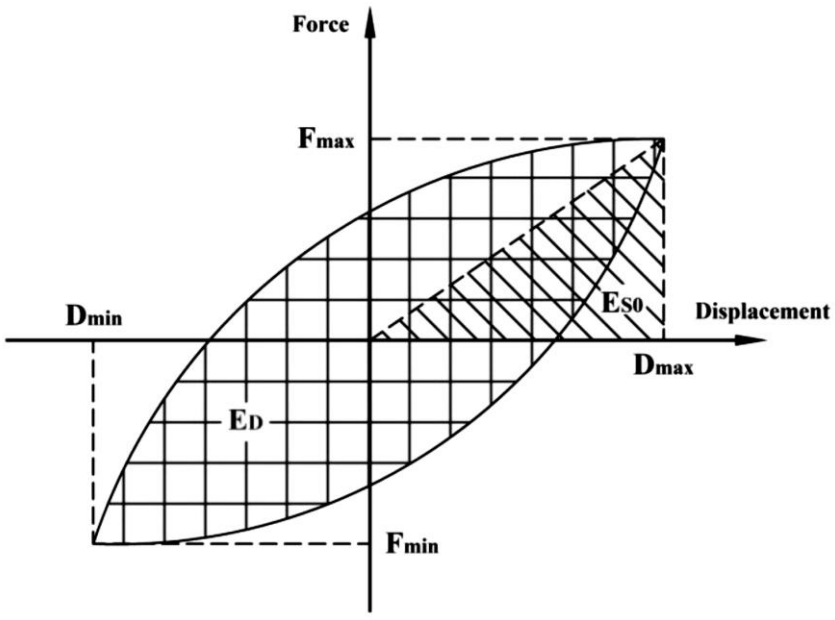

Fig. 6.13: Definition of dissipated energy and equivalent elastic energy (Shahri and Mousavi 2018)

E_{S0} is equivalent elastic energy which can be calculated using Eq. (6.2) as follows: (Shahri and Mousavi 2018)

$$E_{S0} = \frac{F_{max} D_{max}}{2} \tag{6.2}$$

where F_{max} and D_{max} are maximum values of force and displacement during the loading cycle, respectively. The comparison of equivalent damping ratio for elliptical steel slit damper (ESSD), butterfly-shaped steel strut damper (BSSD) and pintle damper (PD) are discussed in the following sections.

6.3.2 Comparison of Equivalent Damping Ratios for ESSD Specimens

The calculated values of dissipated energy, equivalent elastic energy and equivalent damping ratio for ESSD specimens are summarized in Table 6.2.

Table 6.2: Energy quantities for ESSD specimens

Specimens	H_T (mm)	B (mm)	A (mm)	t (mm)	E_D (kJ)	$\boldsymbol{E_{S0}}$ (kJ)	$\boldsymbol{\varepsilon_{eq}}$	$\boldsymbol{\frac{Bt}{H_T}}$
ESSD19	120	70	35	20	32.42	6.91	0.373	11.67
ESSD20	140	70	35	20	27.13	5.73	0.377	10.00
ESSD21	160	70	35	20	23.13	4.85	0.379	8.75
ESSD22	140	60	35	20	23.85	4.99	0.380	8.57
ESSD23	140	80	35	20	29.97	6.41	0.372	11.43
ESSD24	140	70	45	20	34.63	7.40	0.372	10.00
ESSD25	140	70	25	20	18.32	3.86	0.378	10.00
ESSD26	140	70	35	25	33.49	7.12	0.374	12.50
ESSD27	140	70	35	15	20.69	4.31	0.382	7.50

As shown in Fig. 6.14, all ESSD specimens experience desirable values of equivalent damping ratio. Specimen ESSD27 has the highest amount of equivalent damping ratio among all the specimens which is generally due to the low stiffness of thin plate damper.

It is also observed that the equivalent damping ratio is high when the parameter Bt / H_T is less than 10. This is due to the lesser stiffness of elliptic slit dampers, such as using long height or narrow width dampers.

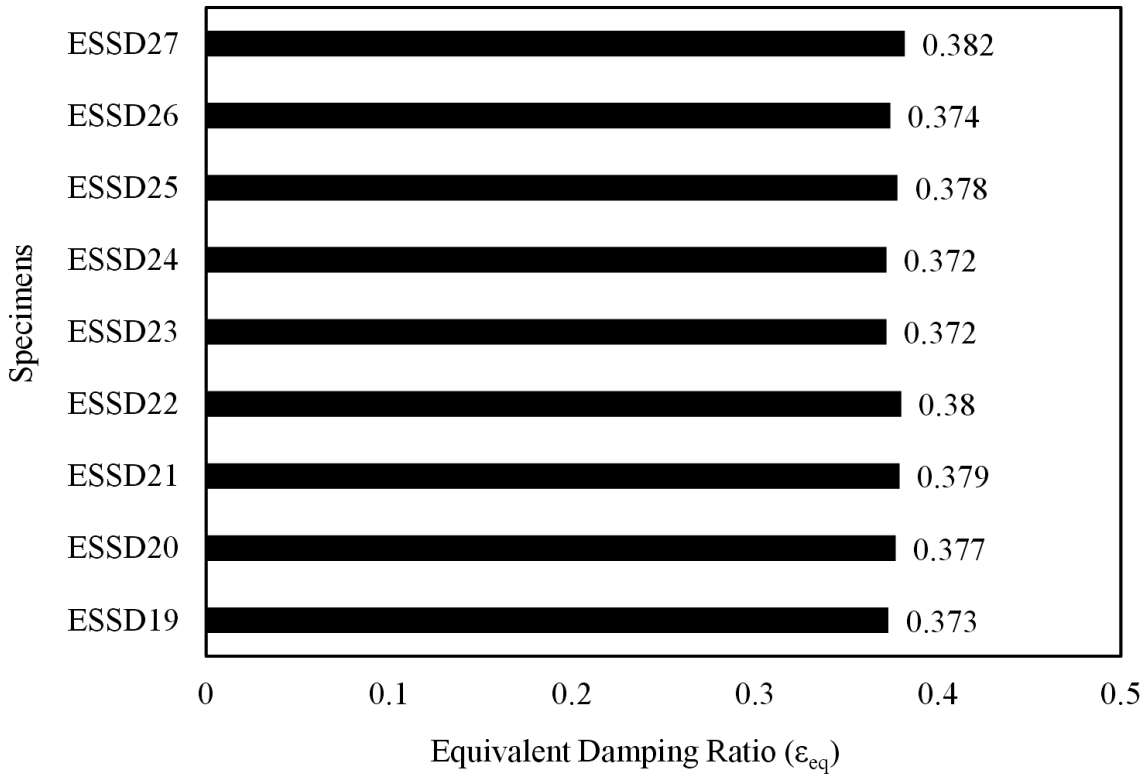

Fig. 6.14: Equivalent damping ratio for ESSD specimens

6.3.3 Comparison of Equivalent Damping Ratios for BSSD Specimens

In Table 6.3, the energy quantities for BSSD specimens are summarized.

Table 6.3: Energy quantities for BSSD specimens

Specimens	H_T (mm)	B (mm)	A (mm)	t (mm)	E_D (kJ)	$\boldsymbol{E_{S0}}$ (kJ)	$\boldsymbol{\varepsilon_{eq}}$	$\boldsymbol{\frac{Bt}{H_T}}$
BSSD16	120	60	30	15	29.12	6.09	0.381	7.50
BSSD17	140	60	30	15	24.53	5.12	0.381	6.43
BSSD18	160	60	30	15	20.82	4.33	0.383	5.63
BSSD19	140	70	30	15	31.04	6.59	0.374	7.50
BSSD20	140	50	30	15	17.72	3.64	0.387	5.36
BSSD21	140	60	40	15	24.89	5.23	0.379	6.43
BSSD22	140	60	20	15	22.59	4.77	0.377	6.43
BSSD23	140	60	30	20	32.07	6.78	0.376	8.57
BSSD24	140	60	30	10	16.81	3.42	0.391	4.29

The results in Fig. 6.15 show that when the parameter Bt / H_T is less than 6.5 the BSSD specimens experience high equivalent damping ratio which is occurred for high flexibility of the dampers. However, all other specimens also exhibit a favorable hysteretic performance and adequate equivalent damping ratio.

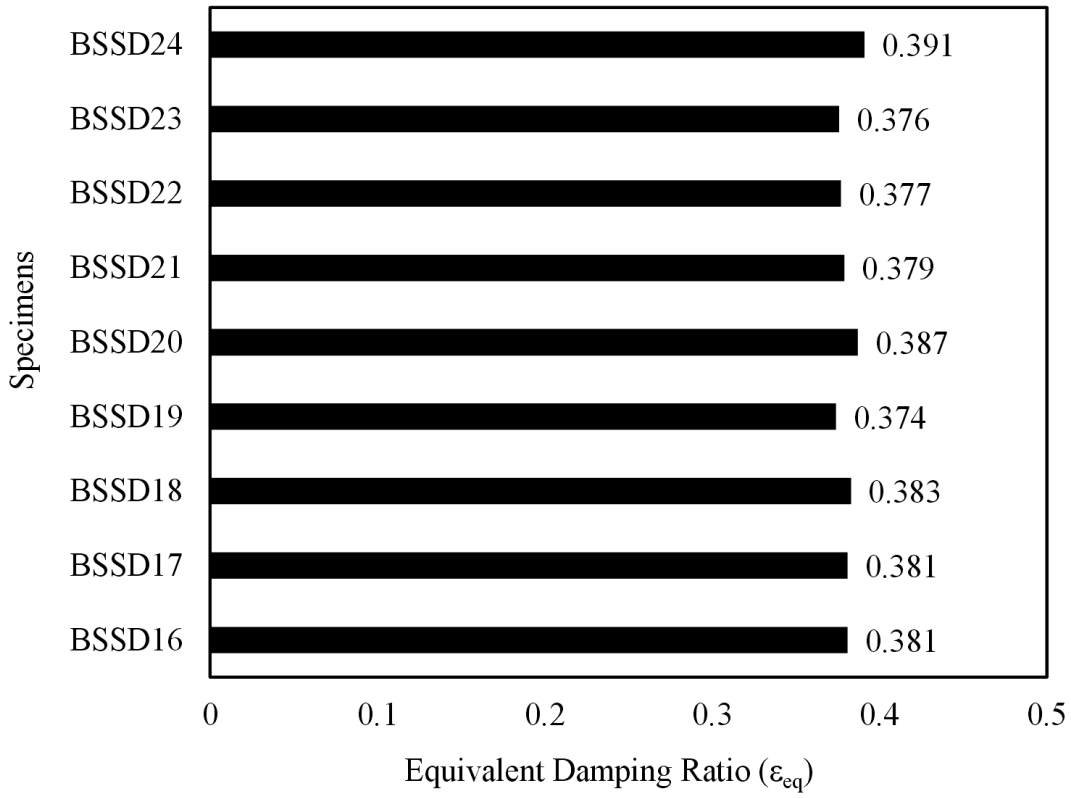

Fig. 6.15: Equivalent damping ratio for BSSD specimens

6.3.4 Comparison of Equivalent Damping Ratios for PD Specimens

For PD specimens, the calculated values of dissipated energy, equivalent elastic energy and equivalent damping ratio are mentioned in Table 6.4.

Table 6.4: Energy quantities for PD specimens

Specimens	H_T (mm)	L (mm)	B (mm)	A (mm)	E_D (kJ)	$\boldsymbol{E_{S0}}$ (kJ)	$\boldsymbol{\varepsilon_{eq}}$	$\boldsymbol{\frac{A}{B}}$	$\boldsymbol{\frac{L}{A}}$
PD22	120	110	50	25	39.86	8.82	0.359	0.5	4.4
PD23	140	130	50	25	33.71	7.37	0.364	0.5	5.2
PD24	160	150	50	25	24.49	6.25	0.312	0.5	6
PD25	140	130	60	25	45.38	10.47	0.345	0.42	5.2
PD26	140	130	40	25	18.97	4.03	0.375	0.63	5.2
PD27	140	130	50	35	36.47	8.06	0.360	0.7	3.7
PD28	140	130	50	15	17.72	4.96	0.284	0.3	8.7

It is seen from Fig. 6.16 that, the PD specimens experience low equivalent damping ratio when the A / B ratio is less than 0.4 and L / A ratio is more than 6. This is due to the excessive stiffness or shear yielding of the pintle dampers.

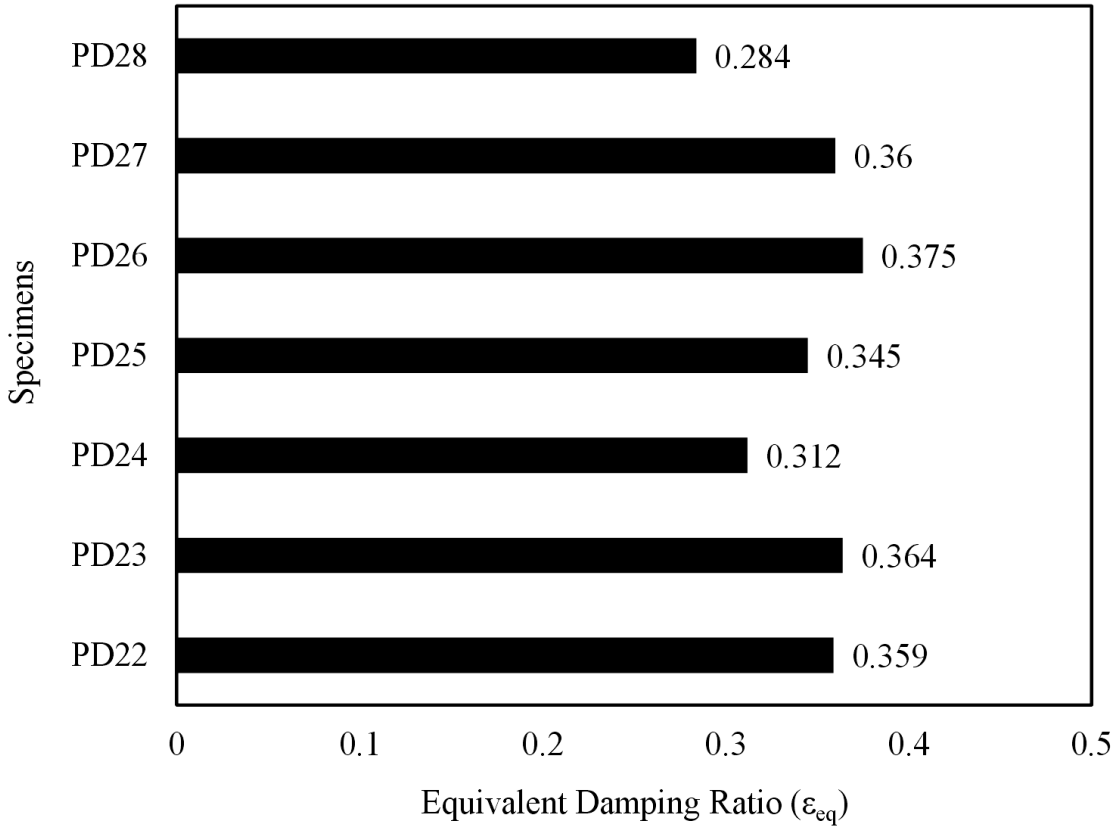

Fig. 6.16: Equivalent damping ratio for PD specimens

6.4 COMPARISON OF MATERIAL REQUIREMENT

The equivalent dampers made of mild steel are developed in section 5.2 for elliptical steel slit damper (ESSD), butterfly-shaped steel strut damper (BSSD) and pintle damper (PD) based on the plastic strength of the oblong steel slit damper (OSSD) using the developed plastic strength formula of these dampers. The weight of steel varies for the equivalent dampers of section 6.2 depending on the geometry as observed in Table 6.5. The average weight variation of total mild steel required for the produced equivalent dampers in section 6.2 are depicted in Fig. 6.17.

As noticed in Fig. 6.17, the equivalent elliptical steel slit damper (ESSD) and butterfly-shaped steel strut damper (BSSD) consume approximately 34% and 49% less material respectively and the pintle damper consumes approximately 203% more material than the equivalent oblong steel slit damper (OSSD). This is happened because stress distribution is distributed uniformly along the strut height of the ESSD and BSSD which has a parabolic profile whereas stress is concentrated at the end parts of the struts in OSSD. Since the PD

has different geometry than the other types of dampers, it requires more amount of steel than others. In assessing the cost of dampers, cost associated with fabrication must be taken into account in addition to the weight of the materials. While oblong steel slit damper, elliptical steel slit damper and butterfly-shaped steel strut damper have simpler geometry than pintle type dampers, fabrication cost of the former ones may be higher than the pintle types.

Table 6.5: Material requirement of equivalent dampers for different plastic strengths

Plastic strength of the damper, P_y (kN)	Volume of steel (cm^3)			
	OSSD	ESSD	BSSD	PD
200	1758.2	1157.9	898.4	4099.8
250	2197.9	1447.8	1123.2	4707.3
300	2637.7	1736.9	1347.9	5272.6
350	3077.4	2026.8	1572.8	5805.9
400	3516.5	2315.8	1796.8	6314.2

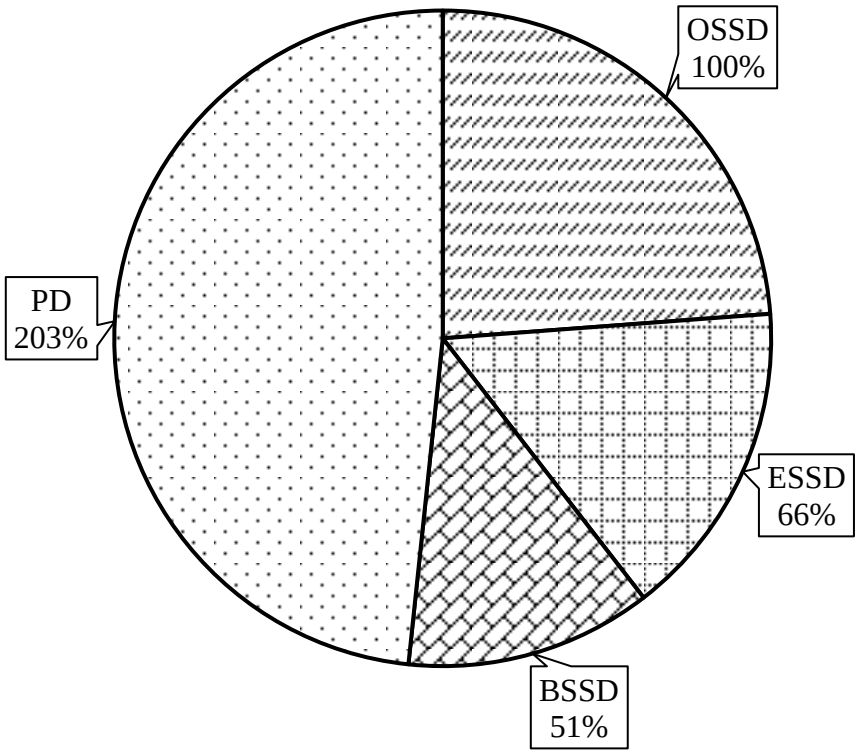

Fig. 6.17: Comparison of total weight of steel for the equivalent dampers

Therefore, from material consumption point of view, the butterfly-shaped steel strut damper (BSSD) requires least amount of material and the pintle damper (PD) requires more

material among the equivalent dampers. The costing of steel required for the damper is negligible compared to the whole structure. Therefore, the designer can choose any one type of damper for earthquake protection of structures. But the elliptical steel slit damper (ESSD) and butterfly-shaped steel strut damper (BSSD) are better among these.

6.5 REMARKS

It can be decided from the study carried in this section that oblong steel slit damper (OSSD), elliptical steel slit damper (ESSD), butterfly-shaped steel strut damper (BSSD) and pintle damper (PD) can be used alternatively in replacement of others at seismic moment connections using the developed plastic strength formula. It has been shown that the proposed closed-form semi-empirical analytical expressions of plastic strength for elliptical steel slit damper (ESSD), butterfly-shaped steel strut damper (BSSD) and pintle damper (PD) show stable hysteretic behavior like oblong steel slit damper (OSSD) for different plastic strengths. In view of the excellent agreement between the developed analytical formulation and finite element analysis results, the proposed formulas for determining plastic strength of the elliptical steel slit damper (ESSD), butterfly-shaped steel strut damper (BSSD) and pintle damper (PD) can be said to be satisfactory for design of any moment connection configuration. The equivalent dampers show satisfactory equivalent damping ratio for all specimens. Considering the parametric studies of developed equivalent dampers it can be said that steel shear dampers of different geometry can enhance the performance of beam-column connection system if the parameters are maintained in an efficient way. Among the equivalent dampers, the butterfly-shaped steel strut damper (BSSD) requires least amount of material and the pintle damper (PD) requires highest amount of material when comaperd to equivalent oblong steel slit damper (OSSD). The fabrication cost of pintle damper is the cheapest among the equivalent dampers. For earthquake protection of structures the designer can choose any one type of damper since the costing for damper is insignificant with respect to the costing of the whole building.

CHAPTER 7
CONCLUSIONS

7.1 GENERAL

In this study, a number of three-dimensional finite element models for steel moment connections with steel shear dampers of different geometry have been developed using finite element package considering both material and geometric non-linearity for the purpose of investigating probable equivalency in behavior of the dampers at the connection under static cyclic loading. Verification of these finite element models have been achieved with reference to the experiments of Chan and Albermani (2008), Oh et al. (2009) and Koken and Koroglu (2014) and these have shown good agreement which establish the reliability of finite element analysis scheme. The proposed models are then used for performing the study on shear dampers made of mild steel and having different geometry such as elliptical steel slit damper, butterfly-shaped steel strut damper and pintle damper and results are compared with the same from oblong steel slit damper. In order to observe the effects of different parameters of these dampers such as strut width, strut height, thickness etc. for different plastic strengths of oblong steel slit damper, some parametric studies have been performed. Refined plastic strength formula of the dampers are proposed depending on the pattern of parametric study results which can predict the plastic strength with reasonable accuracy. The results of the parametric studies have been compared with energy quantities and presented graphically to better understand the effects of different parameters on the system. Based on the parametric study some important relationships have also been observed which are pointed out in the following section.

7.2 GENERAL OBSEVATIONS FROM THE STUDY

The investigation on moment connections with steel shear dampers of different geometry by finite element method concludes with following outcomes:

i. The maximum value of force and moment sustained by the moment connection increases with increasing the strut width or thickness and decreasing the strut height of the dampers.
ii. The amount of energy dissipated by the dampers increases with increasing the strut width or thickness and decreasing the strut height of the dampers.

iii. All the elliptical steel slit damper (ESSD), butterfly-shaped steel strut damper (BSSD) and pintle damper (PD) specimens exhibit adequate equivalent damping ratio.

iv. The pintle damper which is introduced at beam-column connection in this study exhibits good hysteretic performance with excellent energy dissipation and can be used as an alternative of other dampers.

v. The equivalent elliptical steel slit damper (ESSD), butterfly-shaped steel strut damper (BSSD) and pintle damper (PD) absorb 4.62%, 4.90% and 4.68% less energy respectively than the oblong steel slit damper (OSSD) at the connection.

vi. The equivalent elliptical steel slit damper (ESSD) and butterfly-shaped steel strut damper (BSSD) consume approximately 34% and 49% less material respectively and the pintle damper (PD) consumes approximately 203% more material than the oblong steel slit damper.

vii. The oblong steel slit damper (OSSD), elliptical steel slit damper (ESSD), butterfly-shaped steel strut damper (BSSD) and pintle damper (PD) can be used alternatively by replacing the others at seismic moment connections with the help of proposed plastic strength formula of the dampers.

7.3 PROPOSAL FOR ESTIMATING PLASTIC STRENGTH OF DIFFERENT TYPES OF DAMPERS

Based on the parametric study, refined semi-empirical analytical expressions for estimating the plastic shear strength of dampers are proposed for elliptical steel slit damper (ESSD), butterfly-shaped steel strut damper (BSSD) and pintle damper (PD). Proposed expressions are validated against past experimental results and good agreement has been observed. Therefore, these expressions may be used to reasonably estimate the plastic strength of the said three types of dampers. The proposed range of parameters for the dampers need to be maintained in a proficient way to avoid inadequate hysteretic behavior, local buckling, low rotational capacity, low equivalent damping ratio, shear yielding and brittle failure of the connection system. When used appropriately, the proposed expressions of plastic strength of various types of dampers shall enable us to use any one type alternately in a building for earthquake protection of structures.

7.4 SCOPES FOR FUTURE INVESTIGATION

The following recommendations for future research work may be suggested according to the present study:

i. In the present study, the hysteretic behavior of different types of shear dampers made of mild steel are investigated. The behavior of these dampers made of different steel type can be compared and differentiated in future.

ii. The different types of shear dampers are compared based on the plastic strength of the dampers in the present study. In future, a comparative study can be carried based on the maximum displacement until failure of the dampers.

iii. The rate-dependency of material modeling are not incorporated in the study which can be investigated in future.

iv. The proposed more refined formula of plastic strength has not considered the slenderness effect, buckling phenomenon and shear yielding of the dampers which can be studied in future.

v. The equivalency of a few types of steel shear dampers in the moment connection system are investigated at present. Similar studies for other types of dampers can also be done in future.

vi. In the present study, the plastic strength formula of the dampers are developed and validated against numerical results. This formulation can be more justified by comparing with experimental results.

vii. At present, pintle damper is introduced for the beam-column connection system. The performance of this damper can be verified experimentally by using it as a substitute for other dampers.

viii. In the present study, the effect of some parameters of the equivalent dampers are observed in the connection system. The other parameters effect can be observed for further investigation.

REFERENCES

Aghlara, R., Tahir, M. M. and Adnan, A. (2015), "Comparative study of eight metallic yielding dampers", *Jurnal Teknologi*, 77:16, 119–125.

AISC (2016), "Prequalified connections for special and intermediate steel moment frames for seismic applications", *American Institute of Steel Construction*, May.

AISC (2009), "Facts for steel buildings-earthquakes and seismic design", *American Institute of Steel Construction*, November.

ANSYS, Inc. (2018), "ANSYS Help Viewer", *Analysis Systems*.

Bayat, M. and Bayat, M. (2014), "Seismic behavior of special moment-resisting frames with energy dissipating devices under near source ground motions", *Steel Compos. Struct., Int. J.*, 16(5), 533-557.

Benavent-Climent, A. (2010), "A brace-type seismic damper based on yielding the walls of hollow structural sections", *Eng. Struct.*, 32(4), 1113-1122.

Bergman, D. M. and Goel, S. C. (1987), "Evaluation of cyclic testing of steel plate devices for added damping and stiffness", *Report No. UMCE87-10.MI*, University of Michigan, MI, USA.

Chaboche, J. L. (1989), "Constitutive equations for cyclic plasticity and cyclic viscoplasticity", International Journal of Plasticity, 5, 247-302.

Chan, R. W. K. and Albermani, F. (2008), "Experimental study of steel slit damper for passive energy dissipation", *Eng. Struct.*, 30(4), 1058–1066.

Chan, R. W. K., Albermani, F. and Kitipornchai, S. (2013), "Experimental study of perforated yielding shear panel device for passive energy dissipation", *J. Constr. Steel Res.*, 91(2), 14-25.

Chen, S. J. and Chao, Y. C. (2001), "Effect of composite action on seismic performance of steel moment connections with reduced beam sections", *J. Constr. Steel Res.*, 57(4), 417–434.

Clark, P. W., Aiken, I. D., Tajirian, F., Kasai, K., Ko, E. and Kimura, I. (1999), "Design procedures for buildings incorporating hysteretic damping devices", *Proc., Int. Post-SMiRT Conf. Seminar on Seismic Isolation: Passive Energy Dissipation and Active Control of Vibrations of Structures*, Cheju, South Korea, 355–371.

De, L. L., Esguerra, C. and Almazan, J. L. (2004), "Earthquake behavior of structures with copper energy dissipaters", *Earthquake Engineering and Structural Dynamics*, 33:329–58.

Engelhardt, M. D. (2007), "Design of seismic-resistant steel building structures", *Seismic Design Module with the support of the American Institute of Steel Construction*, Version 1, March.

Engelhardt, M. D. and Sabol, T. A. (1998), "Reinforcing of steel moment connections with cover plates: Benefits and limitations", *Eng. Struct.*, 20 (4–6), 510–520.

Erdogan, M. and Ibrahim, G. (2015), "The finite element method and applications in engineering using ANSYS®", *Second Edition, Springer*, ISBN 978-1-4899-7550-8 (eBook).

FEMA-351 (2000), "Recommended seismic evaluation and upgrade criteria for existing welded steel moment-frame buildings", *Federal Emergency Management Agency*, June.

Gray, M. G., Christopoulos, C. and Packer, J. A. (2010), "Cast steel yielding fuse for concentrically braced frames", *In Proceedings of the 9th US National and 10th Canadian Conference on Earthquake Engineering.*

Ghabraie, K., Chan, R., Huang, X. and Xie, Y.M. (2010), "Shape optimization of metallic yielding devices for passive mitigation of seismic energy", *Eng. Struct.*, 32(8), 2258-2267.

Hedayat, A. A. (2015), "Prediction of the force displacement capacity boundary of an unbuckled steel slit damper", *J. Constr. Steel Res.*, 114, 30-50.

Imaoka, S. (2008), "Chaboche nonlinear kinematic hardening model", *Memo Number: STI0805A,* ANSYS Release 12.0.1.

Karavasilis, T. L., Kerawala, S. and Hale, E. (2012), "Hysteretic model for steel energy dissipation devices and evaluation of a minimal-damage seismic design approach for steel buildings", *J. Constr. Steel Res.*, 70, 358-367.

Ke, K. and Chen, Y. (2014), "Energy-based damage-control design of steel frames with steel slit walls", *Struct. Eng. Mech., Int. J.*, 52(6), 1157-1176.

Ke, K. and Yam, M. C. H. (2016), "Energy-factor-based damage-control evaluation of steel MRF systems with fuses", *Steel Compos. Struct., Int. J.*, 22(3), 589-611.

Kelly, I. M., Skinner, I. R. and Heine, A. J. (1972), "Mechanisms of energy absorption in special devices for use in earthquake resistant structures", *Bull. N.Z. Soc. Earthquake Engineering*, 5(3).

Kim, J., Yoon, J. C. and Kang, B. S. (2007), "Finite element analysis and modeling of structure with bolted joints", *Applied Mathematical Modeling*, 31, 895-911.

Kobori, T., Miura, Y., Fukusawa, E., Yamada, T., Arita, T., Takenaka, Y., Miyagawa, N., Tanaka, N. and Fukumoto, T. (1992), "Development and application of hysteresis steel dampers", *Proceedings of the 10th World Conference on Earthquake Engineering*, Madrid, Spain, July, Taylor and Francis, London, 2341–2346.

Koken, A. and Koroglu, M. A. (2011a), "An experimental study on energy absorption capacity of steel dampers subjected to shear force", *Int. J. Arts Sci.*, 4(2), 25–32.s

Koken, A. and Koroglu, M. A. (2011b), “Steel plate slit damper using on steel frames”, *e-J. New World Sci. Acad*., 6(4), 1A0219.

Koken, A. and Koroglu, M. A. (2012), “Waste rubber damper using on steel beam to column connection”, *Int. J. Arts Sci*., 5(4), 217–222.

Koken, A. and Koroglu, M. A. (2014), “Experimental study on beam-to-column connections of steel frame structures with steel slit dampers”, *J. Perform. Constr. Facil., ASCE*, 29(2).

Lee, C. H., Ju, Y. K., Min, J. K., Lho, S. H. and Kim, S. D. (2015), “Non-uniform steel strip dampers subjected to cyclic loadings”, *Eng. Struct*, 99, 192–204.

Lee, M. H. and Kim, J. (2015), “Seismic performance evaluation of moment frames with slit-friction hybrid dampers”, *Earthq. Struct., Int. J.,* 9(6), 1291-1311.

Lee, M. H., Oh, S. H., Huh, C., Oh, Y. S., Yoon, M. H. and Moon, T. S. (2002), "Ultimate energy absorption capacity of steel plate slit dampers subjected to shear force", *Steel Struct*., 2(2), 71-79.

Lee, C. H., Lho, S. H., Kim, D. H., Oh, J. and Ju, Y. K. (2016), “Hourglass-shaped strip damper subjected to monotonic and cyclic loadings”, *Engineering Structures,* 119, 122-134.

Lemaitre, J. and Chaboche, J. L. (1990), “Mechanics of solid materials”, *Cambridge University Press*, English edition.

Li, H., and Li, G. (2007), “Experimental study of structure with dual function metallic dampers”, *Engineering Structures*, 29(8), 1917-1928.

Lima, C., Martinelli, E. and Faella, C. (2015), "Cost-competitive steel devices for seismic retrofitting of RC frames: Model identification and nonlinear analysis", *J. Steel Struct. Constr*., 1, 104.

Maleki, S. and Bagheri, S. (2010a), "Pipe damper, part I: experimental and analytical study", *J. Constr. Steel Res.*, 66(8- 9), 1088-1095.

Maleki, S. and Bagheri, S. (2010b), "Pipe damper, part II: application to bridges", *J. Constr. Steel Res.*, 66(8-9), 1096- 1106.

Maleki, S. and Mahjoubi, S. (2013), "Dual-pipe damper", *J. Constr. Steel Res.*, 85, 81-91.

Maleki, S. and Mahjoubi, S. (2014), "Infilled-pipe Damper", *J. Constr. Steel Res.*, 98.

Nakashima, M., Iwai, S., Iwata, M., Takeuchi, T., Konomi, S., Akazawa, T. and Saburi, K. (1994), "Energy dissipation behaviours of shear panels made of low yield steel", *Earthq. Eng. Struct. Dyn.*, 23(12), 1299-1313.

Nakashima, M., Akazawa, T. and Tsuji, B. (1995), "Strain-hardening behavior of shear panels made of low-yield steel, II: Model", *Journal of Structural Engineering, ASCE*, 121(12), 1750–7.

Oh, S. H., Kim, Y. J. and Ryu, H. S. (2009), "Seismic performance of steel structures with slit dampers", *Eng. Struct.*, 31(9), 1997–2008.

Rai, D. C., Annam, P. K. and Pradhan, T. (2013), "Seismic testing of steel braced frames with aluminum shear yielding dampers", *Eng. Struct.*, 46(5), 737–747.

Sabelli, R., Mahin, S. and Change, C. (2003), "Seismic demands on steel braced frame buildings with buckling-restrained braces." *Eng. Struct.*, 25(5), 655–666.

Saffari, H., Hedayat, A. A. and Nejad, M. P. (2013), "Post-Northridge connections with slit dampers to enhance strength and ductility", *J. Constr. Steel Res.*, 80, 138–152.

Shahri, F. S. and Mousavi, S. R. (2018), "Seismic behavior of beam-to-column connections with elliptic slit dampers", *Steel and Composite Structures,* 26(3), 289-301.

Shen, J., Kitjasateanphun, T. and Srivanich, W. (2000), “Seismic performance of steel moment frames with reduced beam sections”, *Eng. Struct*., 22(8), 968–983.

Soong, T. T. and Spencer, J. B. F. (2002), “Supplemental energy dissipation: State-of-the art and state-of-the-practice”, *Engineering Structures*, 24, 243–59.

Tagawa, H. and Gao, J. (2012), “Evaluation of vibration control system with U-dampers based on quasi-linear motion mechanism”, *J. Constr. Steel Res*., 70, 213-225.

Tagawa, H., Yamanishi, T., Takaki, A. and Chan, R. W. K. (2016), "Cyclic behavior of seesaw energy dissipation system with steel slit dampers", *J. Constr. Steel Res*., 117, 24-34.

Teruna, D. R., Majid, T. A. and Budiono, B. (2015), “Experimental study of hysteretic steel damper for energy dissipation capacity”, *Advances in Civil Engineering*.

Tsai, K., Chen, H., Hong, C. and Su, Y. (1993), "Design of steel triangular plate energy absorbers for seismic-resistant construction", *Earthq. Spectra*, 9(3), 505-528.

Vasdravellis, G., Karavasilis, T. L. and Uy, B. (2014), “Design rules, experimental evaluation, and fracture models for high-strength and stainless-steel hourglass shape energy dissipation devices”, *Journal of Structural Engineering, ASCE*, 140(11), 1-14.

Wada, A., Connor, J. J., Kawai, H. and Iwata, M. (1992), “Damage tolerant structure”, *In: 5th U.S.-Japan workshop on the improvement of building structural design and construction practice*, 1–12.

Wada, A., Huang, Y.H., Yamada, T., Ono, Y., Sugiyama, S., Baba, M. and Miyabara, T. (1997), "Actual size and real time speed tests for hysteretic steel damper", *Proceedings of Stessa*, Kyoto, Japan, August, 778-785.

Woo, S. K., Lee, C. H., Ju, Y. K. and Kim, S. D. (2013), “Performance evaluation of optimized flexure dominated steel strip dampers under monotonic loading”, *J Archit Inst Korea*, 29(2), 3–11.

Xu, Y., Li, A., Zhou, X. and Sun, P. (2011), “Shape optimization study of mild steel slit dampers”, *Advanced Materials Research*, ISSN: 1662-8985, 168-170, 2434-2438.

Zahrai, S.M. (2015), "Cyclic testing of chevron braced steel frames with IPE shear panels", *Steel Compos. Struct., Int. J.*, 19(5), 1167-1184.

Zhang, C., Zhou, Y., Weng, D. G., Lu, D. H. and Wu, C. X. (2015), "A methodology for design of metallic dampers in retrofit of earthquake-damaged frame", *Struct. Eng. Mech., Int. J.*, 56(4), 569-588.